# Heat Death of an Ultracold Dipolar Gas

by

**Reuben R. W. Wang**

B.Eng., Singapore University of Technology and Design, 2019

M.S., University of Colorado Boulder, 2022

A thesis submitted to the

Faculty of the Graduate School of the

University of Colorado in partial fulfillment

of the requirements for the degree of

Doctor of Philosophy

Department of Physics

2024

Committee Members:

John L. Bohn, Chair

Andreas Becker

Josef Michl

Ana Maria Rey

Jun Ye

Wang, Reuben R. W. (Ph.D., Physics)

Heat Death of an Ultracold Dipolar Gas

Thesis directed by Prof. John L. Bohn

Optically trapping bulk gases of atoms and molecules at sub-microKelvin temperatures has become commonplace in several labs around the world. In particular, realizing low temperature samples of dipolar atoms and diatomic molecules has garnered great interest from the ultracold community, due to their long-range and anisotropic nature. At temperatures not yet low enough to achieve macroscopic quantum degeneracy, the gas constituents move about more or less classically, but experience collisions that can only be described accurately with quantum mechanics. By aligning these dipoles with an external field, collisions inherit highly anisotropic cross sections from their dipole-dipole interactions, leading to a wealth of tunable anisotropic collective dynamics.

I focus on characterizing anisotropic thermalization dynamics, which bears importance in many experimental applications. In fact, progressing in parallel with my graduate work has been exciting experiments with ultracold dipolar atoms and molecules. I tell the story of several collaborations in which my work was used to determine the scattering length of erbium atoms, characterize universal dipolar scattering, and open opportunities for optimal evaporative cooling of molecular gases[1] . This thesis lays out the development of several theoretical tools for investigating the relaxation of a nondegenerate dipolar gas, tracking its intricate journey to an eventual heat death.

P.S. If you bore easily, well, this thesis might just do nothing at all to help with that.

"*There will be some math but just endure it for a while and very soon, it will all go away.*"

– Umesh Vazirani (CU Boulder Physics Colloquium), 2023.

[1] All accounts here are based on true events.

## Dedication

For my parents.
To Andrew.

## Acknowledgements

Thank you, John. You've taught me so much both in science and outside of it. How someone with such scientific authority can exude the humility and radical candor you do, truly eludes me. A large part of who I am and want to be has been shaped by your mentorship and for that, I am immeasurably grateful. I don't know how many graduate students would willingly say this by the time they graduate, but I'm genuinely going to miss being your student.

To the wonderful Bohn group members, Eli and Hui, the lovely atmosphere you have created never ceased to foster a deep scientific curiosity in me, day in and day out. Eli (a.k.a. the Bob Ross of physics), your passion for learning and warmth as a senior graduate student has been paramount to my growth as a budding researcher. May you be blessed with all the Illegal Pete's your heart will ever desire. And as though this godsent bunch wasn't enough, the greater JILA ecosystem surrounding our little corner in the S-wing made my PhD a truly unparalleled experience. To the passionate faculty, staff and students, many of whom I owe this thesis to, you have made JILA the world leading scientific institute it is. It's been a privilege being part of it.

Despite what pop culture had me believing as a kid, physics is not done in isolation. Turns out, "evil genius hell-bent on world domination" is not the best model of a scientist to take from. I certainly could not have done most of my PhD work without the many amazing collaborators I was lucky enough to work with. To the wonderful theorists, Bo Xing, Eli Halperin, Hui Li, Anthony Polloreno, Ana Maria Rey, David Wellnitz and Daniel Messenger, you've all made a student out of me. I must also express exceptional gratitude to the experimentalists in the Ye, Ferlaino and Bloch/Luo groups. These include Jun Ye, Jun-Ru Li, Kyle Matsuda, Annette Carroll, Calder Miller, Junyu

Lin, Henrik Hirzler; Francesca Ferlaino, Alex Patscheider, Manfred Mark; Xin-Yu Luo, Andreas Schindewolf, Shrestha Biswas, Xing-Yan Chen and Immanuel Bloch. I'm humbled by the incredible patience you've had in answering the many questions I posed as a naive theorist. Collaborating with you has forever arrested my passion for the intoxicating pas de deux of experimental and theoretical physics. It's an honor to be part of the atomic and molecular physics world you are shaping.

Before my foray into physics (formally), I had first pursued an undergraduate degree in engineering because, well, the robotic arms at open day looked pretty cool. Naturally, my eventual transition into theoretical physics was not without invaluable guidance from my prior research mentors, professors Cheah Chin Wei, Riccardo Comin and Dario Poletti. To Dario, what an introduction to theoretical physics research that was. I owe much of my love and continued interest in the field of quantum science to you. In fact, I probably would not be writing this thesis if not for that summer UROP you offered.

There are also so many people I have to thank outside the context of research. As a first, I would be remiss not to give a massive shout-out to the consistent problem set crew that kept me sane through the nightmare that was classes. Sun, Benton, Luca and Jacob, I could not have done it without any one of you. To Jacob in particular, dude, we finally made it out. I sure hope you're still feeling *peckish* after all of it! Then there's all you other marvelous Boulderites: housemates, physics and non-physics friends. You've made Boulder feel like a home that I'll always want to come back to.

To my beloved family and friends in Singapore, for your unwavering care, love and support. Somehow, you managed to make a global pandemic seem like a time to look fondly back upon. Mom and Dad, you've provided me with more than a son could ever ask for. All of my accomplishments, now and in the future, are yours. HO5, TGIT, CB, LDG, GG, GD, AHAB: acronyms of the group chats with people who have taught me what friendship means. Tricia, for teaching me how to and making me want to be a better person. And Andrew, for always being my inspiration, confidant and guide. Thank you.

Last but certainly not least, I extend my most sincere gratitude to one of my most trea-

sured intellectual mentors, Mr Buddy (pictured in Fig. 1). The lessons in waking early, correcting magically appearing code bugs, and patience you've imparted have been invaluable to my PhD.


Figure 1: A true intellectual mentor. The puss in books, Mr Tesla Buddy.

If nothing else, I'd like to pass on the inspiring words a wise professor once said to us:

"*There are as many ways to be a successful physicist as there are successful physicists.*"

— Prof. Jesse Thaler (MIT 8.033 lecture), 2017.

I've held on to those words ever since and found them to be true, time and time again.

# Contents

**Chapter**

# Tables

**Table**



# Figures

**Figure**

# Chapter 1

# Introduction

Atoms: the very building blocks of observable matter in our universe. Consisting of a positively charged nucleus encased in a probabilistic cloud of electrons, individual atoms host a treasure trove of physics we have likely only scratched the surface of. Their complexities are only amplified in the bulk of many other such partners, whether they are chemically bonded or free to roam around. These are the ruminations of an atomic physicist, endeavoring a pursuit of understanding and control. Although lofty in its conception, great strides have already been made with the development of powerful tools like the laser and its associated technologies. Spectroscopy, optical trapping and quantum state manipulation, these are just some of the vast capabilities opened by our growing prowess in light and matter interaction.

Built off the many monumental works of others before, my work in this field has thus far focused on the collective aspects of atoms and molecules in their gaseous phase. Two crucial properties have made such systems interesting yet tractable for me to study: 1) their cooling down to ultracold temperatures, and 2) the dipolar character of the constituent particles. My job for the remainder of this thesis will be to motivate and communicate my contributions to these topics through the... captivating... medium of print.

## 1.1 Why ultracold?

Ever since the earliest inklings of its necessity [5], quantum mechanics has continued to inspire and yet, oftentimes confuse our scientific sensibilities. It is inevitable that to better understand

quantum mechanics, we need to be able to see more of it at play.

"*As usual, nature's imagination far surpasses our own...*"

—- Richard P. Feynman (The Character of Physical Law), 1965.

Sometimes, nature gives us that almost for free, showcasing quantum properties like semiconductivity in naturally occurring materials such as silicon–"just" needing us to look. Other times, human ingenuity is required to piece together specially designed systems, to probe the faint hum of our universe's quantum symphony. One such way to "hear the music", is to freeze out all thermal tumult, until just a few fundamental modes of the quantum wave are left singing.

This serene simplicity is what ultracold temperatures provide, being just about 10-millionths of a degree above absolute zero (that's a decimal point with 6 zeros behind it before a 1!). In this regime, most aspects of an atom come to a standstill, allowing the manipulation and measurement of each quantum energy level in isolation. Such exact addressability of quantum states is what bolsters the desire for ultracold atomic and molecular systems, but getting there is no easy feat. 1995 was the year that saw the first ever creation of a Bose-Einstein condensate [6], an ultracold state of quantum matter. That Nobel prize winning accomplishment was achieved right here at JILA with Rubidium atoms [7], then also at MIT with Sodium [8], trailblazing a new era of ultracold quantum science.

And so, we are now left to stand on the shoulders of these giants, amongst many others. To continue their legacy and forge a new tomorrow in ultracold physics. From artificial materials made of light [9], to mind numbingly precise measurement devices [10], the immense quantum control that ultracold temperatures bring will undoubtedly continue its unprecedented streak in technological advancement, and push the boundaries of scientific discovery.

## 1.2 Why dipoles?

More than 2000 years ago, some dude in ancient Greece said something like "The whole is greater than the sum of its parts". Point is, although single quantum particles might already be

interesting in and of themselves, what more harmonious melodies might a whole ensemble vocalize in chorus? Therein lies another key ingredient of desire, interactions. When 2 quantum bodies are allowed to interact, they can share energy and quantum information, enriching the physics of the system as a whole. The nature of these interactions plays an important role in this enrichment, with each kind allowing only specific quantum states to talk to one another, and only within certain distances.

Dipole-dipole interactions, in particular, support a variety of appealing properties. For one, they engage at pretty large distances, with the dipole interaction potential falling off only as the inverse cube of inter-particle spacing. Correlations thus develop without having to get too close, facilitating the spread of quantum information throughout a large many-body system of dipoles [11, 12]. For another, the interaction is highly anisotropic, depending on the orientation of each dipole relative to their inter-particle displacement. With rotational symmetry broken, the angular momentum of one dipole around the other can now couple to the internal spins of each dipole. How these dipoles are flung off from one another after a collision might therefore be tunable via their internal quantum spins [13]. Certainly, the allures are many, but most highlighted in this thesis will be the interaction anisotropies, segueing nicely into the next section.

## 1.3 What's in this thesis?

The remainder of the thesis is partitioned into 3 main parts. The first addresses microscopic collisional physics (Chap. 2), where I provide a brief primer on 2-body dipolar scattering in the ultracold regime, leaving in only the relevant details. The second considers the emergent effects of these collisions on macroscopic gas dynamics, both in the dilute and hydrodynamic regimes (Chaps. 3 to 5). The overarching theme here will be a gas' return to equilibrium, showcasing the theoretical tools I employ. The final icing on this thesis cake comes in Chap. 6, which discusses 2 immediate applications that, in many ways, provide motivation to the physics understood from the preceding chapters. Namely, the accurate determination of atomic scattering lengths via rethermalization experiments, and the evaporative cooling of polar molecules to quantum degeneracy.

For convenience, Tab. 1.1 presents a collated list of all the constants and variables that will be used consistently throughout this thesis. If a symbol crops up somewhere down the line that has not been defined within the chapter, don't set this thesis aside just yet! It will have probably been defined in this table. It should also be noted that all the equations used will be written in SI units, as one is inclined to when sitting in an office 2 kilometers away from the National Institute of *Standards* and Technology. On the off chance that one simply wants to go straight to the journal-formatted sources, here are all my publications relevant to the discussions of this thesis: [2, 3, 14–21]. Although I must say, you will necessarily miss out on the fun (if I don't say so myself) narrative this thesis weaves by jumping straight to those.

| Symbol | Descriptor |
|---|---|
| $\hbar$ | Reduced Planck's constant |
| $k_B$ | Boltzmann's constant |
| $\epsilon_0$ | Electric constant |
| $\mu_0$ | Magnetic constant |
| $\mu_B$ | Bohr magneton |
| $a_0$ | Bohr radius |
| $a_s$ | $s$-wave scattering length |
| $m$ | Atomic/molecular mass |
| $\mu$ | Reduced mass |
| $d$ | Magnetic/electric dipole moment |
| $a_d$ | Dipole length |
| $E_{\mathrm{dd}}$ | Dipole energy |
| $\mathcal{B}$ | Magnetic field |
| $\mathcal{E}$ | Electric field |
| $\Theta$ | Dipole tilt angle |

| Symbol | Descriptor |
|---|---|
| $t$ | Time coordinate |
| $\boldsymbol{r}$ | Position coordinate vector |
| $\boldsymbol{p}$ | Momentum coordinate vector |
| $f(\boldsymbol{r},\boldsymbol{p},t)$ | Classical phase space distribution |
| $n(\boldsymbol{r},t)$ | Number density |
| $T$ | Temperature |
| $\mathcal{T}(t)$ | Pseudotemperature |
| $\mathcal{N}(\Theta)$ | Number for rethermalization |
| $\boldsymbol{\varepsilon}(\Theta)$ | Collisional efficiency |
| Kn | Hydrodynamic Knudsen number |
| $\rho(\boldsymbol{r},t)$ | Local mass density |
| $\boldsymbol{U}(\boldsymbol{r},t)$ | Local flow velocity |
| $\boldsymbol{\kappa}(T)$ | Thermal conductivity tensor |
| $\boldsymbol{\mu}(T)$ | Viscosity tensor |
| $\mathcal{E}_{\mathrm{evap}}$ | Evaporation efficiency |

Table 1.1: A table of the notation used for constants and variables that will appear in this thesis. Bolded symbols are used to denote vectors, matrices and tensors.

Without further ado, here comes the music.

# Chapter 2

# Crash, Bam, Pow! Ultracold Dipolar Collisions

Ever found yourself in a vicious game of car-collision-chicken against your evil clone on a 10-lane superhighway? Eyes locked from a mile away. Pedal to the metal. This chapter speaks of much the same scenario, except there are no highspeed cars, no drivers and no highways. Just 2 extremely slow-moving identical particles that interact at long range, colliding not that violently with one another. The makings of a real Hollywood blockbuster. Crash, bam, pow!

This riveting process is exactly what occurs among the constituent particles of a nondegenerate gas. Free to roam around, gaseous particles are prone to bumping into one another, exchanging energy and momentum. These collisions can get rather complicated and are behind much of the interesting physics we will see arise. I provide a rapid overview of ultracold collisional physics in this chapter, setting the stage for the remainder of this thesis. The focus here will be on collisions that primarily result from dipole-dipole forces.

## 2.1 Ultracold collisions of magnetic atoms

### 2.1.1 Lanthanides: Little atomic magnets

Technological advances in the last 2 decades have permitted the cooling and trapping of magnetic lanthanide atoms [22–26], a huge triumph for the field of ultracold dipolar physics [27, 28]. With lanthanide atoms cooled to their electronic ground state, their open-shell electronic structure warrants that the application of a magnetic field results in a splitting of its Zeeman sublevels. For

instance, bosonic ($B$) erbium atoms have a ground state Zeeman sublevel spectrum given by

$$E^{B}_{\text{Zeeman}}(\mathcal{B}) = g_J \mu_B \mathcal{B} m_J, \tag{2.1}$$

where the Landé g-factor is reported in Ref. [29] as $g_J = 1.163801(1)$, $\mathcal{B}$ is the magnetic field strength and $m_J$ is the projection of the total angular momentum $J = 6$, onto the field axis. Fermionic (F) isotopes of erbium, on the other hand, possess a nuclear spin that gives rise to hyperfine structure. The energetically lowest state would reside in the total angular momentum quantum number $F = 19/2$ manifold, which has the Zeeman spectrum

$$E^{F}_{\text{Zeeman}}(\mathcal{B}) = g_F \mu_B \mathcal{B} m_F + 2\pi\hbar z_2 \mathcal{B}^2 (F^2 - m_F^2), \tag{2.2}$$

where $m_F$ is the projection of total angular momentum, while $g_F = 0.735032$ and $z_2 = -12.76(1)$ Hz/G$^2$ are the linear and quadratic Zeeman coefficients respectively [30]. The relevant Zeeman energy splittings for both isotopes are plotted in Fig. 2.1 in units of milliKelvin.

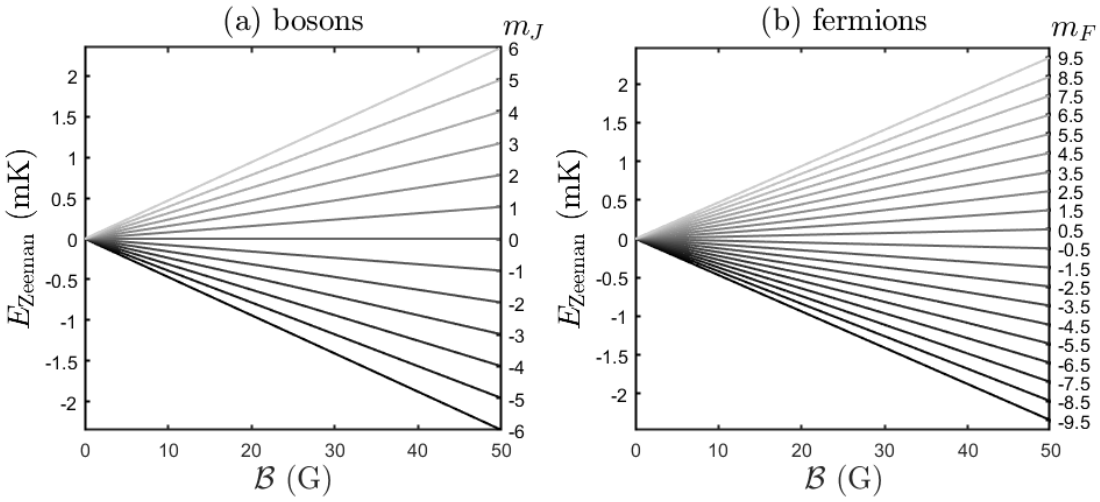


Figure 2.1: Plot of the Zeeman energy levels as a function of applied magnetic field for bosonic $^{166}$Er (a), and fermionic $^{167}$Er (b) isotopes of erbium.

Because of the still mostly linear Zeeman splitting at modest magnetic fields, a magnetic dipole moment $d_J \approx g_J m_J \mu_B$, is induced in the atoms that in their spin-stretched groundstate (i.e. the lowest $m_J$ sublevel), gives both isotopes approximately the same value of $d \approx -6.9828\mu_B$.

So fermionic magnetic atoms, usually collisionally invisible at ultracold temperatures with no $s$-wave scattering, can now experience collisions via their dipole-dipole interactions. You might be concerned that such collisions could jostle these atoms out of their Zeeman groundstates, but here in lies the benefit that ultracold temperatures bring. At temperatures on the order of $T \sim 100$ nK and below, the application of order $\mathcal{B} \sim 10$ G magnetic fields result in a Zeeman energy splitting of $\Delta E/k_B \sim 0.1$ mK as seen from Fig. 2.1. Colliding atoms prepared in their spin-stretched ground state will therefore remain spin polarized in that state, by virtue of all other states being energetically forbidden.

### 2.1.2 Ultracold scattering: A primer

The cool (pun possibly intended) thing about ultracold experiments is that in principle, the interactions between colliders are completely known[1] . Our task as atomic theorists is therefore to exploit this knowledge for computing scattering observables that, god willing all factors of 2 are tracked correctly, can be used to predict and understand experimental phenomena. This runs rather contrary to say high energy physics experiments, where observed scattering data from collider experiments are instead, used to infer the a priori unknown interacting Lagrangian. But that's a topic for someone else's thesis. Ultracold scattering considers 2 particles headed on a collision course with everything else in the universe being negligible to the relevant physics. In this case, the Hamiltonian between the 2 bodies is given by

$$\widehat{H} = -\frac{\hbar^2}{2\mu}\boldsymbol{\nabla}_r^2 + \widehat{h}_1 + \widehat{h}_2 + \widehat{V}_{\rm int}(\boldsymbol{r}), \tag{2.3}$$

where $\boldsymbol{r} = \boldsymbol{r}_1 - \boldsymbol{r}_2$ is the relative position between particles, $\mu = m_1 m_2/(m_1 + m_2)$ is the reduced mass, $\widehat{h}_i$ $(i = 1, 2)$ is the single-particle Hamiltonian containing all the internal atomic/molecular structure stuff, and $\widehat{V}_{\rm int}$ is the interaction potential between the 2 particles. Wide hats are used to denote quantum operators, while normal sized hats will denote unit vectors.

As far as degrees of freedom go, there are the spatial ones relevant to $\boldsymbol{r}$, and the internal state

[1] What I mean here is that technically, you could write down all terms in the 2-particle Hamiltonian, although actually handling it for calculations is usually impossible without some form of approximation.

ones relevant to $\widehat{h}_1 + \widehat{h}_2$. The entire Hilbert space is thus spanned by the basis states:

$$\langle r, \theta, \phi | E; \ell, m_\ell; \nu \rangle = r^{-1} u^E_{\ell, m_\ell, \nu}(r) Y_{\ell, m_\ell}(\theta, \phi) \, |\nu\rangle \,, \tag{2.4}$$

where $Y_{\ell,m_\ell}(\theta, \phi)$ are spherical harmonics and $|\nu\rangle$ diagonalizes both 1-body Hamiltonians

$$\left(\widehat{h}_1 + \widehat{h}_2\right) |\nu\rangle = \epsilon_\nu \, |\nu\rangle \,, \tag{2.5}$$

with associated eigenenergies $\epsilon_\nu$. When asymptotically far apart, the interaction potential $\widehat{V}_{\text{int}}(\boldsymbol{r})$ vanishes to leave a series of energetic *thresholds* $\epsilon_\nu$. The asymptotically good quantum numbers $\nu$, are therefore said to label the asymptotic *scattering channels*. Represented in the basis of Eq. (2.4), the time-independent Schrödinger equation results in a coupled set of radial equations:

$$\begin{aligned} \delta_{\ell,\ell'} \delta_{m_\ell, m'_\ell} \delta_{\nu,\nu'} \left( \frac{d^2}{dr^2} - \frac{\ell(\ell+1)}{r^2} + \frac{2\mu(E - \epsilon_{\nu'})}{\hbar^2} \right) u^E_{\ell', m'_\ell, \nu'}(r) \\ = \frac{2\mu}{\hbar^2} \int d^2\hat{\boldsymbol{r}} \, \langle \nu | \, Y^*_{\ell, m_\ell}(\hat{\boldsymbol{r}}) \widehat{V}_{\text{int}}(\boldsymbol{r}) Y_{\ell', m'_\ell}(\hat{\boldsymbol{r}}) \, \left| \nu' \right\rangle \, u^E_{\ell', m'_\ell, \nu'}(r), \end{aligned} \tag{2.6}$$

that, in general, has interaction matrix elements (right-hand side above) couple the various scattering channels, and possibly even the $|\ell, m_\ell\rangle$ angular momentum partial waves if $\widehat{V}_{\text{int}}$ is anisotropic. These couplings can result in complicated solutions, mostly requiring numerical methods to obtain.

But as with many problems in physics, interpretable quantum scattering solutions are best constructed along with a suitably chosen ansatz. A natural one emerges from the physical picture of 2 particles approaching from infinitely far away (pre-collision), interact strongly within the effective range of their interactions, then depart infinitely far apart once more from the interaction aftermath (post-collision):

$$|\psi_\nu(\boldsymbol{r})\rangle \sim \underbrace{e^{i\boldsymbol{k}_\nu \cdot \boldsymbol{r}} \, |\nu\rangle}_{\text{pre-collision}} + \sum_{\nu'} \underbrace{f_{\nu,\nu'}(\hat{\boldsymbol{r}}) \frac{e^{ik_{\nu'} r}}{r} \left| \nu' \right\rangle}_{\text{post-collision}}, \tag{2.7}$$

where $k_{\nu'} = \sqrt{2\mu(E - \epsilon_{\nu'})/\hbar^2}$ is the scattered wavenumber, and $f_{\nu,\nu'}(\hat{\boldsymbol{r}})$ is the scattering amplitude associated with scattering from channel $\nu$ to $\nu'$. Fig. 2.2 gives a visual reference for Eq. (2.7). Relating the inbound and outbound particle-pair wavefunctions at infinite relative distance is referred

to as a *completed collision*. To connect the ansatz of Eq. (2.7) with the representation of Eq. (2.6), a planewave expansion of the free particle solution can be performed

$$e^{i\boldsymbol{k}_\nu\cdot\boldsymbol{r}}\,|\nu\rangle = 4\pi\sum_{\ell=0}^{\infty}\sum_{m_\ell=-\ell}^{\ell} i^\ell Y^*_{\ell,m_\ell}(\hat{\boldsymbol{k}}_\nu) j_\ell(k_\nu r) Y_{\ell,m_\ell}(\hat{\boldsymbol{r}})\,|\nu\rangle\,, \tag{2.8}$$

which has the $k_\nu r \gg 1$ asymptotic form

$$e^{i\boldsymbol{k}_\nu\cdot\boldsymbol{r}}\,|\nu\rangle \to \frac{2\pi i}{r}\sum_{\ell=0}^{\infty}\sum_{m_\ell=-\ell}^{\ell} i^\ell \frac{Y^*_{\ell,m_\ell}(\hat{\boldsymbol{k}}_\nu)}{\sqrt{k_\nu}}\left(e^{-i(k_\nu r-\ell\pi/2)} - e^{i(k_\nu r-\ell\pi/2)}\right)\frac{Y_{\ell,m_\ell}(\hat{\boldsymbol{r}})}{\sqrt{k_\nu}}\,|\nu\rangle\,. \tag{2.9}$$

The expansion above identifies pieces that are incoming towards ($e^{-i(k_\nu r-\ell\pi/2)}$) and outgoing away from ($e^{i(k_\nu r-\ell\pi/2)}$) the scattering center.

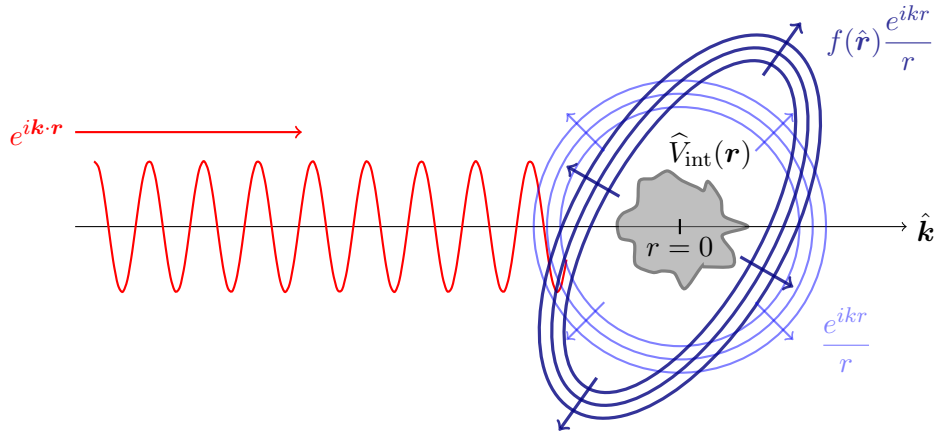


Figure 2.2: Cartoon of quantum scattering. The red curve denotes the incident $e^{i\boldsymbol{k}\cdot\boldsymbol{r}}$ planewave, light blue the $e^{ikr}/r$ spherical wave and dark blue the $f(\hat{\boldsymbol{r}})e^{ikr}/r$ scattered wave. The red and blue wave fronts are **not** to scale.

Because probability must be conserved in quantum mechanics, the outbound flux of particles in the planewave expansion can only be modified only by a unitary transformation after the scattering process:

$$|\psi_\nu(\boldsymbol{r})\rangle \sim \frac{2\pi i}{r}\sum_{\ell,m_\ell}\sum_{\ell',m'_\ell}\sum_{\nu'} i^\ell \frac{Y^*_{\ell,m_\ell}(\hat{\boldsymbol{k}}_\nu)}{\sqrt{k_\nu}}\Big(\delta_{\ell,\ell'}\delta_{m_\ell,m'_\ell}\delta_{\nu,\nu'}e^{-i(k_\nu r-\ell\pi/2)} - S^{\nu,\nu'}_{\ell,m_\ell;\ell',m'_\ell}(k_\nu)e^{i(k_{\nu'}r-\ell'\pi/2)}\Big)\frac{Y_{\ell',m'_\ell}(\hat{\boldsymbol{r}})}{\sqrt{k_{\nu'}}}\,|\nu'\rangle\,, \tag{2.10}$$

where $S^{\nu,\nu'}_{\ell,m_\ell;\ell',m'_\ell}$ is the unitary $S$-matrix that depends on the incident scattering energy. Upon comparing Eq. (2.10) and Eq. (2.7), the scattering amplitude is therefore identified as

$$f_{\nu,\nu'}(\hat{\boldsymbol{r}}) = -\frac{2\pi}{\sqrt{k_\nu k_{\nu'}}} \sum_{\ell,m_\ell} \sum_{\ell',m'_\ell} i^{\ell-\ell'} Y^*_{\ell,m_\ell}(\hat{\boldsymbol{k}}_\nu) T^{\nu,\nu'}_{\ell,m_\ell;\ell',m'_\ell}(k_\nu) Y_{\ell',m'_\ell}(\hat{\boldsymbol{r}}), \tag{2.11}$$

where the $T$-matrix is defined as

$$T^{\nu,\nu'}_{\ell,m_\ell;\ell',m'_\ell}(k_\nu) = i\left(S^{\nu,\nu'}_{\ell,m_\ell;\ell',m'_\ell}(k_\nu) - \delta_{\ell,\ell'}\delta_{m_\ell,m'_\ell}\delta_{\nu,\nu'}\right). \tag{2.12}$$

As will be essential to the rest of this thesis, the scattering amplitude then permits us to evaluate the differential cross section

$$\frac{d\sigma_{\nu,\nu'}}{d\Omega}(\hat{\boldsymbol{r}}) = \frac{k_{\nu'}}{k_\nu}\left|f_{\nu,\nu'}(\hat{\boldsymbol{r}})\right|^2, \tag{2.13}$$

which represents the ratio of differential area $d\sigma$ through which particles are incident, over the differential solid angle $d\Omega$ into which these particles scatter.

### 2.1.3 Dipolar interactions

For 2 particles that interact primarily via dipole-dipole forces, the potential between them is

$$\widehat{V}_{\text{int}}(\boldsymbol{r}) \approx \widehat{V}_{\text{dd}}(\boldsymbol{r}) = \frac{\widehat{\boldsymbol{d}}_1 \cdot \widehat{\boldsymbol{d}}_2 - 3(\widehat{\boldsymbol{d}}_1 \cdot \hat{\boldsymbol{r}})(\widehat{\boldsymbol{d}}_2 \cdot \hat{\boldsymbol{r}})}{4\pi\eta_0 r^3}. \tag{2.14}$$

where $\eta_0 = \epsilon_0$ for electric dipoles and $\eta_0 = \mu_0^{-1}$ for magnetic ones. In the case of identical spin-polarized magnetic atoms described in Sec. 2.1.1, the scattering problem effectively reduces to a single-channel one, involving only the lowest Zeeman sublevel with the rest being energetically disallowed. Only considering 1 channel removes all the operator structure of the dipole operators, so the potential reduces to

$$V_{\text{dd}}(\boldsymbol{r}) = \frac{\mu_0 d^2}{4\pi r^3}\left[1 - 3(\hat{\boldsymbol{\mathcal{B}}} \cdot \hat{\boldsymbol{r}})^2\right], \tag{2.15}$$

where $\hat{\boldsymbol{\mathcal{B}}}$ is the direction of the external magnetic field, along which the dipoles with dipole moment $d$ are polarized. With $V_{\text{dd}}$ being dominant and involving only a single relevant dipole matrix element, it is appropriate to define a system of units around $d$ as presented in Tab. 2.1. Even with this

| dimension | quantity |
|---|---|
| mass | $m_d = \mu$ |
| length | $a_d = \dfrac{\mu d^2}{4\pi\epsilon_0\hbar^2}$ |
| energy | $E_{\rm dd} = \dfrac{\hbar^2}{\mu a_d^2}$ |

Table 2.1: A system of dipole units based on the space-fixed dipole moment $d$.

simplification, the potential retains its coordinate space anisotropy, so that angular momentum is no longer conserved.

Full scattering solutions to Eq. (2.6) between these atoms then require the matrix elements of $V_{\rm dd}(\boldsymbol{r})$ in the partial wave basis, which are evaluated with $\hat{\boldsymbol{\mathcal{B}}} = \hat{\boldsymbol{z}}$ as

$$\begin{aligned}\langle \ell, m_\ell | \, V_{\rm dd}(\boldsymbol{r}) \, | \ell', m' \rangle &= -\frac{d^2}{4\pi\epsilon_0 r^3} \langle \ell, m_\ell | \, 4\sqrt{\frac{\pi}{5}} Y_{2,0}(\theta,\phi) \, | \ell', m'_\ell \rangle \\ &= -\frac{d^2}{4\pi\epsilon_0 r^3} 2(-1)^{m_\ell} \sqrt{(2\ell+1)(2\ell'+1)} \begin{pmatrix} \ell & 2 & \ell' \\ 0 & 0 & 0 \end{pmatrix} \begin{pmatrix} \ell & 2 & \ell' \\ -m_\ell & 0 & m'_\ell \end{pmatrix}. \quad (2.16)\end{aligned}$$

The 2-by-3 arrays in parentheses above are Wigner 3-j symbols. But before finding solutions in such generality, simpler ones can be obtained if collisions are restricted to the regime of ultra low energies. Although strictly approximate, these simpler solutions show incredible accuracy in reproducing experimental data under a variety of circumstances, so much so that most of this thesis leverages this approximation.

### 2.1.4 Close-to-threshold dipolar scattering

At kinetic energies that are small compared to the characteristic energy of the interaction $E \ll E_{\rm dd}$, the collision is considered *close-to-threshold*[2] [31]. Collisions in the close-to-threshold regime are usually associated with few partial waves contributing to the scattering process. This is true for power law interaction potentials $r^{-n}$ with $n > 3$, where Wigner's threshold law dictates that higher partial waves diminish as increasing powers of the wavenumber $k$ [31]. But it turns

[2] Threshold here refers to the scattering energetic thresholds when the atoms are asymptotically far apart, as described in Sec. 2.1.2.

out that approaching zero energy, all the $T$-matrix elements (2.12) from dipolar scattering have the same energy dependence $T_{\ell,m_\ell;\ell',m'_\ell} \sim \sqrt{E}$ [1, 32, 33]. This energy independence translates to the close-to-threshold integral cross section

$$\overline{\sigma} = \Delta_s \frac{\pi}{k^2} \sum_{\ell,m_\ell} \sum_{\ell',m'_\ell} \left| T_{\ell,m_\ell;\ell',m'_\ell}(k) \right|^2, \tag{2.17}$$

being completely independent of energy, seen to emerge in Fig. 2.3 with a plot[3] of $\overline{\sigma}$ vs $E$. In the expression above, $\Delta_s$ is a symmetry factor that accounts for scattering between distinguishable ($\Delta_s = 1$) or indistinguishable ($\Delta_s = 2$) particles [34].

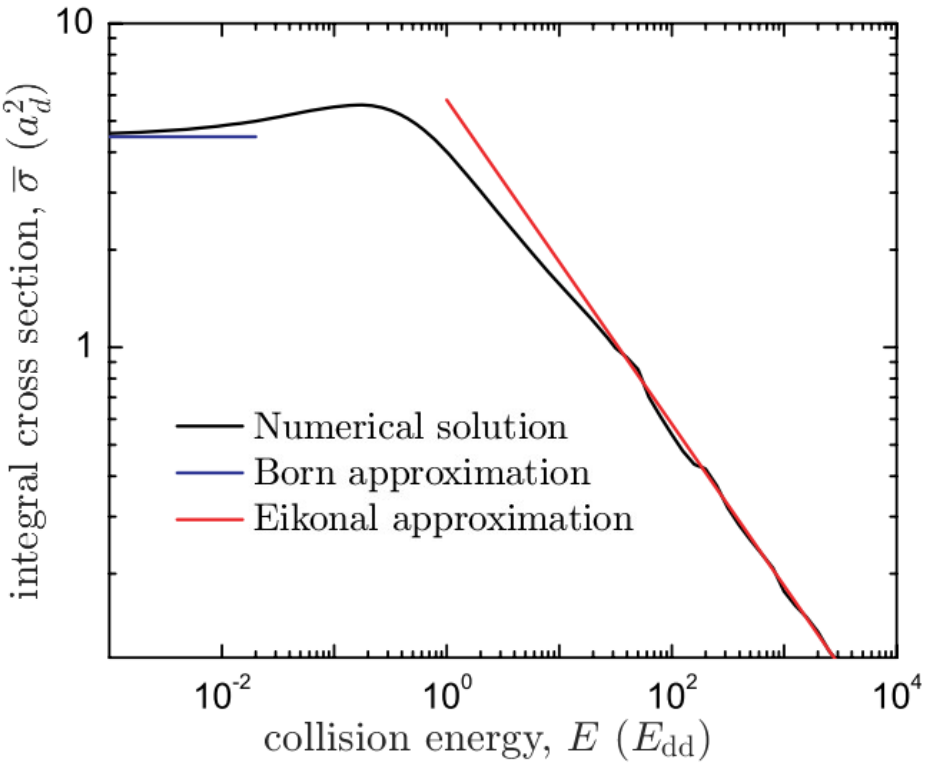


Figure 2.3: Plot of the integral cross section $\overline{\sigma}$, as a function of collision energy $E$ (black curve). The axes are both on a logarithmic scale in dipole units (2.1). For comparison, the low energy Born ($\overline{\sigma} \sim 1$) and high energy Eikonal ($\overline{\sigma} \sim E^{-1/2}$) approximations are also plotted in blue and red respectively. The plot is adapted from Ref. [1].

Because the threshold laws between dipolar atoms are the same for all partial waves, a large

[3] The plot in Fig. 2.3 was computed for distinguishable dipoles (includes all partial waves), with the $s$-wave scattering length carefully tuned to zero (see Sec. 2.1.5).

number of them may be required to converge the scattering calculations of $f(\hat{\boldsymbol{r}})$ (2.11). It is, therefore, more convenient not to expand the wavefunction in terms of partial waves, but to describe the scattering of dipolar species directly in coordinate space [35]. Such a formulation is most easily obtained via the Lippmann-Schwinger equation

$$\psi(\boldsymbol{r}) \sim e^{i\boldsymbol{k}\cdot\boldsymbol{r}} - \frac{2\mu}{\hbar^2}\frac{1}{4\pi}\int d^3\boldsymbol{r}' e^{-i\boldsymbol{k}\cdot\boldsymbol{r}'} V_{\rm dd}(\boldsymbol{r}')\psi(\boldsymbol{r}')\frac{e^{ikr}}{r}, \tag{2.18}$$

that is an asymptotic integral form of the Schrödinger equation [36], from which the scattering amplitude is read off as

$$f(\hat{\boldsymbol{r}}) = -\frac{2\mu}{\hbar^2}\frac{1}{4\pi}\int d^3\boldsymbol{r}' e^{-i\boldsymbol{k}\cdot\boldsymbol{r}'} V_{\rm dd}(\boldsymbol{r}')\psi(\boldsymbol{r}'). \tag{2.19}$$

Itself dependent on the scattering solution $\psi(\boldsymbol{r})$, this complication of evaluating Eq. (2.19) is sidestepped by employing the Born approximation, commonly used for collisions at high energies. It turns out, however, that this approximation works just as well for ultracold dipoles by virtue of the Born approximated $f(\hat{\boldsymbol{r}})$ having the correct close-to-threshold energy dependence: none. In the parlance of partial waves, it is the $\ell(\ell+1)/r^2$ angular momentum barrier that prevents low energy scatterers from seeing much else other than the long-range tail of the dipolar $r^{-3}$ potential before they get reflected. So $V_{\rm dd}$ is but a perturbance to the incident planewave, which echoes the song usually sung about the Born approximation.

The scattering amplitude up to first-order in Born approximation is then evaluated as

$$\begin{aligned}
\lim_{E/E_{\rm dd}\to 0} f(\hat{\boldsymbol{r}}) &\approx -\frac{2\mu}{\hbar^2}\frac{1}{4\pi}\int d^3\boldsymbol{r} e^{-i\boldsymbol{k}'\cdot\boldsymbol{r}} V_{\rm dd}(\boldsymbol{r}) e^{i\boldsymbol{k}\cdot\boldsymbol{r}} \\
&= -\frac{\mu d^2}{4\pi\epsilon_0\hbar^2}\int \frac{d^3\boldsymbol{r}}{2\pi}\frac{1-3\cos^2\theta}{r^3}e^{i\boldsymbol{q}\cdot\boldsymbol{r}}, \quad \text{with } \boldsymbol{q} = \boldsymbol{k} - \boldsymbol{k}', \\
&= \frac{\mu d^2}{4\pi\epsilon_0\hbar^2}\int \frac{d^3\boldsymbol{r}}{\pi}\frac{C_{2,0}(\theta,\phi)}{r^3}e^{i\boldsymbol{q}\cdot\boldsymbol{r}}, \qquad \text{where } C_{2,0}(\theta,\phi) = 2\sqrt{\frac{\pi}{5}}Y_{2,0}(\theta,\phi), \\
&= \frac{\mu d^2}{4\pi\epsilon_0\hbar^2}\int \frac{d^3\boldsymbol{r}}{\pi}\frac{C_{2,0}(\theta,\phi)}{r^3} 4\pi\sum_{\ell,m_\ell} i^\ell Y^*_{\ell,m_\ell}(\hat{\boldsymbol{q}}) j_\ell(qr') Y_{\ell,m_\ell}(\hat{\boldsymbol{r}}') \\
&= \frac{\mu d^2}{4\pi\epsilon_0\hbar^2}\sum_{\ell,m_\ell} 8\sqrt{\frac{\pi}{5}} i^\ell Y^*_{\ell,m_\ell}(\hat{\boldsymbol{q}}) \int d^2\Omega Y_{2,0}(\Omega) Y_{\ell,m_\ell}(\Omega) \int dr \frac{j_\ell(qr)}{r} \\
&= \frac{\mu d^2}{4\pi\epsilon_0\hbar^2}\sum_{\ell,m_\ell} 8\sqrt{\frac{\pi}{5}} i^\ell Y^*_{\ell,m_\ell}(\hat{\boldsymbol{q}}) \delta_{\ell,2}\delta_{m_\ell,0}\frac{\sqrt{\pi}\Gamma(\ell/2)}{4\Gamma((3+\ell)/2)}
\end{aligned} \tag{2.20}$$

$$= a_d \left( \frac{2}{3} - \frac{(\hat{\boldsymbol{k}} \cdot \hat{\boldsymbol{\mathcal{B}}} - \hat{\boldsymbol{k}}' \cdot \hat{\boldsymbol{\mathcal{B}}})^2}{1 - \hat{\boldsymbol{k}} \cdot \hat{\boldsymbol{k}}'} \right), \qquad \text{using} \;\; \cos^2 \theta_q = \frac{(\hat{\boldsymbol{k}} \cdot \hat{\boldsymbol{\mathcal{B}}} - \hat{\boldsymbol{k}}' \cdot \hat{\boldsymbol{\mathcal{B}}})^2}{2(1 - \hat{\boldsymbol{k}} \cdot \hat{\boldsymbol{k}}')}. \tag{2.21}$$

As written, the scattering amplitude above corresponds to the scattering of distinguishable particles, which is not the case for the identical groundstate atoms of interest. Accurate functional forms of $f(\hat{\boldsymbol{r}})$ therefore requires the appropriate symmetrization (+) for bosons, and antisymmetrization (-) for fermions [37]:

$$f_{F,B}(\hat{\boldsymbol{k}}, \hat{\boldsymbol{k}}') = \frac{1}{\sqrt{2}} \left[ f(\hat{\boldsymbol{k}}, \hat{\boldsymbol{k}}') \pm f(\hat{\boldsymbol{k}}, -\hat{\boldsymbol{k}}') \right], \tag{2.22}$$

finally leaving us with

$$f_F(\hat{\boldsymbol{k}}, \hat{\boldsymbol{k}}') = \frac{a_d}{\sqrt{2}} \left( \frac{4(\hat{\boldsymbol{k}} \cdot \hat{\boldsymbol{\mathcal{B}}})(\hat{\boldsymbol{k}}' \cdot \hat{\boldsymbol{\mathcal{B}}}) - 2[(\hat{\boldsymbol{k}} \cdot \hat{\boldsymbol{\mathcal{B}}})^2 + (\hat{\boldsymbol{k}}' \cdot \hat{\boldsymbol{\mathcal{B}}})^2](\hat{\boldsymbol{k}} \cdot \hat{\boldsymbol{k}}')}{1 - (\hat{\boldsymbol{k}} \cdot \hat{\boldsymbol{k}}')^2} \right), \tag{2.23a}$$

$$f_B(\hat{\boldsymbol{k}}, \hat{\boldsymbol{k}}') \overset{\text{almost}}{=} \frac{a_d}{\sqrt{2}} \left( \frac{4}{3} - \frac{2[(\hat{\boldsymbol{k}} \cdot \hat{\boldsymbol{\mathcal{B}}})^2 + (\hat{\boldsymbol{k}}' \cdot \hat{\boldsymbol{\mathcal{B}}})^2] - 4(\hat{\boldsymbol{k}} \cdot \hat{\boldsymbol{\mathcal{B}}})(\hat{\boldsymbol{k}}' \cdot \hat{\boldsymbol{\mathcal{B}}})(\hat{\boldsymbol{k}} \cdot \hat{\boldsymbol{k}}')}{1 - (\hat{\boldsymbol{k}} \cdot \hat{\boldsymbol{k}}')^2} \right). \tag{2.23b}$$

If not already bored stiff by this point, one might notice that the $\ell = 0$ partial wave component of the potential is barrierless, completely unable to defend itself against the imminent atomic flux during a scattering event. Colliding atoms are therefore defenseless against the full might of their dipole-dipole interactions, not forgetting all the shorter range physics on top of that. Surely then, the Born approximation is no longer accurate which warrants the "almost" above equality in Eq. (2.23b). To rectify this shortcoming, Eq. (2.25) is modified by hand with the famed *s-wave scattering length*, another triumph in atomic physics briefly discussed below.

### 2.1.5 s-wave scattering in bosons

If a significant portion of the wavefunction is allowed to enter within $r < a_d$, that region of the potential and wavefunction can be really complicated and difficult to obtain accurately from ab initio calculations. An ingenious observation from Enrico Fermi in the 1930s [38] showed that despite all its complexity, the low energy elastic scattering in the $\ell = 0$ channel just modified the scattered wavefunction by a single parameter, the $s$-wave[4] scattering length $a_s$. Put concisely,

[4] The letter $s$ used here denotes the $\ell = 0$ partial wave, as inherited from atomic orbital theory in chemistry where every angular momentum orbital was assigned letters $s, p, d, f, \ldots$, corresponding to the spherical harmonics in $\ell = 0, 1, 2, 3, \ldots$.

scattering concerns itself with colliding partners as they enter from, and exit to asymptotically far distances from one another (see Sec. 2.1.2). If the collision is elastic (entrance and exit channels are the same), conservation of probability flux mandates that the outbound post-collision piece of the wavefunction can only differ from the inbound pre-collision piece by a phase factor $e^{2i\delta_s}$. The associated phase $\delta_s$, which depends on the scattering energy, is referred to as the *scattering phase shift*. A schematic picture of this process and the phase shift that follows is given in Fig. 2.4.

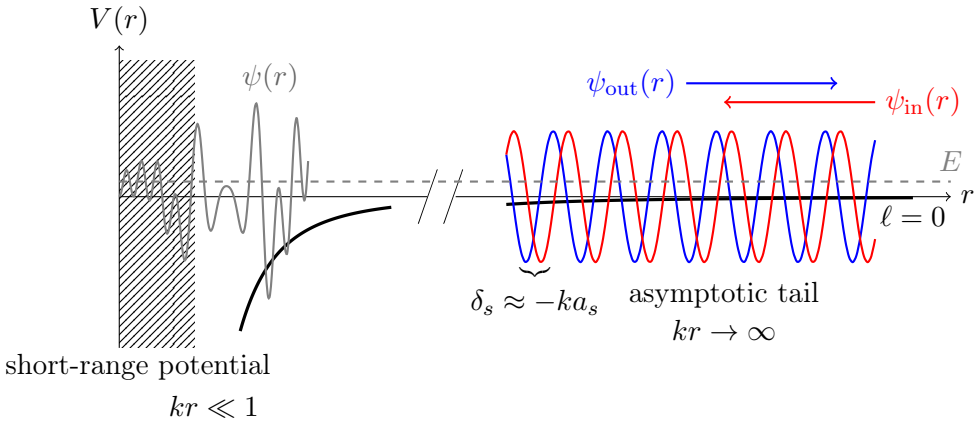


Figure 2.4: Cartoon of the $s$-wave scattering phase shift. The atoms are asymptotically free particles, approaching as planewaves ($\psi_{\text{in}}$, blue curve) before seeing the interaction potential between them. Conservation of probability flux mandates that the asymptotic scattered wavefunction $\psi_{\text{out}}$ (red curve), can only differ from $\psi_{\text{in}}$ in the $s$-wave partial wave channel by a phase shift $\delta_s$.

Going back to the planewave expanded solution in Eq. (2.10), one could also construct equivalent solutions in terms of spherical Bessel and Neumann functions instead. By doing so and comparing solutions partial wave by partial wave, an $s$-wave scattering length is identified in terms of the low energy $\ell = 0$ phase shift as

$$a_s = -\lim_{k\to 0} \frac{\tan \delta_s(k)}{k}. \tag{2.24}$$

Strictly speaking, this result is derived for the case of isotropic interaction potentials, where every partial wave is independent of one another. Considerations of partial wave couplings from dipoles will be treated as higher-order corrections and neglected here. Now equipped with the piece handling barrierless elastic scattering, the scattering amplitude for dipolar Bosons is appropriately amended

from Eq. (2.23b) to [35]

$$f_B(\hat{\boldsymbol{k}},\hat{\boldsymbol{k}}') = -\sqrt{2}a_s + \frac{a_d}{\sqrt{2}}\left(\frac{4}{3} - \frac{2[(\hat{\boldsymbol{k}}\cdot\hat{\boldsymbol{\mathcal{B}}})^2 + (\hat{\boldsymbol{k}}'\cdot\hat{\boldsymbol{\mathcal{B}}})^2] - 4(\hat{\boldsymbol{k}}\cdot\hat{\boldsymbol{\mathcal{B}}})(\hat{\boldsymbol{k}}'\cdot\hat{\boldsymbol{\mathcal{B}}})(\hat{\boldsymbol{k}}\cdot\hat{\boldsymbol{k}}')}{1-(\hat{\boldsymbol{k}}\cdot\hat{\boldsymbol{k}}')^2}\right), \tag{2.25}$$

for a comprehensive solution.

Oftentimes, it is useful to have an estimate of the scattering length without any prior knowledge of the system. For a potential of the form $V_n(r) = -C_n/r^n$, some statistical gargalesis can be used to derive a probability distribution over expected scattering lengths

$$P(a_s) = \frac{1}{\pi}\frac{\overline{a}_s}{(a_s-\overline{a}_s)^2+\overline{a}_s^2}, \tag{2.26}$$

in terms of a most-likely scattering length first derived by Gribakin and Flambaum [39]:

$$\overline{a}_s = \cos\left(\frac{\pi}{n-2}\right)\left(\frac{\sqrt{2\mu C_n}}{\hbar(n-2)}\right)^{\frac{2}{n-2}}\frac{\Gamma\left(\frac{n-3}{n-2}\right)}{\Gamma\left(\frac{n-1}{n-2}\right)}, \tag{2.27}$$

where $\Gamma(x)$ is the gamma function. Moreover, the imaginary part of $a_s$ responsible for inelastic scattering is expected to have a distribution strongly peaked around zero [20]. I therefore opt to ignore $\mathrm{Im}\{a_s\}$ for all subsequent considerations of $a_s$.

## 2.2 Shields up! Turning reactive molecules inert

Strong dipolar scattering is not unique to gases of magnetic atoms, but can also occur in gases of heteronuclear diatomic molecules with externally applied electric fields [40]. In fact, the dipole lengths of these polar molecules can be hundreds of times larger than those in magnetic atoms, accentuating the effects of dipolar physics. A concern of molecular collisions, however, is the possibility of chemical reaction which often results in molecular loss from their optical confinement (detailed in App. B). Lucky for us, several smart cookies (one of which is the chair of this very thesis committee!) have proposed means to mitigate reactive collisions by careful application of external electric fields. Doing so results in what is known as *collisional shielding* [41, 42], whereby barriers are engineered in the potential which prevents molecules from coming too close to one another.

Excitingly, collisional shielding of polar molecules has recently been realized in several experiments, both with static electric [3, 43–45] and microwave fields [4, 46–48], permitting collisionally

stable bulk molecular gas samples. For context and their use later on, it is worthwhile to briefly discuss the effective potentials and resulting scattering cross sections in both these shielding situations. Only the minimal models necessary to capture the essential shielding physics will be discussed here, to prevent this thesis from unfurling down the length of the JILA tower.

### 2.2.1 Scattering of static field shielded KRb molecules

In static electric fields, polar molecules can experience an effective shielded potential between them which is, albeit reminiscent of, different from the familiar dipole-dipole interaction potential [49]. Although theoretically formulated almost a decade ago [50, 51], the first demonstration of electric field shielding in 3-dimensions was only recently demonstrated in 2021 with a gas of $^{40}$K$^{87}$Rb molecules at JILA [3]. All remaining discussions contained in this subsection will refer to this molecular species.

For all intents and purposes, ultracold KRb molecules can be treated as quantum rigid rotors with only rotational degrees of freedom. That is to say, each molecule in isolation only has $|N_i, M_i\rangle$ quantum numbers ($i = 1, 2$) corresponding to the total rotation and its projection onto the space-fixed $z$ axis respectively. Brought closer together, such molecules interact as dipoles (2.14) with the interaction potential matrix elements given in the $|N_1, M_1; N_2, M_2\rangle$ basis as [13]

$$\begin{aligned}\langle N_1, M_1; N_2, M_2|\widehat{V}_{\rm dd}(\boldsymbol{r})\left|N_1', M_1'; N_2', M_2'\right\rangle = &-\frac{\sqrt{30}}{4\pi\epsilon_0 r^3}C_{2,-q}(\theta,\phi)\begin{pmatrix}2 & 1 & 1\\ q & -q_1 & -q_2\end{pmatrix}\\ &\times d(-1)^{M_1}\sqrt{(2N_1+1)(2N_1'+1)}\begin{pmatrix}N_1' & 1 & N_1\\ M_1' & q_1 & -M_1\end{pmatrix}\begin{pmatrix}N_1' & 1 & N_1\\ 0 & 0 & 0\end{pmatrix}\\ &\times d(-1)^{M_2}\sqrt{(2N_2+1)(2N_2'+1)}\begin{pmatrix}N_2' & 1 & N_2\\ M_2' & q_2 & -M_2\end{pmatrix}\begin{pmatrix}N_2' & 1 & N_2\\ 0 & 0 & 0\end{pmatrix},\end{aligned} \tag{2.28}$$

where $q_1 = M_1' - M_1$, $q_2 = M_2' - M_2$, $q = q_1 + q_2$ and

$$C_{2,-q}(\theta,\phi) = \begin{cases} \frac{1}{2}(3\cos^2\theta - 1), & q = 0, \\ \pm\sqrt{\frac{3}{2}}\sin\theta\cos\theta e^{\mp i\phi}, & q = \pm 1, \\ \sqrt{\frac{3}{8}}\sin^2\theta e^{\mp 2i\phi}, & q = \pm 2. \end{cases} \tag{2.29}$$

Collisional shielding then leverages the rotation-coupling interactions above to engineer a barrier in the adiabatic (ignoring the kinetic energy term) potential energy surface that prevents molecules from reaching the short-range. Key to achieving this barrier is the application of an external electric field $\boldsymbol{\mathcal{E}}$. Via the Stark effect, 2 asymptotic energy thresholds are tuned to be almost degenerate, which if coupled through Eq. (2.28), would drastically repel one another within the range of dipolar interactions. One adiabat will be pushed downward, while the other upward to form a repulsive core around $r = 0$. If prepared and allowed to approach only on the upper adiabat, the 2 molecules would be stopped from reaching close enough distances to chemically react.

A minimal, but rather accurate model of shielding assumes the colliding molecules remain polarized along the field axis, here taken to be $\hat{\boldsymbol{\mathcal{E}}} = \hat{\boldsymbol{z}}$. The $M_i$ quantum numbers are thus always zero, which stands as a good approximation at large electric fields $\boldsymbol{\mathcal{E}}$. The good quantum numbers of each molecule, not interacting with any other, are now dressed by the electric field. These states are obtained by diagonalizing the single-molecule Hamiltonian

$$\widehat{H}_i = B_R\widehat{\boldsymbol{N}}_i^2 - \widehat{\boldsymbol{d}}_i \cdot \boldsymbol{\mathcal{E}}, \tag{2.30}$$

which gives the field-dressed (denoted by tildes) basis states

$$\widehat{H}_i|\tilde{N}_i, M_i\rangle = \epsilon_{\tilde{N}_i,M_i}|\tilde{N}_i, M_i\rangle, \tag{2.31}$$

with associated eigenenergies $\epsilon_{\tilde{N}_i,M_i}$. The $M_i$ quantum numbers do not have tildes as they remain good quantum numbers in the presence of the field.

A shielding resonance as just described is then induced between the field-dressed combined molecular states $\left|\tilde{1},0\right\rangle\left|\tilde{1},0\right\rangle$ and $\left|\tilde{0},0\right\rangle\left|\tilde{2},0\right\rangle$, which are asymptotically degenerate at $\mathcal{E} \approx 12.72$

kV/cm and get dipole-coupled upon approach. The result is a barriered upper adiabat that is well approximated by [49]:

$$V_{\mathrm{E}}(r,\theta) = \frac{1}{2}(V_a + V_b) + \frac{1}{2}\sqrt{(V_a - V_b)^2 + 4W^2}, \tag{2.32}$$

constructed out of the diabatic pieces

$$V_a(r,\theta) = -\frac{\chi_a}{\pi\epsilon_0 r^3}\sqrt{\frac{\pi}{5}}Y_{2,0}(\theta) + E_{\tilde{1}\tilde{1}}, \tag{2.33a}$$

$$V_b(r,\theta) = -\frac{\chi_b}{\pi\epsilon_0 r^3}\sqrt{\frac{\pi}{5}}Y_{2,0}(\theta) + E_{\tilde{0}\tilde{2}}, \tag{2.33b}$$

$$W(r,\theta) = -\frac{\chi_W}{\pi\epsilon_0 r^3}\sqrt{\frac{2\pi}{5}}Y_{2,0}(\theta), \tag{2.33c}$$

with energy offsets $E_{\tilde{1}\tilde{1}}$ and $E_{\tilde{0}\tilde{2}}$ corresponding to the energetic thresholds of the $|\tilde{1},0\rangle|\tilde{1},0\rangle$ and $|\tilde{0},0\rangle|\tilde{2},0\rangle$ states respectively. The surface of $V_{\mathrm{E}}$ along $y = 0$, with $E_{\tilde{1}\tilde{1}} \approx E_{\tilde{0}\tilde{2}}$, is plotted in Fig. 2.5.

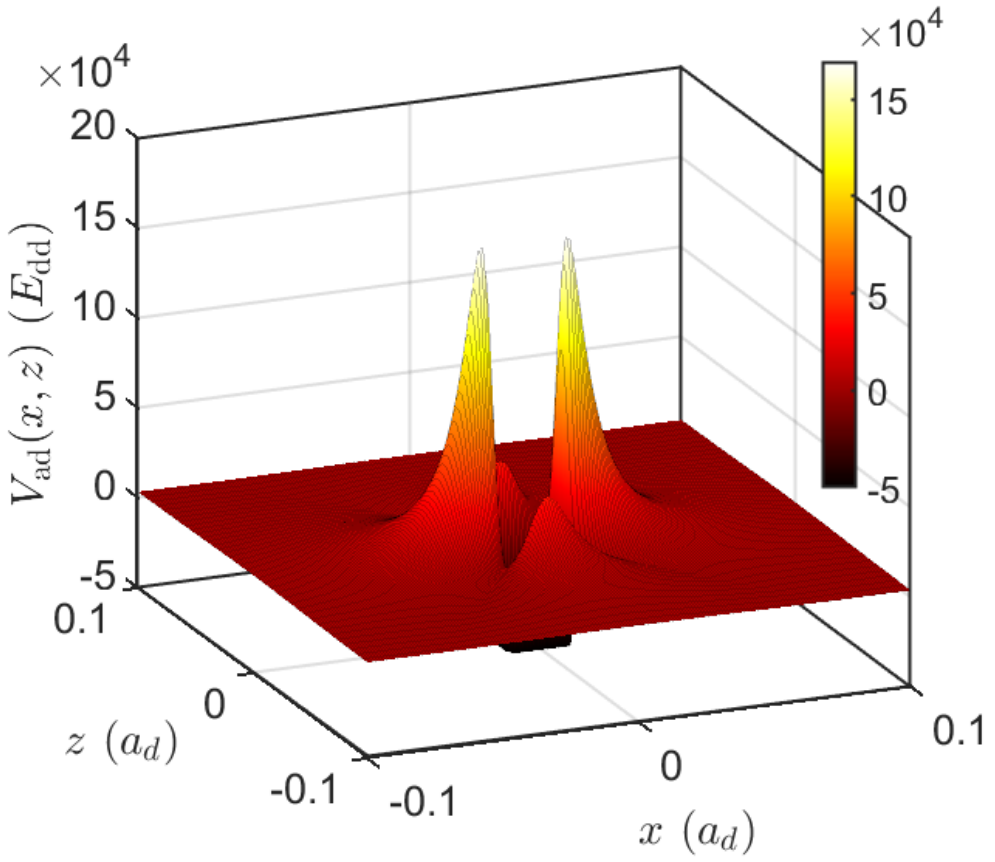


Figure 2.5: A $y = 0$ slice of the effective adiabatic potential energy surface on which colliding molecules would be shielded. The axes are scaled by molecular-frame dipole units (2.1).

Having assumed $M_i = 0$, effective state-dependent dipole moments can then be defined as

$$d^{\tilde{N}\to\tilde{N}'} = d\sum_{N,N'}\langle\tilde{N}|N\rangle\langle N'|\tilde{N}'\rangle\sqrt{2N+1}\sqrt{2N'+1}\begin{pmatrix} N & 1 & N' \\ 0 & 0 & 0 \end{pmatrix}^2, \tag{2.34}$$

with molecular-frame dipole moment $d$, that enter the diabatic potentials via the interaction terms

$$\chi_a = d^{\tilde{1}\to\tilde{1}}d^{\tilde{1}\to\tilde{1}} \approx 0.023\,\mathrm{D}^2, \tag{2.35a}$$

$$\chi_b = d^{\tilde{0}\to\tilde{0}}d^{\tilde{2}\to\tilde{2}} + d^{\tilde{0}\to\tilde{2}}d^{\tilde{2}\to\tilde{0}} \approx -0.037\,\mathrm{D}^2, \tag{2.35b}$$

$$\chi_W = d^{\tilde{1}\to\tilde{0}}d^{\tilde{1}\to\tilde{2}} \approx 0.066\,\mathrm{D}^2. \tag{2.35c}$$

Debye units are denoted with D above. At the resonant value of the electric field, $E_{\tilde{1}\tilde{1}} \approx E_{\tilde{0}\tilde{2}}$, so the effective shielding potential simplifies to a channel energy independent form

$$V_{\mathrm{E}}(r,\theta) \approx -\frac{\sqrt{\pi/5}}{2\pi\epsilon_0 r^3}\left(\left[\chi_a+\chi_b\right]Y_{2,0}(\theta) - \left[(\chi_b-\chi_a)^2+8\chi_W^2\right]^{1/2}|Y_{2,0}(\theta)|\right). \tag{2.36}$$

Above, I have ignored a constant energy offset of $E_{\tilde{1}\tilde{1}} + E_{\tilde{0}\tilde{2}}$ as they are irrelevant to the elastic scattering physics of interest here.

At low enough temperatures, the first-order Born approximation of Eq. (2.20) is once more appropriate to study differential scattering resultant from the effective potential $V_E$. With the same planewave expansion technique used to obtain Eq. (2.21), the scattering amplitude between electric field shielded molecules is computed as

$$\begin{aligned} f_{E,\mathrm{Born}}(\boldsymbol{k},\boldsymbol{k}') = {} & \frac{2\mu(\chi_a+\chi_b)}{\pi\epsilon_0\hbar^2}\sqrt{\frac{\pi}{5}}\sum_{\ell,m} i^\ell Y^*_{\ell,m}(\hat{\boldsymbol{q}})\int d^3r\frac{j_\ell(qr)}{r^3}Y_{2,0}(\theta)Y_{\ell,m}(\theta,\phi) \\ & - \frac{2\mu\left((\chi_b-\chi_a)^2+8\chi_W^2\right)^{1/2}}{\pi\epsilon_0\hbar^2}\sqrt{\frac{\pi}{5}}\sum_{\ell,m} i^\ell Y^*_{\ell,m}(\hat{\boldsymbol{q}})\int d^3r\frac{j_\ell(qr)}{r^3}|Y_{2,0}(\theta)|Y_{\ell,m}(\theta,\phi). \end{aligned} \tag{2.37}$$

For the second term above, the integrals are evaluated as

$$\int_\Omega |Y_{2,0}(\Omega)|Y_{\ell,m}(\Omega) = \delta_{m,0}\begin{cases} \int_\Omega |Y_{2,0}(\Omega)|Y_{\ell,m}(\Omega), & \ell \text{ is even}, \\ 0, & \ell \text{ is odd}. \end{cases} \tag{2.38}$$

With this, the scattering amplitude is given by

$$f_{E,\mathrm{Born}} = f_s + f_d + f_{\mathrm{h.p.}}, \tag{2.39}$$

written in terms of isotropic s-wave ($\ell = 0$), dipole-dipole d-wave ($\ell = 2$) and higher partial-wave components:

$$f_s = -a_{d_\beta}\sqrt{\frac{4\pi}{3}}\left(1 - \lim_{r_0\to 0}\mathrm{Ci}(qr_0)\right)Y_{0,0}(\hat{\boldsymbol{q}}) \tag{2.40a}$$

$$f_d = -a_{d_\beta}\sqrt{\frac{\pi}{5}}\left(1 - \frac{4}{3\sqrt{3}} - \frac{d_\alpha^2}{d_\beta^2}\right)Y_{2,0}(\hat{\boldsymbol{q}}) \tag{2.40b}$$

$$f_{\text{h.p.}} = -a_{d_\beta}\sum_{L=2}^{\infty}\left(\frac{3\pi}{4\sqrt{5}}\frac{(-1)^L\Gamma(L)}{\Gamma(\frac{3}{2}+L)}\int d^2\Omega|Y_{2,0}(\Omega)|Y_{2L,0}(\Omega)\right)Y_{2L,0}(\hat{\boldsymbol{q}}), \tag{2.40c}$$

respectively, having defined the effective dipole moments

$$d_\alpha^2 = \chi_a + \chi_b \approx -0.026\,\mathrm{D}^2, \tag{2.41a}$$

$$d_\beta^2 = \sqrt{(\chi_b - \chi_a)^2 + 8\chi_W^2} \approx 0.17\,\mathrm{D}^2, \tag{2.41b}$$

and effective dipole length $a_{d_\beta} = md_\beta^2/(3\pi\epsilon_0\hbar^2)$. $\mathrm{Ci}(x)$ is the cosine integral which when $x \to 0$, is pathological but vanishes after antisymmetrization of the cross section. In the expression for $f_{\text{h.p.}}$, the summation index $L$ is used as a proxy for the even quantum numbers $\ell$, with the factor of 2 accounted for by each term in the sum explicitly.

At the resonant shielding field strength, subplot (b) of Fig. 2.6 shows that the sum over $L$ is convergent, and partial-waves of $\ell > 2$ contribute but a small amount to the scattering amplitude of KRb molecules. A comparison of the anisotropic components of the scattering amplitudes with partial waves truncated at $\ell_{\max} = 2$ (solid black curve) and $\ell_{\max} = 100$ (dashed red curve) is plotted in subplot (a) of Fig. 2.6 against the momentum transfer inclination angle $\theta_q$. These curves are maximally separated at $\theta_q = 0, \pi$ with an absolute relative error of $\sim 9\%$. Truncating the sum at $\ell = 2$, the scattering amplitude is simply given as $f_{E,\text{Born}} \approx f_s + f_d$. At this level of approximation, the angular dependence of this scattering amplitude exactly resembles that between 2 regular point dipoles [35]

$$f_{E,\text{Born}} \approx f_s + a_{d_{\text{eff}}}\left(\frac{(\hat{\boldsymbol{k}}\cdot\hat{\boldsymbol{\mathcal{E}}} - \hat{\boldsymbol{k}}'\cdot\hat{\boldsymbol{\mathcal{E}}})^2}{(1 - \hat{\boldsymbol{k}}\cdot\hat{\boldsymbol{k}}')} - \frac{2}{3}\right), \tag{2.42}$$

with an effective dipole length

$$a_{d_{\text{eff}}} = \frac{md_\beta^2}{8\pi\epsilon_0\hbar^2}\left(1 - \frac{4}{3\sqrt{3}} - \frac{d_\alpha^2}{d_\beta^2}\right). \tag{2.43}$$

Antisymmetrizing Eq. (2.42) then results in the scattering amplitude identical to that in Eq. (2.23a), up to a substitution of the effective dipole length.

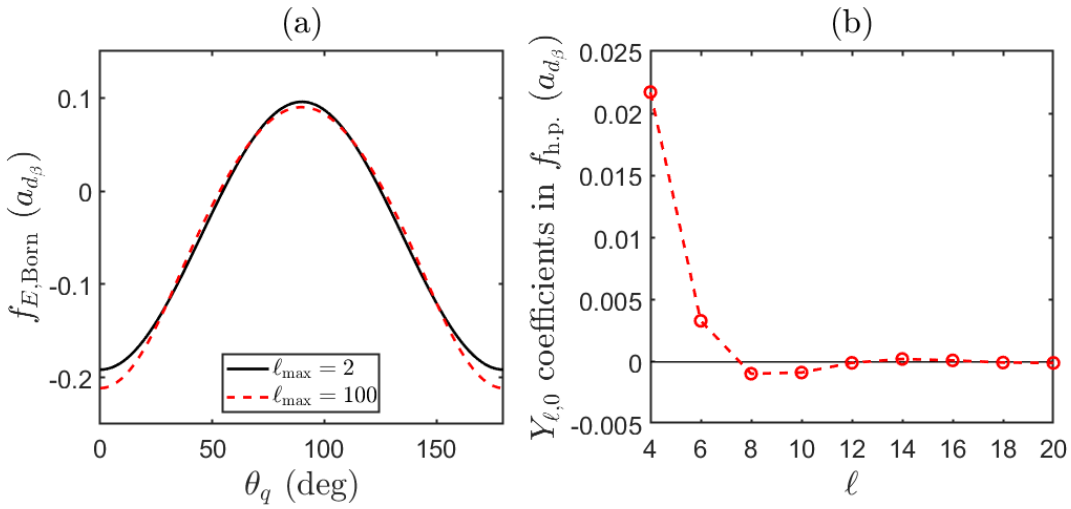


Figure 2.6: Subplot (a) plots the anisotropic components of the scattering amplitude $f_d + f_{\mathrm{h.p.}}$, between static field shielded molecules, for partial-waves up to $\ell_{\max} = 2$ (solid black curve) and $\ell_{\max} = 100$ (dashed red curve), as a function of $\theta_q$. The scattering amplitudes are plotted in units of $a_{d_\beta}$. Subplot (b) plots the coefficients (red circles) multiplying each partial-wave spherical harmonic $Y_{\ell,0}$ in $f_{\mathrm{h.p.}}$, as a function of the angular momentum quantum number $\ell$. A horizontal zero-line is also plotted for reference.

Turns out, static field resonantly shielded $^{40}$K$^{87}$Rb molecules collide at threshold just as point dipoles would! Experimental evidence of this will be discussed a little down the road in Chap. 4.

### 2.2.2 Scattering of microwave shielded NaK molecules

Just like with static electric fields, polar molecules can also be shielded using microwave fields [4, 42, 47, 48, 52–54]. The detailed shielding mechanism with these time-dependent fields is slightly more involved, but has much the same flavor as with static fields: i.e. apply a microwave field that dresses rotational states, have these dressed states repel via resonant dipole-dipole interactions, pick the incident channel that has a repulsive barrier, and tune the microwaves such that the collision follows this repulsive adiabat. Conveniently, Ref. [55] derives an effective potential relevant to elastic

scattering between microwave shielded molecules:

$$V_\mu(\boldsymbol{r}) = \frac{C_6}{r^6}\left[1-(\hat{\boldsymbol{r}}\cdot\hat{\boldsymbol{\mathcal{E}}})^4\right] + \frac{\overline{d}^2}{4\pi\epsilon_0 r^3}\left[3(\hat{\boldsymbol{r}}\cdot\hat{\boldsymbol{\mathcal{E}}})^2-1\right], \tag{2.44}$$

with circularly polarized microwaves, where $\overline{d} = d_0/\sqrt{12(1+(\Delta/\Omega)^2)}$ is the effective molecular dipole moment and $C_6 = d_0^4(1+(\Delta/\Omega)^2)^{-3/2}/(128\pi^2\epsilon_0^2\hbar\Omega)$. Here $\Omega$ and $\Delta$ are the Rabi frequency and detuning of the microwave respectively. A $y=0$ plane slice of $V_\mu(\boldsymbol{r})$ is provided in Fig. 2.7, between $^{23}$Na$^{40}$K molecules with molecular frame dipole moment $d_0 = 2.72$ D, subjected to microwaves of Rabi frequency $\Omega = 2\pi\times 15$ MHz and detuning $\Delta = 2\pi\times 9.5$ MHz. Chemical reactions are suppressed with the shielding core, depicted as a white patch surrounding the coordinate origin that saturates the color bar at $V_{\text{eff}} > 200E_{\text{dd}}$.

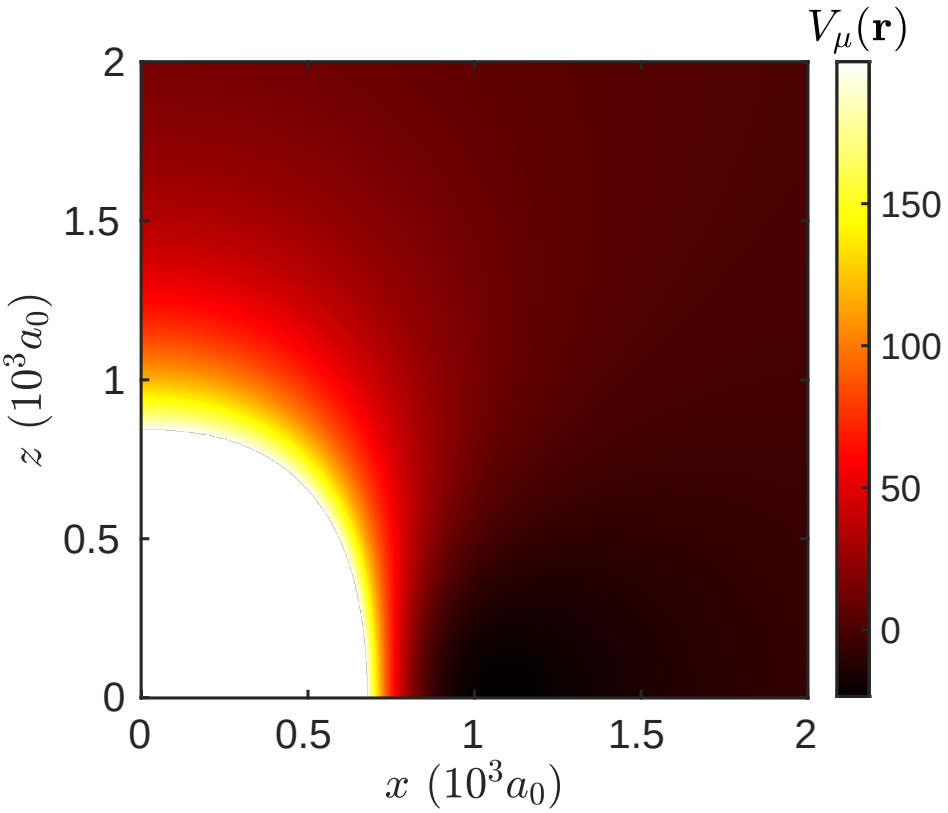


Figure 2.7: A $y=0$ plane slice of the effective microwave shielded potential between $^{23}$Na$^{40}$K molecules, in units of $E_{\text{dd}}$ (see Tab. 2.1). Circularly polarized microwaves are applied with Rabi frequency $\Omega = 2\pi\times 15$ MHz and a detuning of $\Delta = 2\pi\times 9.5$ MHz.

With the long-ranged dipolar tail being, apart from an overall minus sign, identical to the dipole-dipole potential between points dipoles [(2.15) but with $\mu_0$ replaced with $\epsilon_0^{-1}$], the close-to-threshold differential cross section in microwave shielded molecules would be exactly that obtained from Eqs. (2.23a) and (2.25) in Born approximation. In higher energy collisions, however, more general solutions require close-coupling calculations. This is certainly also true for the case of static field shielded molecules, but analysis here will focus on the case with microwaves.

#### 2.2.2.1 Close-coupling calculations for non-threshold collisions

Close-coupling calculations are used to obtain scattering solutions of the time-independent Schrödinger equation (2.6) with all relevant quantum degrees of freedom [56]. I compute these by utilizing a log-derivative propagation method, which avoids direct evaluation of the radial wavefunction $u^E_{\ell,m_\ell,\nu}(r)$, but instead computes its logarithmic-derivative:

$$\boldsymbol{Y}(r) = \boldsymbol{U}^{-1}(r)\frac{\partial \boldsymbol{U}(r)}{\partial r} = \frac{\partial \log \boldsymbol{U}(r)}{\partial r}, \tag{2.45}$$

where $\boldsymbol{U}(r)$ is the fundamental matrix of $u^E_{\ell,m_\ell,\nu}(r)$ solutions. Conveniently, the effective potential of Eq. (2.44) only requires us to consider 1 asymptotic channel for elastic scattering, so matrix indices only need to be considered for partial waves. Then defining the matrices

$$D^{\ell',m'_\ell}_{\ell,m_\ell} = \delta_{\ell,\ell'}\delta_{m_\ell,m'_\ell}\frac{d^2}{dr^2}, \tag{2.46a}$$

$$W^{\ell',m'_\ell}_{\ell,m_\ell} = \delta_{\ell,\ell'}\delta_{m_\ell,m'_\ell}\left(k^2 - \frac{\ell(\ell+1)}{r^2}\right) - \frac{2\mu}{\hbar^2}\left\langle \ell, m_\ell\right| \widehat{V}_\mu(\boldsymbol{r}) \left|\ell', m'_\ell\right\rangle, \tag{2.46b}$$

with matrix elements of $\left\langle \ell, m_\ell\right| \widehat{V}_\mu(\boldsymbol{r}) \left|\ell', m'_\ell\right\rangle$ provided in App. A, this single-channel version of Eq. (2.6) can be recast as the compact system of equations $[\boldsymbol{D} + \boldsymbol{W}]\,\boldsymbol{U} = \boldsymbol{0}$, or in terms of the log-derivative,

$$\boldsymbol{Y}'(r) + \boldsymbol{Y}^2(r) + \boldsymbol{W}(r) = \boldsymbol{0}. \tag{2.47}$$

In principle, the equation above can be solved numerically at a given collision energy $E$, by propagating the log derivative matrix from $r = 0$ to $r \to \infty$. In practice however, propagating to

$\infty$ is not possible so we only do so up to $r = r_{\rm match}$, then match $\boldsymbol{Y}(r)$ to the asymptotic solutions where the distant colliders no longer interact. Moreover, we sidestep the issue of singularities at the origin by imposing a short-range boundary condition by starting the propagation at a minimum radius $r = r_{\rm min}$. For our considerations of reactive molecules, we assume that short-range chemical loss is universal so that the log-derivative matrix at $r_{\rm min}$ is diagonal and given as [34, 57]

$$Y^{\ell,m_\ell}_{\ell,m_\ell}(r_{\rm min}) = -i\sqrt{W^{\ell,m_\ell}_{\ell,m_\ell}(r_{\rm min})}. \tag{2.48}$$

This boundary condition prevents dipolar scattering resonances [58, 59] which simplifies things. I've chosen to do numerical propagation of $\boldsymbol{Y}(r)$ with an adaptive radial step size version of Johnson's algorithm [60]. For shielded collisions, the engineered short-range barrier typically extends out to $\sim 1000a_0$, so numerically accurate propagation can safely commence from $r_{\rm min} \sim 100a_0$. On the other hand, matching at long-range is done adaptively depending on the collision energy

$$r_{\rm match} = \sqrt{\frac{\hbar^2\ell_{\rm max}(\ell_{\rm max}+1)}{mE}} + 20a_d, \tag{2.49}$$

where $\ell_{\rm max}$ is the largest value of $\ell$ utilized in the calculation. Typically, we utilize $\ell_{\rm max} = 121$ or as many as is required for numerical convergence (i.e. adding more partial waves does not significantly change the quantities of interest).

The asymptotic solutions to Eq. (2.6) arise by considering the domain where $r$ is much larger than the range of the potential, so that Eq. (2.6) is well approximated by

$$\left(\frac{d^2}{dr^2} - \frac{\ell(\ell+1)}{r^2} + k^2\right) u_{E,\ell,m_\ell}(r) = 0. \tag{2.50}$$

This asymptotic radial equation is solved with 2 independent solutions:

$$f_{E,\ell}(r) = krj_\ell(kr), \tag{2.51a}$$

$$g_{E,\ell}(r) = krn_\ell(kr), \tag{2.51b}$$

where $j_\ell(kr)$ and $n_\ell(kr)$ are the spherical Bessel and Neumann functions respectively. Then with matrices

$$F^{\ell',m'_\ell}_{\ell,m_\ell}(r;E) = \delta_{\ell,\ell'}\delta_{m_\ell,m'_\ell}f_{E,\ell}(r), \tag{2.52a}$$

$$G^{\ell',m'_\ell}_{\ell,m_\ell}(r;E) = \delta_{\ell,\ell'}\delta_{m_\ell,m'_\ell} g_{E,\ell}(r), \tag{2.52b}$$

arbitrary solutions to Eq. (2.6) can be written as

$$\boldsymbol{U}(r) = \boldsymbol{N}\left[\boldsymbol{F}(r) - \boldsymbol{K}\boldsymbol{G}(r)\right], \tag{2.53}$$

where $\boldsymbol{K}$ is the reactance matrix that is responsible for matching the numerical scattering solutions $\boldsymbol{U}$ to the asymptotic solutions in Eq. (2.52) at $r = r_{\text{match}}$. In particular, the off-diagonal elements of $\boldsymbol{K}$ provide information on the channel couplings that arise due to the interaction potential for a given incident collision channel. The matrix $\boldsymbol{N}$ is relevant only for normalization. The reactance matrix can be written in terms of the logarithmic derivative via

$$\boldsymbol{K} = \left.\frac{\boldsymbol{F}(r)\boldsymbol{Y}(r) - \frac{\partial}{\partial r}\boldsymbol{F}(r)}{\boldsymbol{G}(r)\boldsymbol{Y}(r) - \frac{\partial}{\partial r}\boldsymbol{G}(r)}\right|_{r=r_{\text{match}}}, \tag{2.54}$$

from which we can compute other scattering matrices via the relations [1]

$$\boldsymbol{S} = \frac{\boldsymbol{I} + i\boldsymbol{K}}{\boldsymbol{I} - i\boldsymbol{K}}, \tag{2.55a}$$

$$\boldsymbol{T} = i(\boldsymbol{S} - \boldsymbol{I}). \tag{2.55b}$$

Carrying out the algorithm just described gives the integral cross section with $V_\mu(\boldsymbol{r})$, over a broad range of collision energies $E$. The resulting energy dependence is plotted in Fig. 2.8 (solid black curve), where I compare it with the integral cross section between point dipole scatterers (dotted blue curve) with $V_{\text{dd}}(\boldsymbol{r})$. For comparison, I also plot the low energy Born and high energy Eikonal [1] approximations with dashed red lines. Worth pointing out is that the collision energy in Fig. 2.8 is given in units of dipole energy $E_{\text{dd}}$ (see Tab. 2.1), which scales as $d^{-4}$. Larger dipole moments would therefore require ever lower energies to reach the threshold regime, a problem faced by gases of diatomic molecules even at sub-microKelvin temperatures. Access to the differential cross section from close-coupling calculations is therefore important for studying ultracold molecular gases, as will become clear in the following chapter.

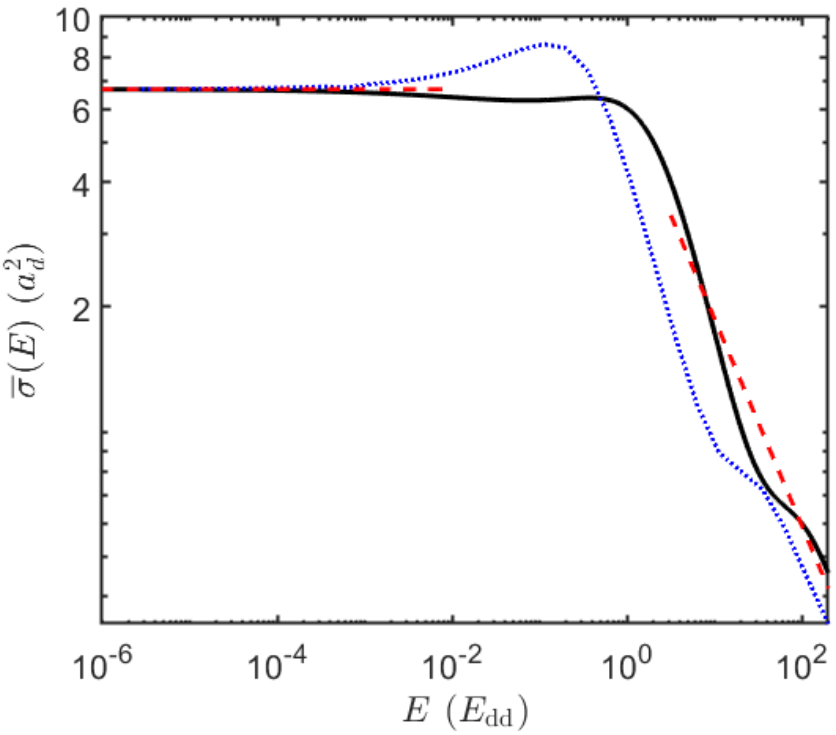


Figure 2.8: Energy dependence of the angular averaged total cross section $\overline{\sigma}$ between microwave shielded $^{23}$Na$^{40}$K (dashed black curve). The energy dependence clearly differs from the total cross section between fermionic point dipoles (dotted blue curve). For comparison, I plot the low energy Born and high energy Eikonal approximations with dashed red lines. The inset shows a $y = 0$ slice of the effective microwave shielding interaction potential, with Rabi frequency $\Omega = 2\pi \times 15$ MHz and microwave detuning $\Delta = 2\pi \times 9.5$ MHz. The shielding core is depicted as a white patch surrounding the coordinate origin which saturates the colorbar at $V_{\rm eff} > 200 E_{\rm dd}$. Coordinate axes are plotted in units of $10^3$ Bohr radii $a_0$.

# Chapter 3

## The Jostle and Bustle of Dipoles

Step back a little. This chapter zooms out from the microscopic collisional physics and instead, explores the resultant collective behavior of a whole ensemble of dipolar colliders. At ultracold but not yet quantum degenerate temperatures, the constituent particles of the gas whiz around on classical trajectories where every once in a while, two of them collide (cue flashbacks from Chap. 2). Such interplay of classical motion with quantum scattering is most readily treated with the celebrated Boltzmann transport equation, a cornerstone for dynamical studies of rarefied gases in non-equilibrium statistical mechanics. What's to come is a short introduction to the Boltzmann equation and the approaches I use to solve it.

### 3.1 The Boltzmann transport equation

The state of a classical point particle of mass $m$ is fully characterized by its position $\boldsymbol{r}$ and momentum $\boldsymbol{p}$. A statistical ensemble of such identical particles can then be described by a phase space distribution $f(\boldsymbol{r}, \boldsymbol{p}, t)$, that gives the differential number of particles $dN$ within a differential volume $d^3\boldsymbol{r}d^3\boldsymbol{p}$ at position $\boldsymbol{r}$ and time $t$, with momentum $\boldsymbol{p}$. Describing the gas collectively, this distribution is taken to be normalized over phase space such that the integral $\int d^3\boldsymbol{r}d^3\boldsymbol{p}f(\boldsymbol{r}, \boldsymbol{p}, t)$, evaluates to the total number of ensemble particles $N$. In general, dynamical evolution of $f$ involves a combination of advective transport, response to applied forces and collisions, all of which are

encapsulated by the Boltzmann equation [61, 62]

$$\left(\underbrace{\frac{\partial}{\partial t}+\frac{\boldsymbol{p}}{m}\cdot\boldsymbol{\nabla}}_{\text{advection}}-\underbrace{\boldsymbol{\nabla}V(\boldsymbol{r})\cdot\boldsymbol{\nabla}_p}_{\text{response}}\right)f(\boldsymbol{r},\boldsymbol{p},t)=\underbrace{\mathcal{I}_{\text{coll}}[f]}_{\text{collisions}}, \tag{3.1}$$

where $V(\boldsymbol{r})$ is any external potential felt by the particles and $\boldsymbol{\nabla}_p$ is the gradient operator on momentum coordinates. For most of what follows, the confinement will be taken as a harmonic trap

$$V(\boldsymbol{r})=\frac{1}{2}m\sum_i\omega_i^2r_i^2, \tag{3.2}$$

with harmonic trapping frequencies $\omega_i$, which is a good approximation to the optical potentials normally used to confine ultracold gases (see App. B for further details).

A fundamental property of classical gases is that once brought out-of-equilibrium and left alone, they will return to thermal equilibrium as is mandated by the second law of thermodynamics [63]. A *heat death* foretold, although phrased slightly differently, by Boltzmann [64]. When dilute, the route to thermalization occurs primarily by means of two-body collisions, incorporated in the Boltzmann equation via the entropy generating collision integral

$$\mathcal{I}_{\text{coll}}[f]=\int\frac{d^3\boldsymbol{p}_1}{m}|\boldsymbol{p}-\boldsymbol{p}_1|\int d\Omega'\frac{d\sigma}{d\Omega'}\left[f'f_1'\left(1\pm h^3f\right)\left(1\pm h^3f_1\right)-ff_1\left(1\pm h^3f'\right)\left(1\pm h^3f_1'\right)\right]. \tag{3.3}$$

As is conventional, the expression above uses the shorthand notations $f_1=f(\boldsymbol{r},\boldsymbol{p}_1,t)$ and primes to indicate the post-collision distributions of collision partners. The collision integral in Eq. (3.3) above has been modified from its purely classical form by the addition of quantum statistical factors $\pm h^3f$ ($+$ for collisional enhancement in Bose gases and $-$ for Pauli blocking in Fermi gases) [65–67] with Planck's constant $h$. Although relevant to the discussions of evaporative cooling in Chap. 6, much of this thesis is concerned with temperatures where the thermal de Broglie wavelength is far smaller than the mean particle spacing. This regime lends to negligibly small phase space occupancies within $h^3$, so we ignore these factors unless otherwise stated:

$$\mathcal{I}_{\text{coll}}[f]\approx\int\frac{d^3\boldsymbol{p}_1}{m}|\boldsymbol{p}-\boldsymbol{p}_1|\int d\Omega'\frac{d\sigma}{d\Omega'}\left(f'f_1'-ff_1\right). \tag{3.4}$$

At its final thermalized state, the entropy of a gas is maximized and so requires that the collision integral vanishes identically. This statement is a tenet of the Boltzmann H-theorem [62], which leads to the equilibrium Maxwell-Boltzmann solution

$$f^{\text{eq}}(\boldsymbol{r},\boldsymbol{p}) = n^{\text{eq}}(\boldsymbol{r})c^{\text{eq}}(\boldsymbol{p}), \tag{3.5a}$$

$$\text{where,} \qquad n^{\text{eq}}(\boldsymbol{r}) = \frac{N}{Z_r}\exp\left(-\frac{V(\boldsymbol{r})}{k_BT}\right), \tag{3.5b}$$

$$c^{\text{eq}}(\boldsymbol{p}) = \frac{1}{Z_p}\exp\left(-\frac{\boldsymbol{p}^2}{2mk_BT}\right), \tag{3.5c}$$

with partition functions $Z_r = \int d^3r \exp\left(-\frac{V(\boldsymbol{r})}{k_BT}\right)$ and $Z_p = (2\pi m k_B T)^{3/2}$.

Nonequilibrium solutions to Eq. (3.1) on the other hand, are less readily available to us [68], especially so when dealing with dipoles and their anisotropic cross sections. In particular circumstances, taking the gas only perturbatively away from equilibrium permits simpler approximate treatments of the gas dynamics. Aided by a suitable choice of a nonequilibrium ansatz for $f(\boldsymbol{r},\boldsymbol{p},t)$, a closed set of ordinary differential equations that track ensemble averaged observables can then be derived [62, 69]. Here's one way to do that.

## 3.2 Variational solutions: Gaussians, Gaussians, Gaussians!

Following the Maxwell Boltzmann distribution of Eq. (3.5) at thermal equilibrium, it is plausible that weak perturbations will leave $f(\boldsymbol{r},\boldsymbol{p},t)$ approximately Gaussian [68]. When asserted in real space, the even property of Gaussians restricts the types of perturbations to ones that do not change the gas' center of mass. But even with such a restriction, Gaussians take us a long way for the experiments of interest to this thesis. Enacting this approximation for nonequilibrium studies requires the spatial and momentum variances, $\langle r_j^2\rangle$ and $\langle p_j^2\rangle$, to be made time-dependent:

$$f(\boldsymbol{r},\boldsymbol{p},t) = c(\boldsymbol{p},t)n(\boldsymbol{r},t); \tag{3.6a}$$

$$c(\boldsymbol{p},t) \equiv \prod_j \frac{1}{\sqrt{2\pi\langle p_j^2\rangle(t)}}\exp\left(-\frac{p_j^2}{2\langle p_j^2\rangle(t)}\right), \tag{3.6b}$$

$$n(\boldsymbol{r},t) \equiv N\prod_j \frac{1}{\sqrt{2\pi\langle r_j^2\rangle(t)}}\exp\left(-\frac{r_j^2}{2\langle r_j^2\rangle(t)}\right), \tag{3.6c}$$

with subscripts $j = x, y, z$ (see Fig. 3.1). Angle brackets are used to denote a phase space average:

$$\langle \ldots \rangle = \frac{1}{N} \iint d^3\boldsymbol{p} d^3\boldsymbol{r} f(\boldsymbol{r}, \boldsymbol{p}, t)(\ldots). \tag{3.7}$$

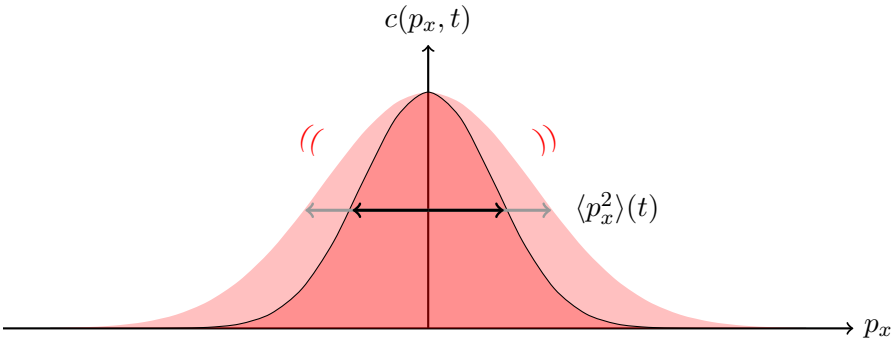


Figure 3.1: Illustration of the Gaussian time-dependent *ansatz* for $c(\boldsymbol{p}, t)$ along $x$.

Utilizing the Gaussian *ansatz* then admits equations of motion for the ensemble averaged values of arbitrary dynamical variables $\chi(\boldsymbol{r}, \boldsymbol{p}, t)$, an approach known as the method of averages [62]. The evolution equations governing $\langle \chi \rangle$ are then derived by multiplying the Boltzmann equation by $\chi$ and integrating over all of phase-space, detailed in App. C. Picking $\chi$ to come from the set of nine variables $\{r_j^2, p_j^2, r_j p_j\}$ with $j = x, y, z$, gives a closed set of equations [70, 71]:

$$\frac{d\langle r_j^2 \rangle}{dt} - \frac{2}{m}\langle r_j p_j \rangle = \mathcal{C}[\Delta r_j^2], \tag{3.8a}$$

$$\frac{d\langle p_j^2 \rangle}{dt} + 2m\omega_j^2 \langle r_j p_j \rangle = \mathcal{C}[\Delta p_j^2], \tag{3.8b}$$

$$\frac{d\langle r_j p_j \rangle}{dt} - \frac{1}{m}\langle p_j^2 \rangle + m\omega_j^2 \langle r_j^2 \rangle = \mathcal{C}[\Delta r_j p_j]. \tag{3.8c}$$

In these equations, collisions are incorporated through the integral

$$\mathcal{C}[\Delta\chi] = \frac{1}{N} \int d^3\boldsymbol{r} \iint \frac{d^3\boldsymbol{p} d^3\boldsymbol{p}_1}{m} |\boldsymbol{p} - \boldsymbol{p}_1| f f_1 \int d\Omega' \frac{d\sigma}{d\Omega'} \Delta\chi, \tag{3.9}$$

where $\Delta\chi \equiv \chi' + \chi_1' - \chi - \chi_1$ denotes the amount by which $\chi$ changes during a collision event. These nonlinear, coupled differential equations are known as the *Enskog equations of change*. Arguably easier to solve than Boltzmann's partial differential equation (3.1), the simplicity of Eqs. (3.8)

provides a ready-for-use theory of nondegenerate trapped gases. Conveniently, the momentum space variances $\langle p_j^2 \rangle$ solved for in Eqs. (3.8) are directly the observables with time-of-flight thermometry, a measurement protocol common to ultracold gas experiments.

Notice that, in the absence of collisions ($\mathcal{C} = 0$), all three coordinate axes are decoupled in Eqs. (3.8). In this case, the normal modes of the Enskog equations along each axis coordinate come in two varieties: a breathing mode of angular frequency $2\omega_j$, in which $\langle r_j^2 \rangle$ and $\langle p_j^2 \rangle$ are out of phase; and a stationary mode of frequency $\omega_j = 0$, corresponding to the equilibrium configuration [70]. These modes are naturally modified by the presence of collisions which will, of course, depend on the dipolar properties of the cross section [14]. A beast we now turn to taming.

### 3.2.1 Taming the collision integral

Eqs. (3.8) are only complete upon evaluation of the collision integrals (3.9). The key to evaluating these integrals is the assertion of, you guessed it, a Gaussian ansatz for $f(\boldsymbol{r}, \boldsymbol{p}, t)$ once more. Recast into center of mass coordinates, we get a decomposition of momenta into a center of mass component $\boldsymbol{P} = (\boldsymbol{p} + \boldsymbol{p}_1)/2$ and a relative component $\boldsymbol{p}_r = \boldsymbol{p} - \boldsymbol{p}_1$. These coordinates grant a reformulation of the collision integral from Eq. (3.9) to

$$\mathcal{C}[\Delta\chi] = \frac{1}{N} \int d^3\boldsymbol{r} n^2(\boldsymbol{r}) \int d^3\boldsymbol{p}_r c_r(\boldsymbol{p}_r) \frac{p_r}{2m} \int d\Omega' \frac{d\sigma}{d\Omega'} \Delta\chi \tag{3.10}$$

where $c_r(\boldsymbol{p}_r)$ takes the same form of $c(\boldsymbol{p})$ but with the replacement $\boldsymbol{p} \to \boldsymbol{p}_r$ and all factors of 2 converted to 4. $\mathcal{C}[\Delta r_j^2]$ vanishes since the collisions are assumed instantaneous and therefore do not vary the particle positions ($\Delta r_j^2 = 0$). Additionally, the collision integral for $\chi = r_j p_j$ is also observed to vanish since

$$\Delta\left(r_j p_j\right) = r_j \Delta p_j = r_j \left(P_j' - P_j\right), \tag{3.11}$$

in which $P_j' = P_j$ during elastic collisions, so $\mathcal{C}[\Delta r_j p_j] = 0$.

As such, the only quantities left that provide a non-trivial collision integral term are $\chi = p_j^2$, for which its collisional variation can be written only in terms of relative momenta as

$$\Delta p_j^2 = p_j'^2 + p_{1,j}'^2 - p_j^2 - p_{1,j}^2$$

$$= \frac{1}{2}\left(p_{r,j}'^2 + P_j'^2 - p_{r,j}^2 - P_j^2\right)$$
$$= \frac{1}{2}\left(p_{r,j}'^2 - p_{r,j}^2\right). \tag{3.12}$$

This reduction renders the integrals as separable (i.e. can be evaluated separately) in position and momentum variables

$$\mathcal{C}[\Delta p_j^2] = \frac{1}{N}\int d^3\boldsymbol{r} n^2(\boldsymbol{r}) \int d^3\boldsymbol{p}_r c_r(\boldsymbol{p}_r)\frac{p_r}{2m}\int d\Omega' \frac{d\sigma}{d\Omega'}\Delta p_j^2, \tag{3.13}$$

with the integral over $d^3\boldsymbol{r}$ evaluating to

$$\langle n\rangle = \frac{1}{N}\int d^3\boldsymbol{r} n^2(\boldsymbol{r}) = \frac{N}{8\pi^{3/2}\sqrt{\langle x^2\rangle\langle y^2\rangle\langle z^2\rangle}}. \tag{3.14}$$

This leaves the integrals over post and pre-collision momenta.

Evaluating the momentum integrals in Eq. (3.13) is a difficult task for dipoles, predominantly because the differential cross-section is anisotropic. Consistency therefore requires a suitable frame transformation, for which I adopt one where the lab-frame (LF) is defined such that the dipole alignment axis points relative to it as $\hat{\boldsymbol{\mathcal{E}}} = (\sin\Theta,\, 0,\, \cos\Theta)^T$, and a collision-frame (CF) defined by the relative momenta of collision partners with $\hat{\boldsymbol{z}}_{\rm CF} = \hat{\boldsymbol{p}}_r = (\sin\theta_{\rm LF}\cos\phi_{\rm LF}, \sin\theta_{\rm LF}\sin\phi_{\rm LF}, \cos\theta_{\rm LF})$. In principle, the transverse axes could be defined to your liking so long as $\hat{\boldsymbol{x}}_{\rm CF}\cdot\hat{\boldsymbol{z}}_{\rm CF} = 0$ and $\hat{\boldsymbol{y}}_{\rm CF} = \hat{\boldsymbol{z}}_{\rm CF}\times\hat{\boldsymbol{x}}_{\rm CF}$, but the ones I chose were

$$\hat{\boldsymbol{x}}_{\rm CF} = \begin{pmatrix} \sin\phi_{\rm LF} \\ -\cos\phi_{\rm LF} \\ 0 \end{pmatrix}, \quad \hat{\boldsymbol{y}}_{\rm CF} = \begin{pmatrix} \cos\theta_{\rm LF}\cos\phi_{\rm LF} \\ \cos\theta_{\rm LF}\sin\phi_{\rm LF} \\ -\sin\theta_{\rm LF} \end{pmatrix}. \tag{3.15}$$

It is necessary to perform integrals over both the lab-frame coordinates $\{p_r, \theta_{\rm LF}, \phi_{\rm LF}\}$ in which $\Theta$ is defined, and collision-frame coordinates $\{\theta_{\rm CF}, \phi_{\rm CF}\}$ that defines the post-collision relative momentum (the subscript CF is used instead of primes to disambiguate frames). A visualization of these two frames is provided in Fig. 3.2. As such, a transformation that relates these two sets of

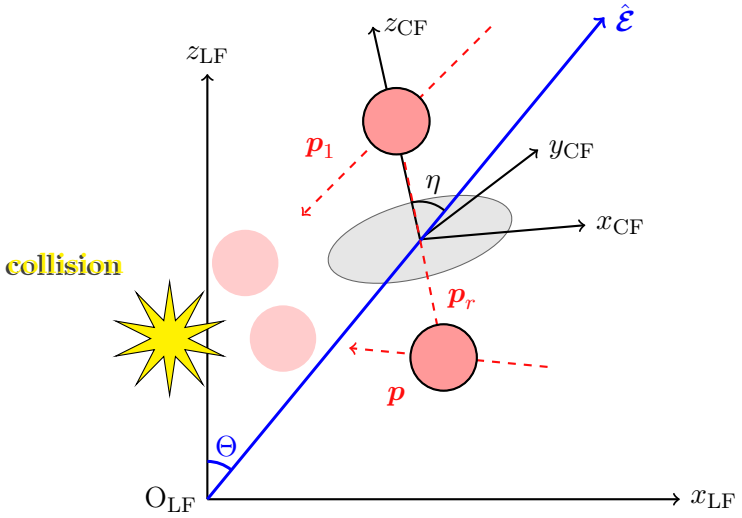


Figure 3.2: Visualization of 2 colliding partners (red spheres) relative to the collision-frame (CF) and lab-frame (LF). The collision frame (black) is defined in the laboratory frame (blue) with the relative collision momenta. The angle $\eta$ is that between the vectors $\boldsymbol{p}_r$ and $\hat{\boldsymbol{\mathcal{E}}}$.

variables is necessary and constructed using the method of direction cosines

$$
\begin{aligned}
R(\mathrm{CF} \rightarrow \mathrm{LF}) &= \begin{pmatrix} \hat{\boldsymbol{x}}_{\mathrm{LF}} \cdot \hat{\boldsymbol{x}}_{\mathrm{CF}} & \hat{\boldsymbol{x}}_{\mathrm{LF}} \cdot \hat{\boldsymbol{y}}_{\mathrm{CF}} & \hat{\boldsymbol{x}}_{\mathrm{LF}} \cdot \hat{\boldsymbol{z}}_{\mathrm{CF}} \\ \hat{\boldsymbol{y}}_{\mathrm{LF}} \cdot \hat{\boldsymbol{x}}_{\mathrm{CF}} & \hat{\boldsymbol{y}}_{\mathrm{LF}} \cdot \hat{\boldsymbol{y}}_{\mathrm{CF}} & \hat{\boldsymbol{y}}_{\mathrm{LF}} \cdot \hat{\boldsymbol{z}}_{\mathrm{CF}} \\ \hat{\boldsymbol{z}}_{\mathrm{LF}} \cdot \hat{\boldsymbol{x}}_{\mathrm{CF}} & \hat{\boldsymbol{z}}_{\mathrm{LF}} \cdot \hat{\boldsymbol{y}}_{\mathrm{CF}} & \hat{\boldsymbol{z}}_{\mathrm{LF}} \cdot \hat{\boldsymbol{z}}_{\mathrm{CF}} \end{pmatrix} \\
&= \begin{pmatrix} \sin\phi_{\mathrm{LF}} & \cos\theta_{\mathrm{LF}}\cos\phi_{\mathrm{LF}} & \sin\theta_{\mathrm{LF}}\cos\phi_{\mathrm{LF}} \\ -\cos\phi_{\mathrm{LF}} & \cos\theta_{\mathrm{LF}}\sin\phi_{\mathrm{LF}} & \sin\theta_{\mathrm{LF}}\sin\phi_{\mathrm{LF}} \\ 0 & -\sin\theta_{\mathrm{LF}} & \cos\theta_{\mathrm{LF}} \end{pmatrix} .
\end{aligned} \tag{3.16}
$$

With this, the differential cross-section can be obtained in the CF with Eqs. (2.25) and (2.23a), for which the relevant unit vectors are given as

$$
\hat{\boldsymbol{k}}_{\mathrm{CF}} = \begin{pmatrix} 0 \\ 0 \\ 1 \end{pmatrix} , \quad \hat{\boldsymbol{k}}'_{\mathrm{CF}} = \begin{pmatrix} \sin\theta_{\mathrm{CF}}\cos\phi_{\mathrm{CF}} \\ \sin\theta_{\mathrm{CF}}\sin\phi_{\mathrm{CF}} \\ \cos\theta_{\mathrm{CF}} \end{pmatrix} , \quad \hat{\boldsymbol{\mathcal{E}}}_{\mathrm{CF}} = \begin{pmatrix} \sin\Theta\sin\phi_{\mathrm{LF}} \\ \sin\Theta\cos\theta_{\mathrm{LF}}\cos\phi_{\mathrm{LF}} - \cos\Theta\sin\theta_{\mathrm{LF}} \\ \sin\Theta\sin\theta_{\mathrm{LF}}\cos\phi_{\mathrm{LF}} + \cos\Theta\cos\theta_{\mathrm{LF}} \end{pmatrix} , \tag{3.17}
$$

denoting $\hat{\boldsymbol{k}} = \hat{\boldsymbol{p}}_r$. These result in the dot product terms

$$
\hat{\boldsymbol{k}} \cdot \hat{\boldsymbol{k}}' = \cos\theta_{\mathrm{CF}}, \tag{3.18a}
$$

$$\hat{\boldsymbol{k}} \cdot \hat{\boldsymbol{\mathcal{E}}} = \sin\Theta \sin\theta_{\mathrm{LF}} \cos\phi_{\mathrm{LF}} + \cos\Theta \cos\theta_{\mathrm{LF}}, \tag{3.18b}$$

$$\begin{aligned}\hat{\boldsymbol{k}}' \cdot \hat{\boldsymbol{\mathcal{E}}} = {} & \sin\theta_{\mathrm{CF}} \cos\phi_{\mathrm{CF}} \sin\theta_{\mathrm{LF}} \sin\phi_{\mathrm{LF}} \\ & + \sin\theta_{\mathrm{CF}} \sin\phi_{\mathrm{CF}} \left(\sin\Theta \cos\theta_{\mathrm{LF}} \cos\phi_{\mathrm{LF}} - \cos\Theta \sin\theta_{\mathrm{LF}}\right) \\ & + \cos\theta_{\mathrm{CF}} \left(\sin\Theta \sin\theta_{\mathrm{LF}} \cos\phi_{\mathrm{LF}} + \cos\Theta \cos\theta_{\mathrm{LF}}\right). \end{aligned} \tag{3.18c}$$

In these coordinates, the integral over post-collision angles $d\Omega'$ can then be performed in coordinates defined by the LF and CF:

$$\mathcal{I}_p^{(\mathrm{CF})}(p_r, \theta, \phi) \equiv \int d\Omega' \left( \frac{d\sigma^{(0)}}{d\Omega'} + \frac{d\sigma^{(1)}}{d\Omega'} + \frac{d\sigma^{(2)}}{d\Omega'} \right) \Delta p_j^2, \tag{3.19}$$

where we utilize the threshold dipolar differential cross-section [see Eqs. (2.25) and (2.23a)] and factorized it into terms of various powers in $a_d$ (denoted with superscripts)

$$\frac{d\sigma}{d\Omega'}(\Theta) = \frac{d\sigma^{(0)}}{d\Omega'}(\Theta) + \frac{d\sigma^{(1)}}{d\Omega'}(\Theta) + \frac{d\sigma^{(2)}}{d\Omega'}(\Theta). \tag{3.20}$$

to help with algebraic bookkeeping.

Now for the integral over LF coordinates, here comes an explicit perturbative approximation. A Taylor expansion of $c_r(\boldsymbol{p}_r)$ is done up to first-order around thermal equilibrium

$$\begin{aligned} c_r(\boldsymbol{p}_r) \approx c_r^{\mathrm{eq}}(\boldsymbol{p}_r) \Bigg[ 1 + \delta p_x \left( \frac{p_r^2 \sin^2\theta_{\mathrm{LF}} \cos^2\phi_{\mathrm{LF}}}{4\langle p_z^2 \rangle_0} - \frac{1}{2} \right) + \delta p_y \left( \frac{p_r^2 \sin^2\theta_{\mathrm{LF}} \sin^2\phi_{\mathrm{LF}}}{4\langle p_z^2 \rangle_0} - \frac{1}{2} \right) \\ + \delta p_z \left( \frac{p_r^2 \cos^2\theta}{4\langle p_z^2 \rangle_0} - \frac{1}{2} \right) \Bigg], \end{aligned} \tag{3.21}$$

where

$$\delta p_j \equiv \frac{\langle p_j^2 \rangle}{\langle p_z^2 \rangle_0} - 1 \tag{3.22}$$

$$c_r^{\mathrm{eq}}(\boldsymbol{p}_r) \equiv \frac{1}{(4\pi \langle p_z^2 \rangle_0)^{3/2}} \exp\left( -\frac{p_r^2}{4\langle p_z^2 \rangle_0} \right), \tag{3.23}$$

with $c_r^{\mathrm{eq}}(\boldsymbol{p}_r)$ being the equilibrium distribution of relative momenta. It is noted that all terms in $c_r(\boldsymbol{p}_r)$ with constant coefficients multiplying $c_r^{\mathrm{eq}}(\boldsymbol{p}_r)$ are trivial since the collision integral vanishes at thermal equilibrium. Putting all these integrals with Eq. (3.14) and Eq. (3.19) together gives

$$\mathcal{C}[\Delta p_j^2] = \langle n \rangle \int d^3\boldsymbol{p}_r c_r(\boldsymbol{p}_r) \frac{p_r}{2m} \mathcal{I}_p^{(\mathrm{CF})}(p_r, \theta_{\mathrm{LF}}, \phi_{\mathrm{LF}}). \tag{3.24}$$

The remaining legwork of integration can be handed off to your favorite symbolic software. The one I used was Mathematica® [72]. For the reader's convenience, I tabulate all the analytic collision integrals below. For bosons (B), they are:

$$\begin{aligned}\mathcal{C}_{\mathrm{B}}[\Delta p_x^2] \approx{}& \left(\frac{8N}{15\pi}\right)\left(\frac{m\overline{\omega}^3 a_{\mathrm{eff}}^2}{k_B T_0}\right)\left[\langle p_y^2\rangle + \langle p_z^2\rangle - 2\langle p_x^2\rangle\right] \\ &+ \left(\frac{64N}{105\pi}\right)\left(\frac{m\overline{\omega}^3 a_s a_d}{k_B T_0}\right)\left[\left(\langle p_x^2\rangle - \langle p_y^2\rangle\right)\cos(2\Theta) - 5\langle p_x^2\rangle + 2\langle p_y^2\rangle + 3\langle p_z^2\rangle\right] \\ &+ \left(\frac{4N}{315\pi}\right)\left(\frac{m\overline{\omega}^3 a_d^2}{k_B T_0}\right)\left[\left(\langle p_z^2\rangle - \langle p_x^2\rangle\right)\cos(4\Theta)\right. \\ &\qquad \left. - 4\left(\langle p_x^2\rangle - \langle p_y^2\rangle\right)\cos(2\Theta) + 61\langle p_x^2\rangle - 28\langle p_y^2\rangle - 33\langle p_z^2\rangle\right], \end{aligned} \tag{3.25a}$$

$$\begin{aligned}\mathcal{C}_{\mathrm{B}}[\Delta p_y^2] \approx{}& \left(\frac{8N}{15\pi}\right)\left(\frac{m\overline{\omega}^3 a_{\mathrm{eff}}^2}{k_B T_0}\right)\left[\langle p_x^2\rangle + \langle p_z^2\rangle - 2\langle p_y^2\rangle\right] \\ &- \left(\frac{64N}{105\pi}\right)\left(\frac{m\overline{\omega}^3 a_s a_d}{k_B T_0}\right)\left[\left(\langle p_x^2\rangle - \langle p_z^2\rangle\right)\cos(2\Theta) - 2\langle p_x^2\rangle + 4\langle p_y^2\rangle - 2\langle p_z^2\rangle\right] \\ &+ \left(\frac{16N}{315\pi}\right)\left(\frac{m\overline{\omega}^3 a_d^2}{k_B T_0}\right)\left[\left(\langle p_x^2\rangle - \langle p_z^2\rangle\right)\cos(2\Theta) - 7\langle p_x^2\rangle + 14\langle p_y^2\rangle - 7\langle p_z^2\rangle\right], \end{aligned} \tag{3.25b}$$

$$\begin{aligned}\mathcal{C}_{\mathrm{B}}[\Delta p_z^2] \approx{}& \left(\frac{8N}{15\pi}\right)\left(\frac{m\overline{\omega}^3 a_{\mathrm{eff}}^2}{k_B T_0}\right)\left[\langle p_x^2\rangle + \langle p_y^2\rangle - 2\langle p_z^2\rangle\right] \\ &+ \left(\frac{64N}{105\pi}\right)\left(\frac{m\overline{\omega}^3 a_s a_d}{k_B T_0}\right)\left[\left(\langle p_y^2\rangle - \langle p_z^2\rangle\right)\cos(2\Theta) + 3\langle p_x^2\rangle + 2\langle p_y^2\rangle - 5\langle p_z^2\rangle\right] \\ &+ \left(\frac{4N}{315\pi}\right)\left(\frac{m\overline{\omega}^3 a_d^2}{k_B T_0}\right)\left[\left(\langle p_x^2\rangle - \langle p_z^2\rangle\right)\cos(4\Theta)\right. \\ &\qquad \left. - 4\left(\langle p_y^2\rangle - \langle p_z^2\rangle\right)\cos(2\Theta) - 33\langle p_x^2\rangle - 28\langle p_y^2\rangle + 61\langle p_z^2\rangle\right], \end{aligned} \tag{3.25c}$$

where $a_{\mathrm{eff}}^2 = 2\left(a_s^2 - 4a_s a_d/3 + 4a_d^2/9\right)$. In the absence of dipoles, the expressions above reduce to

$$\mathcal{C}_s[\Delta p_\perp^2] = \left(\frac{16N}{15\pi}\right)\left(\frac{m\overline{\omega}^3 a_s^2}{k_B T_0}\right)\left[\langle p_z^2\rangle - \langle p_\perp^2\rangle\right], \tag{3.26a}$$

$$\mathcal{C}_s[\Delta p_z^2] = \left(\frac{16N}{15\pi}\right)\left(\frac{m\overline{\omega}^3 a_s^2}{k_B T_0}\right)\left[\langle p_\perp^2\rangle - \langle p_z^2\rangle\right], \tag{3.26b}$$

with purely $s$-wave scattering, where $p_\perp^2 = p_x^2 + p_y^2$.

Likewise, for fermions (F), the collision integrals are:

$$\begin{aligned}\mathcal{C}_{\mathrm{F}}[\Delta p_x^2] = \left(\frac{4N}{315\pi}\right)\left(\frac{m\overline{\omega}^3 a_d^2}{k_B T_0}\right)&\left[4\left(\langle p_x^2\rangle - \langle p_y^2\rangle\right)\cos(2\Theta) + 17\left(\langle p_x^2\rangle - \langle p_z^2\rangle\right)\cos(4\Theta)\right. \\ &\left. - 45\langle p_x^2\rangle + 12\langle p_y^2\rangle + 33\langle p_z^2\rangle\right], \end{aligned} \tag{3.27a}$$

$$\mathcal{C}_{\rm F}[\Delta p_y^2] = \left(\frac{16N}{315\pi}\right)\left(\frac{m\bar{\omega}^3 a_d^2}{k_B T_0}\right)\left[3\langle p_x^2\rangle - 6\langle p_y^2\rangle + 3\langle p_z^2\rangle - \left(\langle p_x^2\rangle - \langle p_z^2\rangle\right)\cos(2\Theta)\right], \tag{3.27b}$$

$$\mathcal{C}_{\rm F}[\Delta p_z^2] = \left(\frac{4N}{315\pi}\right)\left(\frac{m\bar{\omega}^3 a_d^2}{k_B T_0}\right)\left[4\left(\langle p_y^2\rangle - \langle p_z^2\rangle\right)\cos(2\Theta) - 17\left(\langle p_x^2\rangle - \langle p_z^2\rangle\right)\cos(4\Theta) + 33\langle p_x^2\rangle + 12\langle p_y^2\rangle - 45\langle p_z^2\rangle\right]. \tag{3.27c}$$

Refs. [14, 15] also have all these collision integrals listed.

I should emphasize that these analytic forms hold only in the close-to-threshold scattering regime (see Sec. 2.1.4), otherwise, numerical integrators are required to compute $\mathcal{C}[\Delta p_i^2]$. Moreover, caution should be taken for temperatures approaching absolute zero, where quantum statistics start to have a significant effect on the gas ensemble distributions. In particular, the equilibrium particle distribution deviates from one described by Maxwell-Boltzmann statistics, in turn requiring that the collision integral also be modified to satisfy the quantum Boltzmann equation (3.3). These quantum statistical corrections, along with more general forms of out-of-equilibrium dynamics, require more general methods of solutions. So as not to leave you hanging, let me tell you about a solution method of the numerical variety I've used.

## 3.3 Direct simulation Monte Carlo solutions

Time evolution of a dynamical system can be performed numerically by advancing the equations of motion with discrete time steps. Ideally, these time steps are made adaptive to efficiently cater for the various phenomena of interest that might occur on different time scales [73]. For the Boltzmann equation, dynamics that arise from it can be separated into two main processes: a) classical Hamiltonian evolution in phase space [left-hand side of Eq. (3.1)], and b) two-body collisional interactions [right-hand side of Eq. (3.1)]. This partitioning implies two distinct time scales relevant to the solver, $\tau_V$ and $\tau_{\rm coll}$, that can be related to a characteristic confinement potential time scale and the collision rate respectively. For instance, a harmonically trapped dilute gas would have these time scales set by

$$\tau_V = 2\pi\bar{\omega}^{-1}, \tag{3.28a}$$

$$\tau_{\text{coll}} = \langle n\sigma v_r \rangle^{-1}, \tag{3.28b}$$

where $\overline{\omega}$ is the geometric mean of the harmonic trapping frequencies, $\sigma = \int d\Omega' \frac{d\sigma}{d\Omega'}$ is the total cross section and $v_r$ is the relative velocity of collision partners. My implementation thus takes Hamiltonian evolution to occur in time steps of size $\Delta t \ll \tau_V$, and collisions in time steps of size $\delta t \ll \tau_{\text{coll}}$. I further allow $\delta t$ to change during the simulation, setting it as a function of the mean collision rate at any given time [1] . A visual summary of the numerical time integration scheme is provided in Fig. 3.3.

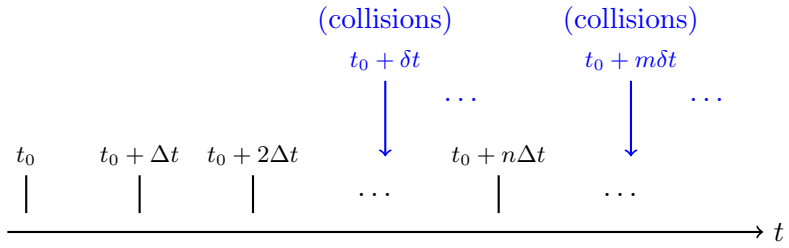


Figure 3.3: The numerical time integration scheme. Two time steps are utilized: a) $\Delta t$ for Hamiltonian evolution of the particles under $V(\boldsymbol{r})$, and b) $\delta t$ for collisional processes ($m, n \in \mathbb{N}$).

### 3.3.1 Evolution in classical phase space

As formulated, the phase space distribution is a continuous function of particle positions and momenta, and so requires an appropriate discretization scheme for numerical simulation. I do so by sampling points in phase space which I refer to as “test particles", such that

$$f(\boldsymbol{r}, \boldsymbol{p}) \approx \xi \sum_{k=1}^{N_T} \delta^3(\boldsymbol{r} - \boldsymbol{r}^{(k)}) \delta^3(\boldsymbol{p} - \boldsymbol{p}^{(k)}), \tag{3.29}$$

where $\xi = N/N_T$ is the ratio of the actual number of particles to test particles. A continuous distribution is then retrieved in the limit of $N_T \to \infty$. Each test particle undergoes a classical trajectory subject to the potential $V(\boldsymbol{r})$, progressing in time numerically with the Störmer-Verlet

[1] In studies where large variations in local density are expected, $\delta t$ could be a function of local density and velocity distributions. This would however be way more involved, so I have kept $\delta t$ as defined by the mean collision rate.

symplectic integrator method:

$$\boldsymbol{q}^{(k)} = \boldsymbol{r}^{(k)}(t) + \frac{\Delta t}{2m}\boldsymbol{p}^{(k)}(t), \tag{3.30a}$$

$$\boldsymbol{p}^{(k)}(t+\Delta t) = \boldsymbol{p}^{(k)}(t) + \boldsymbol{F}^{(k)}\Delta t, \tag{3.30b}$$

$$\boldsymbol{r}^{(k)}(t+\Delta t) = \boldsymbol{q}^{(k)} + \frac{\Delta t}{2m}\boldsymbol{p}^{(k)}(t+\Delta t), \tag{3.30c}$$

which is constructed to preserve Hamiltonian flow [74]. Superscripts $k$ on the phase space variables index the various test particles, while $\Delta t$ is the numerical time step size as previously prescribed.

### 3.3.2 The two-body collision integral

To tackle the collision integral of Eq. (3.3), I utilize the direct simulation Monte Carlo (DSMC) method [75, 76] as a means of numerical integration. At time intervals of $\delta t$, the DSMC recipe apportions various chunks of 3-dimensional real space volume for Monte Carlo sampling, by constructing a discrete spatial grid. Just as is done for time, I adopt a locally adaptive space-discretization scheme that allows the grid to account for local density variations, performed in two phases. Phase one is the construction of a master-grid, by first establishing the relevant simulation volume from the ensemble of test particle positions $\{\boldsymbol{r}^{(k)}\}$:

$$V_{\text{sim}} = \prod_{j=1}^{3}\Big(\max_k\{r_j^{(k)}\} - \min_k\{r_j^{(k)}\}\Big). \tag{3.31}$$

This volume is then partitioned uniformly into cells of equal volume $\Delta V_{\text{sim}}$, and test particles binned into them based on their positions (visualized in subplot a of Fig. 3.4). The number of such cells is preferably set such that the hyperparameter[2] $(\Delta V_{\text{sim}})^{1/3}$ is much larger than the molecular mean-free path, since phase two proceeds to further refine the grid with an octree algorithm [77]. By taking each master-grid cell and recursively subdividing it into eight octants, the octree algorithm terminates only when each octant has at most $N_{\text{oc}}^{\max}$ test particles, another hyperparameter. In my implementation, each octree division of a sub-volume is performed such that the central vertex is located at the barycentric coordinate of simulation particles in that sub-volume. An example of

[2] *Hyperparameters* are numerical parameters tuned by the user for optimality of computational efficiency and stochastic convergence.

the octree refinement algorithm (with uniform subdivisions) applied to a system of $N_T = 100$ test particles and $N_{\text{oc}}^{\max} = 10$, is provided in Fig. 3.4.

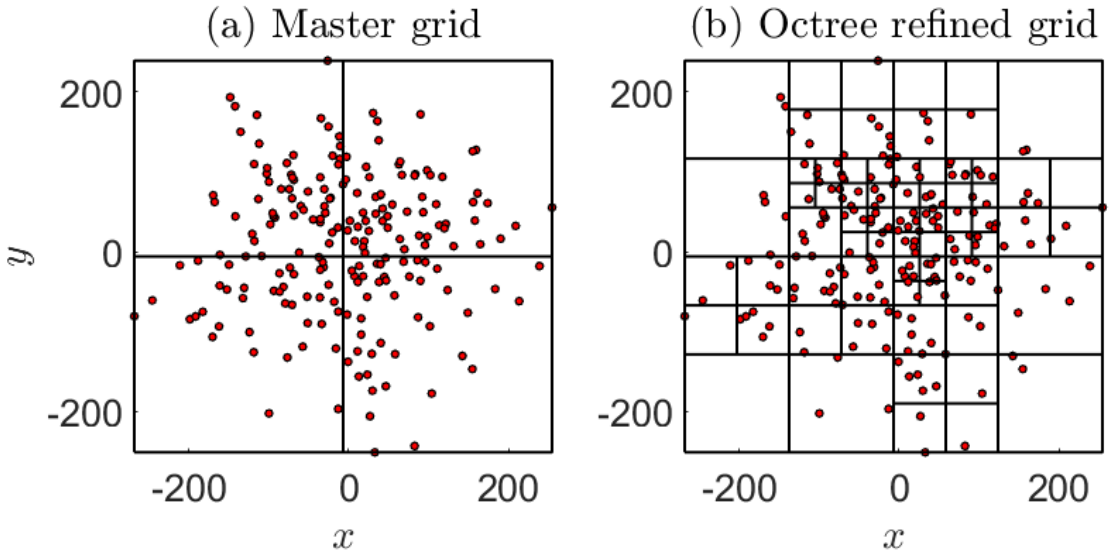


Figure 3.4: Visualization of the octree algorithm refinement (b), applied to the master-grid (a), projected in the $x, y$-plane. There are initially 8 master-grid cells with $N = 200$, and $N_{\text{cell}}^{\max} = 3$, with Gaussian distributed points in arbitrary units.

When sufficiently discretized, collisions can be assumed to only occur within each grid cell and not between them. Collisions between particles result in them exiting a phase space volume element $d^3\boldsymbol{r}d^3\boldsymbol{p}$, at a rate given by

$$d^3\boldsymbol{r}d^3\boldsymbol{p}\frac{\delta f^{\text{out}}}{\delta t} = d^3\boldsymbol{r}d^3\boldsymbol{p}\mathcal{I}_{\text{coll}}^{\text{out}}[f], \tag{3.32a}$$

$$\text{where} \quad \mathcal{I}_{\text{coll}}^{\text{out}}[f] = -\int \frac{d^3\boldsymbol{p}_1}{m}|\boldsymbol{p}-\boldsymbol{p}_1|\int d\Omega' \frac{d\sigma}{d\Omega'} f f_1 \left(1 \pm h^3 f'\right)\left(1 \pm h^3 f_1'\right). \tag{3.32b}$$

In the simulation, products of pre-scattering distributions in a differential phase space volume $d^3\boldsymbol{r}d^3\boldsymbol{p}ff_1$, are replaced by pairs of test particles in any given grid cell along with their associated momenta $\boldsymbol{p}$ and $\boldsymbol{p}_1$. In the event of a collision, the post-scattering momenta $\boldsymbol{p}'$ and $\boldsymbol{p}_1'$, are then sampled from $d\sigma/d\Omega'$ to obtain an approximation of $d^3\boldsymbol{r}d^3\boldsymbol{p}f'f_1'$. Application of these steps to all grid cells effectively results in Monte Carlo integration of the collision integral for a time step $\delta t$.

In practice, collision sampling described above is performed sequentially by determining a) collision occurrences, and then b) post-collision momenta.

In step (a), a collision occurs between test particles $i$ and $j$, with probability

$$P_{ij} = \xi \Gamma_{\rm coll}(\boldsymbol{p}_{ij})\delta t \tag{3.33}$$

with a local collision rate between particles $i$ and $j$ of relative momentum $\boldsymbol{p}_{ij} = \boldsymbol{p}_i - \boldsymbol{p}_j$ defined as:

$$\Gamma_{\rm coll} = \frac{(1+Q)^2}{\Delta V_{\rm cell}} \sigma(\boldsymbol{p}_{ij}) \frac{p_{ij}}{m}, \tag{3.34}$$

where quantum statistics requires $Q = 1$ for bosons or $Q = 0$ for fermions. In general, the total cross section comprises a sum of elastic and inelastic parts $\sigma = \sigma_{\rm el} + \sigma_{\rm inel}$, the latter of which typically leads to 2-body losses from the trap. If present, an additional step (a′) is added which removes particle pairs from the simulation with probability $P_{\rm loss} = \sigma_{\rm inel}/\sigma$. Otherwise, a collision progresses the simulation to step (b), where the elastic portion of Eq. (3.33) carves out an upper bound for its sampling domain. Particle momenta following an elastic collision are obtained from the anisotropic dipolar differential cross section of Ref. [35], with an accept-reject scheme [75].

#### 3.3.2.1 Accept-reject collision sampling

An elastic collision causes a rotation of the relative momentum vector between colliders, directing the particles along a new set of scattering angles $(\theta', \phi')$. Numerical instances of these angles $(\bar{\theta}', \bar{\phi}')$ are sampled from a probability distribution

$$p(\hat{\boldsymbol{p}}_r, \hat{\boldsymbol{p}}'_r) = \frac{1}{\sigma_{\rm el}(\hat{\boldsymbol{p}}_r)} \frac{d\sigma_{\rm el}}{d\Omega}(\hat{\boldsymbol{p}}_r, \hat{\boldsymbol{p}}'_r) \sin\theta', \tag{3.35}$$

where I adopt the convention in which the distribution is defined with the Jacobian $\sin\theta'$. This has a concise form for both bosons (B) and fermions (F), written explicitly in the collision-frame (CF) of Sec. 3.2.1 as [76]:

$$p_B(\theta', \phi'; \eta) = \frac{2\left[2 - 3\tilde{a} - 3\cos^2\eta - 3\cos^2\phi' \sin^2\eta\right]^2 \sin\theta'}{\pi\left[72\tilde{a}^2 + 11 - 30\cos^2\eta + 27\cos^4\eta - 24\tilde{a}\,(1 - 3\cos^2\eta)\right]}, \tag{3.36a}$$

$$p_F(\theta', \phi'; \eta) = \frac{6\left[\cos\theta\cos^2\eta - \cos^2\phi' \sin^2\eta + \cos\phi' \sin\theta' \sin(2\eta)\right]^2 \sin\theta'}{\pi\left[3 + 18\cos^2\eta - 13\cos^4\eta\right]}, \tag{3.36b}$$

where $\tilde{a} = a_s/a_d$ and $\eta = \cos^{-1}(\hat{\boldsymbol{p}}_r \cdot \hat{\boldsymbol{\mathcal{E}}})$. However, sampling directly from these distributions is not straightforward, so an accept-reject algorithm is employed as an alternative. This algorithm proceeds as follows:

(1) First, sample the variables $(\bar{\theta}', \bar{\phi}')$ and $\bar{u}$ by

$$\bar{\theta}' = \pi r_{\theta'}, \tag{3.37a}$$

$$\bar{\phi}' = 2\pi r_{\phi'}, \tag{3.37b}$$

$$\bar{u} = r_u, \tag{3.37c}$$

where $r_{\theta'}, r_{\phi'}$ and $r_u$ are all random samples from a uniform distribution $\mathcal{U}(0,1)$;

(2) compute a normalization $M = 2\pi^2 p_{F,B}^{(\max)}(\bar{\theta}', \bar{\phi}'; \eta)$, where

$$p_{F,B}^{(\max)}(\eta) = \max_{\theta',\phi'} \left\{ p_{F,B}(\theta', \phi'; \eta) \right\}; \tag{3.38}$$

(3) check if the rejection criterion:

$$\bar{u} < \frac{p_{F,B}(\bar{\theta}', \bar{\phi}'; \eta)}{M g(\bar{\theta}', \bar{\phi}')}, \tag{3.39}$$

is met. If met, $(\bar{\theta}, \bar{\phi})$ is accepted as a realization of effective sampling from $p_{F,B}$. Otherwise, start over from step 1 until the condition is met.

Because the scattering angles are sampled within the collision frame, it is necessary to perform a frame rotation to convert these angles back into the lab frame. The post-collision relative momentum vector in the lab-frame (LF) is given by

$$\boldsymbol{p}_r' = \hat{\boldsymbol{e}}_1^{\mathrm{CF}} \sin\theta' \cos\phi' + \hat{\boldsymbol{e}}_2^{\mathrm{CF}} \sin\theta' \sin\phi' + \hat{\boldsymbol{e}}_3^{\mathrm{CF}} \cos\theta', \tag{3.40}$$

as written in terms of the collision-frame unit-vectors

$$\hat{\boldsymbol{e}}_1^{\mathrm{CF}} = \begin{pmatrix} \cos\gamma \cos\theta_{\mathrm{LF}} \cos\phi_{\mathrm{LF}} - \sin\gamma \sin\phi_{\mathrm{LF}} \\ \cos\gamma \cos\theta_{\mathrm{LF}} \sin\phi_{\mathrm{LF}} + \sin\gamma \cos\phi_{\mathrm{LF}} \\ -\cos\gamma \sin\theta_{\mathrm{LF}} \end{pmatrix}, \tag{3.41a}$$

$$\hat{\boldsymbol{e}}_2^{\mathrm{CF}} = \begin{pmatrix} -\sin\gamma\cos\theta_{\mathrm{LF}}\cos\phi_{\mathrm{LF}} - \cos\gamma\sin\phi_{\mathrm{LF}} \\ -\sin\gamma\cos\theta_{\mathrm{LF}}\sin\phi_{\mathrm{LF}} + \cos\gamma\cos\phi_{\mathrm{LF}} \\ \sin\gamma\sin\theta_{\mathrm{LF}} \end{pmatrix}, \tag{3.41b}$$

$$\hat{\boldsymbol{e}}_3^{\mathrm{CF}} = \begin{pmatrix} \sin\theta_{\mathrm{LF}}\cos\phi_{\mathrm{LF}} \\ \sin\theta_{\mathrm{LF}}\sin\phi_{\mathrm{LF}} \\ \cos\theta_{\mathrm{LF}} \end{pmatrix}, \tag{3.41c}$$

where

$$\gamma = \tan^{-1}\left(\frac{\sin\phi\sin\Theta}{\sin\theta\cos\Theta - \cos\theta\cos\phi\sin\Theta}\right). \tag{3.42}$$

These coordinate transformations can be rather confusing, but I refer the reader back to Fig. 3.2 as a visual aid.

Convergence of the accept-reject algorithm to $p_F(\theta, \phi, \eta)$ with an increasing number of samples is illustrated in Fig. 3.5. As plotted, I have set $\eta = \pi/4$ and utilized (a) $10^5$, (b) $10^6$ and (c) $10^7$ random samples to approximate the analytic distribution (d). The respective color bar ranges corresponding to each subplot also show a suppression of statistical fluctuations with more samples.

#### 3.3.2.2 Accounting for quantum statistics

Before calling it a day, quantum mechanics requires of us one additional accept-reject step [78]. The collisions we simulate here do not simply occur in a vacuum, but are in fact, surrounded by a sea of many other quantum bodies. And these quantum bodies will have a say on the final scattering state outcome. Bosons accept more of these final states, while fermions do quite the opposite. Consequently, the sampled post-collision momenta are only accepted with probability

$$P_{ij}^{Q} = \frac{\left(1 \pm h^3 f_i'\right)\left(1 \pm h^3 f_j'\right)}{(1+Q)^2}, \tag{3.43}$$

otherwise no collision is said to have occurred in the first place. Going back to retroactively throw away simulated collisions is a little cumbersome, but that is just what quantum mechanics requires.

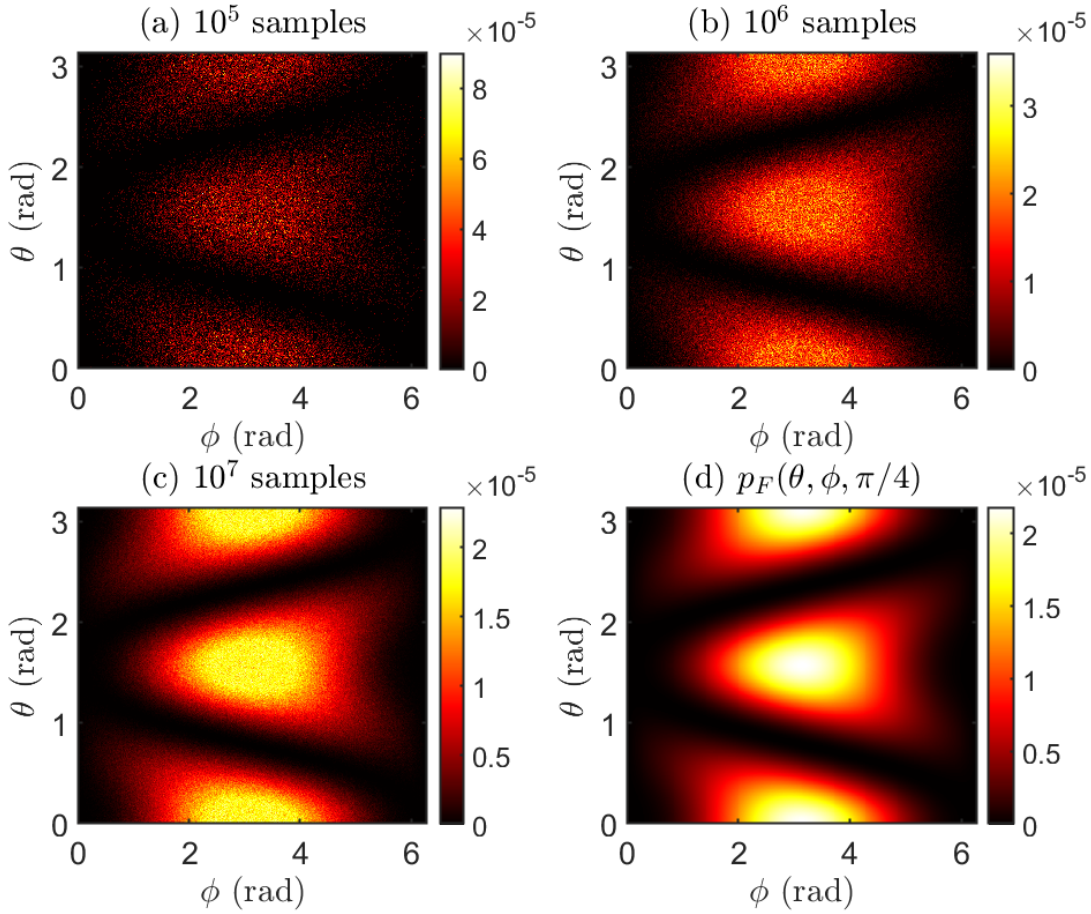


Figure 3.5: The probability distribution $p_F(\theta, \phi, \eta)$ with $\eta = \pi/4$ (d), and its approximations as obtained from the accept-reject algorithm with (a) $10^5$, (b) $10^6$ and (c) $10^7$ random samples.

Computing $f'$ in Eq. (3.43) is, however, problematic since the particle distributions $f_i'$ and $f_j'$ are discretized in the simulation. We resolve this issue by "smearing" the $\delta$-functions in Eq. (3.29) with a Gaussian convolutional kernel [78–80]:

$$\begin{aligned} f(\boldsymbol{r}, \boldsymbol{p}, t) &\approx \xi \sum_{k=1}^{N_T} \delta^3(\boldsymbol{r} - \boldsymbol{r}^{(k)}) \delta^3(\boldsymbol{p} - \boldsymbol{p}^{(k)}) \\ &\to \quad \xi \sum_{k=1}^{N_T} \left( \prod_{j=1}^{3} \frac{e^{-(r-r_k)^2/w_j^2}}{\sqrt{\pi w_j^2}} \right) \left( \prod_{j=1}^{3} \frac{e^{-(p-p_k)^2/w_{p_j}^2}}{\sqrt{\pi w_{p_j}^2}} \right). \end{aligned} \tag{3.44}$$

These Gaussian kernels are taken to have spatial width $w_j$, and momentum width $w_{p_j}$, such that the discretization noise is smoothed out while the distribution function remains physically consistent.

These criteria are encapsulated by the conditions [79]:

$$w_p \overline{w}_r \gg h \left( \frac{N}{N_{\text{sim}}} \right)^{1/3}, \tag{3.45a}$$

$$w_i \ll R_i \frac{T}{T_F}, \tag{3.45b}$$

$$w_p \ll p_F \frac{T}{T_F}, \tag{3.45c}$$

where $p_F = \hbar(3\pi^2\langle n \rangle)^{1/3}$ is the Fermi momentum, $R_i = p_F/(m\omega_i)$ are the Thomas-Fermi radii and bars denote geometric means. We use widths defined by the geometric means of these upper and lower bounds, multiplied by yet another hyperparameter $\beta$. With a large number of test particles, it is sufficient for smearing to be done with $N_s < N_T$ random samples of test particles rather than all of them. This greatly speeds up simulation time while maintaining physical accuracy, given that $N_s$ and $\beta$ are chosen appropriately. Fig. 3.6 shows an example of a Gaussian distributed ensemble of $N_s = N_T = 1000$ particles (a), smeared by a Gaussian kernel (b) as described above and plotted in the $x, y$-plane. All units used for this plot are arbitrary.

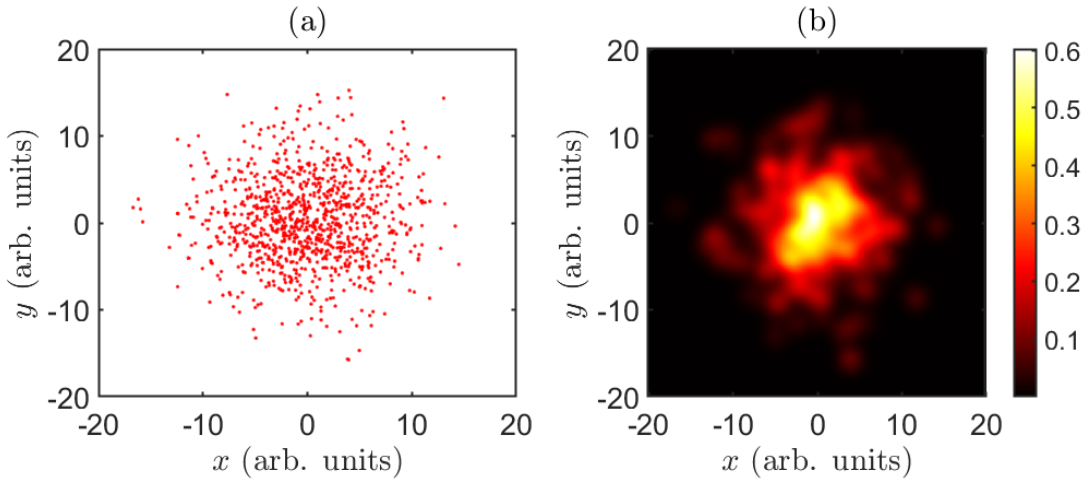


Figure 3.6: A discrete ensemble of 1000 Gaussian distributed particles (a), smeared against a Gaussian kernel to generate a smooth distribution (b). The plot is a projection of the distributions in the $y = 0$ plane in arbitrary units.

Only now, does the algorithm conclude. To summarize, I have laid out an efficient implementation of the DSMC method to numerically integrate the Boltzmann equation. Combining

Hamiltonian evolution in discrete phase space (3.3.1) with Monte Carlo sampling of 2-body collisions (3.3.2), this tool allows for accurate and general simulations of dipolar gas dynamics. An isolated theorist's proxy for running real ultracold experiments!

### 3.3.3 Some considerations and comments

I will end this chapter with some final practical tips and remark on issues one might encounter. For one, when simulating a gas with very large collision rates, computing collisions by iterating over all grid cells can be extremely computationally expensive. This time cost can, however, be mitigated with parallel processing in the far from degenerate regime. Without the need to include quantum statistics, the DSMC algorithm only samples collisions within each cell, making collision sampling independent between cells and thus, parallelizable. But before you snatch up all the cores you can get from your nearest Best Buy®, the computational overhead of dispatching collision computations to multiple cores should be weighed against how much parallelization speed up you get over plain sequential iteration. These time savings are pretty machine dependent, so the decision to parallelize is best left to the hands of the programmer.

Upon construction of the DSMC solver, accurate simulations require you to ensure that your numerics are appropriately converged. A good way to verify this is by *convergence in distribution* [81]. Knowing that the Boltzmann equation necessarily brings a nonequilibrium gas of elastic colliders back to thermal equilibrium, one could check that the DSMC solver satisfies this property too. That is, the steady state phase space distribution of the gas, without the inclusion of quantum statistics, should converge closer and closer to that in Eq. (3.5) as $N$ increases. If not, one could consider increasing the number of simulation test particles $N_T$, or varying the maximum number of simulation particles per grid cell $N_{\text{oc}}^{\max}$ until such convergence is achieved. With quantum statistical effects included, the simulation should instead converge to the equilibrium Bose-Einstein (BE) or Fermi-Dirac (FD) distributions:

$$f_{\text{BE}}(\boldsymbol{r},\boldsymbol{p}) = \frac{E^2}{2(\hbar\overline{\omega})^3}\left[\exp\left(\frac{E-\mu_c}{k_B T}\right)-1\right]^{-1}, \tag{3.46a}$$

$$f_{\mathrm{FD}}(\boldsymbol{r},\boldsymbol{p}) = \frac{E^2}{2(\hbar\overline{\omega})^3}\left[\exp\left(\frac{E-\mu_c}{k_BT}\right)+1\right]^{-1}, \tag{3.46b}$$

where $\mu_c$ is the chemical potential defined such that $\int f(E)dE = N$. The $N_s$ and $\beta$ hyperparameters must, therefore, also be tuned accordingly to ensure convergence in these distributions.

One final remark. When dealing with a bulk gas of dipoles, one might be concerned about long-range forces modifying the particle dynamics. Conveniently though, the temperatures and densities considered in this thesis mostly render these forces negligible. For quantitative reassurance, one could compare the thermal energy to the average dipolar mean-field energy experienced per particle:

$$\varepsilon_{\mathrm{mf}} = \frac{N}{24\sqrt{\pi}}h\left(\frac{\sigma_\perp}{\sigma_z}\right)\frac{d^2\left[1-3\cos^2(\Theta)\right]}{4\pi\epsilon_0\sigma_\perp^2\sigma_z}, \tag{3.47a}$$

$$h(x) = \frac{1+2x^2}{1-x^2} - \frac{3x^2\operatorname{arctanh}\sqrt{1-x^2}}{(1-x^2)^{3/2}}, \tag{3.47b}$$

derived in App. D. For the most part, $\varepsilon_{\mathrm{mf}}/(k_BT)$ remains $\lesssim 0.01$ for the regimes of interest, allowing $\varepsilon_{\mathrm{mf}}$ to be safely ignored. But if one needed to simulate a gas with $\varepsilon_{\mathrm{mf}} \gtrsim k_BT$, say for polar molecules with massive dipole moments, I'd recommend a pseudospectral method like those in Refs. [82, 83], for efficient handling of dipolar mean-field forces.

# Chapter 4

## Return to Equilibrium I: Dilute Gases

Macroscopia? No, this is not an illusion[1] ! This chapter explores the macroscopic anisotropy that directly results from the microscopic anisotropies in dipolar scattering. Part one of a two-part saga. More specifically, this manifestation of anisotropy in collective gas dynamics is studied in the context of the gas' route to equilibrium. I start first with the dilute case, where collisions occur infrequently over the course of a dipole's journey across the gaseous sample. Think offensive phase with running backs trying to avoid tackles for a touchdown, as opposed to defensive phase with defensive guards perpetually colliding into the opposing offense[2] . The latter of which is likened to the hydrodynamic regime of the next chapter.

### 4.1 Anisotropic thermalization of dilute dipolar gases

Although the Boltzmann equation preaches a certainty of thermalization, the *rate* at which this equilibrium is achieved may vary in direction due to the anisotropy dipoles bring. These rates can be probed in experiments known as *cross-dimensional rethermalization*, where a gas initially at equilibrium is preferentially heated along a particular coordinate axis, then left alone to rethermalize. Rethermalization occurs by means of elastic collisions that redistribute thermal energy throughout the gas, at a rate proportional to the integral cross section, $\overline{\sigma}$ [84–87]. However, not every collision counts the same toward rethermalization: if the differential cross section favors forward scattering,

[1] Unless our universe is a simulation then perhaps it is one.

[2] I don't even watch American football (except for the Super Bowl halftime shows), but you can't blame a physicist for trying to draw analogies. Sko buffs!

it is not useful, since the collision would have done nothing to redistribute energy into the other axes not coincident with the incident one. A mantra of collisional thermalization that holds exceptionally true for anisotropic scattering. Fig. 4.1 shows a cartoon of the cross-dimensional rethermalization process and a schematic of collisions that aid or evade thermalization.

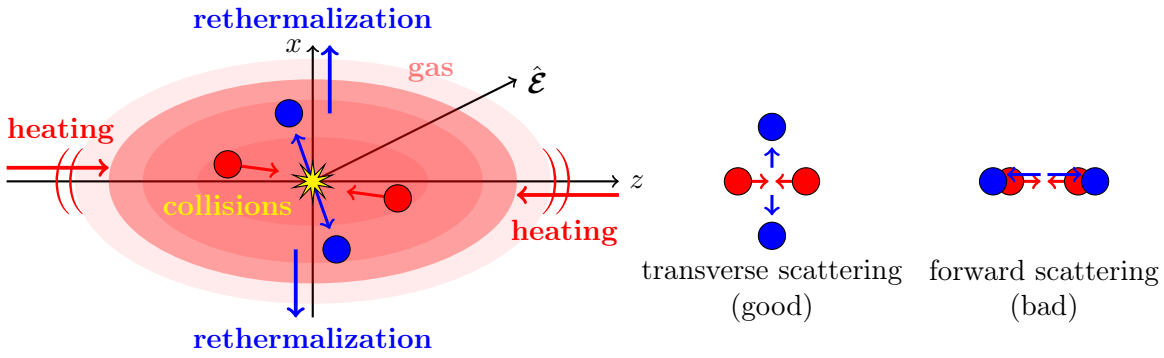


Figure 4.1: Cartoon of a cross-dimensional rethermalization experiment. Collisions that scatter primarily into the transverse directions promote thermalization, whereas forward scattering hinders it. Red indicates pre-collision colliders, while post-collision ones are blue.

### 4.1.1 How many collisions before one is thermalizing?

When dilute, a gas that is heated along the $i$-th coordinate will rethermalization along the $j$-th coordinate at a rate $\gamma_{ij}(\Theta)$, following the decay law of Eq. (3.8). This rate depends on the density and temperature of the given experiment, whereby it is useful to compare the rethermalization rate to a standard collision rate

$$\gamma_{\text{coll}} = \langle n\sigma v_r \rangle. \tag{4.1}$$

At threshold, $\sigma$ is energy independent and permits the factorization $\langle n \rangle \overline{\sigma} \langle v_r \rangle$, where $\overline{\sigma}$ is the integral cross section, $\langle n \rangle$ is the average number density of the gas (3.14) and $\langle v_r \rangle = \sqrt{8k_BT/(\mu\pi)}$ is the mean collision velocity. Thus for relaxation considerations, the rethermalization rate is proportional to the standard collision rate via

$$\gamma_{ij}(\Theta) = \frac{\gamma_{\text{coll}}}{\mathcal{N}_{ij}(\Theta)}, \tag{4.2}$$

whose proportionality constant $\mathcal{N}_{ij}$, is known as the *number of collisions per rethermalization* [84]. The number for rethermalization, a truncation of its full name I will adopt for succinctness, quantifies the average number of collision instances required before a collision useful for thermalization occurs.

In a harmonic trap, the position and momentum widths, quantified by $\langle r_j^2 \rangle$ and $\langle p_j^2 \rangle$, will experience more or less out-of-phase oscillations at the trap frequency en route to rethermalization. Easing the extraction of rethermalization rates in theoretical studies then motivates the definition of non-equilibrium pseudotemperatures:

$$\mathcal{T}_j = \frac{m\omega_j^2 \langle {r_j}^2 \rangle}{2k_B} + \frac{\langle {p_j}^2 \rangle}{2mk_B}, \tag{4.3}$$

that suppresses trap oscillations in time-evolution. In fact, oscillations are innately suppressed in time-of-flight thermometry common to ultracold experiments, making the quantity above the relevant one to model. Then with experimental data, $\gamma_{ij}$ is extracted by fitting an exponential decay curve to the measured time trace of kinetic temperature along each direction. An example of such a fit is provided by the red dashed curve in Fig. 4.2, that is fitted to data (red diamonds) from a real cross-dimensional rethermalization experiment with ultracold $^{166}$Er atoms done at Innsbruck [2]. But more on this experiment later in Chap. 6.

Assuming that the rethermalization dynamics is dominated by a single decay rate, this rate can be determined from short-time behavior of the decay and permits a derivation of analytic expressions for $\mathcal{N}$. I refer to this scheme as the *short-time approximation*. To formulate this approximation, I define the phase space averaged quantity

$$\langle \chi_j \rangle = k_B(\mathcal{T}_j - T_{\mathrm{eq}}), \tag{4.4}$$

which quantifies the system's deviation from its equilibration temperature $T_{\mathrm{eq}}$. From Eqs. (3.8), the relaxation of $\langle \chi_j \rangle$ would follow the differential equation $d\langle \chi_j \rangle = \mathcal{C}[\Delta\chi_j]dt$, approximated as

$$\mathcal{C}[\chi_j] \approx -\gamma \langle \chi_j \rangle, \tag{4.5}$$

in the short-time approximation with a decay rate $\gamma$. The relation above thus identifies

$$\gamma = -\frac{1}{(\mathcal{T}_j(t) - T_{\mathrm{eq}})} \frac{d\mathcal{T}_j(t)}{dt}\bigg|_{t=0} \approx -\frac{\mathcal{C}[\Delta p_j^2]}{2m\,(\mathcal{T}_j(0) - T_{\mathrm{eq}})}, \tag{4.6}$$

as the rethermalization rate.

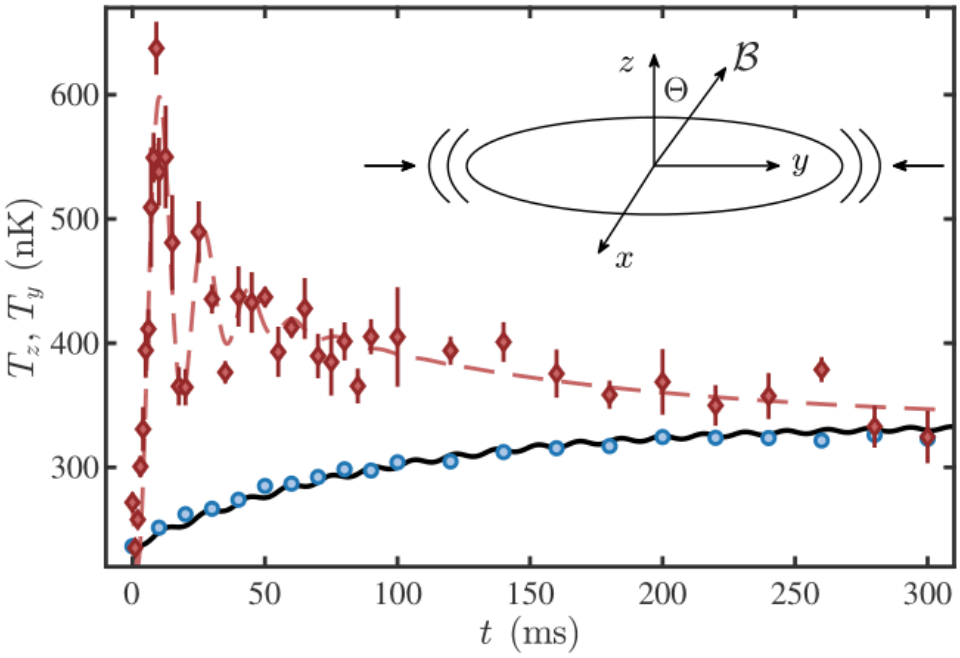


Figure 4.2: Experimentally measured momentum space temperatures $T_z$ (blue circles) and $T_y$ (red diamonds) after a trap frequency quench of the confining potential along $y$. The measurement was performed at  = 1 G and $\Theta = 0$ for $^{166}$Er. The red dashed line is an exponential+sinusoidal fit to the data. The black solid line denotes the results of the Enskog theory (3.8) for this specific data set. The error bars denote the standard error for three repetitions. The inset shows a schematic of the experimental setup. This plot is adapted from Ref. [2].

From $\gamma$ and the standard collision rate $\langle n\rangle\overline{\sigma}\langle v_r\rangle$, we can extract the value of $\mathcal{N}_{ij}$ via the relation in Eq. (4.2). As before, we consider an excitation of axis $i$, following which the rethermalization rate is measured along axis $j$. This is modeled by taking axis $i$ to have an initial out-of-equilibrium pseudotemperature

$$\mathcal{T}_i = T_0 + \frac{\delta_i}{k_B}, \tag{4.7}$$

where $\delta_i$ is a perturbance to the energy, while the initial temperatures along the 2 other axes are simply $T_0$. By construction of Eq. (4.6), $\delta_i$ stands as an auxiliary variable that cancels out in the derivation. For clarity, I present an explicit derivation for $\mathcal{N}_{xx}$ with bosons as follows.

An excitation along $x$ results in the equilibration temperature

$$T_{\rm eq} = \frac{2}{3}T_0 + \frac{1}{3}\left(T_0 + \frac{\delta_x}{k_B}\right) = T_0 + \frac{\delta_x}{3k_B}, \tag{4.8}$$

which follows from the equipartition theorem. Then measuring the rethermalization along the $x$-axis, the initial pseudotemperature deviation is inserted into the collision integral $\mathcal{C}[\Delta p_x^2]$ of Eq. 3.25, to give

$$\begin{aligned}\mathcal{C}[\Delta p_x^2] = \left(\frac{8Nm^2\overline{\omega}^3 a_{\rm eff}^2}{15\pi k_B T_0}\right)[-2\delta_x] + \left(\frac{64Nm^2\overline{\omega}^3 a_s a_d}{105\pi k_B T_0}\right)[\delta_x\cos(2\Theta) - 5\delta_x] \\ + \left(\frac{4Nm^2\overline{\omega}^3 a_d^2}{315\pi k_B T_0}\right)[61\delta_x - 4\delta_x\cos(2\Theta) - \delta_x\cos(4\Theta)]\,,\end{aligned} \tag{4.9}$$

where, to remind the reader, $\overline{\omega}$ is the geometric mean of trapping frequencies. Dividing this by $2m$ gives the thermalization rate

$$\begin{aligned}\gamma_{xx} &= -\frac{\mathcal{C}[\Delta p_x^2]}{2m\left(\mathcal{T}_x(0) - T_{\rm eq}\right)} \\ &= -\frac{3}{2}\frac{\mathcal{C}[\Delta p_x^2]}{m\delta_x} \\ &= \left(\frac{4Nm^2\overline{\omega}^3 a_{\rm eff}^2}{5\pi k_B T_0}\right) + \left(\frac{16Nm^2\overline{\omega}^3 a_s a_d}{35\pi k_B T_0}\right)[5 - \cos(2\Theta)] \\ &\quad + \left(\frac{Nm^2\overline{\omega}^3 a_d^2}{105\pi k_B T_0}\right)[\cos(4\Theta) + 4\cos(2\Theta) - 61]\,.\end{aligned} \tag{4.10}$$

Finally to get $\mathcal{N}$, the mean collision rate is computed as

$$\langle n\rangle\overline{\sigma}\langle v\rangle = N\left(\frac{m\overline{\omega}^2}{4\pi k_B T_0}\right)^{3/2}\left(8\pi a_s^2 + \frac{32\pi}{45}a_d^2\right)\left(\frac{16k_B T_0}{\pi m}\right)^{1/2} = \frac{4Nm^2\overline{\omega}^3\left(45a_s^2 + 4a_d^2\right)}{45\pi k_B T_0}, \tag{4.11}$$

and divided by $\gamma$. Utilizing the procedure just described, analytic forms for all $\mathcal{N}_{ij}$ are worked out for bosons as

$$\mathcal{N}_{xx}^B(\Theta) = \frac{4\left[a_s^2 + (4/45)a_d^2\right]}{a_{\rm eff}^2(4/5) + a_d a_s(16/35)[5 - \cos(2\Theta)] + a_d^2(1/105)[\cos(4\Theta) + 4\cos(2\Theta) - 61]}, \tag{4.12a}$$

$$\mathcal{N}_{xy}^B(\Theta) = \frac{4\left[a_s^2 + (4/45)a_d^2\right]}{a_{\rm eff}^2(4/5) + a_s a_d(32/35)[2 - \cos(2\Theta)] + a_d^2(8/105)[\cos(2\Theta) - 7]}, \tag{4.12b}$$

$$\mathcal{N}_{xz}^B(\Theta) = \frac{4\left[a_s^2 + (4/45)a_d^2\right]}{a_{\rm eff}^2(4/5) + a_s a_d(96/35) + a_d^2(2/105)[\cos(4\Theta) - 33]}, \tag{4.12c}$$

$$\mathcal{N}_{yy}^B(\Theta) = \frac{4\left[a_s^2 + (4/45)a_d^2\right]}{a_{\rm eff}^2(4/5) + a_s a_d(64/35) - a_d^2(56/105)}, \tag{4.12d}$$

$$\mathcal{N}^B_{yz}(\Theta) = \frac{4\left[a_s^2 + (4/45)a_d^2\right]}{a_{\text{eff}}^2\,(4/5) + a_s a_d\,(32/35)\,[2+\cos(2\Theta)] - a_d^2\,(8/105)\,[\cos(2\Theta)+7]}, \tag{4.12e}$$

$$\mathcal{N}^B_{zz}(\Theta) = \frac{4\left[a_s^2 + (4/45)a_d^2\right]}{a_{\text{eff}}^2\,(4/5) + a_s a_d\,(16/35)\,[5+\cos(2\Theta)] + a_d^2\,(1/105)\,[\cos(4\Theta) - 4\cos(2\Theta) - 61]}. \tag{4.12f}$$

In the absence of dipoles, bosons with purely $s$-wave scattering require $\mathcal{N}_s = 2.5$ collisions per rethermalizing collision [88], a result obtained by setting $a_d = 0$ in the expressions above. Fig. 4.3 plots $\mathcal{N}_{xz}$ as an illustrative example of its functional dependence on $\Theta$ and $a_s$ (in units of $a_d$). Subplot (b) shows that after an initial decrease, $\mathcal{N}_{xz}$ increases for $a_s \gtrsim 0.4a_d$ – and thus the thermalization loses efficiency – moving to the regime of contact dominated interaction, eventually retrieving the pure $s$-wave scattering result. A similar plot appears in Ref. [2].

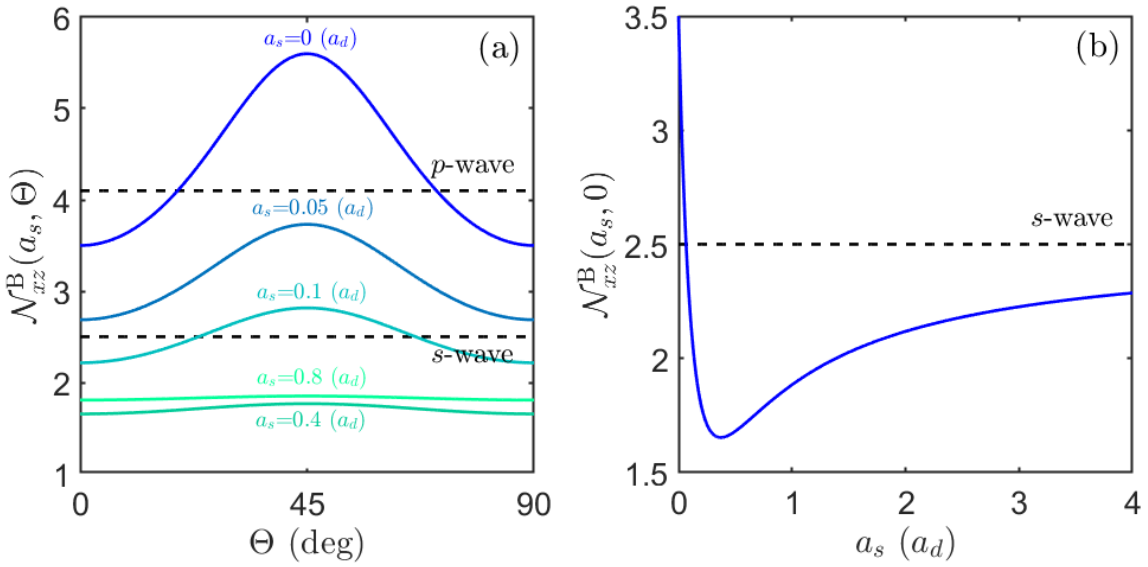


Figure 4.3: Subplot (a) shows the dependence of $\mathcal{N}^{\mathrm{B}}_{xz}$ on $\Theta$ and $a_s$, for $a_s/a_d = 0, 0.05, 0.1, 0.4$ and 0.8. Subplot (b) shows the functional dependence of $\mathcal{N}^{\mathrm{B}}_{xz}$ on $a_s$ at $\Theta = 0$. The black dashed lines show the values of $\mathcal{N}$ for $s$-wave and $p$-wave scattering, labeled respectively.

As for fermions, $\mathcal{N}^F_{ij}$ are functions of only $\Theta$, taking the much more concise forms:

$$\mathcal{N}^F_{xx}(\Theta) = \frac{112}{45 - 4\cos(2\Theta) - 17\cos(4\Theta)}, \tag{4.13a}$$

$$\mathcal{N}^F_{yx}(\Theta) = \frac{14}{3 - \cos(2\Theta)}, \tag{4.13b}$$

$$\mathcal{N}^F_{zx}(\Theta) = \frac{56}{33 - 17\cos(4\Theta)}, \tag{4.13c}$$

$$\mathcal{N}^F_{yy}(\Theta) = \frac{14}{3}, \tag{4.13d}$$

$$\mathcal{N}^F_{zy}(\Theta) = \frac{14}{3+\cos(2\Theta)}, \tag{4.13e}$$

$$\mathcal{N}^F_{zz}(\Theta) = \frac{112}{45+4\cos(2\Theta)-17\cos(4\Theta)}. \tag{4.13f}$$

All the quantities above are plotted in Fig. 4.4, where symmetries imply $\mathcal{N}_{ij}(\Theta) = \mathcal{N}_{ji}(\Theta)$. Evidently, thermalization rates can vary drastically depending on how the dipoles are orientated in space, presenting a tuning knob for thermalizing dynamics.

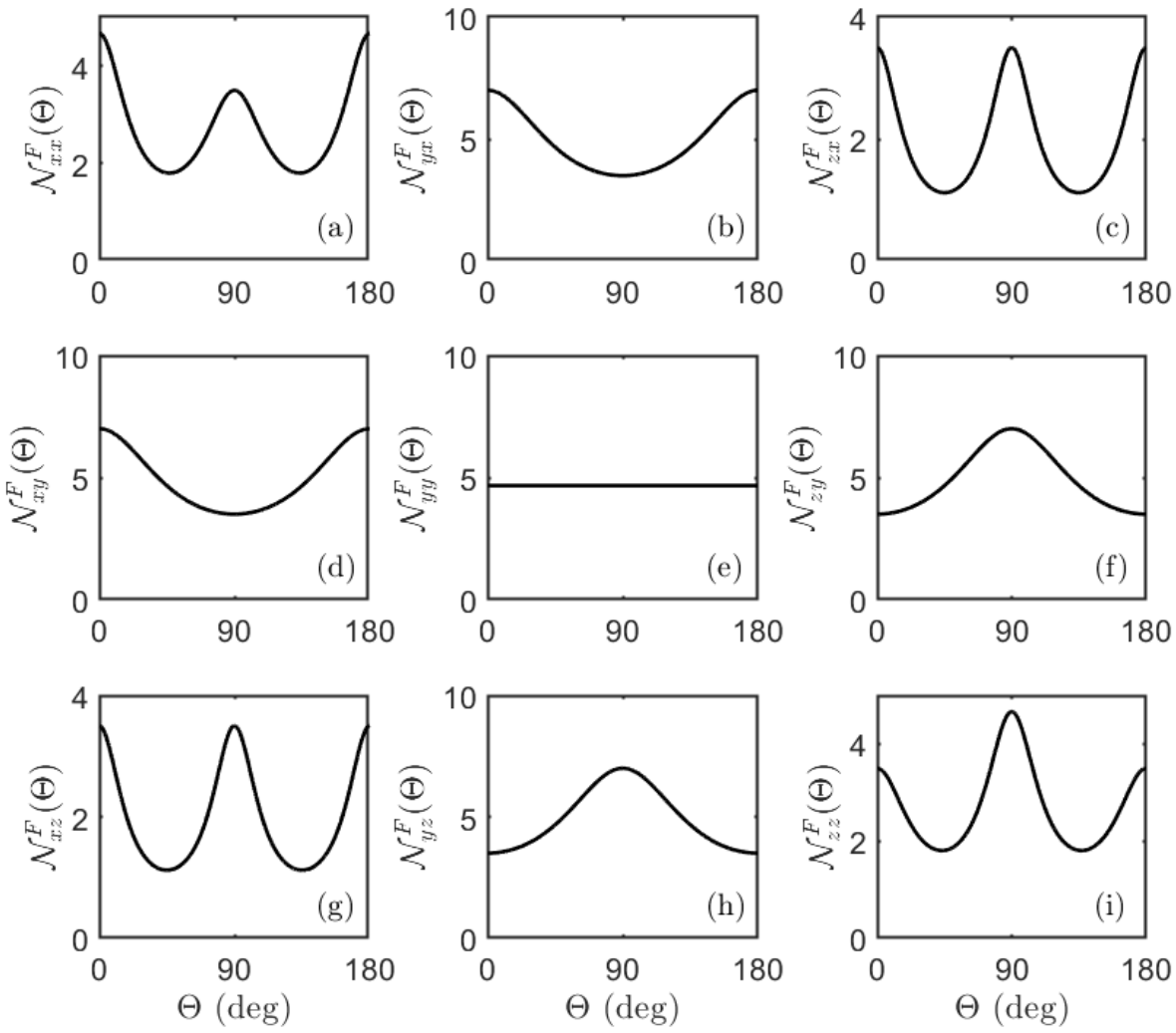


Figure 4.4: The analytically derived number of collisions per rethermalization for fermions $\mathcal{N}^{\mathrm{F}}_{ij}$, as a function of $\Theta$ for all nine excitation-rethermalization configurations.

In certain situations like evaporative cooling (discussions to come in Chap. 6), the relevant thermalization rate is not just that of a single axis, but one that is averaged over all of them:

$$\overline{\gamma}_i = \frac{1}{3}(\gamma_{ix} + \gamma_{iy} + \gamma_{iz}) = \frac{\gamma_{\text{coll}}}{3}\left(\mathcal{N}_{ix}^{-1} + \mathcal{N}_{iy}^{-1} + \mathcal{N}_{iz}^{-1}\right), \tag{4.14}$$

where $i$ still remains the axis of excitation. The averaged number for rethermalization is therefore extracted as

$$\overline{\mathcal{N}}_i(\Theta) = 3\left(\mathcal{N}_{ix}^{-1}(\Theta) + \mathcal{N}_{iy}^{-1}(\Theta) + \mathcal{N}_{iz}^{-1}(\Theta)\right)^{-1} = \mathcal{N}_{ii}(\Theta), \tag{4.15}$$

the diagonal elements of the non-averaged number of collisions. So the collective thermalization rate is still tunable via the dipoles for any single-axis excitation.

### 4.1.2 Universal signatures of dipolar thermalization in KRb

In a recent groundbreaking work by the Ye group at JILA [3], a bulk gas of ultracold $^{40}$K$^{87}$Rb molecular fermions was made stable in three dimensions, facilitated by an electric field-induced shielding resonance (see Sec. 2.2.1) that suppressed reactive losses by a factor of $\sim 30$. The resulting favorable ratio of elastic to inelastic collisions enabled direct dipolar thermalization, with rate depending on dipole orientation controllable by the external electric field.

Thermalization of these shielded molecules was demonstrated and characterized with exactly the cross-dimensional thermalization experiments described above, with geometry shown in subplot (a) of Fig. 4.5. Initially heated along the tightly confined $y$ direction, elastic collisions then aid in redistributing excess kinetic energy from $y$ into $x$ and $z$. Temperatures along each axis were extracted by Gaussian fits to the gas cloud from time-of-flight imaging, resulting in the $T_x$ and $T_y$ data points shown in Fig. 4.5. Rethermalization rates were then obtained by fitting these temperature data points, after parametric excitation along $y$, to a set of coupled differential equations [89]:

$$\frac{dn}{dt} = -K_L(T_y + 2T_x)n^2 - \frac{n}{2}\frac{1}{T_y}\frac{dT_y}{dt} - \frac{n}{2}\frac{1}{T_x}\frac{dT_x}{dt}, \tag{4.16a}$$

$$\frac{dT_y}{dt} = \frac{n}{4}K_L(2T_x - T_y)T_y - \frac{2\Gamma_{\text{th}}}{3}(T_y - T_x) + c_y, \tag{4.16b}$$

$$\frac{dT_x}{dt} = \frac{n}{4} K_L T_y T_x + \frac{\Gamma_{\rm th}}{3}(T_y - T_x) + c_x, \tag{4.16c}$$

where $\Gamma_{\rm th}, K_L, c_x$, and $c_y$ are fit parameters corresponding to a rethermalization rate, two-body loss-rate and background heating rates respectively. The latter 3 quantities are required because real molecular experiments neither have perfect optical traps nor purely elastic scattering, a shocking revelation for naive young Reuben back in 2021. Conversion of the experimental geometry into one utilized in my theory is done by swapping the $y$ and $z$ axes labels.

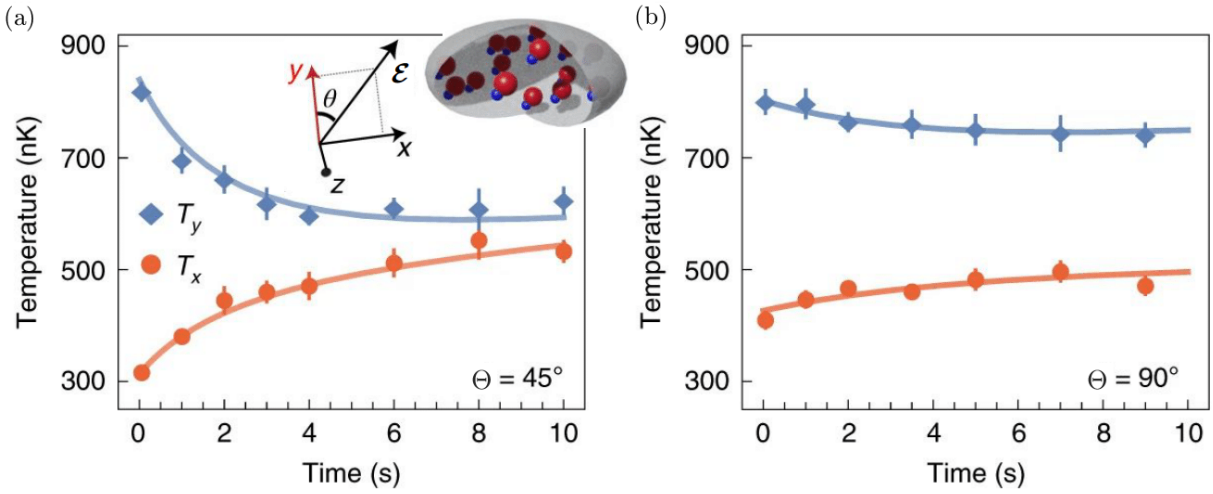


Figure 4.5: Time evolution of the temperature for $\Theta = 45°$ (a) and $\Theta = 90°$ (b) after parametric heating along $y$. The solid lines are fits to the thermalization model in Eq. (4.16). The thermalization is faster at $\Theta = 45°$. The molecular gas is heated parametrically along the $y$ direction to create an initial condition of $\mathcal{T}_y(0) \approx 2.5\mathcal{T}_x(0)$, $\mathcal{T}_x(0) = \mathcal{T}_z(0)$. Figure adapted from Ref. [3].

With collision energies on the order of 500 nK and an electric dipole moment of $d \approx 0.08$ D, collisions are expected to remain close-to-threshold where the number for rethermalization works out to be that in Eq. (4.13). But with a large initial temperature anisotropy of $\mathcal{T}_y(0) \approx 2.5\mathcal{T}_x(0)$, an accurate comparison with the experiment must account for $\gamma_{\rm coll}$ changing during the relaxation process because of thermal energy redistribution [90]. As such, $\overline{\mathcal{N}}_z(\Theta)$ is multiplied by the factor

$$\alpha(\varpi) = \frac{6\varpi}{1+2\varpi}\left(1 + \frac{\varpi \tan^{-1}\sqrt{\varpi - 1}}{\sqrt{\varpi - 1}}\right)^{-1}, \tag{4.17}$$

where $\varpi = \mathcal{T}_{x,y}(0)/\mathcal{T}_z(0)$ is the initial temperature anisotropy. So with $\varpi = 2.5$, $\overline{\mathcal{N}}_z(\Theta)$ is modified by a factor of $\alpha(2.5) \approx 0.89$. A comparison between the theory and experimentally extracted values

of $\alpha(\varpi)\overline{\mathcal{N}}_z^F(\Theta)$ is plotted in Fig. 4.6, showing remarkable agreement. This not only showcases the accuracy of Eq. (4.13), but the validity of assuming point-dipole threshold scattering for KRb molecules as argued for in Sec. 2.2.1. Similar agreement has been observed in ultracold gases of fermionic erbium isotopes [91], lending this dipole-angle dependence of the $\mathcal{N}$ to be a smoking gun signature of universal dipolar scattering at threshold.

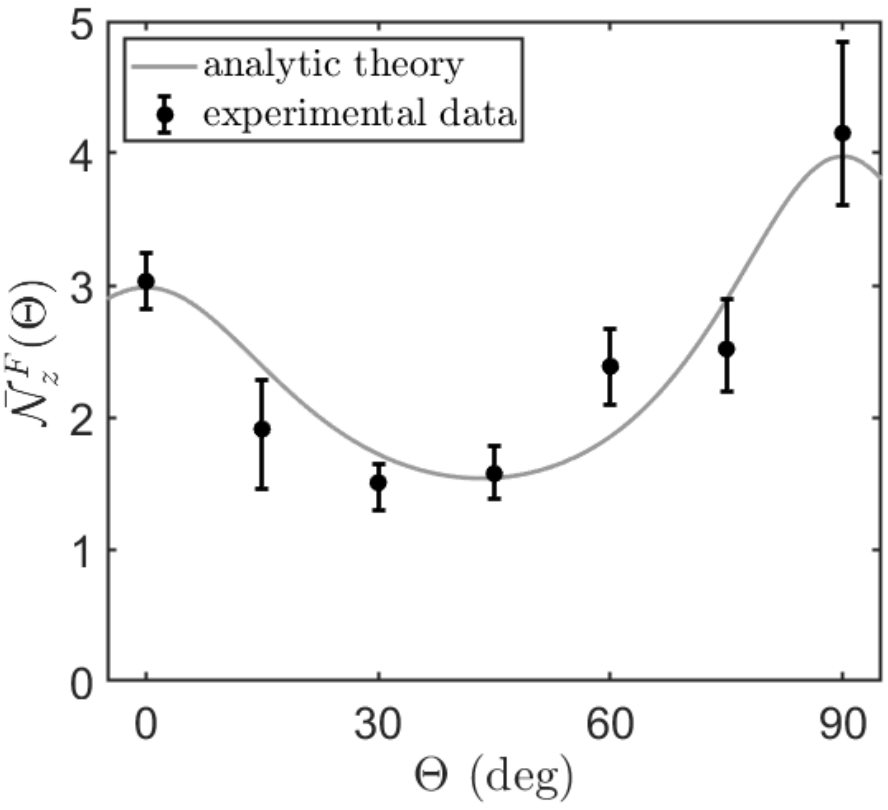


Figure 4.6: Comparison of the averaged number of collisions per thermalization $\overline{\mathcal{N}}_z^F(\Theta)$. The solid (grey) curve shows the theoretical results from Eqs. (4.13) and (4.17), whereas the (black) circles with error bars are results from the JILA KRb experiment.

## 4.2 Turn up the heat: Dipolar thermalization far from threshold

In some ways, we got lucky that KRb has a pretty small dipole moment at its resonant shielding field, keeping it in the collisional threshold regime at hundreds of nK. Other diatomic molecules may not be so fortunate (or unfortunate if large dipole moments are wanted). Take for

instance $^{23}$Na$^{40}$K molecules, collisionally shielded with circularly polarized microwaves [4]. Such a species could have its dipole moment up to $\sim 10$ times larger than those of shielded $^{40}$K$^{87}$Rb, typically requiring collision energies to be $\sim 10^4$ times lower for the threshold regime (see Sec. 2.2.2.1 for the relevant arguments). Nonegenerate gases of $^{23}$Na$^{40}$K and other strongly polar molecules should, therefore, have their collisional physics be treated with the energy dependent cross sections away from threshold (Fig. 2.8). But that means no more Born approximation and unfortunately for us, no more analytic cross sections also means no more analytic collision integrals for cross-dimensional rethermalization.

Fret not! We can still compute these integrals numerically, either by direct evaluation of Eq. (3.24) or via the DSMC algorithm of Sec. 3.3. Though in both these methods, a high resolution of the differential cross section in angular and energy space is required to accurately evaluate $\mathcal{N}_{ij}$. Performing close-coupling calculations (Sec. 2.2.2.1) for each sampled point would be highly impractical given the computational cost of each one. So I present an alternative solution.

### 4.2.1 Gaussian process interpolation of differential cross sections

At a given collision energy, the elastic differential cross section (here denoted $\mathcal{D}_{\text{el}}$ for convenience of notation), is a function of the dipole alignment axis $\hat{\boldsymbol{\mathcal{E}}}$, and the relative ingoing and outgoing momentum vectors $\hbar\boldsymbol{k}$ and $\hbar\boldsymbol{k}'$, respectively. Collectively, I shall denote this set of parameters as $\boldsymbol{\beta}$. By first performing close-coupling calculations at several well chosen collision energies $E = \hbar^2k^2/(2\mu)$, the resultant scattering data is used to infer an $M$-dimensional continuous hypersurface that approximates $\mathcal{D}_{\text{el}}$, with a Gaussian process (GP) model [92–95].

GP regression is a machine learning technique used to interpolate discrete data points, stitching them together to form a continuous global surface. To do so, a GP assumes that $\mathcal{D}_{\text{el}}(\boldsymbol{\beta})$ evaluated any 2 nearby points in its coordinate space, $\boldsymbol{\beta}_i$ and $\boldsymbol{\beta}_j$, are Gaussian distributed with a covariance given in terms of a function $K(\boldsymbol{\beta}_i, \boldsymbol{\beta}_j)$, called the *kernel*. A parameterized functional form for the kernel is chosen prior to the surface fitting process, reducing the task of combing through an infinite space of possible functions that best match the data, to a minimization over the kernel parameters.

This minimization step is referred to as *training* the GP model.

Several symmetries in the differential cross section help to reduce the computational load of training slightly. Rotated into the frame where $\hat{\boldsymbol{\mathcal{E}}}$ points along the $z$ axis, which I refer to as the dipole-frame, the unique hypersurface regions effectively live in an $M = 4$ dimensional space, with coordinates $\boldsymbol{\beta} = (E, \eta, \theta_s, \phi_s)$. As defined, $\eta = \cos^{-1} \hat{\boldsymbol{k}} \cdot \hat{\boldsymbol{\mathcal{E}}}$ is the angle between the dipole and incident relative momentum directions, where it is convenient to select $\hat{\boldsymbol{k}}$ to lie in its $x, z$ plane. The angles $\theta_s$ and $\phi_s$, denote the inclination and azimuthal scattering angles respectively, in this frame. Doing so, the differential cross section possesses the symmetry

$$\mathcal{D}_{\rm el}(E, \eta, \theta_s, \phi_s) = \mathcal{D}_{\rm el}(E, \eta, \theta_s, -\phi_s). \tag{4.18}$$

Consequently, we only need to specify the differential cross section for angles within the domain $\eta, \theta_s, \phi_s \in [0, \pi]$, to fully describe its global structure.

To perform the interpolation with GP regression, I utilize the Matérn-$\frac{5}{2}$ kernel [93]:

$$K(\boldsymbol{\beta}_i, \boldsymbol{\beta}_j) = \left(1 + \frac{\sqrt{5}|\boldsymbol{\beta}_i - \boldsymbol{\beta}_j|}{w} + \frac{5(\boldsymbol{\beta}_i - \boldsymbol{\beta}_j)^2}{3w^2}\right) \exp\left(-\frac{\sqrt{5}|\boldsymbol{\beta}_i - \boldsymbol{\beta}_j|}{w}\right), \tag{4.19}$$

which is better able to capture the sharp jumps in a non-smooth function, over higher-order differentiable kernels such as the radial basis function. This kernel contains a parameter $w$ that sets a length scale over which features of the data vary in coordinate space, that is optimized during the model training process. This kernel is typically not ideal for periodic input data, so we make the periodicity of the angles $(\eta, \theta_s, \phi_s)$ explicitly known to the GP model by training it with the cosine of these angles, instead of the angles themselves. Furthermore, $\log_{10}(E/E_{\rm dd})$ is fed into the GP model in place of $E$, to reduce the disparity in fitting domains between each coordinate of $\boldsymbol{\beta}$. The GP model is trained over the range $\log_{10}(E/E_{\rm dd}) = -6$ to 2, corresponding to collision energies of $E/k_B \approx 0.36$ pK to 36 $\mu$K relevant to ultracold experiments. After training on $\sim 10,000$ samples of $\mathcal{D}_{\rm el}(E, \eta, \theta_s, \phi_s)$, the resulting GP fit obtains a mean-squared error of $\approx 0.5\%$ against close-coupling calculations, which are taken to represent the actual cross section accurately.

For proof of principle and to ensure the accuracy of subsequently computed quantities, I utilized more points than is usually necessary for the GP fitting. I also optimize the model's

hyperparameters [96] on top of just the kernel parameters. Even so, the Gaussian process model still has issues faithfully reproducing the differential cross section around $\eta, \theta_s = 90°$, known to have a discontinuity at threshold [35]. Fortunately, this angular segment corresponds to forward scattering, which does not contribute to the cross-dimensional thermalization process of interest here. Present Reuben will leave this as a worry for future Reuben.

Fig. 4.7 plots the total cross section $\sigma(E, \eta) = \int \mathcal{D}_{\text{el}}(E, \eta, \Omega_s) d\Omega_s$, at various collision energies. There is a marked variation in the $\eta$ dependence, indicating a higher tendency for side-to-side collisions ($\eta = 90°$) over head-to-tail ones ($\eta = 0°$) at higher energies. To highlight the dominant anisotropic scattering process, Fig. 4.7 also provides plots of the differential cross section at $\eta = 45°$, the approximate angle at which $\sigma$ is maximal. As energy increases from subplots (a) to (d), the scattered angle dependence of $\mathcal{D}_{\text{el}}$ becomes biased toward forward scattering, reducing the effectiveness of collisions for thermalization as discussed in Sec. 4.1. Alphabetic labels in Fig. 4.7 consistently correspond to the collision energies: (b) $E = 0.2E_{\text{dd}}$, (c) $E = 2E_{\text{dd}}$ and (d) $E = 20E_{\text{dd}}$. The Born approximated cross sections at threshold [35] are labeled with (a).

### 4.2.2 Energy dependent collisional efficiencies

Earlier, the thermalization rate was related to the standard collision rate through the number of collisions per rethermalization. The inverse of this quantity, however, has perhaps a more intuitive interpretation: the ratio $\varepsilon_{ij} = \gamma_{ij}/\gamma_{\text{coll}}$ represents the *efficiency* of each collision toward thermalization of the gas. This collisional efficiency is formally cast in terms of the integral

$$\varepsilon_{ij} \approx \alpha_{ij} \frac{\pi^2}{64} \int \frac{d^3\boldsymbol{\kappa}}{(2\pi)^3} \frac{e^{-\kappa^2/4}}{\sqrt{\pi}} \int d^2\Omega' \frac{\mathcal{D}'_{\text{el}} \kappa}{\langle \sigma\kappa \rangle} \Delta\kappa_i^2 \Delta\kappa_j^2, \tag{4.20}$$

where $\Delta\kappa_i^2 = \kappa_i'^2 - \kappa_i^2$ is the collisional change in adimensional relative momenta $\boldsymbol{\kappa} = \boldsymbol{p}_r (m k_B T_0)^{-1/2}$, $\alpha_{ij} = 3/2$ if $i = j$, and $\alpha_{ij} = -3$ otherwise. See App. E for further details on deriving $\varepsilon_{ij}$.

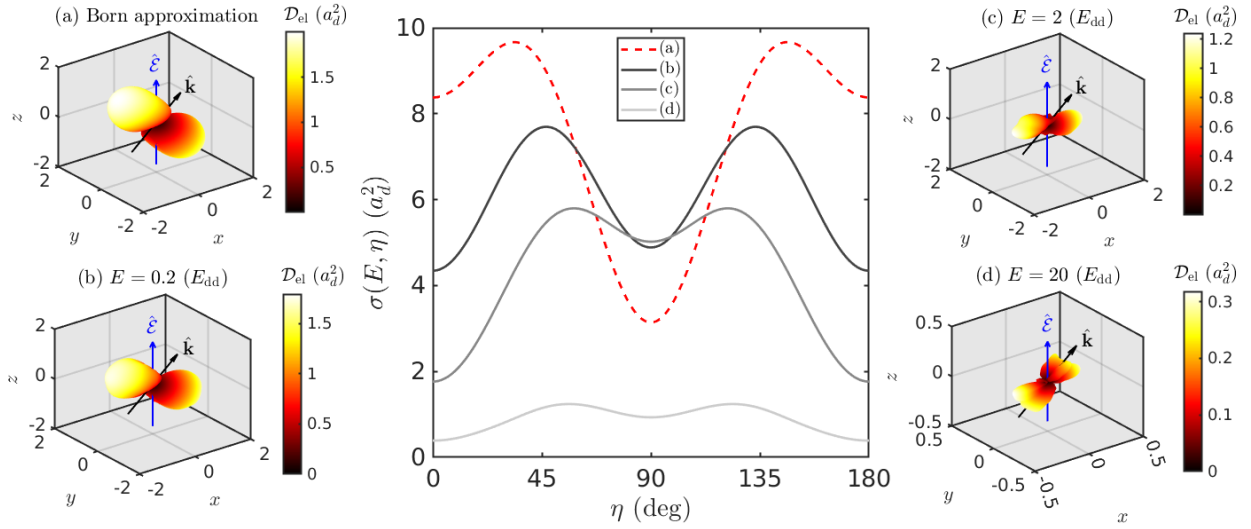


Figure 4.7: The central plot shows the total cross section as a function of the incident collision angle, obtained from (a) the Born approximation (red dashed curve), and from GP interpolation (solid curves) for 3 different collision energies: (b) $E = 0.2E_{\rm dd}$ (black), (c) $E = 2E_{\rm dd}$ (gray) and (d) $E = 20E_{\rm dd}$ (light gray). In alphabetical correspondence, are angular plots of the differential cross section (in units of $a_d^2$) in subplots with the respective collision energies, assuming dipoles pointing along $\hat{\boldsymbol{\mathcal{E}}} = \hat{\boldsymbol{z}}$ and incident collision angle $\eta = 45°$ lying in the $x, z$-plane. Subplot (d) uses a smaller domain for clarity of presentation.

Evidently from Eq. (4.20), $\varepsilon_{ij}$ is symmetric in its indices which leaves only 6 unique configurations of $i$ and $j$. Asserting once more that the dipoles lie in the $x, z$-plane and tilted with angle $\Theta = \cos^{-1}(\hat{\boldsymbol{\mathcal{E}}} \cdot \hat{\boldsymbol{z}})$, I compute Eq. (4.20) with Monte Carlo integration[3] and plot the results in Fig. 4.8. Each subplot (a to f) shows a different $(i, j)$ configuration, within which, $\varepsilon_{ij}$ is plotted against the dipole tilt angle $\Theta$ as solid curves, for the temperatures $T = 10$ nK (black), $T = 100$ nK (dark gray), $T = 400$ nK (gray) and $T = 1$ $\mu$K (light gray). Interestingly, the $\varepsilon_{ij}$ terms involving excitation or rethermalization along $y$ essentially lose their dependence on $\Theta$ around 400 nK, beyond which collisions are less efficient than even nondipolar $p$-wave scattering (dashed-dotted blue line in Fig. 4.8) [88] for all $\Theta$. This decrease can be intuited by looking at the differential cross section around $\eta = 45°$, around which the total cross section is maximal. As evidenced from the subplots of $\mathcal{D}_{\rm el}$ in Fig. 4.7, forward scattering is favored at higher collision energies, limiting momentum transfer between axes and therefore, also the efficiency of collisions toward rethermalization.

[3] The Monte Carlo integration gives a $\lesssim 1\%$ error, which is mostly imperceptible in the log-linear plot.

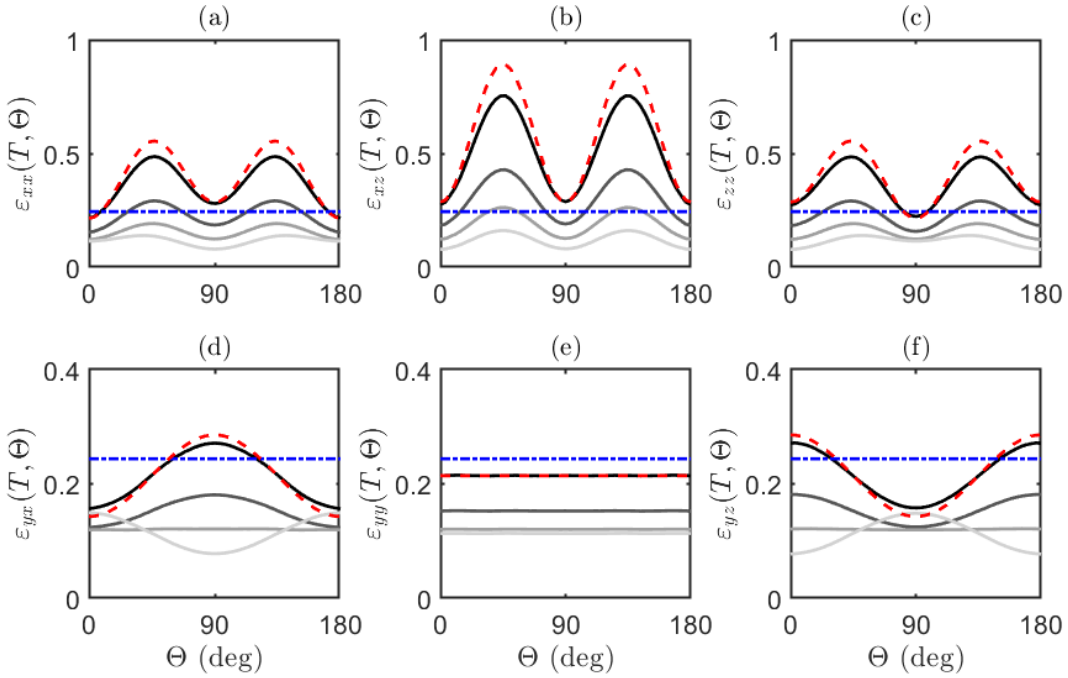


Figure 4.8: $\varepsilon_{ij}$ as a function of the dipole tilt angle $\Theta$, for all 6 unique configurations (subplots a to f) of the excitation axis $i$, and measured thermalization axis $j$. The dashed red curves are the analytic $\varepsilon_{ij}$ results derived with the Born approximated cross section at threshold, whereas the solid curves are those from Monte Carlo integration using the GP interpolated cross sections, at temperatures $T = 10$ nK (black), $T = 100$ nK (dark gray), $T = 400$ nK (gray), and $T = 1$ $\mu$K (light gray). The dashed-dotted blue lines are the efficiency for purely $p$-wave collisions, $\varepsilon_p = 1/4.1$.

Without much additional effort, GP interpolated differential cross sections are easily deployed in the DSMC solver of Sec. 3.3, allowing for a broad range of nonequilibrium molecular gas studies away from threshold. Moreover, the GP techniques developed here are broadly applicable to arbitrary collision partners, so long as their elastic scattering matrices are accurately obtainable from close-coupling calculations. The road forward to exciting nondegenerate physics is evermore so pristinely paved for anyone who will take it.

# Chapter 5

## Return to Equilibrium II: Hydrodynamic Gases

The epic saga continues. But now, the gas is dense, collisionally thick, and a bold-cold *weltering* machine. A description most appropriate to fluids.

"*... the White Whale darted through the weltering ocean.*"

– Herman Melville (Moby Dick, Chap. 135), 1851.

With much larger dipole moments, the significant collisional cross sections of molecules cause collision rates to skyrocket, sending the ultracold gas straight into its hydrodynamic regime. There, relaxation dynamics can be drastically different from its dilute counterpart and has its own tale to tell. I unpack some of that story here, keeping in mind that many hydrodynamic stones are still left unturned.

### 5.1 How do fluids flow?

A gas is said to be hydrodynamic when collisions result in fast local thermalization, so much so that the nonequilibrium thermodynamics is overshadowed by long wavelength scale fluid motion. Subplot (a) of Fig. 5.1 illustrates the number density one might expect from a (very) dilute gas, sparse and granular. Whereas subplot (b) shows one that is hydrodynamic, jam-packed with particles and smooth.

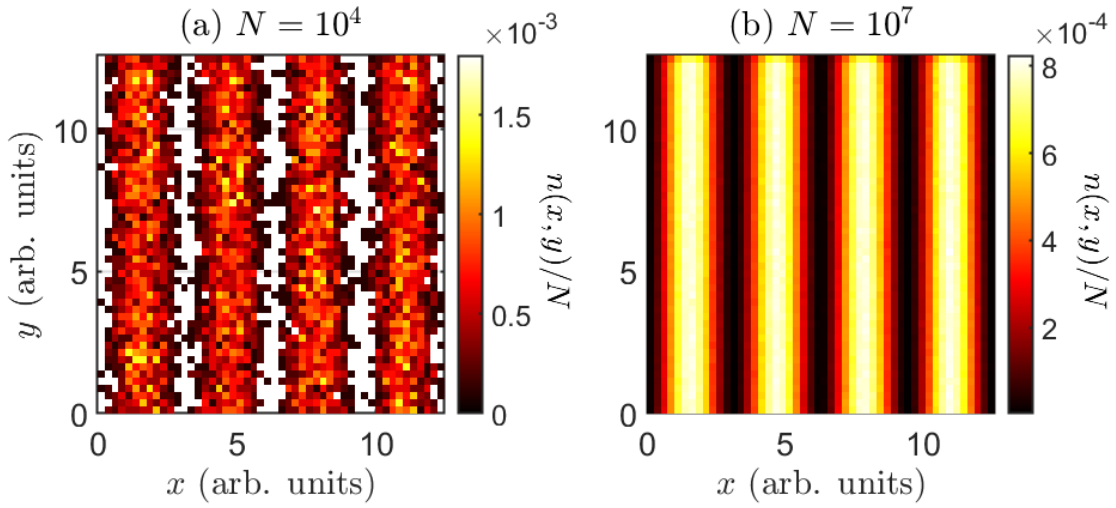


Figure 5.1: Single body number density function projected in $x, y$-plane, comparing the $N = 10^4$ dilute (a) and $N = 10^7$ hydrodynamic (b) regimes. The spatial distributions are both the same and assumed to be a sinusoid along $x$, but uniform along $y$ (chosen arbitrarily for illustrative purposes).

Hydrodynamic gases are best described in terms of the continuous field variables of mass density $\rho$, flow velocity $\boldsymbol{U}$ and kinetic temperature $T$ [97], each of which are dependent on space and time. Defined as the molecular-velocity-averaged quantities

$$\rho(\boldsymbol{r},t) = mn(\boldsymbol{r},t) = \int d^3\boldsymbol{v} f(\boldsymbol{r},\boldsymbol{v},t)m, \tag{5.1a}$$

$$\boldsymbol{U}(\boldsymbol{r},t) = \frac{1}{n(\boldsymbol{r},t)} \int d^3\boldsymbol{v} f(\boldsymbol{r},\boldsymbol{v},t)\boldsymbol{v}, \tag{5.1b}$$

$$T(\boldsymbol{r},t) = \frac{2}{3n(\boldsymbol{r},t)k_B} \int d^3\boldsymbol{v} f(\boldsymbol{r},\boldsymbol{v},t)\frac{1}{2}m\left[\boldsymbol{v} - \boldsymbol{U}(\boldsymbol{r},t)\right]^2, \tag{5.1c}$$

these variables undergo dynamics governed by the continuity [98], Navier-Stokes [99, 100] and temperature balance equations [101]:

$$\frac{\partial \rho}{\partial t} + \partial_j\left(\rho U_j\right) = 0, \tag{5.2a}$$

$$\frac{\partial\left(\rho U_i\right)}{\partial t} + \partial_j\left(\rho U_j U_i\right) = \partial_j \tau_{ij} - \partial_i P - \frac{\rho}{m}\partial_i V(\boldsymbol{r},t), \tag{5.2b}$$

$$\frac{\partial(\rho T)}{\partial t} + \partial_j\left(\rho T U_j\right) = \frac{2m}{3k_B}\left(\varsigma_{ij}\partial_j U_i - \kappa_{ij}\partial_i\partial_j T\right), \tag{5.2c}$$

where $\varsigma_{ij}$ is the fluid stress tensor. Repeated indices are assumed summed over, and will be for the remainder of this chapter. The external potential in consideration here is that from any external

confinement $V_{\rm trap}$, and the dipolar mean-field $V_{\rm DMF}(\boldsymbol{r},t) = n(\boldsymbol{r},t) * V_{\rm dd}(\boldsymbol{r})$ [1] , where $*$ denotes a convolution and $V_{\rm dd}(\boldsymbol{r})$ is the dipole-dipole interaction potential from Eq. (2.15). It is worth pointing out that the local fluid kinetic temperature is related to the flow velocity via

$$\frac{3}{2}n(\boldsymbol{r},t)k_BT(\boldsymbol{r},t) = \int d^3\boldsymbol{v} f(\boldsymbol{r},\boldsymbol{v},t)\frac{1}{2}m\boldsymbol{v}^2 - \frac{1}{2}\rho\boldsymbol{U}(\boldsymbol{r},t)^2, \tag{5.3}$$

where the integral term is the local kinetic energy density. This relation will come in handy down the road.

Studying fluid dynamics with Eqs. (5.2) requires knowledge of the rank-2 thermal conductivity tensor $\kappa_{ij}$ and the rank-4 viscosity tensor $\mu_{ijk\ell}$ (discussed below). These transport tensors are dissipative coefficients that relax fluid motion, arising from finite local thermalization times. They are, therefore, a direct consequence of dipolar collisions, a process we are rather familiar with by now. So with ultracold molecular gas platforms now available to us and hydrodynamic physics ripe for exploration, I turn to deriving these collision-emergent coefficients.

## 5.2 Surfaces this way, fluxes that way

The switch from solving Boltzmann's equation (3.1) to solving the hydrodynamic ones, is better motivated by establishing a separation of scales between the phenomena of interest. Of concern here is the regime in which macroscopic fluid dynamics is governed by length scales $\lambda$ (e.g. wavelengths), much larger than the mean-free path $L = \langle n\sigma\rangle^{-1}$ of its constituent molecules. The corresponding dimensionless ratio $\mathrm{Kn} = L\lambda^{-1}$, referred to as the Knudsen number, quantifies the onset of hydrodynamics when $\mathrm{Kn} \ll 1$. Furthermore, the period over which such dynamics occur is much longer than the timescales associated with collisions. Appropriately, I will refer to fluid dynamics as occurring on *macro-scales*, whereas collisions are said to occur on *micro-scales*.

[1] One might be concerned that the DMF is already treated microscopically when deriving the transport tensors, and so will be double counted if also included in Eq. (5.2). However, I show in App. F that this is not the case since the DMF vanishes in the first-order Chapman-Enskog expansion.

### 5.2.1 Microscopic collisions to macroscopic transport

If only weakly perturbed, the local response of a fluid system is completely described by linear constitutive relations and the associated, medium-specific, transport coefficients of viscosity and thermal conductivity [102]. These coefficients are derivable from the microscopic physics with methods established by Chapman and Enskog [69, 103], which I closely follow [16–18]. Starting from the Boltzmann equation (3.1), the out-of, but close to, equilibrium atomic distribution can be taken to have the form

$$f(\boldsymbol{r},\boldsymbol{u},\beta) \approx f_0(\boldsymbol{u},\beta)\left[1+\Phi(\boldsymbol{r},\boldsymbol{u},\beta)\right], \tag{5.4}$$

where $\boldsymbol{u}=\boldsymbol{v}-\boldsymbol{U}$ is the comoving molecular velocity, $\beta=(k_BT)^{-1}$ is the standard inverse temperature and

$$f_0(\boldsymbol{u},\beta)=n_0(\beta)c_0(\boldsymbol{u},\beta)=n_0(\beta)\left(\frac{m\beta}{2\pi}\right)^{3/2}\exp\left(-\frac{m\beta}{2}\boldsymbol{u}^2\right), \tag{5.5}$$

is the steady flow local equilibrium phase space distribution. Following mass, momentum and energy conservation, the perturbation function $\Phi$, must respectively satisfy the relations

$$\int d^3\boldsymbol{u} f_0(\boldsymbol{u})\Phi(\boldsymbol{r},\boldsymbol{u},\beta)m=0, \tag{5.6a}$$

$$\int d^3\boldsymbol{u} f_0(\boldsymbol{u})\Phi(\boldsymbol{r},\boldsymbol{u},\beta)m\boldsymbol{u}=0, \tag{5.6b}$$

$$\int d^3\boldsymbol{u} f_0(\boldsymbol{u})\Phi(\boldsymbol{r},\boldsymbol{u},\beta)\frac{1}{2}m\boldsymbol{u}^2=0. \tag{5.6c}$$

Enskog's prescription of successive approximations then simplifies the Boltzmann equation, such that to leading non-trivial order, it simply becomes

$$\left(\frac{\partial}{\partial t}+v_k\partial_k-\frac{\partial_k V(\boldsymbol{r})}{m}\frac{\partial}{\partial u_k}\right)f_0\approx C[f_0\Phi]. \tag{5.7}$$

With the phase space distribution at equilibrium on the left but perturbed on the right, the equation above is interpreted as making an adiabatic approximation that separates the macro and micro-scale phenomena. In other words, the macro-scale fluid flow still looks more or less steady amid all the micro-scale collisional events.

What usually follows is a rather lengthy derivation of the transport tensors, starting from Eq. (5.7). Although, the main text of a physics thesis is probably already dry enough as is to warrant skipping that. So, if you are willing to trust my math, here is the resulting thermal conductivity tensor for dipolar fermions:

$$\boldsymbol{\kappa} = \frac{175\mu_d k_B}{512m}\begin{pmatrix} 5+\cos(2\Theta) & 0 & -\sin(2\Theta) \\ 0 & 6 & 0 \\ -\sin(2\Theta) & 0 & 5-\cos(2\Theta) \end{pmatrix}, \tag{5.8}$$

where

$$\mu_d = \frac{5}{16a_d^2}\sqrt{\frac{m}{\pi\beta}} \tag{5.9}$$

is the Chapman-Enskog viscosity assuming a hard sphere diameter of $a_d$ [69].

The 13 unique viscosity tensor elements, for fermions, are tabulated below as a function of scattering length $a_s$, dipole length $a_d$ and dipole orientation angle $\Theta$:

$$\mu_{1111} = \frac{\mu_d}{512}(117\cos(4\Theta) + 84\cos(2\Theta) + 415), \tag{5.10a}$$

$$\mu_{1113} = -\frac{3\mu_d}{512}(39\sin(4\Theta) + 14\sin(2\Theta)), \tag{5.10b}$$

$$\mu_{1122} = -\frac{7\mu_d}{128}(3\cos(2\Theta) + 11), \tag{5.10c}$$

$$\mu_{1133} = -\frac{\mu_d}{512}(117\cos(4\Theta) + 107), \tag{5.10d}$$

$$\mu_{1212} = \frac{9\mu_d}{128}(5\cos(2\Theta) + 9), \tag{5.10e}$$

$$\mu_{1223} = -\frac{45\mu_d}{128}\sin(2\Theta), \tag{5.10f}$$

$$\mu_{1313} = -\frac{9\mu_d}{512}(13\cos(4\Theta) - 29), \tag{5.10g}$$

$$\mu_{1322} = \frac{21\mu_d}{128}\sin(2\Theta), \tag{5.10h}$$

$$\mu_{1333} = \frac{3\mu_d}{512}(39\sin(4\Theta) - 14\sin(2\Theta)), \tag{5.10i}$$

$$\mu_{2222} = 77\mu_d, \tag{5.10j}$$

$$\mu_{2233} = \frac{7\mu_d}{128}(3\cos(2\Theta) - 11), \tag{5.10k}$$

$$\mu_{2323} = -\frac{9\mu_d}{128}(5\cos(2\Theta) - 9), \tag{5.10l}$$

$$\mu_{3333} = \frac{\mu_d}{512}(117\cos(4\Theta) - 84\cos(2\Theta) + 415). \tag{5.10m}$$

All other non-trivial viscosity terms are specified by the tensor symmetry identities

$$\mu_{ijmn} = \mu_{jimn}, \tag{5.11a}$$

$$\mu_{ijmn} = \mu_{jinm}, \tag{5.11b}$$

$$\mu_{ijmn} = \mu_{mnij}, \tag{5.11c}$$

$$\mu_{ijmn}\delta_{ij} = \mu_{ijmn}\delta_{mn} = \mu_{ijmn}\delta_{ijmn} = 0, \tag{5.11d}$$

where $\delta_{ijmn}$ is 1 if $i = j = k = \ell$ and 0 otherwise. All other unspecified tensor elements are zero. As for the less trusting (perhaps rightfully so), the integrals and indices of derivation in all their tedious glory are found in App. G. Knock yourself out!

By the way, $\boldsymbol{\kappa}$ and $\boldsymbol{\mu}$ have also been derived for dipolar bosons which also includes the scattering length $a_s$. For brevity of this thesis, however, I refer the reader to Refs. [16, 17] where these have already been tabulated, instead of including them here.

## 5.3 And whispered in the sound... of dipoles

If you played Simon and Garfunkel's hit song, "The Sound of Silence", from a point source speaker in an ultracold dipolar gas, it would sound pretty different depending on where you stand. A little softer, a little louder, maybe even out of sync between both ears. What's causing this is our old familiar friend: dipolar anisotropy, both in the speed of sound and its attenuation.

In more technical terms, I've already shown that anisotropy emerges in transport tensors from dipolar collisions, but a dense ensemble of dipoles could also generate a long-ranged anisotropic mean-field from their cumulative dipolar potential. If strong enough, the anisotropic push and pull of the dipolar mean-field can distort wave fronts that propagate through the fluid. Best used to study such physics is a uniform density gas of ultracold polar molecules, possibly realized in optical box traps [104]. And let's consider them fermionic because why not[2] . If only weakly perturbed,

[2] Three-body losses [105], that's why not.

the dynamical fields can be written in terms of small deviations from equilibrium:

$$\rho(\boldsymbol{r},t) = \rho_0\left[1+\chi(\boldsymbol{r},t)\right], \tag{5.12a}$$

$$U_i(\boldsymbol{r},t) = c\xi_i(\boldsymbol{r},t), \tag{5.12b}$$

$$T(\boldsymbol{r},t) = T_0\left[1+\epsilon(\boldsymbol{r},t)\right], \tag{5.12c}$$

having defined the unit-free fluctuation fields $\chi, \xi_i, \epsilon \ll 1$, with $c = \sqrt{5k_BT_0/(3m)}$ being the ideal gas thermal speed of sound. Quantities at equilibrium are denoted with a naught subscript. To linear order in the fluctuation field variables, the fluid equations (5.2) become

$$\frac{\partial\chi}{\partial t} + c\partial_j\xi_j \approx 0, \tag{5.13a}$$

$$\frac{\partial\xi_i}{\partial t} + \frac{3}{5}c\partial_i(\epsilon+\chi) \approx \frac{\mu_{ijk\ell}}{\rho_0}\partial_j\partial_\ell\xi_k - \frac{\rho_0}{m^2c}\partial_i\left[\chi(\boldsymbol{r},t) * \Phi_{\rm dd}(\boldsymbol{r})\right], \tag{5.13b}$$

$$\frac{\partial\epsilon}{\partial t} + \frac{2}{3}c\partial_j\xi_j \approx \frac{2}{3n_0k_B}\kappa_{ij}\partial_i\partial_j\epsilon, \tag{5.13c}$$

supporting acoustic wave solutions [97]. Such solutions can be found by employing a plane wave *ansatz* $\chi, \xi_i, \epsilon \sim \exp\left[i(\boldsymbol{K}^T\boldsymbol{r} - \omega t)\right]$, where conveniently, the dipolar mean-field potential just becomes a Fourier transform of $\Phi_{\rm dd}(\boldsymbol{r})$:

$$\begin{aligned}\chi(\boldsymbol{r},t) * \Phi_{\rm dd}(\boldsymbol{r}) &= \int d^3\boldsymbol{r}'\chi(\boldsymbol{r}-\boldsymbol{r}')\Phi_{\rm dd}(\boldsymbol{r}') \\ &= \chi e^{i(\boldsymbol{K}^T\boldsymbol{r}-\omega t)}\varphi_{\rm dd}(\hat{\boldsymbol{K}}, \hat{\boldsymbol{\mathcal{E}}}),\end{aligned} \tag{5.14}$$

with $\varphi_{\rm dd} = \int d^3\boldsymbol{r}' e^{-i\boldsymbol{K}^T\boldsymbol{r}'}\Phi_{\rm dd}(\boldsymbol{r}')$ already computed in Ref. [106].

Rendering the derivatives of fluctuation variables $\partial_j \to iK_j$ and $\frac{\partial}{\partial t} \to -i\omega$, plane waves reduce the partial differential equations of (5.13) into an eigenvalue problem:

$$\omega\begin{pmatrix}\chi\\ \boldsymbol{\xi}\\ \epsilon\end{pmatrix} = \begin{pmatrix} 0 & c\boldsymbol{K}^T & 0 \\ \left(\frac{3}{5}c + \frac{\rho_0\varphi_{\rm dd}}{m^2c}\right)\boldsymbol{K} & i\boldsymbol{\Lambda} & \frac{3}{5}c\boldsymbol{K} \\ 0 & \frac{2}{3}c\boldsymbol{K}^T & i\Gamma \end{pmatrix}\begin{pmatrix}\chi\\ \boldsymbol{\xi}\\ \epsilon\end{pmatrix}, \tag{5.15}$$

having defined the thermal conductivity and viscosity associated rates

$$\Gamma = -\frac{2}{3n_0k_B}\kappa_{ij}K_iK_j, \tag{5.16a}$$

$$\Lambda_{ik} = -\frac{1}{\rho_0}\mu_{ijk\ell}K_jK_\ell, \tag{5.16b}$$

respectively. With no other processes to break the symmetry of the system, the anisotropy that arises in the mode solutions only depends on the relative angle $\Theta$, between the dipole orientation $\hat{\boldsymbol{\mathcal{E}}}$ and plane wave propagation direction $\hat{\boldsymbol{K}}$. Thus, all essential physics is captured by setting $\hat{\boldsymbol{K}} = \hat{\boldsymbol{z}}$ but allowing $\Theta$ to vary. In these coordinates, which I assert for the remainder of this section, the transport associated rate functions have the forms

$$\Gamma(\Theta) = \frac{875K^2}{12288a_d^2n_0\sqrt{\pi m\beta_0}}\left(\cos(2\Theta) - 5\right), \tag{5.17a}$$

$$\boldsymbol{\Lambda}(\Theta) = \frac{5K^2}{2048a_d^2n_0\sqrt{\pi m\beta_0}} \times \begin{pmatrix} \frac{9}{4}(13\cos(4\Theta) - 29) & 0 & \frac{3}{4}(14\sin(2\Theta) - 39\sin(4\Theta)) \\ 0 & 9(5\cos(2\Theta) - 9) & 0 \\ \frac{3}{4}(14\sin(2\Theta) - 39\sin(4\Theta)) & 0 & \frac{1}{4}(84\cos(2\Theta) - 117\cos(4\Theta) - 415) \end{pmatrix}, \tag{5.17b}$$

and $\varphi_{\text{dd}}$ becomes

$$\varphi_{\text{dd}}(\Theta) = \frac{d^2}{3\epsilon_0}(3\cos^2\Theta - 1). \tag{5.18}$$

The $\Theta$ angle dependence of $\Gamma$ and $\boldsymbol{\Lambda}$ is showcased in unit-free versions (multiplied by $a_d^2n_0\sqrt{m\beta_0}/K^2$) of them plotted in Fig. 5.2.

Any fluid dynamics resultant from Eq. (5.15) can be described by normal mode solutions, comprising of mode frequencies $\omega_a$, and their corresponding mode amplitudes $\boldsymbol{\psi}_a = (\chi_a, \boldsymbol{\xi}_a, \epsilon_a)^T$ with $a = 1$ to 5. These normal modes can be obtained analytically by considering only long wavelength excitations such that $\delta = KL \ll 1$. Since the transport coefficients scale as $\mu_{ijk\ell}, \kappa_{ij} \sim \delta$, long wavelengths permit a series expansion of the mode solutions in increasing powers of the transport tensors via Taylor expansions in $\delta$. Diagonalizing Eq. (5.15) then gives the mode frequencies

$$\omega_\pm = \pm K\sqrt{c^2 + \mathscr{E}_{\text{dd}}(\Theta)} + \frac{i}{2}\left(\Lambda_{33} + \frac{2\Gamma c^2}{5(c^2 + \mathscr{E}_{\text{dd}})}\right), \tag{5.19a}$$

$$\omega_{\mu,1} = i\Lambda_{11}, \tag{5.19b}$$

$$\omega_{\mu,2} = i\Lambda_{22}, \tag{5.19c}$$

$$\omega_{\kappa} = i\Gamma \frac{\left(3c^2 + 5\mathscr{E}_{\rm dd}\right)}{5\left(c^2 + \mathscr{E}_{\rm dd}\right)}, \tag{5.19d}$$

to first order in $\delta$, where $\mathscr{E}_{\rm dd}(\Theta) = n_0\varphi_{\rm dd}(\Theta)/m$ is the specific dipolar mean-field energy. Now for the reason we're all here, interpreting the physics of these modes.

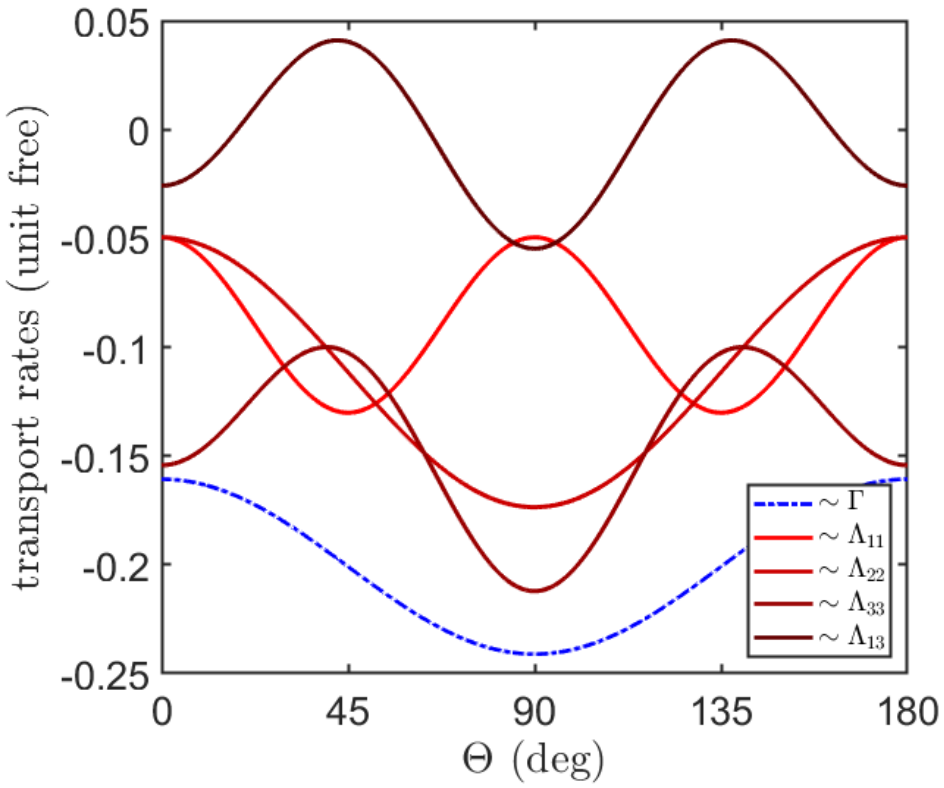


Figure 5.2: Unit-free versions of the non-trivial $\Gamma$ and $\mathbf{\Lambda}$ rate coefficients with identical dipolar fermions, as a function of $\Theta$.

### 5.3.1 The speed of dipolar sound

The first two modes, with frequencies $\omega_{\pm}$, represent propagating sound waves and identify the anisotropic speed of sound $c_{\rm dd}(\Theta) = \lim_{K\to 0}\omega_+(K)/K = \sqrt{c^2 + \mathscr{E}_{\rm dd}(\Theta)}$. This is usefully written in terms of the dimensionless parameter

$$\eta = \frac{2\pi\rho_0}{5}\left(\frac{d^2}{\epsilon_0}\right)\left(\frac{\lambda_{\rm th}}{h}\right)^2, \tag{5.20}$$

presented as a function of the thermal de Broglie wavelength $\lambda_{\rm th} = h/\sqrt{2\pi m k_B T_0}$ with $h$ as Planck's constant. The speed of sound is then written in terms of $\eta$ as

$$c_{\rm dd}(\Theta) = c\sqrt{1 + \eta\,(3\cos^2\Theta - 1)}. \tag{5.21}$$

Look, $\Theta$ appears in the formula. That's the dipolar mean-field at play, changing the speed of sound at different $\Theta$! In fact, with a modest value of $\eta = 0.8$, you can see in Fig. 5.3 that wave fronts of a spherical wave get distorted exactly because sound travels faster in certain directions over others.

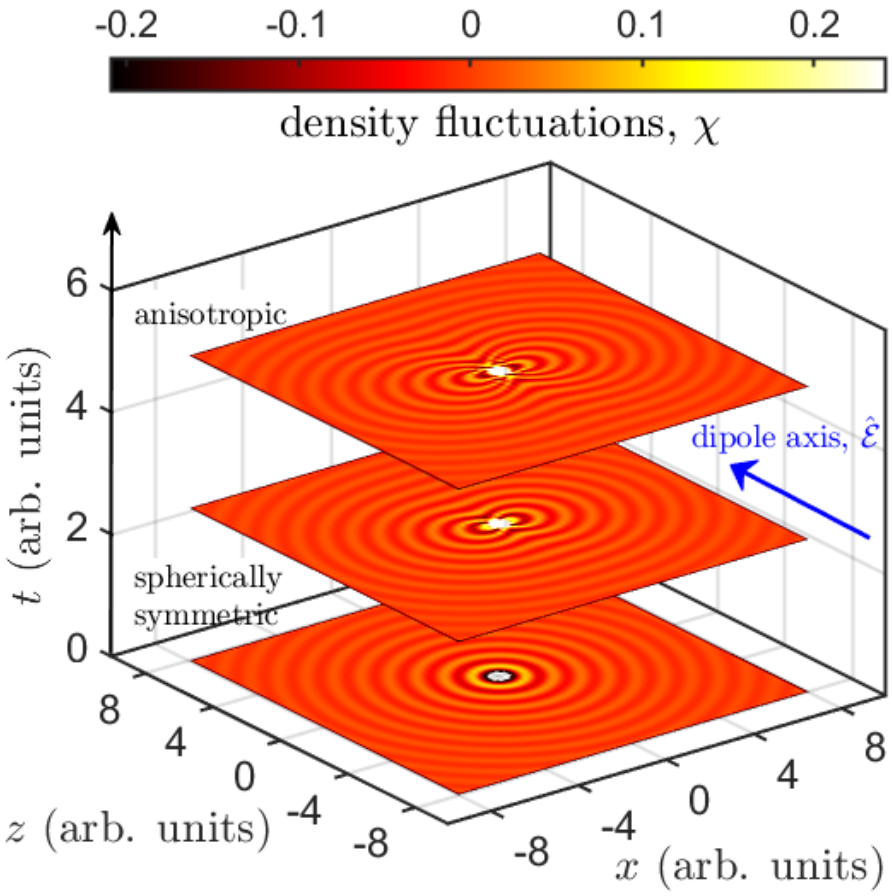


Figure 5.3: A schematic diagram over anisotropic radial sound wave propagation from a point source, following the evolution $\chi(t) = \chi_0 \cos[K(r - c_{\rm dd}t)]/r$ with $\eta = 0.8$. There are 3 time slices that showcase the growing anisotropy of wavefronts due to the speed of sound dependence on $\Theta$.

In a classical gas, quantum statistics enters only in the collision cross sections. Hence, the mean-field

result in (5.21) applies equally to both bosons and fermions. As written, the speed of sound in a normal dipolar gas has an anisotropy similar to that for a dipolar Bose-Einstein condensate (DBEC) [107–109], but with temperature replacing the role of quantum fluctuations. The quantity $\eta$ compares the magnitude of the dipolar mean-field with thermal energies, which at a fixed temperature $T_0$, varies by means of the background density $\rho_0$ and dipole moment $d$ [3, 4, 46, 49].

For propagation of sound waves along the direction of dipole polarization, $\Theta \sim 0$, this propagation is stable. That is, the value of $c_{\rm dd}$ remains real-valued. However, for sufficiently large $\eta$, there is a critical value of $\eta_c(\Theta) \equiv -(3\cos^2\Theta - 1)^{-1}$, past which the dipolar mean-field interactions overcomes the thermal kinetic energy, causing $c_{\rm dd}(\Theta)$ to become imaginary [3] . An imaginary speed of sound indicates a dipolar instability, also predicted and observed in DBEC [107, 110–114]. Notably, $\eta_c$ is only well defined within the interval bounded by the dipolar magic angles $\Theta_{\rm magic} \approx 54.7°$ and 125.3°, at which $\varphi_{\rm dd}(\Theta_{\rm magic}) = 0$ [4] . Within the range of dipolar magic angles, $\eta_c$ has a minima of 1 at $\Theta = 90°$.

### 5.3.2 Undulating sound waves

The physics of sound gets more interesting at finite $K$, where transport tensors now enter the dynamical arena. To ground discussions, I'll envision an experiment with a box-trapped [104] uniform density sample of microwave shielded $^{23}$Na$^{40}$K molecules cooled to $T_0 = 250$ nK [4]. When $\eta \ll 1$, say at $n_0 = 10^{12}$ cm$^{-3}$ and $d = 0.75$ D ($\eta \approx 0.04$), the dipolar mean-field, and therefore $\mathscr{E}_{\rm dd}$, becomes negligible compared to kinetic processes. In this regime, the speed of sound reverts to that of an ideal gas $c_{\rm dd} \approx c$, while the imaginary part of $\omega_\pm$ is strictly negative, leading to sound attenuation. Resulting directly from dipolar collisions, the observed attenuation for an excitation with $\delta = 0.1$ is anisotropic, varying by a factor of $\sim 2$ with $\Theta$ as shown in Fig. 5.4.

[3] Even at this higher density of $n_0 = 2 \times 10^{12}$ cm$^{-3}$, the transport coefficients presented in Eqs. (5.8) and (5.10) are accurate to 10% in higher density corrections [69].

[4] The critical value $\eta_c$ appears to be a pole of certain solutions in Eqs. (5.19). This divergence is, however, only a feature of the series expansion in $\delta$. Exact solutions to Eq. (5.15) remain finite valued across $\eta = \eta_c$.

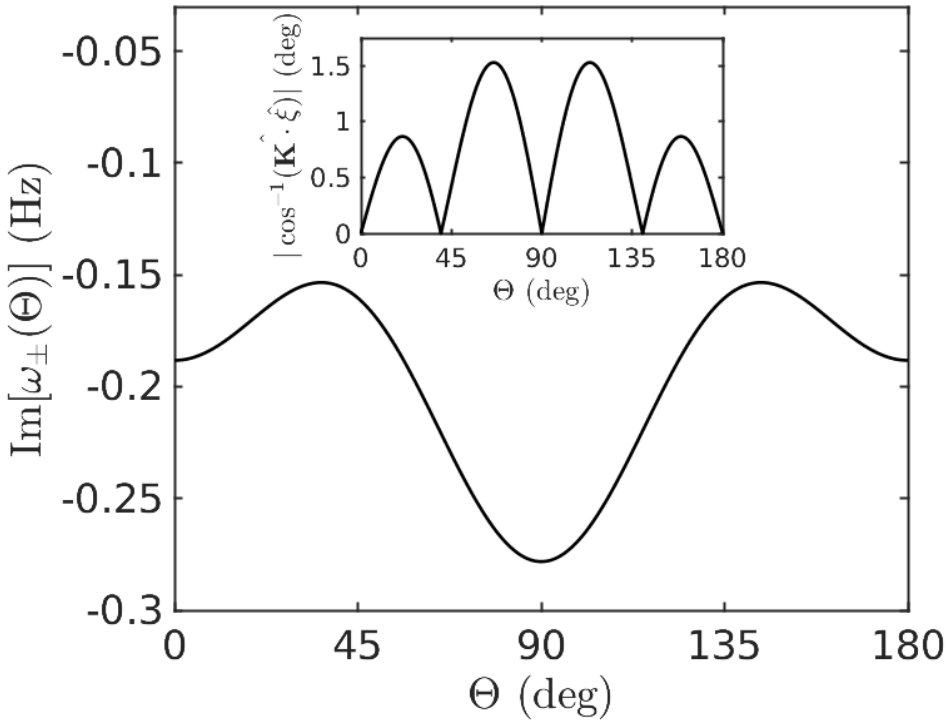


Figure 5.4: Imaginary part of the propagating mode frequency solutions $\mathrm{Im}[\omega_\pm(\Theta)]$ in Hertz (Hz), as a function of the dipole tilt angle $\Theta$ in degrees (deg) at $\eta \approx 0.04$. The figure inset plots the absolute relative angle between $\hat{\boldsymbol{K}}$ and $\hat{\boldsymbol{\xi}}$, $|\cos^{-1}(\hat{\boldsymbol{K}} \cdot \hat{\boldsymbol{\xi}})|$, also as a function of $\Theta$.

The $\omega_\pm$ modes have associated eigenvectors of the form

$$\boldsymbol{\psi}_\pm = \begin{pmatrix} 1 \\ 0 \\ 0 \\ \pm\frac{c_{\mathrm{dd}}}{c} \\ \frac{2}{3} \end{pmatrix} + \begin{pmatrix} \mp i\frac{\Gamma}{c_{\mathrm{dd}}K} \\ i\frac{\Lambda_{13}}{cK} \\ 0 \\ -i\left(\frac{\Gamma}{5cK}\left(4+\frac{\mathscr{E}_{\mathrm{dd}}}{c_{\mathrm{dd}}^2}\right)+\frac{\Lambda_{33}}{2cK}\right) \\ 0 \end{pmatrix}, \tag{5.22}$$

defined up to an overall scale factor. The first term of the sum in the expression above has nonzero and comparable amplitudes in the fractional density shift $\chi$, fractional $z$-velocity $\xi_z$, and fractional temperature shift $\epsilon$, as expected for a longitudinal wave propagating in the $z$ direction. The second term in $\boldsymbol{\psi}_\pm$ shows the additional effects introduced by viscous and thermal damping. Specifically, terms in the density and $z$-velocity are explicitly damped, while the temperature is not yet damped at this level of approximation. Along with these effects, a new one appears, namely, a damped

motion in the $x$-velocity $\xi_x$.

Therefore, despite initiating sound along $\hat{\boldsymbol{K}} = \hat{\boldsymbol{z}}$, the fluctuations in flow velocity could occur in a slightly different direction depending on the dipole orientation. That is, along with regular sound propagation along $z$ that alternately compresses and rarefies the gas, the fluid velocity simultaneously alternates between flow along the $\pm x$ directions. The general fluid motion is therefore of a slightly undulatory nature. This effect, albeit small, is one unique to anisotropic transport which I illustrate with a plot of the absolute relative angle between $\hat{\boldsymbol{K}}$ and $\hat{\boldsymbol{\xi}}$, $|\cos^{-1}(\hat{\boldsymbol{K}}\cdot\hat{\boldsymbol{\xi}})|$, against $\Theta$ in the inset of Fig. 5.4. These weak transverse motions are potentially observable in Doppler spectroscopy of the undulating molecules.

### 5.3.3 Shear silence

Even in the absence of sound, a silent hydrodynamic gas of dipoles still has a story to tell. This narrative is populated by the latter 3 modes of Eq. (5.19), all of which have purely imaginary frequencies for any value of $\eta$ and $\Theta$. Once again with $\eta \approx 0.04$ and $\delta = 0.1$, suppressing the dipolar mean-field, anisotropic damping is accentuated in these silent modes with plots of the imaginary parts of their mode frequencies in Fig. 5.5.

One of these modes, with frequency $\omega_{\mu,2}$, has a particularly simple form:

$$\boldsymbol{\psi}_{\mu,2} = \begin{pmatrix} 0 & 0 & 1 & 0 & 0 \end{pmatrix}^T. \tag{5.23}$$

This mode consists exclusively of flow velocity in the $\pm y$ directions, the velocity being sinusoidally modulated along $z$ with wavelength $2\pi/K$. If one were to "grab" the $z = 0$ layer of the fluid and shake it with frequency $|\omega_{\mu,2}|$, a shear wave would thus develop. This is an overdamped mode, hence its amplitude reaches only to approximately a certain penetration depth, defined as the inverse absolute imaginary part of the wave-number [17, 97]:

$$r_{\mu,2} = \sqrt{\frac{\mu_{2323}}{2\omega\rho_0}} \approx \frac{3}{64}\sqrt{\frac{5(9-5\cos(4\Theta))}{\omega a_d^2 n_0\sqrt{\pi m\beta_0}}}. \tag{5.24}$$

The expression above is obtained from Eq. (5.19), by instead solving for $K$ in terms of a fixed driving frequency $\omega$. Such waves are, of course, already familiar in ordinary, isotropic fluids.

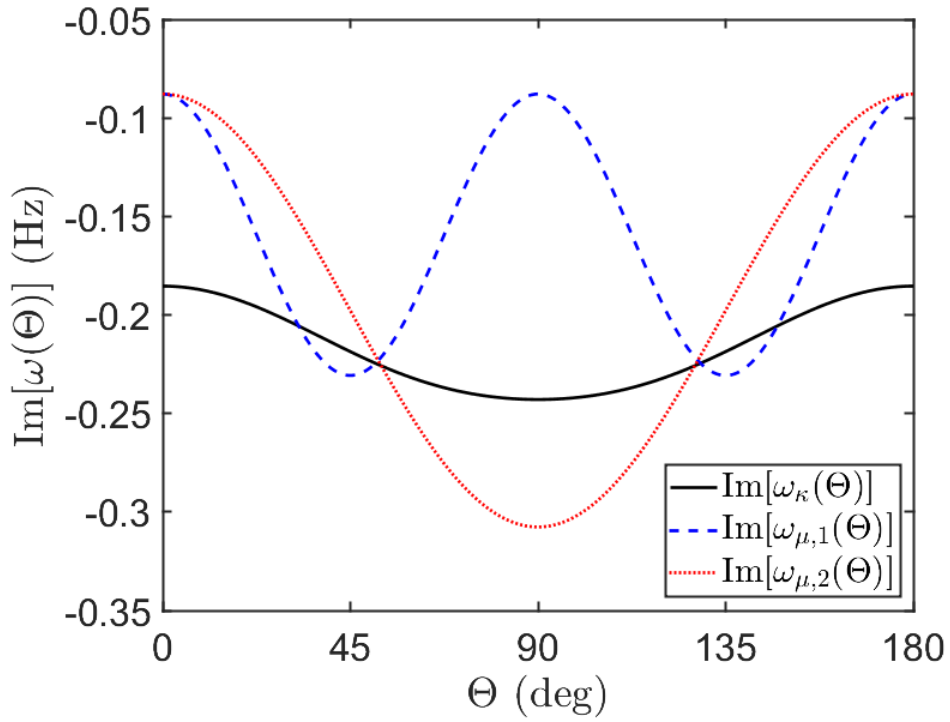


Figure 5.5: The imaginary parts of the mode frequency solutions, $\mathrm{Im}[\omega_\kappa]$ (solid black curve), $\mathrm{Im}[\omega_{\mu,1}]$ (dashed blue curve) and $\mathrm{Im}[\omega_{\mu,2}]$ (dotted red curve), as a function of $\Theta$ in a gas of $^{23}$Na$^{40}$K molecules with $n_0 = 10^{12}$ cm$^{-3}$ and $d = 0.75$ D ($\eta \approx 0.04$).

A shear mode with fluid flow in the $\pm x$ direction is, however, affected by the anisotropy of dipolar collisions, given by

$$\boldsymbol{\psi}_{\mu,1} = \begin{pmatrix} 0 \\ \left(1 - \frac{\Gamma}{\Lambda_{11}}\right)\frac{5c_{\mathrm{dd}}^2}{2c^2} + \frac{\Gamma}{\Lambda_{11}} \\ 0 \\ 0 \\ 0 \end{pmatrix} + \begin{pmatrix} i\frac{\Gamma}{cK}\frac{c^2\Lambda_{13}}{c_{\mathrm{dd}}^2\Lambda_{11}} \\ 0 \\ 0 \\ 0 \\ -i\frac{5\Lambda_{13}}{3cK} \end{pmatrix}. \tag{5.25}$$

Here, once more, the first term accounts for the dominant motion, namely, oscillations in the $\pm x$ directions induced by shear. The penetration depth for this $x$-shear mode under an oscillatory shear drive is, not surprisingly, also dipole angle dependent, and given by the relation

$$r_{\mu,1} = \sqrt{\frac{\mu_{1313}}{2\omega\rho_0}} \approx \frac{3}{128}\sqrt{\frac{5(29 - 13\cos(4\Theta))}{\omega a_d^2 n_0\sqrt{\pi m\beta_0}}}. \tag{5.26}$$

The second term in $\psi_{\mu.1}$ denotes additional accompanying effects associated with this shear mode, which in this case are damped modulations in the density and temperature fields. In this circumstance, where the dipoles are oriented somewhere in the $x, z$ plane, and the shear flow in the $x$ direction, the anisotropy of the collision cross section is capable of shoveling both matter and kinetic energy preferentially into the $\pm z$ directions, the same as it ordinarily does for momentum. Because shear modes are a direct consequence of viscosity in the gas, they present themselves as an experimental means to measure the viscosity coefficients [5] [18].

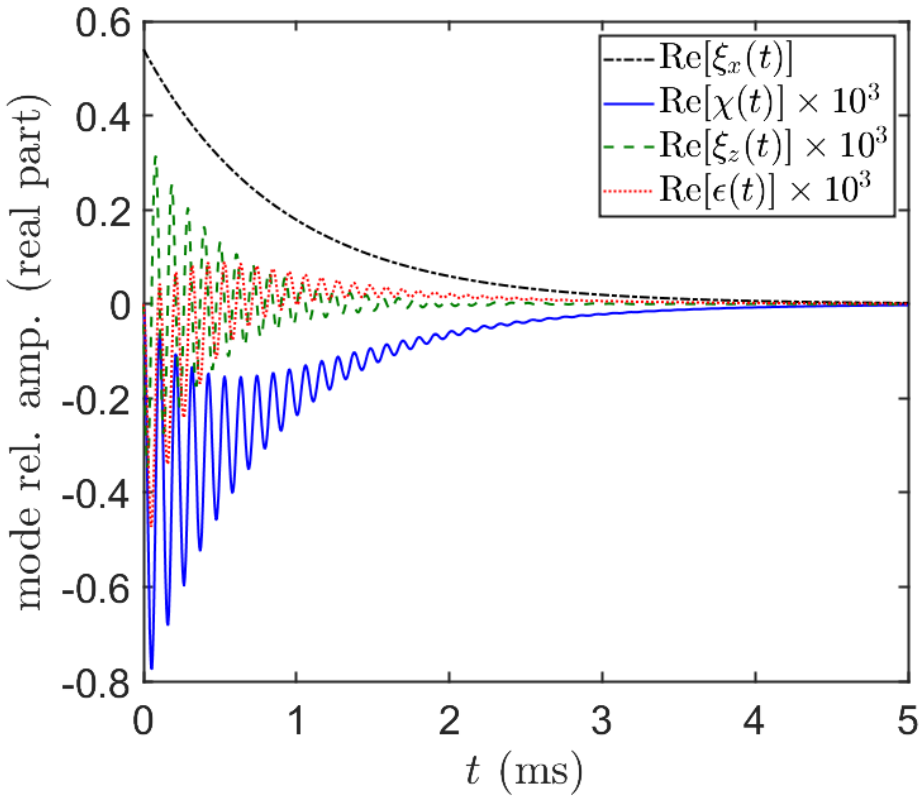


Figure 5.6: Relative fluid variable fluctuation amplitudes $\xi_x(t)$ (dashed-dotted black curve), $\chi(t)$ (solid blue curve), $\xi_z(t)$ (dashed green curve), $\epsilon(t)$ (dotted red curve) as a function of time $t$ at $z/L = 10$, after an impulse shear flow perturbation along $\hat{\boldsymbol{x}}$. The dipoles are oriented with $\Theta = \pi/4$. The relative amplitudes for $\chi(t), \epsilon(t)$ and $\xi_z(t)$ are rescaled by a factor of $10^3$ for clarity.

[5] The shear viscosity has also been measured in harmonically confined unitary Fermi gases with breathing mode damping experiments [115]. These measurements were, however, performed for non-dipolar gases with a single shear viscosity coefficient.

The time evolution of relative mode amplitudes $\boldsymbol{\psi}(t)$ in Fig. 5.6 demonstrate this anomalous shear excitation, following an impulse shear flow perturbation along $\hat{\boldsymbol{x}}$ with $\Theta = \pi/4$. Along with $\chi$ and $\epsilon$, $\xi_z$ is also subsequently excited. In the plot, the relative amplitudes for $\chi(t), \epsilon(t)$ and $\xi_z(t)$ are rescaled by a factor of $10^3$ for ease of visualization, but indicate that this effect is indeed a small one. Temperature field variations via the introduction of heat into a fluid are commonly referred to as entropy waves [116, 117], which if initiated by laminar shear flow, motivates the title *shear-entropy waves*. As far as I know, this phenomenon is not present in existing shear flow literature, making for a brand new scientific discovery!

Not forgetting the fifth and final mode $\boldsymbol{\psi}_\kappa$, within the range of $\Theta$ where $\mathscr{E}_{\rm dd} < 0$, $\omega_\kappa$ can vanish identically at suitably large values of $n_0$ and $a_d$ such that $\mathscr{E}_{\rm dd} = -3c^2/5$ (i.e. $\eta = 3\eta_c/5$). Satisfying this condition would lead to a mode where $\epsilon = \xi_x = \xi_y = \xi_z = 0$ but $\chi \neq 0$, as made evident from its functional form

$$\boldsymbol{\psi}_\kappa = \begin{pmatrix} 0 \\ \frac{3}{5}\left(1 - \frac{\Gamma}{\Lambda_{11}}\frac{3c^2+5\mathscr{E}_{\rm dd}}{5c_{\rm dd}^2}\right)\left(1 + \frac{5\mathscr{E}_{\rm dd}}{3c^2}\right) \\ 0 \\ 0 \\ 0 \end{pmatrix} + \begin{pmatrix} i\frac{\Lambda_{13}}{cK} \\ 0 \\ 0 \\ 0 \\ -i\frac{\Lambda_{13}}{cK}\left(1 + \frac{5\mathscr{E}_{\rm dd}}{3c^2}\right) \end{pmatrix}. \tag{5.27}$$

Such a mode implies the existence of long-lived density modulations due to a balance between thermal and dipolar mean-field energies. This could be rather cool to observe in an experiment, but I cater further analysis to some other future publication.

## 5.4 Viscous welter of a trapped dipolar fluid

What happens when a dipolar gas gets really collisionally dense (i.e. more collisions per unit volume per second), while confined in a harmonic trap? Maybe the central region of the gas is hydrodynamic, but surely its Gaussian density profile makes the peripheries dilute (see Figs. 3.1 and 5.7). Would hydrodynamics fail and cause relaxation to revert to that seen in Sec. 4.1? How do we best describe the dynamics then? Well, previous works have reported cross-dimensional relaxation

rates being close to the trapping frequency in the hydrodynamic regime [4, 118, 119], unlike the dilute regime being closely related to the collision rate. So surely the faster collision rates result in dynamics different from the dilute limit. The gist of my investigations into these questions thus far, is that harmonically trapped gases can be hydrodynamic, well described by equations derived from (5.2). These equations do work pretty well, but only up to ad hoc corrections which beckon further study. The following will get you up to speed on the status of things.

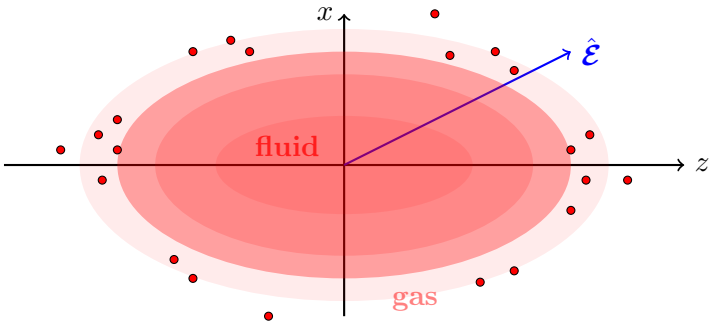


Figure 5.7: Cartoon of a Gaussian distributed gas with a hydrodynamic center and dilute corona.

Right from the get go, the disparity between dilute and hydrodynamic trapped gases is clearly revealed in cross-dimensional rethermalization experiments (Sec. 4.1), illustrated with time trace plots of the pseudotemperatures (4.3) in Fig. 5.8 (obtained from the Monte Carlo solver of Sec. 3.3). In both panels, a collection of $^{23}$Na$^{40}$K molecules is subjected to the same harmonic trapping potential (3.2), excited along $z$, then subsequently left to relax. The only systemic difference is the molecule number: for fewer molecules in the upper panel (a), the gas is dilute, while for a greater number of molecules in the lower panel (b), it is hydrodynamic. As opposed to the gradual melting of pseudotemperatures back to equilibrium seen in (a), the behavior in (b) is distinctly fluid-like, resembling the wobble of a water balloon after squishing it along some direction. This latter type of motion has been christened *weltering dynamics* [19], and done so quite proudly I might add.

"*Welter, my boy – welter like the wind!*"

– John L. Bohn (random email thread), 2023.

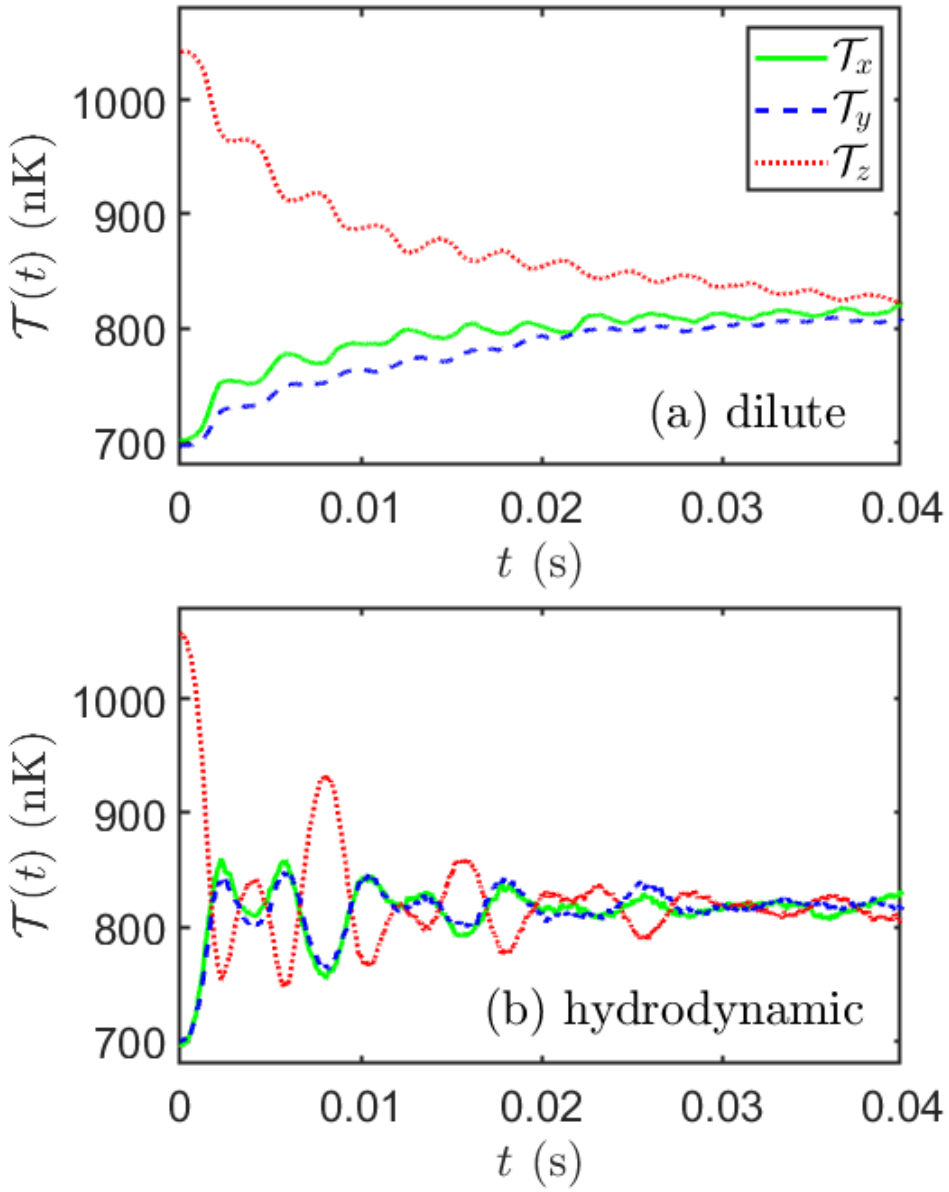


Figure 5.8: Pseudotemperatures (4.3) obtained from Monte Carlo simulations in the dilute (upper panel, a) and hydrodynamic (lower panel, b) regimes. The gas consists of microwave shielded $^{23}$Na$^{40}$K molecules with dipole moment $d = 0.75$ D, oriented along $\hat{\boldsymbol{x}}$, at temperature $T = 700$ nK. The gas is initially excited along $z$ by an instantaneous trap frequency ramp to $\omega_z = 2\pi \times 147$ Hz, while $\omega_x = \omega_y = 2\pi \times 82.5$ Hz remain constant. The regimes are differentiated by the number of molecules $N$, which are $N = 10^4$ in panel (a), and $N = 2 \times 10^5$ in panel (b).

For a more quantitative delineation, the change in $N$ between subplots (a) and (b) results in a significant difference in the Knudsen number. For these trapped gases, Kn is appropriately defined

by the ratio of the mean-free path $L = \langle n\sigma\rangle^{-1}$, to the thermal width of the gas $R_{\rm th} = \sqrt{k_B T/m\bar{\omega}^2}$:

$$\mathrm{Kn} = \frac{L}{R_{\rm th}} = \frac{8\pi^{3/2} k_B T}{N m \bar{\omega}^2 \bar{\sigma}}. \tag{5.28}$$

In this definition, subplot (a) has the gas with $\mathrm{Kn} \approx 2.2$, while in subplot (b), $\mathrm{Kn} \approx 0.1$ [6] .

### 5.4.1 An effective model for damped welter

Affecting its response and route toward equilibrium, the quest for new hydrodynamic physics motivates constructing a model for the welter in these gases. Yes I know, Eq. (5.2) is already such a model, but look at how hard it is to solve, even numerically. Instead, I adopt a variational ansatz approach to solving these partial differential equations much like that done in Sec. 3.2[7] . External confinement from a harmonic potential (3.2) results in the equilibrium (denoted by subscript 0) density distribution following

$$\rho_0(\boldsymbol{r}) = \frac{mN}{Z} \exp\!\left(-\frac{V(\boldsymbol{r})}{k_B T_0}\right), \tag{5.29}$$

where $Z = \int d^3\boldsymbol{r} \mathrm{e}^{-\frac{V(\boldsymbol{r})}{k_B T_0}}$ gives the appropriate normalization. Considering collective oscillations and damping from long wavelength excitations that do not induce center-of-mass sloshing, Eq. (5.29) motivates a Gaussian variational ansatz for the local density:

$$\rho(\boldsymbol{r}, t) = mN \prod_{i=1}^{3} \frac{1}{\sqrt{2\pi\sigma_i^2(t)}} \exp\left(-\frac{r_i^2}{2\sigma_i^2(t)}\right), \tag{5.30}$$

where $\sigma_i(t)$ is the distribution width along each axis $i$, that varies in time (depicted in Fig. 3.1).

Plugging the ansatz of Eq. (5.30) into the continuity equation (5.2a) gives

$$\sum_{i=1}^{3} \left[\partial_i U_i(\boldsymbol{r}) - U_i(\boldsymbol{r}) \left(\frac{r_i}{\sigma_i^2(t)}\right) + \left(\frac{r_i^2}{\sigma_i^2(t)} - 1\right) \frac{\dot{\sigma}_i(t)}{\sigma_i(t)}\right] = 0, \tag{5.31}$$

which admits the velocity field solution

$$U_i(\boldsymbol{r}) = \left(\frac{\dot{\sigma}_i(t)}{\sigma_i(t)}\right) r_i. \tag{5.32}$$

[6] The relations above provide an approximate mean Knudsen number. In practice, the thermal width can differ in directions with different trap frequencies, while the cross section, for dipolar scattering, can depend on the direction of the collision axis. Thus the boundary between hydrodynamic and dilute flow can be anisotropic, a topic to be dealt with below.

[7] Our method has similarities to the scaling ansatz employed in Ref. [120–122], but formulated slightly differently and with the inclusion of transport tensors.

For clarity, I'll revert to treating repeated indices as *un*summed in this section, unless following an explicit summation symbol $\Sigma$. The $\rho$ and $\boldsymbol{U}$ above then render the Navier-Stokes equation (5.2b)

$$\ddot{\sigma}_i(t) + \omega_i^2 \sigma_i(t) = \frac{k_B}{m}\left(\frac{1}{\sigma_i(t)} - \frac{\sigma_i(t)}{r_i}\partial_i\right) T(\boldsymbol{r},t) + \sigma_i \sum_{j,k,\ell} \frac{\partial_j \mu_{ijk\ell}(T)}{r_i \rho(\boldsymbol{r})} \delta_{k,\ell} \frac{\dot{\sigma}_k}{\sigma_\ell}, \tag{5.33}$$

which bears no dependence on thermal conductivity. Since $\sigma_i(t)$ does not depend on spatial coordinates, consistency requires taking a spatial average to suppress local fluctuations of the temperature field in Eq. (5.33). This average is taken by multiplying Eq. (5.33) and the temperature balance equation (5.2c), by $n(\boldsymbol{r},t)$, then integrating over $d^3\boldsymbol{r}$. App. H gives further details of the spatial averaging procedure, which results in

$$\ddot{\sigma}_i(t) + \omega_i^2 \sigma_i(t) + \frac{1}{3\sigma_i(t)} \sum_j \left[\omega_j^2 \sigma_j^2(t) + \dot{\sigma}_j^2(t)\right] - \frac{2k_B T_0}{m\sigma_i(t)} \approx -\frac{2}{5}\frac{\mathcal{V}_{\rm hy}}{Nm} \sum_j \frac{\mu_{iijj}(T(t))}{\sigma_i(t)} \frac{\dot{\sigma}_j(t)}{\sigma_j(t)}. \tag{5.34}$$

The relevant viscosity matrix elements can be recast in terms of a unit-free matrix

$$\begin{aligned} M_{ij}(\Theta) &\equiv \frac{\mu_{iijj}(T;\Theta)}{\mu_d(T)} \\ &= \frac{1}{512}\begin{pmatrix} 117\cos(4\Theta) + 84\cos(2\Theta) + 415 & -28(3\cos(2\Theta)+11) & -(117\cos(4\Theta)+107) \\ -28(3\cos(2\Theta)+11) & 616 & 28(3\cos(2\Theta)-11) \\ -(117\cos(4\Theta)+107) & 28(3\cos(2\Theta)-11) & 117\cos(4\Theta) - 84\cos(2\Theta) + 415 \end{pmatrix}, \end{aligned} \tag{5.35}$$

as is read off from Eq. (5.10), where $\mu_d$ was that defined in Eq. (5.9). For a gas of $^{23}$Na$^{40}$K molecules microwave shielded to have an effective dipole moment $d = 0.75$ D, its isotropic viscosity at $T_0 = 700$ nK takes a value of $\mu_0 \approx 2.5 \times 10^{-15}$ Pa·s, around $10^{10}$ times less than air at room temperature and pressure [123]. These parameters are assumed for the rest of what follows. The $M_{ij}(\Theta)$ matrix elements are plotted in Fig. 5.9, with components coupled to the $x$ and $z$ axes showcasing a significant variation with $\Theta$. The magnitude of off-diagonal matrix elements $M_{13} = M_{xz}$ and $M_{23} = M_{yz}$ become maximally separated around $\Theta \approx 45°$, explaining the slight separation of $\mathcal{T}_x(t)$ and $\mathcal{T}_y(t)$ in Fig. 5.10, otherwise negligible when $\Theta = 0°, 90°$.

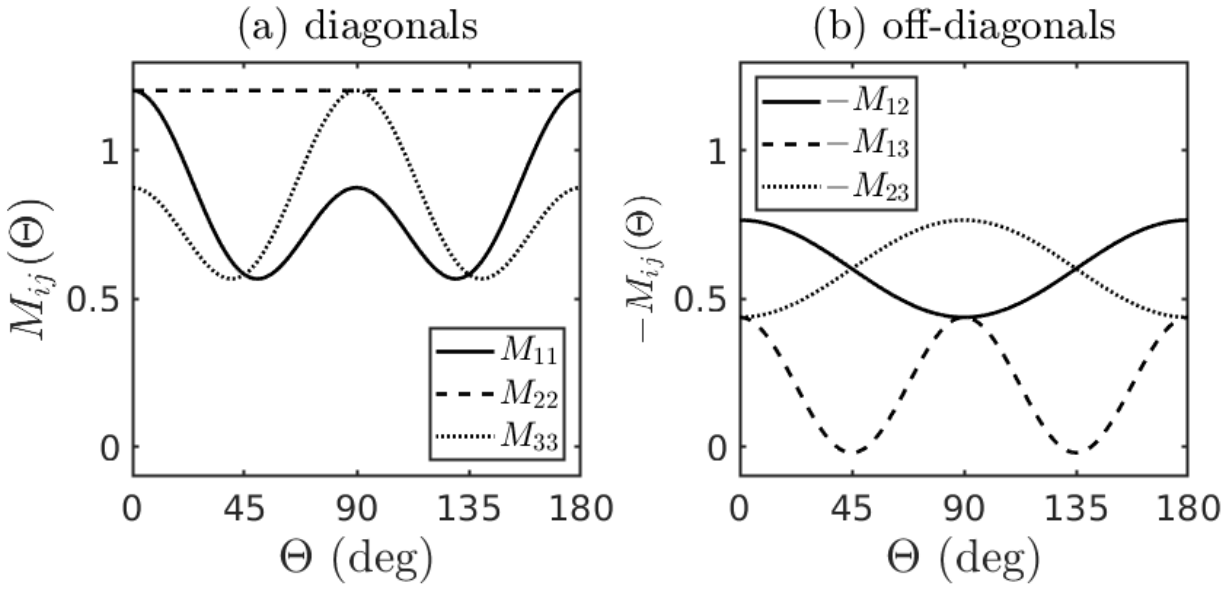


Figure 5.9: $M_{ij}$ matrix elements as a function of $\Theta$. The diagonal elements are plotted on the left in subplot (a), whereas the negated (multiplied by a minus sign) off-diagonal elements are plotted on the right in subplot (b).

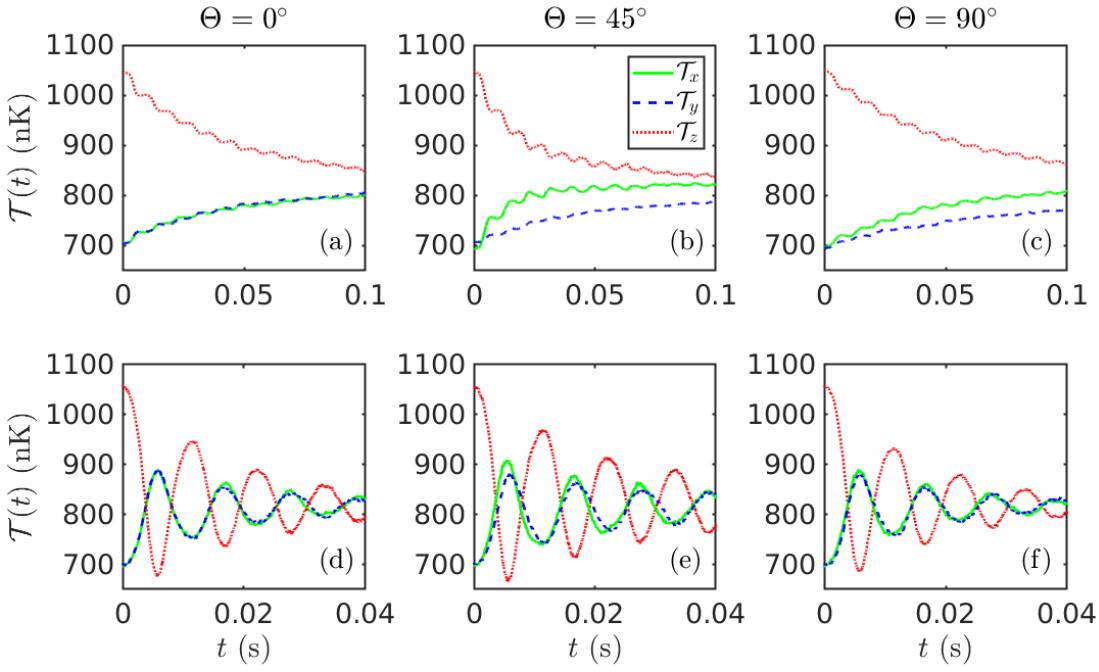


Figure 5.10: Times traces of $\mathcal{T}_x(t)$ (solid green curves), $\mathcal{T}_y(t)$ (dashed blue curves) and $\mathcal{T}_z(t)$ (dotted red curves) for 3 values of $\Theta = 0°, 45°, 90°$, in subplots (a, d), (b, e) and (c, f) respectively. The 2 rows are differentiated by the number of molecules, with the upper row (subplots a, b, c) having $N = 2 \times 10^3$ (Kn $\approx 11.10$), while the lower row (subplots d, e, f) has $N = 3 \times 10^5$ (Kn $\approx 0.07$). Note that the simulation times are different between the upper ($t = 0$ to 0.1s) and lower ($t = 0$ to 0.04s) rows.

For the relevance of time-of-flight imaging, the momentum space temperature, which differs from the local temperature of Eq. (5.1c), can also be obtained from solutions to Eq. (5.34) via the relation

$$\begin{aligned} k_B T_p(t) &= \frac{1}{3N}\int d^3\boldsymbol{r} d^3\boldsymbol{v} f(\boldsymbol{r},\boldsymbol{v},t) m\boldsymbol{v}^2 \\ &= 2k_B T_0 - \frac{1}{3}\sum_i m\omega_i^2\sigma_i^2(t), \end{aligned} \tag{5.36}$$

as follows from Eqs. (5.3) and (5.32), along with the total energy relation $E_{\rm total} = 3k_B T_0$ from the equipartition theorem.

Eq. (5.34) above treats the temperature field appearing in $\mu_{ijk\ell}(T)$ to be spatially uniform over the region where the gas is hydrodynamic. Such an approximation follows from the form of collective oscillations implied by the density (5.30) and flow velocity fields (5.32) in an initially isothermal gas, disallowing a spatial temperature variation on the order of the gas spatial widths [124, 125]. Hence, temperature as appears in the viscosity is simply treated as $T \approx T(t)$. Doing so, requires defining an effective hydrodynamic volume $\mathcal{V}_{\rm hy} = \int d^3\boldsymbol{r}$[8] , over which viscosity is relevant. Proper identification of this volume, including its dependence on aspect ratio, density, and dipole tilt, is essential to the performance of the model (5.34). This is going to be a real undertaking, but I'll leave most of the details to App. I. Here are the just highlights.

First, I define this volume to be the spheroidal volume bounded by the outer classical turning radius of the trap, multiplied by an empirical factor $\eta$. The outer turning radius is obtained by equating $E_{\rm total} = V(R_{\rm HD},\theta,\phi)$, to give (see App. H)

$$R_{\rm HD}^2(\theta) = \frac{6k_B T(t)}{m\omega_\perp^2}\left[\sin^2\theta + \lambda\cos^2\theta\right]^{-1}, \tag{5.37}$$

where $\lambda = (\omega_z/\omega_\perp)^2$ quantifies the trapping anisotropy. The effective hydrodynamic volume is then computed as

$$\mathcal{V}_{\rm hy}(\lambda,{\rm Kn}) = \frac{\eta(\lambda,{\rm Kn})}{3}\int R_{\rm HD}^3(\Omega)d\Omega = \frac{4\pi}{3}\left(\frac{6k_B T(t)}{m\omega_\perp^2}\right)^{3/2}\frac{\eta(\lambda,{\rm Kn})}{\sqrt{\lambda}}. \tag{5.38}$$

[8] Refs. [124, 126] provides another estimate for the effective hydrodynamic volume which, however, we find systematically underestimates the results from our numerical Monte Carlo simulations.

As written, I have assumed that $\eta$ could depend on the trapping geometry through $\lambda$ and on the Knudsen number, which in turn, also implicitly depends on $N$ and the dipole angle $\Theta$. Such generality allows $\eta$ to act as a coarse-graining parameter which accounts for all non-hydrodynamic effects excluded from the current theoretical treatment. Additionally, Eq. (5.9) implies the temperature dependence of viscosity goes as $\mu_{iijj}(T) \propto \sqrt{T}$, for which I will simply approximate as $T \approx T_0$ for all times [9] .

Then by careful comparison of Eq. (5.34) to a large batch of numerical simulations (detailed in App. I), I find that the effective volume in a prolate (i.e. cigar shaped) trap is best described by the functional form

$$\mathcal{V}_{\rm hy}(\lambda, N, \Theta) \approx \frac{4\pi}{3}\left(\frac{6k_B T_0}{m\omega_\perp^2}\right)^{3/2} \frac{1}{\sqrt{\lambda}}\left[2.21 + 0.67\left(1 + 0.26\frac{\sigma(\Theta)}{\overline{\sigma}}\right)\frac{N}{10^5}\right], \tag{5.39}$$

where

$$\sigma(\Theta) = \frac{\pi a_d^2}{3}\left[3 + 18\cos^2\Theta - 13\cos^4\Theta\right], \tag{5.40}$$

is the total cross section. With the parametrization above, Eq. (5.34) can now be used to reliably determine the cross-dimensional relaxation dynamics of a hydrodynamic dipolar Fermi gas, subject to excitation along the long axis of the prolate trap. As presented, Eq. (5.39) shows that the hydrodynamic volume, at a fixed temperature and harmonic confinement, grows linearly with the number of molecules $N$. This trend is inferred from the numerical simulation reflected in subplot (a) of Fig. 5.11. Notably, subplot (b) of Fig. 5.11 also endows Eq. (5.39) with a dipolar angle dependence, which can be intuited as follows. In a prolate trap, the gas has a larger thermal width along the weak trapping axis $z$. As a result, the mean-free path along that axis is relatively smaller compared to the sample size, and consequently more hydrodynamic. Collisions that occur with relative momentum directed along the long axis, are then most able to keep molecules behaving collectively as hydrodynamic. So by attributing collisions incident along $\hat{\boldsymbol{z}}$ as most effective toward viscous damping, the hydrodynamic volume can be taken as dependent on dipolar scattering via the total cross section with $\hat{\boldsymbol{k}} = \hat{\boldsymbol{z}}$.

[9] Incorporating time-dependence in the temperature $T(t)$, requires more sophisticated treatments such as second-order hydrodynamics [127], that I cater to a future study.

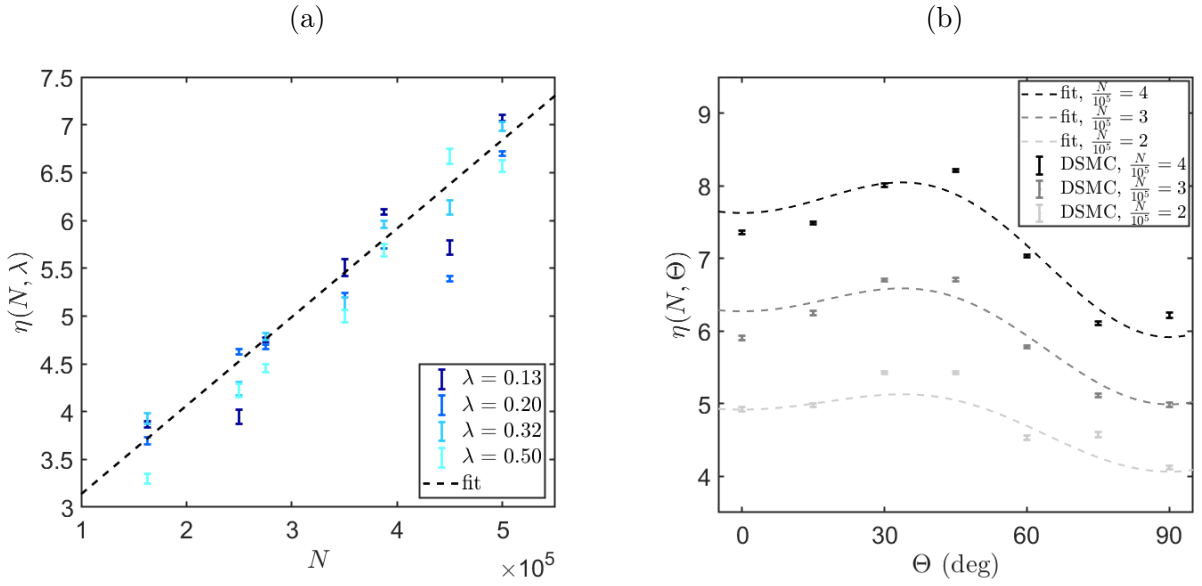


Figure 5.11: The points with errorbars (standard errors) give $\eta$ as obtained from DSMC simulations, performed over different values of $N, \lambda$ and $\Theta$. The linear trend of $\eta$ vs $N$ is provided in subplot (a), being largely consistent over various values of $\lambda = 0.13, 0.20, 0.32, 0.50$, all of which are prolate (cigar) geometries. Subplot (b) shows how $\eta$ varies with $\Theta$, closely following the angle dependence in Eq. (5.40). The data for this latter trend is obtained with $\lambda = 0.2$, for $N = 4 \times 10^5$ (black data, Kn $\approx 0.06$), $N = 3 \times 10^5$ (gray data, Kn $\approx 0.07$) and $N = 2 \times 10^5$ (light gray data, Kn $\approx 0.11$)

Evidently from Eq. (5.39), $\mathcal{V}_{\text{hy}}$ remains a stagnant parameter through the gas' dynamical evolution. There is, however, no physical reason why such a volume has to be so. A new avenue of research thus presents itself. Can $\mathcal{V}_{\text{hy}}$ be formulated self-consistently from first principles? Or perhaps a machine might better be able to help with this task [128, 129]. All terribly captivating, these prospects must surely be pursued with haste. Though it is not this thesis that I will answer to the cry of these scientific curiosities. Perchance a work to come soon just might.

The physics of Eq. (5.34) is made more accessible in the language of normal modes, motivating a linear analysis. If only taken perturbatively out-of-equilibrium, the time variation of the ensemble widths can be written in terms of small deviations away from its equilibrium values $\sigma_i(t) = \sigma_{0,i} + \delta\sigma_i(t)$. Then expanding to first-order in $\delta\sigma_i(t)$, Eq. (5.34) becomes

$$\ddot{\delta\sigma}_i(t) + 2\sum_j \Gamma_{ij}\dot{\delta\sigma}_j(t) + \sum_j O_{ij}\delta\sigma_j(t) \approx 0, \tag{5.41}$$

with squared-frequency and damping matrices

$$O_{ij} = 2\omega_i^2\delta_{i,j} + \frac{2}{3}\omega_i\omega_j, \tag{5.42a}$$

$$\Gamma_{ij} = \frac{\mu_0\mathcal{V}_{\rm hy}}{5Nk_BT_0}\omega_i M_{ij}(\Theta)\omega_j. \tag{5.42b}$$

The matrices above encode the anisotropies from both the trap and anisotropic collisions. Well what do you know, Eq. (5.41) tells us that weltering perturbations are simply the motion of damped coupled harmonic oscillators! With $\boldsymbol{\Gamma}$ multiplying the first-order time derivative terms $\delta\dot{\sigma}_i$, it is made clear that damping of weltering oscillations results from the trap frequency weighted viscosities within the hydrodynamic volume. A factor 2 multiplies $\boldsymbol{\Gamma}$ in Eq. (5.41) as is convention in damped harmonic oscillators.

Diagonalizing the squared-frequency matrix $\boldsymbol{O}$ gives the eigenfrequencies

$$\omega_0^2 = 2\omega_\perp^2, \tag{5.43a}$$

$$\omega_\pm^2 = \frac{1}{3}\left(4\lambda + 5 \pm \sqrt{16\lambda^2 - 32\lambda + 25}\right)\omega_\perp^2, \tag{5.43b}$$

which are exactly those obtained for inviscid Euler flow in Refs. [124, 130], and correspond to the respective eigenmodes (up to arbitrary normalization)

$$\boldsymbol{o}_0 = \begin{pmatrix} 1 \\ -1 \\ 0 \end{pmatrix}, \tag{5.44a}$$

$$\boldsymbol{o}_\pm = \begin{pmatrix} 5 - 4\lambda \pm \sqrt{25 + 16\lambda(\lambda - 2)} \\ 5 - 4\lambda \pm \sqrt{25 + 16\lambda(\lambda - 2)} \\ 4\sqrt{\lambda} \end{pmatrix}. \tag{5.44b}$$

The eigenmode $\boldsymbol{o}_0$ is a strictly radial quadrupole mode, while $\boldsymbol{o}_-$ and $\boldsymbol{o}_+$ are 3-dimensional quadrupole and breathing modes respectively. See Fig. 5.12 for a visual reference of these modes.

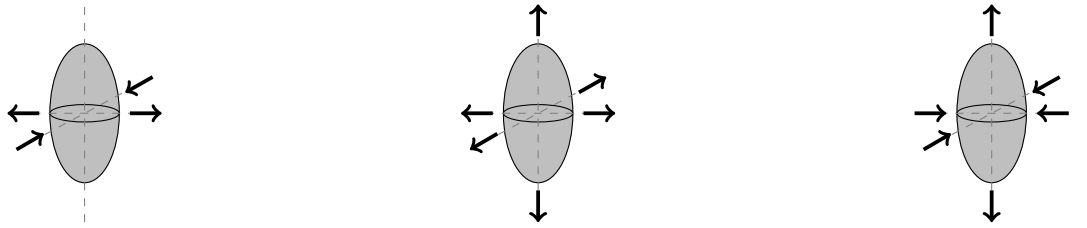


Figure 5.12: Visualization of the dominant dynamics in oscillatory modes. Arrows that point in opposing directions relative to the gas cloud (ellipsoid) indicate dynamics that are out-of-phase. These figures are for illustrative purposes.

Similarly, $\mathbf{\Gamma}$ results in two nontrivial eigenvalues $\gamma_{\pm}$, that constitute the eigen rates of $\mathbf{\Gamma}$. Although it is tempting to assign one of these eigenrates as the overall relaxation rate, the eigenmodes associated with each $\gamma_{\pm}$, are in general, not the eigenmodes of $\boldsymbol{O}$. Consequently, coupling between the eigenmodes of $\mathbf{\Gamma}$ is inevitable during dynamical evolution, enforcing that accurate relaxation trajectories are best obtained from full solutions to Eq. (5.41), if not Eq. (5.34).

The physics predicted by our weltering theory has yet to be validated by experiments. If you, the reader, are an experimentalist looking for fun hydrodynamics to do with your ultracold molecular setup, my digital door remains open for the welter wonderland we could pursue.

# Chapter 6

## Theory and Experiment Collide

An allure to working in atomic and molecular physics is the bevy of incredible experiments happening around the globe. At the very cutting edge of scientific discovery, these experiments are often pushing the boundaries of what theorists have to propose and can predict. Like any healthy competition, I've found that this exhilarating scientific back-and-forth drives much ingenuity and progress. Still, world leading experimentalists will every so often look to theorists for modeling, understanding and interpreting the physics observed in their experiments. Such collaboration also provides opportunities to actually validate the otherwise purely intellectual musings of how the universe truly behaves. Here are two experiments that utilized some of my musings.

"*Theory will take you only so far.*"

— J. Robert Oppenheimer (Oppenheimer), 2023.

### 6.1 Innsbruck: Cold mountains, ultracold atoms, hot science!

By this point, Sec. 2.1.5 has already explained all the details one needs to know about scattering lengths to follow along here. Although, knowing its numerical value, outside the context of thermalization, has thus far gone rather unmotivated. It turns out, the scattering length lends itself to parameterizing interactions in multiple models of quantum many-body physics. Like the Gross-Pitaevskii equation for studying Bose-Einstein condensates [131, 132], and the Bose-Hubbard model for describing the superfluid to Mott insulator transition [133], amongst others [9].

More recently, interest has grown in ultracold atom platforms for studying many-body physics with dipole-dipole interactions [27, 28, 134]. Such systems utilizing bosonic isotopes still require knowledge of the scattering length, which is really difficult to obtain from ab initio calculations. An alternative is to extract it from experimental measurements, which is what I've done with the Ferlaino group at Innsbruck. Together, we accurately determined $a_s$ in much the same scheme as that for Dysprosium atoms by the Lev group [87], but now supercharged with analytic expressions for thermalization. Here's the inside scoop of how we did it.

### 6.1.1 Extracting scattering lengths from thermalization

At Innsbruck, spin-polarized thermal clouds of erbium (Er) atoms were produced in their lowest Zeeman sublevel [2], primed for rethermalization experiments. To achieve this, Er atomic ensembles are first cooled and trapped in a narrow-line magneto-optical trap [135], then transferred into a crossed optical dipole trap (see App. B). The gas temperature is further lowered via evaporative cooling, following which the optical confinement is re-tightened to prevent further atom loss from residual evaporation at final trap frequencies $(\omega_x, \omega_y, \omega_z) \approx 2\pi \times (65, 19, 300)$ Hz. Simultaneously, $\boldsymbol{\mathcal{B}}$ is ramped to its desired value, which for all those considered (up to $\boldsymbol{\mathcal{B}} = 5$ G), the Zeeman splitting is linear and gives $a_d = 98.2a_0$ (see Sec. 2.1.1). At this stage, the gas is typically at a temperature between $T = 250$ to 300 nK with a population of $N \approx 10^5$ atoms. The calculated critical temperature for the onset of Bose-Einstein condensation $T_c$ [136] lies between 150 nK and 200 nK, around 1.5 times less than $T$, ensuring a nondegenerate sample. The orientation of the magnetic dipoles is controlled by the direction of the polarizing magnetic field and is parameterized by the angle $\Theta$ between $\boldsymbol{\mathcal{B}}$ and the vertical direction $z$ (see inset Fig. 4.2). Careful now, notice that the $\Theta$ is defined in the $y, z$-plane for the experiment, but in the $x, z$-plane in Chap. 4. That's going to be important when characterizing anisotropy.

With the thermal sample prepared, cross-dimensional thermalization can commence [91]. The cloud is heated almost instantaneously along $y$, after which thermalization dynamics is probed along $z$. This excitation scheme relies on a rapid increase in power of one trapping beam, leading to a

60% increase of the $y$ trapping frequency. Thermometry of the effective temperatures $T_z$ ($T_y$) over a time interval $t$ is obtained from widths of the momentum distribution $\sigma_z(t)$ ($\sigma_y(t)$) after time of flight expansion for $t_{\mathrm{ToF}} = 25$ ms (20 ms). This scheme leads to an out-of-equilibrium cloud with an effective temperature increase along $y$ from about 300 nK to 600 nK. Fig. 4.2 plots the subsequent relaxation time traces of $T_z$ and $T_y$ to the same equilibrium temperature, at $\mathcal{B} = 1$ G. Despite some oscillations attributed to a breathing mode induced by the finite-time excitation, the observed $T_z$ displays a dominant exponential behavior of the form:

$$T_z(t) = \left(T_{\mathrm{eq}} + \Delta T_z e^{-\gamma_{\mathrm{Er}} t}\right), \tag{6.1}$$

where $T_{\mathrm{eq}}$ is the equilibration temperature and $\Delta T_z$ denotes the change in temperature due to the added energy. However, applying this simple fit does not immediately give $a_s$ unless we know the explicit functional dependence of $\gamma_{\mathrm{Er}}(a_s, \Theta)$ on $a_s$. Well, aren't we fortunate, for this dependence is exactly what Eqs. (4.2) and (4.12) give us with

$$\mathcal{N}_{\mathrm{Er}}(a_s, \Theta) = \frac{14\left(45a_s^2 + 4a_d^2\right)}{252a_s^2 + 96a_s a_d + (3\cos(4\Theta) + 13)a_d^2}. \tag{6.2}$$

As presented, $\mathcal{N}_{\mathrm{Er}}$ corresponds to $\mathcal{N}_{xz}$ in theory-land axes, and $\mathcal{N}_{yz}$ in the real-world experimental setup.

A competition between the anisotropic character of $\mathcal{N}_{\mathrm{Er}}(a_s, \Theta)$ is clearly seen in Fig. 4.3, with plots of it as a function of $\Theta$ (a) and $a_s$ (b). Although a pronounced dipole angle dependence with maxima at 45° is observed at small $a_s$ ($\lesssim 10a_0$), such behavior progressively washes out for increasing $a_s$. Around $a_s \approx 70a_0$, the thermalization behavior becomes basically independent of $\Theta$ but $\mathcal{N}_{\mathrm{Er}}(a_s, \Theta)$ is still smaller than the case of purely $s$-wave collisions. Much faster thermalization is thus expected, arising from a more efficient distribution of momenta from dipolar scattering scattering. The experiment only measures rethermalization for relatively large values of $a_s \gtrsim 30a_0$ with little $\Theta$-dependence in $\mathcal{N}_{\mathrm{Er}}(a_s, \Theta)$. So $\Theta$ is simply fixed at 0° which simplifies Eq. (6.2) to

$$\mathcal{N}_{\mathrm{Er}}(a_s, 0^\circ) = \frac{14\left(45a_s^2 + 4a_d^2\right)}{252a_s^2 + 96a_s a_d + 16a_d^2}. \tag{6.3}$$

Notably at $\Theta = 0°$, the number for rethermalization is minimized at $a_d/a_s \approx 2.7$ with value $\mathcal{N}_{\mathrm{Er}} \approx 1.65$, indicating highly efficient collisional thermalization. This efficiency is directly attributed to the innate anisotropic differential cross section in dipolar bosons [35].

### 6.1.2 Scattering lengths galore!

Before taking cross-dimensional thermalization measurements for $^{166}$Er, a high resolution scan of the atom number as a function of the magnetic field is performed in order to record the dense spectrum of Fano-Feshbach resonances [137, 138]. The Fano-Feshbach spectra is tabulated in Tabs. 6.1 and 6.2, with $\boldsymbol{\mathcal{B}}$ oriented along $z$, and taking values from $\mathcal{B} = 0$ G to 5 G (see Fig. 6.1).

Table 6.1: Fano-Feshbach resonance positions and widths included into the fit of Eq. (6.5) to $a_s$ for $^{164}$Er (left) and $^{166}$Er (right). The error denotes the fit error of one standard deviation. Values without error are fixed in the fitting procedure.

| Position $\mathcal{B}_i$ (G) | Width $\Delta\mathcal{B}_i$ (G) |
|---|---|
| 1.52 | 0.22(3) |
| 2.67 | 0.005 |
| 2.83 | 0.005 |
| 3.26 | 0.10(3) |

| Position $\mathcal{B}_i$ (G) | Width $\Delta\mathcal{B}_i$ (G) |
|---|---|
| 0.02(5) | 0.05(2) |
| 3.04(5) | 0.15(2) |
| 4.208 | 0.01 |
| 4.96 | 0.005 |

Table 6.2: Fano-Feshbach resonance positions and widths included into the fit of Eq. (6.5) to $a_s$ for $^{168}$Er (left) and $^{170}$Er (right). The error denotes the fit error of one standard deviation. Values without error are fixed in the fitting procedure.

| Position $\mathcal{B}_i$ (G) | Width $\Delta\mathcal{B}_i$ (G) |
|---|---|
| 0.49 | 0.005 |
| 0.911(6) | 0.032(2) |
| 1.51 | 0.01 |
| 2.174(4) | 0.038(2) |
| 2.471(9) | 0.19(1) |
| 2.86 | 0.005 |
| 3.79 | 0.006(5) |
| 4.23 | 0.005 |
| 4.5 | 0.005 |

| Position $\mathcal{B}_i$ (G) | Width $\Delta\mathcal{B}_i$ (G) |
|---|---|
| 0.35 | 0.005 |
| 0.86 | 0.028(12) |
| 1.12 | 0.005 |
| 1.62 | 0.01 |
| 2.17 | 0.067(7) |
| 2.74 | 0.134(9) |
| 3.3 | 0.01(1) |
| 3.57 | 0.01 |
| 4.38 | 0.005 |
| 4.49 | 0.01 |
| 6.91 | 0.8(7) |

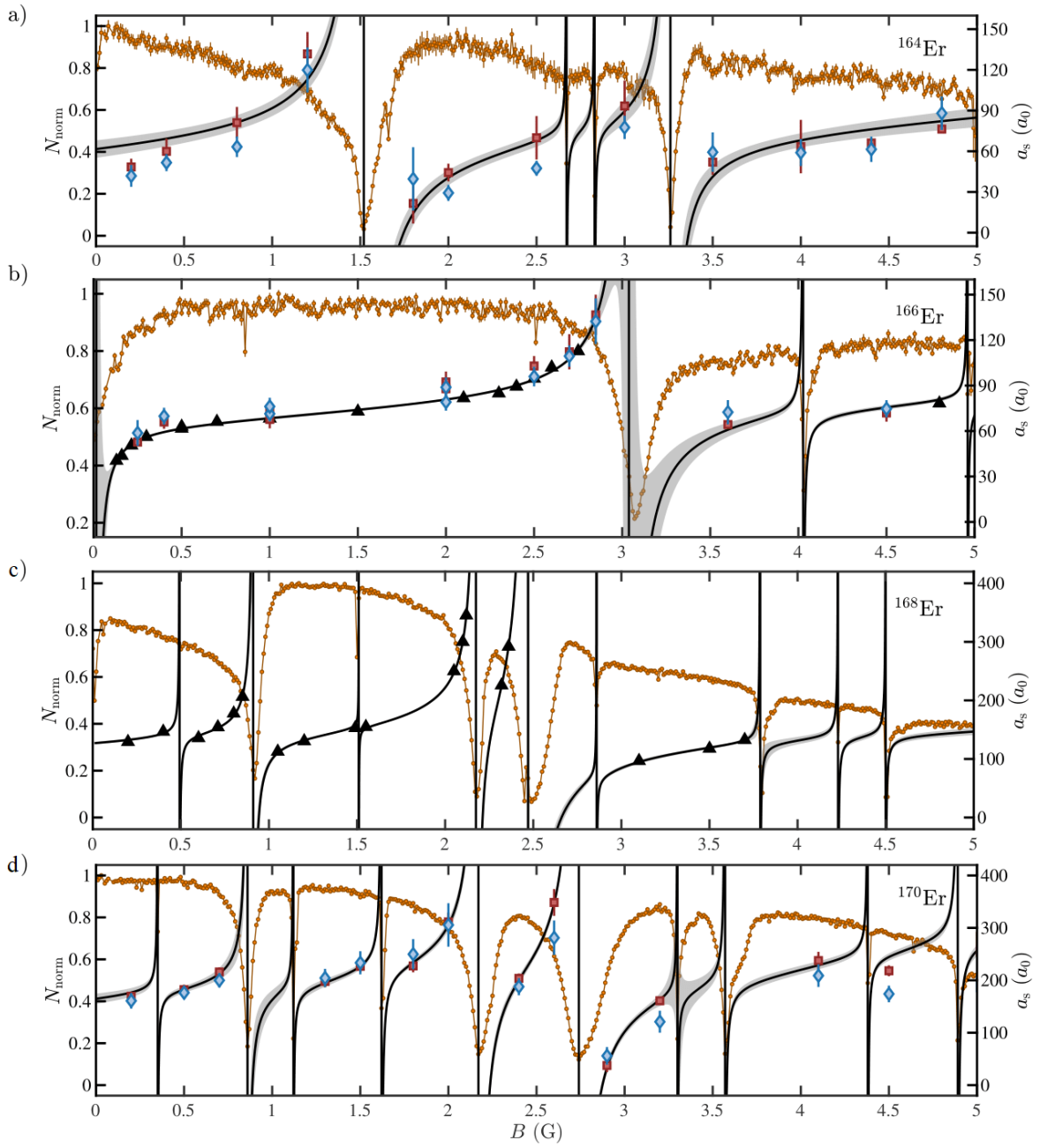


Figure 6.1: Atom-loss spectroscopy (orange circles) as a function of $\mathcal{B}$ for a fixed hold time of 250 ms. For each value of $\mathcal{B}$, each data point is an average of 3 repetitions and normalized to the maximum averaged atom number recorded. The values of $a_s$ are those extracted from cross-dimensional thermalization measurements using both, the Enskog equations (red squares) and the analytic formula of Eq. (6.2) (blue diamonds), for $^{164}$Er (a), $^{166}$Er (b), $^{168}$Er (c) and $^{170}$Er (d). The black triangles are $a_s$ values obtained from lattice modulation spectroscopy measurements (see Ref. [2]). The solid black lines represent a fit of Eq. (6.5) to $a_s$. Error bars and the shaded area of the fitting results denote the standard error. The figure is adapted from Ref. [2].

Thermalization measurements are then performed at values of $\mathcal{B}$ where the system is not dominated by resonant atom loss. For each thermalization curve, we extract $a_s$ using two different approaches, one numerical and one semi-analytical. The first, constitutes a direct fit of the full Enskog solutions to the experimental data, leaving $a_s$ as a float parameter of the theory. That is, we numerically evolve Eq. 3.8 for various values of $a_s$ until the one that minimizes

$$\min_{\boldsymbol{\omega},a_s} \sum_{t=t_0}^{t_{\text{end}}} \left( \frac{T(t) - \mathcal{T}_{\text{E}}\left[T(0); a_s\right](t)}{\delta T(t)} \right)^2, \tag{6.4}$$

is obtained, where the sum runs over measurement time instances $t$, $T(t)$ is the temperature data from the experiment, $\delta T(t)$ is the temperature measurement uncertainty, and $\mathcal{T}_{\text{E}}\left[T(0); a_s\right]$ is the solution to the Enskog equations with initial condition $T(0)$.

The second method is based on the exponential decay rate $\gamma$ from Eq. (4.2), using the analytic expression for $\mathcal{N}_{\text{Er}}(a_s, 0°)$ in Eq. (6.3). Since $a_s$ is a priori unknown, we use an iterative approach to determine $\mathcal{N}_{\text{Er}}(a_s, 0°)$ starting from the Gribakin-Flambaum mean scattering length value of Eq. (2.27), $\overline{a}_s \approx 100 a_0$. We use the calculated $a_s$ and the analytic formula (6.3) to obtain a new value for $\mathcal{N}_{\text{Er}}(a_s, 0°)$. We stop the iteration once the relative change of $\mathcal{N}_{\text{Er}}(a_s, 0°)$ is $\leq 10^{-7}$. Fig. 6.1 summarizes $a_s$ for $^{164}$Er (subplot a), $^{166}$Er (subplot b), $^{168}$Er (subplot c) and $^{170}$Er (subplot d) in the region from 0 G to 5 G. The values of $a_s$ extracted from both the Enskog model and the analytic formulas are in very good agreement with one another, reflecting the strength of the analytic formula of Eq. (6.3). A triumph for theory!

As an added assurance, lattice modulation spectroscopy was also performed to extract $a_s$ for the $^{166}$Er and $^{168}$Er isotopes [139–141] (see the black triangles in subplots b and c of Fig. 6.1). This technique is rather involved but gives highly accurate measurements, serving as a useful benchmark for the thermalization methods of focus here.

### 6.1.3 Mass scaling of the background scattering length

More broadly, the global behavior of $a_s$ with $\mathcal{B}$ can be described by generalizing the well-known formula in Ref. [142], to

$$a_{\mathrm{s}}(\mathcal{B}) = \left(a_{\mathrm{s}}^{\mathrm{bg}} + s\mathcal{B}\right) \prod_{i=1}^{N_{\mathrm{res}}} \left(1 - \frac{\Delta\mathcal{B}_i}{\mathcal{B} - \mathcal{B}_i}\right), \tag{6.5}$$

allowing for $N_{\mathrm{res}}$ overlapping resonances at positions $\mathcal{B}_i$ with widths $\Delta\mathcal{B}_i$. Fitting Eq. (6.5) to the thermalization measured values of $a_s$ (see the solid lines in Fig. 6.1) then allows us to map out its complete functional dependence on $\mathcal{B}$, for all 4 bosonic isotopes $^{164}$Er, $^{166}$Er, $^{168}$Er, and $^{170}$Er. Knowledge of $a_s$ as a function of the magnetic field then allows us to extract an effective background scattering length $a_{\mathrm{s}}^{\mathrm{bg}}$ for each isotope. Various mechanisms could lead to an off-resonant variation of $a_s$, such as broad Fano-Feshbach resonances not within the measurement range [143] or dipole couplings to higher Zeeman sublevels [144]. We thus allow for a smooth off-resonant variation of $a_s$ with $\mathcal{B}$, by including a linear slope parameter $s$ in Eq. (6.5) that already reproduces the data well. The zero field value of $a_{\mathrm{s}}(0)$ is then identified as the effective background scattering length.

Fig. 6.2 shows the value of $a_s^{\mathrm{bg}}$ from the fit as a function of the isotope mass. We observe a monotonic rise of $a_s^{\mathrm{bg}}$ with increasing $m$, compatible with a variety of functional forms. For convenience, we pick the one consistent with ytterbium and cesium [39, 145, 146], which assumes only a Van der Waals potential $V_6(r) = -C_6/r^6$, with $C_6$ being the Van der Waals coefficient. This might not be a great approximation for magnetic erbium, but in the absence of alternative models, this will have to do for the time being.

Starting from Eq. (2.27), we write $a_s$ as

$$a_s = \bar{a}\left[1 - \tan\left(\phi_s - \frac{\pi}{8}\right)\right], \tag{6.6a}$$

$$\phi_s = \frac{\sqrt{m}}{\hbar}\int_{R_0}^{\infty} dr\sqrt{-V_{\mathrm{int}}(r)}, \tag{6.6b}$$

with the classical turning points of $V_{\mathrm{int}}(r)$ denoted as $R_0$. Although the exact shape of $V_{\mathrm{int}}(r)$ is unknown, Eq. (6.6a) can be employed to extract a mass-scaling due to the dependence of $\phi_s \propto \sqrt{m}$ [145]. Such a scaling is valid, as long as the mass-dependent modification of $V_{\mathrm{int}}(r)$ is negligible.

Furthermore, $\phi_s$ allows for the calculation of the number of bound states $N_\mathrm{B}$, via Levinson's theorem $N_\mathrm{B} = \lfloor \phi_s/\pi - 5/8 \rfloor$ [147], where $\lfloor \ldots \rfloor$ denotes the integer floor function. Applied to our case of erbium, we fit Eq. (6.6a) to the experimental data and obtain Fig. 6.2. The optimal fit gives $\phi_s/\pi = 144(1)$, implying $N_\mathrm{B} = 143(1)$ boundstates for $^{168}$Er, a factor of 2 larger than ytterbium despite their similar $C_6$ coefficients [145].

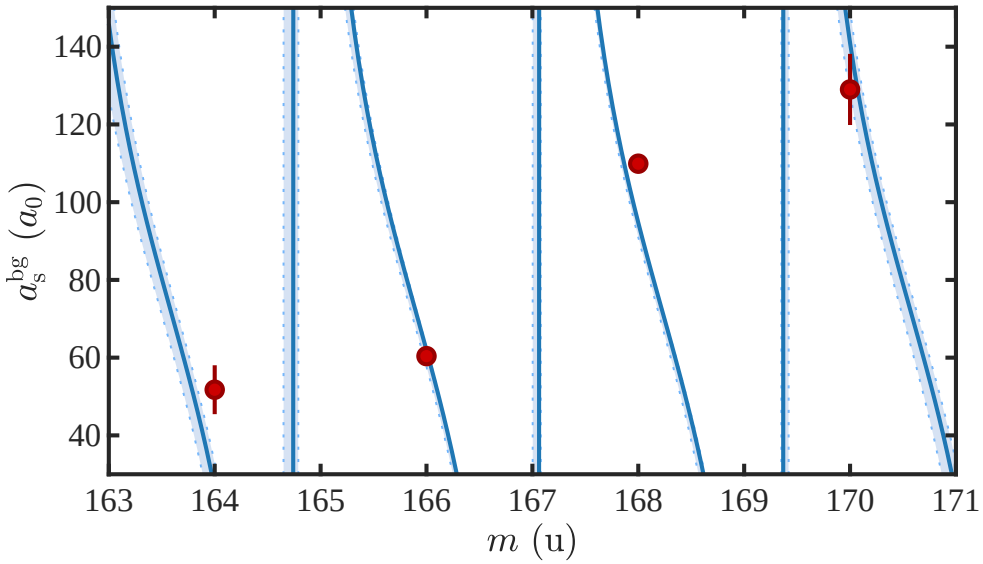


Figure 6.2: Background scattering length $a_s^{\mathrm{bg}}$ for four bosonic isotopes (red circles). The solid line represents the best fit with $\phi_s/\pi = 144(1)$; see text. The shaded area, enclosed by the dotted lines, represents the fitting function for $\phi_s = 143$ and $\phi_s = 145$. The errorbars denote the standard error of the fit of Eq. (6.5) to the experimental data.

## 6.2 MPQ: The road to deeper Fermi degeneracy with molecules

If you've ever left the lid off your morning cup of coffee, you would have likely found it already cooled off by the time you're done checking your emails. This disappointment is driven by a process known as evaporative cooling, where the hot water molecules are free to evaporate away, transporting thermal energy to the surrounding room temperature air. The remaining coffee then quickly thermalizes its now less energetic distribution, leaving behind a sad lukewarm beverage but a spanking new thermoflask in your Amazon cart.

In very much the same way, this continuous cycle of evaporation and rethermalization is what enabled the 2001 Nobel laureates to achieve Bose-Einstein condensates of atoms [7, 8]. More recently, the advent of collision shielding (see Sec. 2.2) has also allowed diatomic molecules to see the likes of Bose-Einstein condensation [54] and Fermi degeneracy [4, 44], ushering us into a new age of molecular quantum gases. Toward explorations of many-body quantum physics with deeply degenerate molecular fermions, I have been collaborating with the group at the *Max-Planck-Institut für Quantenoptik* (MPQ), in the hopes of reaching $T/T_F < 0.1$. However, evaporating these molecular fermions to such low temperatures is problematic for several reasons: 1) Fermi statistics become significant at low temperatures, Pauli-blocking elastic collisions from thermalizing the sample during evaporation, while 2) 2-body losses continue to occur even with microwave shielding applied, which are not Pauli-blocked. Nevertheless, we would still like to optimize the evaporative cooling procedure as much as possible, which would minimally provide us with an extremely low temperature sample to then commence further cooling protocols down to $T/T_F < 0.1$.

### 6.2.1 Let it flow, let it flow!

The harmonic approximation of Eq. (3.2) is only valid in deep optical dipole traps, where laser powers are large enough to keep most of the molecules close to the trap's energetic minimum. In actuality, optical dipole traps have a Gaussian shape due to the profile of the laser beams, just like what you see in Fig. 6.3. In the figure, I've plotted a realistic model of the optical dipole trap (see App. B) along the $y = 0$ plane, utilizing the laser parameters in Tab. 6.3. These parameters are adopted as the starting point for all evaporation experiments in our current investigations.

This finite energetic height of the trap, controllable by varying the laser beam power, is exactly how hot molecules are forced to evaporate out of the trap. In the process of doing so however, a significant fraction of molecules will now see a large region of this potential energy landscape, rendering the anharmonicities of this potential, especially the sag along $z$ due to gravity, highly relevant to the evaporation experiments of interest here. A faithful representation of the trap should therefore be adopted for accurate evaporation simulations, which is exactly what we employ.

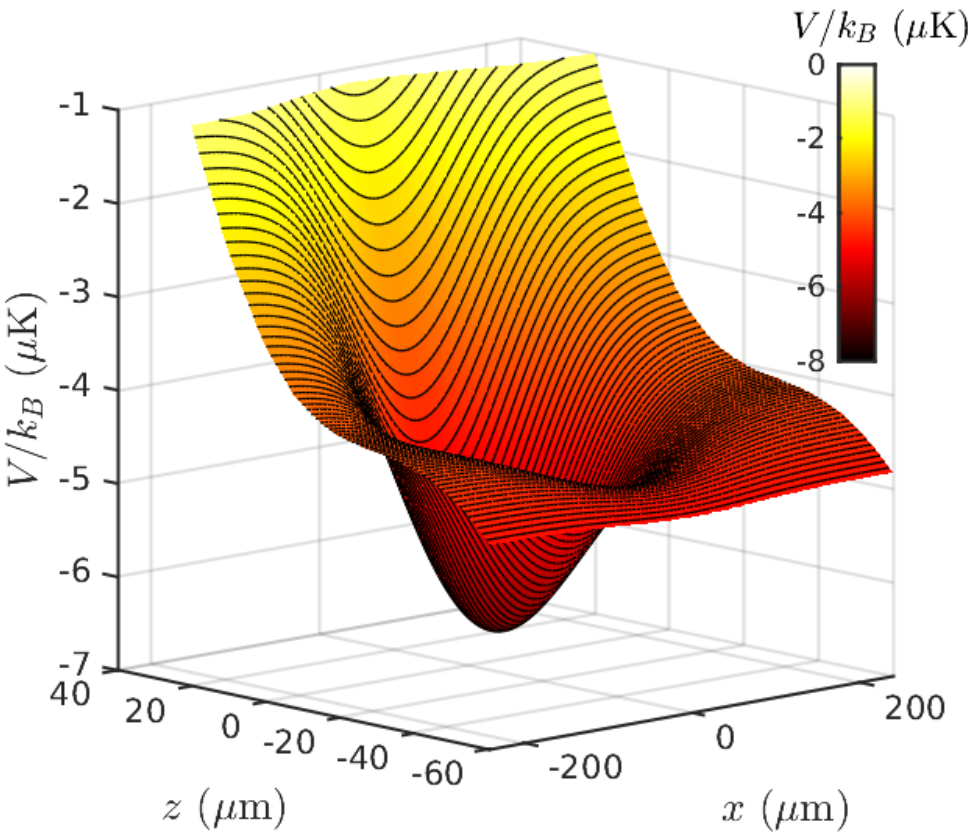


Figure 6.3: The optical trap potential energy surface $V(\boldsymbol{r})$, plotted as a function of coordinates $x$ and $z$, along $y = 0$.

Table 6.3: Table of parameter values for the potential confining a gas of fermionic $^{23}$Na$^{40}$K molecules. $h$ denotes Planck's constant.

| Parameter | Symbol | Value | Unit |
|---|---|---|---|
| Beam 1 vertical width | $W_{1,z}$ | 57.5 | $\mu$m |
| Beam 1 horizontal width | $W_{1,\perp}$ | 113 | $\mu$m |
| Beam 1 wavelength | $\lambda_1$ | 1064 | nm |
| Beam 1 power | $P_1$ | 0.242 | W |
| Polarizability in beam 1 | $\alpha_1$ | $2.79 \times 10^{-3} h$ | m$^2$Hz/W |
| Beam 2 vertical width | $W_{1,z}$ | 45 | $\mu$m |
| Beam 2 horizontal width | $W_{1,\perp}$ | 156 | $\mu$m |
| Beam 2 wavelength | $\lambda_2$ | 1064 | nm |
| Beam 2 power | $P_2$ | 0.253 | W |
| Polarizability in beam 2 | $\alpha_2$ | $2.79 \times 10^{-3} h$ | m$^2$J/W |

To effectively simulate the evaporation of molecules out of the trap, I have opted to use a position space cutoff scheme. That is, a molecule is taken as evaporated if it falls past the outer

turning point along $z$, or goes past a position that is 6 times the thermal width of the initial cloud from the trap minimum:

$$|r_i - r_{i,\min}| > 6\sqrt{\frac{k_B T_0}{m\omega_i^2(0)}}, \tag{6.7a}$$

$$\text{and} \quad z < z_{\max}, \tag{6.7b}$$

where $T_0$ is the initial equilibrium temperature, $r_{i,\min}$ is the position of the trap minimum along axis $i$ and $z_{\max} < 0$ is the trap local maxima along $z$. The criteria above allow us to account for the anisotropic molecular loss in space, resulting from the gravitational trap sag. Furthermore, the Gaussian trap profiles in the transverse directions imply that if molecules are too far away from the trap minima, they will no longer experience a large enough restorative potential, nor collisions, to return toward the trap center and are thus effectively evaporated.

Following the experiment, evaporation is forced by gradually reducing the trapping laser power, in turn lowering the trap depth and promoting the loss of hot molecules. During this process, the trap powers follow an exponential time-dependence

$$P_i(t) = P_i(0) - \Delta P_i \left( \frac{1 - e^{-2t/\tau}}{1 - e^{-2}} \right), \tag{6.8}$$

where $\Delta P_i$ is the change in laser power along axis $i$, and $\tau$ is the forced evaporation time. During this ramp, the efficiency of evaporation $\mathcal{E}_{\text{evap}}$, is measured by the slope of log phase space density (PSD) vs the log number decrease [148]:

$$\mathcal{E}_{\text{evap}} = -\frac{\partial \log_{10} \rho_{\text{PSD}}}{\partial \log_{10} N}, \tag{6.9}$$

where PSD is defined as

$$\rho_{\text{PSD}} = \langle n \rangle \lambda_{\text{th}}^3, \tag{6.10}$$

comparing the ensemble averaged number density $\langle n \rangle$ against the cubed thermal de Broglie wavelength $\lambda_{\text{th}} = h/\sqrt{2\pi m k_B T}$. In practice, $\mathcal{E}_{\text{evap}}$ is extracted from a linear fit to the evaporation trajectory data. The PSD is extracted from temperature measurements of the simulation ensemble

through the relation

$$\mathrm{Li}_3\left(\frac{\rho_{\mathrm{PSD}}}{\rho_{\mathrm{PSD}}-1}\right)=-\frac{1}{6}\left(\frac{T}{T_F}\right)^{-3}, \tag{6.11}$$

where $T_F=\hbar\overline{\omega}(6N)^{1/3}/k_B$ is the Fermi temperature confined with geometric mean trapping frequencies $\overline{\omega}$ [149] and $\mathrm{Li}_3(z)$ is the trilogarithmic function.

I'll point out that although $\mathcal{E}_{\mathrm{evap}}$ provides a useful guide for experiments, it does not guarantee to achieve the highest phase space density amongst other schemes with possibly lower predicted efficiencies. For instance, a rapid decrease in the trap depth would still allow favorable evacuation of hot molecules and a seemingly efficient decrease in total energy. Unfortunately, the subsequent sample would have had no time to thermalize during the fast quench, disallowing the thermal tails of the distribution from being re-populated for further evaporative cooling beyond the initial evacuation. It is therefore useful to also track the final $T/T_F$ and $\rho_{\mathrm{PSD}}$ achieved, toward the goal of deeply degenerate Fermi gases.

### 6.2.2 In-simulation thermometry

As the gas enters into deeper quantum degeneracy from evaporation, Fermi statistics become significant. Consequently, Pauli blocking $-h^3f$ factors in the collision integral (3.3) become significant at PSD of order $\rho_{\mathrm{PSD}}\gtrsim 0.1$, requiring its inclusion in the simulation which shifts the equilibrium distribution from Maxwell-Boltzmann to Fermi-Dirac, illustrated in Fig. 6.4 (description in caption). So to accurately extract the values of $T$, we utilize a Fermi-Dirac fit to the $y$-integrated simulation ensemble, likened to the optical density (OD) from absorption imaging of the molecular cloud [4, 150, 151]:

$$\mathrm{OD}(x,z)=\frac{\mathrm{OD}_{\mathrm{max}}}{\mathrm{Li}_2\left(-\zeta\right)}\mathrm{Li}_2\left(-\zeta e^{-\frac{x^2}{2\sigma_x^2}-\frac{z^2}{2\sigma_z^2}}\right). \tag{6.12}$$

Above, $\mathrm{OD}_{\mathrm{max}}$ is the peak optical depth, $\sigma_i$ are the distribution widths, $\zeta$ is the fugacity and $\mathrm{Li}_2(z)$ is the dilogarithmic function. In time-of-flight imaging, the distribution widths will evolve in time

for every time-of-flight instance as

$$\sigma_i = \sqrt{1+\omega_i^2 t_{\mathrm{TOF}}^2}\sqrt{\frac{k_B T_i}{m\omega_i^2}}, \tag{6.13}$$

over the time interval $t_{\mathrm{TOF}}$. In the long time limit, this time-dependence changes the density images from position to momentum space distributions, since $r_i \to v_i t_{\mathrm{TOF}}$ and $\sigma_i \to t_{\mathrm{TOF}}\sqrt{k_B T/m}$, rendering

$$\begin{aligned} \mathrm{OD}(x,z)|_{t_{\mathrm{TOF}}\to\infty} &= \mathrm{OD}(v_x, v_z) \\ &= \frac{\mathrm{OD}_{\max}}{\mathrm{Li}_2(-\zeta)}\mathrm{Li}_2\left(-\zeta e^{-\frac{m(v_x^2+v_z^2)}{2k_B T}}\right), \end{aligned} \tag{6.14}$$

where $v_i$ is the molecular velocity along axis $i$.

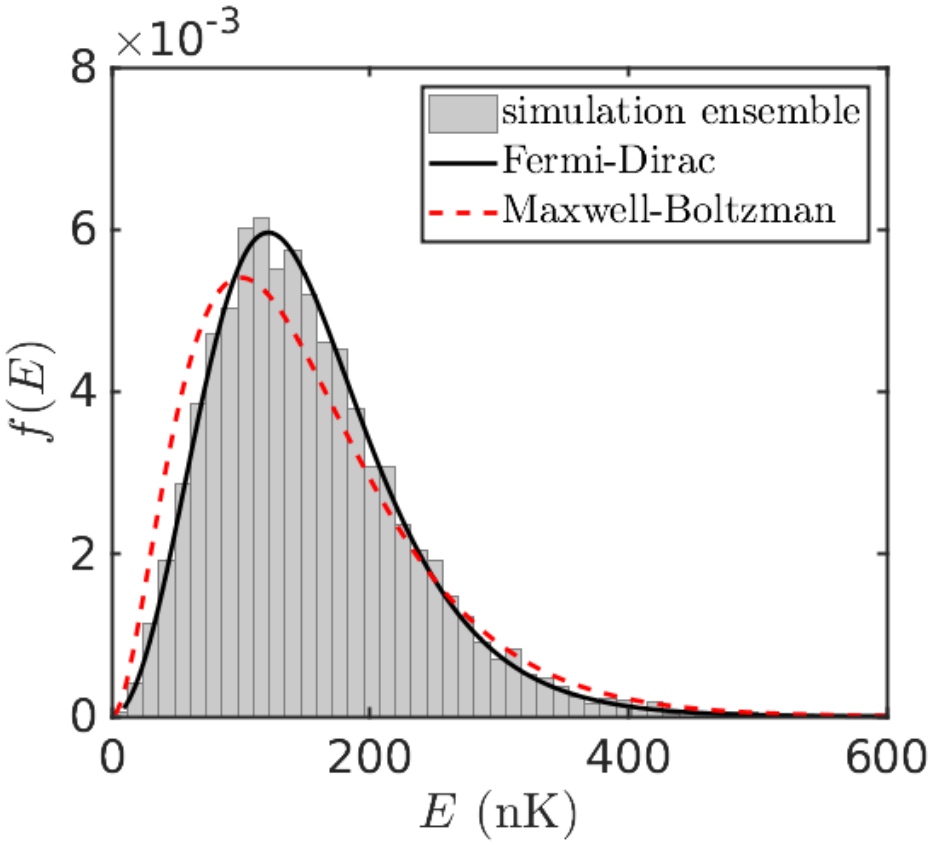


Figure 6.4: Simulation ensemble energy distribution with $N = 10,000$ molecules (gray histogram), after collisional thermalization for $t = 0.5$ s from an initial Maxwell-Boltzmann distribution at 50 nK (dotted red curve). The simulation achieves a Fermi-Dirac distribution (solid black curve) at $T \approx 42$ nK with a chemical potential of $\mu/k_B \approx 87$ nK.

Leaving $T$ and $\zeta$ as float parameters, $\mathrm{OD}(v_x, v_z)$ is then fitted to the simulation distribution, obtained by constructing an appropriately normalized 2D histogram from the simulated particle ensemble, projected into the $x, z$ plane. In practice, obtaining the fugacity by fitting to the shape of the distribution results in large errors with noisy data. So we opt to utilize the relation

$$\mathrm{Li}_3(-\zeta) = -\frac{1}{6}\left(\frac{T}{T_F}\right)^{-3}, \tag{6.15}$$

to infer the fugacity, floating only $T$. If $T > T_F$, we simply revert to assuming a Boltzmann distributed gas, with temperature related to the mean-squared momenta $T = \langle \boldsymbol{p}^2 \rangle / (3mk_B)$.

### 6.2.3 Numerical results and prospects

Implementing the components for forced evaporation above into my DSMC solver (see Sec. 3.3), I was able to reproduce the trends in evaporative cooling observed in the experiment at MPQ [4]. In that study, the final trap depth was varied over several experimental instances with forced evaporation occurring over 150 ms, resulting in various molecule numbers and gas temperatures attained at the end of each evaporation trajectory [1] . Fig. 6.5 showcases the favorable agreement of our numerically simulated data points (red crosses) with the experimental measurements (black circles with error bars), except for disagreement at low molecule numbers attributed to experimental trap jitter at low laser powers.

With the DSMC solver benchmarked against experimental data, we are now assured that further explorations with it will be informative of actual experimental observation. Moreover, the versatility of our solver makes incorporating other relevant aspects such as accurate 2-body loss rates or energy dependent elastic cross sections a simple modification. However, since utilizing this tool for attaining $T/T_F < 0.1$ is still an ongoing pursuit, I will leave all further details to upcoming works that will soon be published.

[1] Reported to commence in an excited sloshing mode of the molecular distribution, our simulated evaporation accounts for resultant heating by simply using a constant 2-body loss rate of $\beta_L = 10^{-12}$ cm$^3$/s, and adds an estimated $h = 100$ nK/s background heating rate. Background heating was included with momentum kicks during our simulated time evolution, taking the momentum of particle $k$, and increasing it by $\boldsymbol{p}_k \to \boldsymbol{p}_k \left(1 + 2p_k^{-2} mk_B h \Delta t\right)$, after the second Verlet integration step of Eq. (3.30) in Sec. 3.3.1.

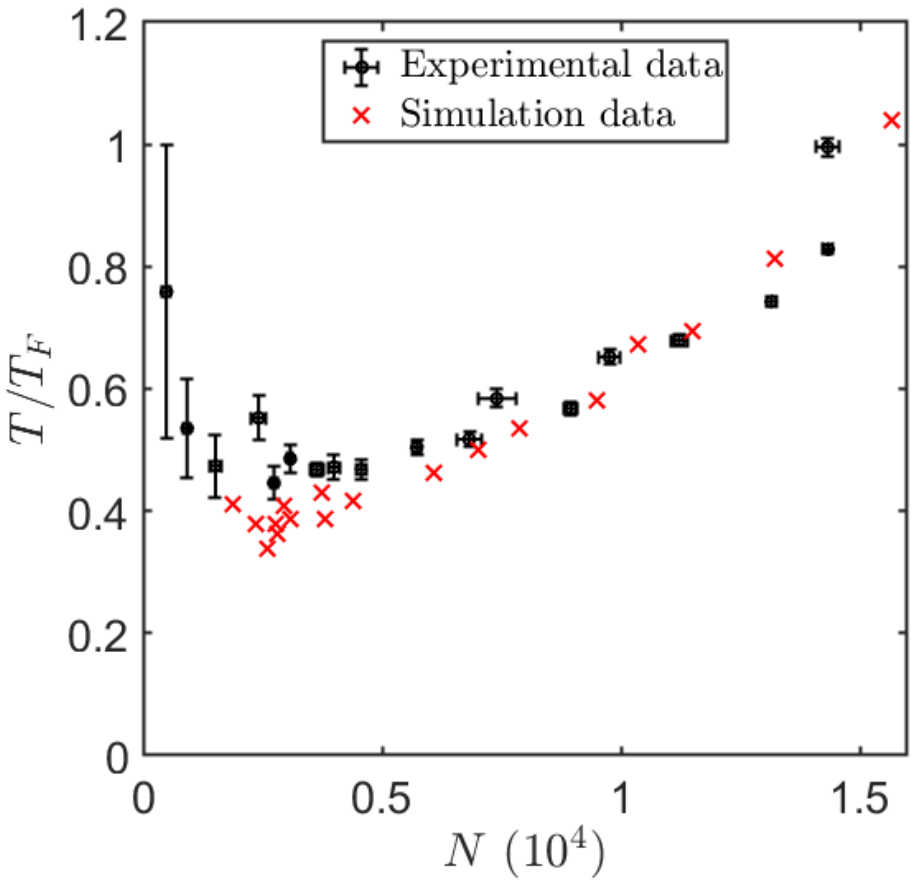


Figure 6.5: Plot of $T/T_F$ values after evaporating down to $N$ molecules in the experiment at the Max-Planck-Institut für Quantenoptik [4] (black circles with error bars) with different final trap depths, compared to those obtained from our numerical simulations (red crosses).

## 6.3 Curtain call

Before I let the credits roll (i.e. the bibliography section), I want to quickly recount several key highlights of this thesis to cap it all off.

Setting the foundation for most of my work here was an understanding of ultracold dipolar collisions, provided in Chap. 2 for both magnetic atoms and field-shielded polar molecules. The anisotropy of dipole-dipole interactions gives rise not only to anisotropic 2-body differential scattering, but also manifests in the collective dynamics of a nondegenerate gas. When dilute, these gases thermalize at rates that are highly dependent on the direction of excitation, measurement, and dipole orientation (Chap. 3). This sensitivity to direction allowed experimentalists to observe

universal signatures of threshold dipolar scattering in potassium-rubidium molecules (Sec. 4.1.2), and accurately extract the $s$-wave scattering length in dipolar erbium atoms (Sec. 6.1). My first encounters with experimental collaboration.

As with the mentioned examples, a deeper understanding of dipolar collisional thermalization can better inform experimental applications such as evaporative cooling (Sec. 6.2), and unexplored phenomena like hydrodynamic excitations. So came my works in Chap. 5, exploring exactly these hydrodynamic gases that support a rich tapestry of fluid dynamics such as acoustics (Sec. 5.3), and weltering excitations (Sec. 5.4). The latter arises in harmonically trapped gases, where dipolar collisions serve, once more, to return the gas to equilibrium. The manner in which equilibration occurs, however, does not immediately follow from our intuition on dilute gases, so much so that I had to derive an entirely new set of equations to capture it. Although initiated here, more work is still required to fully grasp and characterize nonegenerate dipolar fluids in all their weltering intricacies (Sec. 5.4.1): the inklings of evermore pertinent questions, awaiting exciting new discoveries.

And with that, I'll declare this the end of my thesis and PhD journey.

"*Those were the days of our lives.*"

— Freddie Mercury (Innuendo), 1991.

## Bibliography


[1] JL Bohn, M Cavagnero, and C Ticknor. Quasi-universal dipolar scattering in cold and ultracold gases. New Journal of Physics, 11(5):055039, 2009. URL https://iopscience.iop.org/article/10.1088/1367-2630/11/5/055039/meta.

[2] A. Patscheider, L. Chomaz, G. Natale, D. Petter, M. J. Mark, S. Baier, B. Yang, R. R. W. Wang, J. L. Bohn, and F. Ferlaino. Determination of the scattering length of erbium atoms. Phys. Rev. A, 105:063307, Jun 2022. doi: 10.1103/PhysRevA.105.063307. URL https://link.aps.org/doi/10.1103/PhysRevA.105.063307.

[3] Jun-Ru Li, William G Tobias, Kyle Matsuda, Calder Miller, Giacomo Valtolina, Luigi De Marco, Reuben RW Wang, Lucas Lassablière, Goulven Quéméner, John L Bohn, et al. Tuning of dipolar interactions and evaporative cooling in a three-dimensional molecular quantum gas. Nature Physics, 17(10):1144–1148, 2021. URL https://www.nature.com/articles/s41567-021-01329-6.

[4] Andreas Schindewolf, Roman Bause, Xing-Yan Chen, Marcel Duda, Tijs Karman, Immanuel Bloch, and Xin-Yu Luo. Evaporation of microwave-shielded polar molecules to quantum degeneracy. Nature, 607(7920):677–681, Jul 2022. ISSN 1476-4687. doi: 10.1038/s41586-022-04900-0. URL https://doi.org/10.1038/s41586-022-04900-0.

[5] Max Planck. Ueber das gesetz der energieverteilung im normalspectrum. Annalen der Physik, 309(3):553–563, 1901. doi: https://doi.org/10.1002/andp.19013090310. URL https://onlinelibrary.wiley.com/doi/abs/10.1002/andp.19013090310.

[6] A. Einstein. Quantentheorie des einatomigen idealen Gases. Zweite Abhandlung, pages 245–257. John Wiley & Sons, Ltd, 2005. ISBN 9783527608959. doi: https://doi.org/10.1002/3527608958.ch28. URL https://onlinelibrary.wiley.com/doi/abs/10.1002/3527608958.ch28.

[7] Mike H Anderson, Jason R Ensher, Michael R Matthews, Carl E Wieman, and Eric A Cornell. Observation of bose-einstein condensation in a dilute atomic vapor. science, 269(5221):198–201, 1995. URL https://www.science.org/doi/abs/10.1126/science.269.5221.198?casa_token=6kNM-kP7EeoAAAAA:C9HWx7U4cPDkZVtgX8Wwu8RDcYrx0CDR-1klVcYvswcMWFU-GBhzctiVfGFMAsFiCSsPKGVn04se2Q.

[8] K. B. Davis, M. O. Mewes, M. R. Andrews, N. J. van Druten, D. S. Durfee, D. M. Kurn, and W. Ketterle. Bose-einstein condensation in a gas of sodium atoms. Phys. Rev. Lett., 75:3969–3973, Nov 1995. doi: 10.1103/PhysRevLett.75.3969. URL https://link.aps.org/doi/10.1103/PhysRevLett.75.3969.

[9] Immanuel Bloch, Jean Dalibard, and Wilhelm Zwerger. Many-body physics with ultracold gases. Rev. Mod. Phys., 80:885–964, Jul 2008. doi: 10.1103/RevModPhys.80.885. URL https://link.aps.org/doi/10.1103/RevModPhys.80.885.

[10] Andrew D. Ludlow, Martin M. Boyd, Jun Ye, E. Peik, and P. O. Schmidt. Optical atomic clocks. Rev. Mod. Phys., 87:637–701, Jun 2015. doi: 10.1103/RevModPhys.87.637. URL https://link.aps.org/doi/10.1103/RevModPhys.87.637.

[11] M. Saffman, T. G. Walker, and K. Mølmer. Quantum information with rydberg atoms. Rev. Mod. Phys., 82:2313–2363, Aug 2010. doi: 10.1103/RevModPhys.82.2313. URL https://link.aps.org/doi/10.1103/RevModPhys.82.2313.

[12] M. L. Wall, K. R. A. Hazzard, and A. M. Rey. Quantum Magnetism with Ultracold Molecules, chapter Chapter 1, pages 3–37. World Scientific, 2015. doi: 10.1142/9789814678704_0001. URL https://www.worldscientific.com/doi/abs/10.1142/9789814678704_0001.

[13] John L Bohn. Electric dipoles at ultralow temperatures. In Cold Molecules, pages 71–100. CRC Press, 2009. URL https://www.taylorfrancis.com/chapters/edit/10.1201/9781420059045-9/electric-dipoles-ultralow-temperatures-john-bohn.

[14] Reuben R. W. Wang, Andrew G. Sykes, and John L. Bohn. Linear response of a periodically driven thermal dipolar gas. Phys. Rev. A, 102:033336, Sep 2020. doi: 10.1103/PhysRevA.102.033336. URL https://link.aps.org/doi/10.1103/PhysRevA.102.033336.

[15] Reuben R. W. Wang and John L. Bohn. Anisotropic thermalization of dilute dipolar gases. Phys. Rev. A, 103:063320, Jun 2021. doi: 10.1103/PhysRevA.103.063320. URL https://link.aps.org/doi/10.1103/PhysRevA.103.063320.

[16] Reuben R. W. Wang and John L. Bohn. Thermal conductivity of an ultracold paramagnetic bose gas. Phys. Rev. A, 106:023319, Aug 2022. doi: 10.1103/PhysRevA.106.023319. URL https://link.aps.org/doi/10.1103/PhysRevA.106.023319.

[17] Reuben R. W. Wang and John L. Bohn. Thermoviscous hydrodynamics in nondegenerate dipolar bose gases. Phys. Rev. A, 106:053307, Nov 2022. doi: 10.1103/PhysRevA.106.053307. URL https://link.aps.org/doi/10.1103/PhysRevA.106.053307.

[18] Reuben R. W. Wang and John L. Bohn. Anisotropic acoustics in dipolar fermi gases. Phys. Rev. A, 107:033321, Mar 2023. doi: 10.1103/PhysRevA.107.033321. URL https://link.aps.org/doi/10.1103/PhysRevA.107.033321.

[19] Reuben R. W. Wang and John L. Bohn. Viscous dynamics of a quenched trapped dipolar fermi gas. Phys. Rev. A, 108:013322, Jul 2023. doi: 10.1103/PhysRevA.108.013322. URL https://link.aps.org/doi/10.1103/PhysRevA.108.013322.

[20] John L. Bohn and Reuben R. W. Wang. Probability distributions of atomic scattering lengths, 2023. URL https://arxiv.org/abs/2309.15236.

[21] Reuben R. W. Wang and John L. Bohn. Prospects for thermalization of microwave-shielded ultracold molecules, 2023. URL https://arxiv.org/abs/2310.17812.

[22] Axel Griesmaier, Jörg Werner, Sven Hensler, Jürgen Stuhler, and Tilman Pfau. Bose-einstein condensation of chromium. Phys. Rev. Lett., 94:160401, Apr 2005. doi: 10.1103/PhysRevLett.94.160401. URL https://link.aps.org/doi/10.1103/PhysRevLett.94.160401.

[23] Mingwu Lu, Nathaniel Q. Burdick, Seo Ho Youn, and Benjamin L. Lev. Strongly dipolar bose-einstein condensate of dysprosium. Phys. Rev. Lett., 107:190401, Oct 2011. doi: 10.1103/PhysRevLett.107.190401. URL https://link.aps.org/doi/10.1103/PhysRevLett.107.190401.

[24] K. Aikawa, A. Frisch, M. Mark, S. Baier, A. Rietzler, R. Grimm, and F. Ferlaino. Bose-einstein condensation of erbium. Phys. Rev. Lett., 108:210401, May 2012. doi: 10.1103/PhysRevLett.108.210401. URL https://link.aps.org/doi/10.1103/PhysRevLett.108.210401.

[25] A. Trautmann, P. Ilzhöfer, G. Durastante, C. Politi, M. Sohmen, M. J. Mark, and F. Ferlaino. Dipolar quantum mixtures of erbium and dysprosium atoms. Phys. Rev. Lett., 121:213601, Nov 2018. doi: 10.1103/PhysRevLett.121.213601. URL https://link.aps.org/doi/10.1103/PhysRevLett.121.213601.

[26] Yuki Miyazawa, Ryotaro Inoue, Hiroki Matsui, Gyohei Nomura, and Mikio Kozuma. Bose-einstein condensation of europium. Phys. Rev. Lett., 129:223401, Nov 2022. doi: 10.1103/PhysRevLett.129.223401. URL https://link.aps.org/doi/10.1103/PhysRevLett.129.223401.

[27] T Lahaye, C Menotti, L Santos, M Lewenstein, and T Pfau. The physics of dipolar bosonic quantum gases. Reports on Progress in Physics, 72(12):126401, nov 2009. doi: 10.1088/0034-4885/72/12/126401. URL https://dx.doi.org/10.1088/0034-4885/72/12/126401.

[28] Lauriane Chomaz, Igor Ferrier-Barbut, Francesca Ferlaino, Bruno Laburthe-Tolra, Benjamin L Lev, and Tilman Pfau. Dipolar physics: a review of experiments with magnetic quantum gases. Reports on Progress in Physics, 86(2):026401, dec 2022. doi: 10.1088/1361-6633/aca814. URL https://dx.doi.org/10.1088/1361-6633/aca814.

[29] J. G. Conway and B. G. Wybourne. Low-lying energy levels of lanthanide atoms and intermediate coupling. Phys. Rev., 130:2325–2332, Jun 1963. doi: 10.1103/PhysRev.130.2325. URL https://link.aps.org/doi/10.1103/PhysRev.130.2325.

[30] S. Baier. Ultracold dipolar erbium atoms : from scattering phenomena to quantum simulations. PhD thesis, University of Innsbruck, 2018. URL http://inis.iaea.org/search/search.aspx?orig_q=RN:51085169. Bibliographic information available from INIS: http://inis.iaea.org/search/search.aspx?orig_q=RN:51085169; Available from Library of the University of Innsbruck, Innrain 50, 6020 Innsbruck, Austria and available from https://permalink.obvsg.at/AC15226424.

[31] HR Sadeghpour, JL Bohn, MJ Cavagnero, BD Esry, II Fabrikant, JH Macek, and ARP Rau. Collisions near threshold in atomic and molecular physics. Journal of Physics B: Atomic, Molecular and Optical Physics, 33(5):R93, 2000. URL https://iopscience.iop.org/article/10.1088/0953-4075/33/5/201/meta.

[32] Vladimir Roudnev and Michael Cavagnero. Universal resonant ultracold molecular scattering. Phys. Rev. A, 79:014701, Jan 2009. doi: 10.1103/PhysRevA.79.014701. URL https://link.aps.org/doi/10.1103/PhysRevA.79.014701.

[33] V Roudnev and M Cavagnero. Resonance phenomena in ultracold dipole–dipole scattering. Journal of Physics B: Atomic, Molecular and Optical Physics, 42(4):044017, feb 2009. doi: 10.1088/0953-4075/42/4/044017. URL https://dx.doi.org/10.1088/0953-4075/42/4/044017.

[34] Olivier Dulieu and Andreas Osterwalder. Cold Chemistry: Molecular Scattering and Reactivity Near Absolute Zero. The Royal Society of Chemistry, 12 2017. ISBN 978-1-78262-597-1. doi: 10.1039/9781782626800. URL https://doi.org/10.1039/9781782626800.

[35] John L. Bohn and Deborah S. Jin. Differential scattering and rethermalization in ultracold dipolar gases. Phys. Rev. A, 89:022702, Feb 2014. doi: 10.1103/PhysRevA.89.022702. URL https://link.aps.org/doi/10.1103/PhysRevA.89.022702.

[36] J. J. Sakurai and Jim Napolitano. Modern Quantum Mechanics. Cambridge University Press, 3 edition, 2020. URL https://www.cambridge.org/highereducation/books/modern-quantum-mechanics/DF43277E8AEDF83CC12EA62887C277DC#overview.

[37] J. Burke Jr. Theoretical Investigation of Cold Alkali Atom. PhD thesis, University of Colorado Boulder, 1999. URL https://www.proquest.com/docview/304500195?pq-origsite=gscholar&fromopenview=true&sourcetype=Dissertations%20&%20Theses.

[38] Enrico Fermi. Sopra lo spostamento per pressione delle righe elevate delle serie spettrali. Il Nuovo Cimento (1924-1942), 11(3):157–166, Mar 1934. ISSN 1827-6121. doi: 10.1007/BF02959829. URL https://doi.org/10.1007/BF02959829.

[39] G. F. Gribakin and V. V. Flambaum. Calculation of the scattering length in atomic collisions using the semiclassical approximation. Phys. Rev. A, 48:546–553, Jul 1993. doi: 10.1103/PhysRevA.48.546. URL https://link.aps.org/doi/10.1103/PhysRevA.48.546.

[40] K-K Ni, S Ospelkaus, D Wang, G Quéméner, Brian Neyenhuis, MHG De Miranda, JL Bohn, Jun Ye, and DS Jin. Dipolar collisions of polar molecules in the quantum regime. Nature, 464(7293):1324–1328, 2010. URL https://www.nature.com/articles/nature08953.

[41] A. V. Gorshkov, P. Rabl, G. Pupillo, A. Micheli, P. Zoller, M. D. Lukin, and H. P. Büchler. Suppression of inelastic collisions between polar molecules with a repulsive shield. Phys. Rev. Lett., 101:073201, Aug 2008. doi: 10.1103/PhysRevLett.101.073201. URL https://link.aps.org/doi/10.1103/PhysRevLett.101.073201.

[42] Alexander V. Avdeenkov. Dipolar collisions of ultracold polar molecules in a microwave field. Phys. Rev. A, 86:022707, Aug 2012. doi: 10.1103/PhysRevA.86.022707. URL https://link.aps.org/doi/10.1103/PhysRevA.86.022707.

[43] Kyle Matsuda, Luigi De Marco, Jun-Ru Li, William G. Tobias, Giacomo Valtolina, Goulven Quéméner, and Jun Ye. Resonant collisional shielding of reactive molecules using electric fields. Science, 370(6522):1324–1327, 2020. doi: 10.1126/science.abe7370. URL https://www.science.org/doi/abs/10.1126/science.abe7370.

[44] Giacomo Valtolina, Kyle Matsuda, William G Tobias, Jun-Ru Li, Luigi De Marco, and Jun Ye. Dipolar evaporation of reactive molecules to below the fermi temperature. Nature, 588 (7837):239–243, 2020. URL https://www.nature.com/articles/s41586-020-2980-7.

[45] Bijit Mukherjee, Matthew D. Frye, C. Ruth Le Sueur, Michael R. Tarbutt, and Jeremy M. Hutson. Shielding collisions of ultracold caf molecules with static electric fields. Phys. Rev. Res., 5:033097, Aug 2023. doi: 10.1103/PhysRevResearch.5.033097. URL https://link.aps.org/doi/10.1103/PhysRevResearch.5.033097.

[46] Loïc Anderegg, Sean Burchesky, Yicheng Bao, Scarlett S. Yu, Tijs Karman, Eunmi Chae, Kang-Kuen Ni, Wolfgang Ketterle, and John M. Doyle. Observation of microwave shielding of ultracold molecules. Science, 373(6556):779–782, 2021. doi: 10.1126/science.abg9502. URL https://www.science.org/doi/abs/10.1126/science.abg9502.

[47] Niccolò Bigagli, Claire Warner, Weijun Yuan, Siwei Zhang, Ian Stevenson, Tijs Karman, and Sebastian Will. Collisionally stable gas of bosonic dipolar ground-state molecules. Nature Physics, 19(11):1579–1584, Nov 2023. ISSN 1745-2481. doi: 10.1038/s41567-023-02200-6. URL https://doi.org/10.1038/s41567-023-02200-6.

[48] Junyu Lin, Guanghua Chen, Mucan Jin, Zhaopeng Shi, Fulin Deng, Wenxian Zhang, Goulven Quéméner, Tao Shi, Su Yi, and Dajun Wang. Microwave shielding of bosonic narb molecules. Phys. Rev. X, 13:031032, Sep 2023. doi: 10.1103/PhysRevX.13.031032. URL https://link.aps.org/doi/10.1103/PhysRevX.13.031032.

[49] Lucas Lassablière and Goulven Quéméner. Model for two-body collisions between ultracold dipolar molecules around a förster resonance in an electric field. Phys. Rev. A, 106:033311, Sep 2022. doi: 10.1103/PhysRevA.106.033311. URL https://link.aps.org/doi/10.1103/PhysRevA.106.033311.

[50] Goulven Quéméner and John L. Bohn. Shielding $^2\Sigma$ ultracold dipolar molecular collisions with electric fields. Phys. Rev. A, 93:012704, Jan 2016. doi: 10.1103/PhysRevA.93.012704. URL https://link.aps.org/doi/10.1103/PhysRevA.93.012704.

[51] Maykel L. González-Martínez, John L. Bohn, and Goulven Quéméner. Adimensional theory of shielding in ultracold collisions of dipolar rotors. Phys. Rev. A, 96:032718, Sep 2017. doi: 10.1103/PhysRevA.96.032718. URL https://link.aps.org/doi/10.1103/PhysRevA.96.032718.

[52] Lucas Lassablière and Goulven Quéméner. Controlling the scattering length of ultracold dipolar molecules. Phys. Rev. Lett., 121:163402, Oct 2018. doi: 10.1103/PhysRevLett.121.163402. URL https://link.aps.org/doi/10.1103/PhysRevLett.121.163402.

[53] Tijs Karman and Jeremy M. Hutson. Microwave shielding of ultracold polar molecules. Phys. Rev. Lett., 121:163401, Oct 2018. doi: 10.1103/PhysRevLett.121.163401. URL https://link.aps.org/doi/10.1103/PhysRevLett.121.163401.

[54] Niccolò Bigagli, Weijun Yuan, Siwei Zhang, Boris Bulatovic, Tijs Karman, Ian Stevenson, and Sebastian Will. Observation of bose-einstein condensation of dipolar molecules, 2023. URL https://arxiv.org/abs/2312.10965.

[55] Fulin Deng, Xing-Yan Chen, Xin-Yu Luo, Wenxian Zhang, Su Yi, and Tao Shi. Effective potential and superfluidity of microwave-shielded polar molecules. Phys. Rev. Lett., 130: 183001, May 2023. doi: 10.1103/PhysRevLett.130.183001. URL https://link.aps.org/doi/10.1103/PhysRevLett.130.183001.

[56] AM Arthurs and Alexander Dalgarno. The theory of scattering by a rigid rotator. Proceedings of the Royal Society of London. Series A. Mathematical and Physical Sciences, 256(1287):540–551, 1960. URL https://royalsocietypublishing.org/doi/abs/10.1098/rspa.1960.0125.

[57] Gaoren Wang and Goulven Quéméner. Tuning ultracold collisions of excited rotational dipolar molecules. New Journal of Physics, 17(3):035015, 2015. URL https://iopscience.iop.org/article/10.1088/1367-2630/17/3/035015/meta.

[58] Zbigniew Idziaszek, Goulven Quéméner, John L. Bohn, and Paul S. Julienne. Simple quantum model of ultracold polar molecule collisions. Phys. Rev. A, 82:020703, Aug 2010. doi: 10.1103/PhysRevA.82.020703. URL https://link.aps.org/doi/10.1103/PhysRevA.82.020703.

[59] Tijs Karman. Resonances in non-universal dipolar collisions. The Journal of Physical Chemistry A, 127(9):2194–2211, 2023. doi: 10.1021/acs.jpca.3c00797. URL https://doi.org/10.1021/acs.jpca.3c00797. PMID: 36825902.

[60] B.R Johnson. The multichannel log-derivative method for scattering calculations. Journal of Computational Physics, 13(3):445–449, 1973. ISSN 0021-9991. doi: https://doi.org/10.1016/0021-9991(73)90049-1. URL https://www.sciencedirect.com/science/article/pii/0021999173900491.

[61] Carlo Cercignani. The Boltzmann Equation and Its Applications. Applied Mathematical Sciences. Springer, New York, NY, 1988. ISBN 9781461210399. doi: https://doi.org/10.1007/978-1-4612-1039-9. URL https://link.springer.com/book/10.1007/978-1-4612-1039-9.

[62] Frederick Reif. Fundamentals of statistical and thermal physics. Waveland Press, Long Grove, Illinois, 2009. URL https://www.waveland.com/browse.php?t=520.

[63] Kerson Huang. Statistical mechanics, john wily & sons. John Wiley & Sons, Inc New York, 1963. URL https://www.wiley.com/en-sg/Statistical+Mechanics,+2nd+Edition-p-9780471815181.

[64] Ludwig Boltzmann. Weitere Studien über das Wärmegleichgewicht unter Gasmolekülen. k. und k. Hof-und Staatsdr., 1872. URL https://search.worldcat.org/title/917676909.

[65] LW Nordhiem. On the kinetic method in the new statistics and application in the electron theory of conductivity. Proceedings of the Royal Society of London. Series A, Containing Papers of a Mathematical and Physical Character, 119(783):689–698, 1928. URL https://royalsocietypublishing.org/doi/abs/10.1098/rspa.1928.0126.

[66] E. A. Uehling and G. E. Uhlenbeck. Transport phenomena in einstein-bose and fermi-dirac gases. i. Phys. Rev., 43:552–561, Apr 1933. doi: 10.1103/PhysRev.43.552. URL https://link.aps.org/doi/10.1103/PhysRev.43.552.

[67] Aldo Bonasera, Francesca Gulminelli, and J Molitoris. The boltzmann equation at the borderline. a decade of monte carlo simulations of a quantum kinetic equation. Physics reports, 243(1-2):1–124, 1994. URL https://www.sciencedirect.com/science/article/pii/0370157394901082?casa_token=XpMJHZ7nEG4AAAAA:5CtGC7yWqlbAZoWhTy27zGzB71rydveqqLPrzeMHCJqKMLcX0Q64GXxlTFuk3dWGXSHE-KQk2A.

[68] Max Krook and Tai Tsun Wu. Exact solutions of the boltzmann equation. The Physics of Fluids, 20(10):1589–1595, 1977. URL https://aip.scitation.org/doi/abs/10.1063/1.861780.

[69] S. Chapman, T.G. Cowling, D. Burnett, and C. Cercignani. The Mathematical Theory of Non-uniform Gases: An Account of the Kinetic Theory of Viscosity, Thermal Conduction and Diffusion in Gases. Cambridge Mathematical Library. Cambridge University Press, 1990. ISBN 9780521408448. URL https://books.google.com/books?id=Cbp5JP2OTrwC.

[70] David Guéry-Odelin, Francesca Zambelli, Jean Dalibard, and Sandro Stringari. Collective oscillations of a classical gas confined in harmonic traps. Phys. Rev. A, 60:4851–4856, Dec 1999. doi: 10.1103/PhysRevA.60.4851. URL https://link.aps.org/doi/10.1103/PhysRevA.60.4851.

[71] V E Colussi, Cameron J E Straatsma, Dana Z Anderson, and M J Holland. Undamped nonequilibrium dynamics of a nondegenerate bose gas in a 3d isotropic trap. New Journal of Physics, 17(10):103029, oct 2015. doi: 10.1088/1367-2630/17/10/103029. URL https://dx.doi.org/10.1088/1367-2630/17/10/103029.

[72] Wolfram Research, Inc. Mathematica 12.0, 2022. URL https://www.wolfram.com.

[73] Daan Frenkel and Berend Smit. Understanding molecular simulation: from algorithms to applications, volume 1. Elsevier, 2001. URL https://www.sciencedirect.com/book/9780122673511/understanding-molecular-simulation.

[74] Ernst Hairer, Christian Lubich, and Gerhard Wanner. Geometric numerical integration illustrated by the störmer–verlet method. Acta Numerica, 12:399–450, 2003. doi: 10.1017/S0962492902000144. URL https://www.cambridge.org/core/journals/acta-numerica/article/abs/geometric-numerical-integration-illustrated-by-the-stormerverlet-method/E55395D5DD7A4E0526D10EA74DA6C46B.

[75] G. A. Bird. Direct simulation and the boltzmann equation. The Physics of Fluids, 13(11):2676, 1970. URL https://aip.scitation.org/doi/abs/10.1063/1.1692849.

[76] A. G. Sykes and J. L. Bohn. Nonequilibrium dynamics of an ultracold dipolar gas. Phys. Rev. A, 91:013625, Jan 2015. doi: 10.1103/PhysRevA.91.013625. URL https://link.aps.org/doi/10.1103/PhysRevA.91.013625.

[77] Wm Randolph Franklin and Varol Akman. Octree data structures and creation by stacking. In Computer-Generated Images, pages 176–185. Springer, 1985. URL https://link.springer.com/chapter/10.1007/978-4-431-68033-8_16.

[78] Olga Goulko, Frédéric Chevy, and Carlos Lobo. Boltzmann equation simulation for a trapped fermi gas of atoms. New Journal of Physics, 14(7):073036, 2012. URL https://iopscience.iop.org/article/10.1088/1367-2630/14/7/073036/meta.

[79] Thomas Lepers, Dany Davesne, Silvia Chiacchiera, and Michael Urban. Numerical solution of the boltzmann equation for the collective modes of trapped fermi gases. Phys. Rev. A, 82:023609, Aug 2010. doi: 10.1103/PhysRevA.82.023609. URL https://link.aps.org/doi/10.1103/PhysRevA.82.023609.

[80] Pierre-Alexandre Pantel, Dany Davesne, and Michael Urban. Numerical solution of the boltzmann equation for trapped fermi gases with in-medium effects. Phys. Rev. A, 91:013627, Jan 2015. doi: 10.1103/PhysRevA.91.013627. URL https://link.aps.org/doi/10.1103/PhysRevA.91.013627.

[81] P. Billingsley. Convergence of Probability Measures. Wiley Series in Probability and Statistics. Wiley, 2013. ISBN 9781118625965. URL https://www.wiley.com/en-us/Convergence+of+Probability+Measures%2C+2nd+Edition-p-9780471197454.

[82] Shai Ronen, Daniele C. E. Bortolotti, and John L. Bohn. Bogoliubov modes of a dipolar condensate in a cylindrical trap. Phys. Rev. A, 74:013623, Jul 2006. doi: 10.1103/PhysRevA.74.013623. URL https://link.aps.org/doi/10.1103/PhysRevA.74.013623.

[83] Eli J. Halperin, Shai Ronen, and J. L. Bohn. Frustration in a dipolar bose-einstein condensate introduced by an optical lattice. Phys. Rev. A, 107:L041301, Apr 2023. doi: 10.1103/PhysRevA.107.L041301. URL https://link.aps.org/doi/10.1103/PhysRevA.107.L041301.

[84] C. R. Monroe, E. A. Cornell, C. A. Sackett, C. J. Myatt, and C. E. Wieman. Measurement of cs-cs elastic scattering at t=30 $\mu$k. Phys. Rev. Lett., 70:414–417, Jan 1993. doi: 10.1103/PhysRevLett.70.414. URL https://link.aps.org/doi/10.1103/PhysRevLett.70.414.

[85] P. O. Schmidt, S. Hensler, J. Werner, A. Griesmaier, A. Görlitz, T. Pfau, and A. Simoni. Determination of the $s$-wave scattering length of chromium. Phys. Rev. Lett., 91:193201, Nov 2003. doi: 10.1103/PhysRevLett.91.193201. URL https://link.aps.org/doi/10.1103/PhysRevLett.91.193201.

[86] N. R. Newbury, C. J. Myatt, and C. E. Wieman. s-wave elastic collisions between cold ground-state $^{87}$Rb atoms. Phys. Rev. A, 51:R2680–R2683, Apr 1995. doi: 10.1103/PhysRevA.51.R2680. URL https://link.aps.org/doi/10.1103/PhysRevA.51.R2680.

[87] Yijun Tang, Andrew Sykes, Nathaniel Q. Burdick, John L. Bohn, and Benjamin L. Lev. $s$-wave scattering lengths of the strongly dipolar bosons $^{162}$Dy and $^{164}$Dy. Phys. Rev. A, 92:022703, Aug 2015. doi: 10.1103/PhysRevA.92.022703. URL https://link.aps.org/doi/10.1103/PhysRevA.92.022703.

[88] B. DeMarco, J. L. Bohn, J. P. Burke, M. Holland, and D. S. Jin. Measurement of $p$-wave threshold law using evaporatively cooled fermionic atoms. Phys. Rev. Lett., 82:4208–4211, May 1999. doi: 10.1103/PhysRevLett.82.4208. URL https://link.aps.org/doi/10.1103/PhysRevLett.82.4208.

[89] K-K Ni, S Ospelkaus, MHG De Miranda, A Pe'Er, B Neyenhuis, JJ Zirbel, S Kotochigova, PS Julienne, DS Jin, and Jun Ye. A high phase-space-density gas of polar molecules. science, 322(5899):231–235, 2008. URL https://www.science.org/doi/full/10.1126/science.1163861.

[90] J. Goldwin, S. Inouye, M. L. Olsen, and D. S. Jin. Cross-dimensional relaxation in bose-fermi mixtures. Phys. Rev. A, 71:043408, Apr 2005. doi: 10.1103/PhysRevA.71.043408. URL https://link.aps.org/doi/10.1103/PhysRevA.71.043408.

[91] K. Aikawa, A. Frisch, M. Mark, S. Baier, R. Grimm, J. L. Bohn, D. S. Jin, G. M. Bruun, and F. Ferlaino. Anisotropic relaxation dynamics in a dipolar fermi gas driven out of equilibrium. Phys. Rev. Lett., 113:263201, Dec 2014. doi: 10.1103/PhysRevLett.113.263201. URL https://link.aps.org/doi/10.1103/PhysRevLett.113.263201.

[92] Jerome Sacks, Susannah B. Schiller, and William J. Welch. Designs for computer experiments. Technometrics, 31(1):41–47, 1989. doi: 10.1080/00401706.1989.10488474. URL https://www.tandfonline.com/doi/abs/10.1080/00401706.1989.10488474.

[93] Carl Edward Rasmussen and Christopher K. I. Williams. Gaussian Processes for Machine Learning. The MIT Press, 11 2005. ISBN 9780262256834. doi: 10.7551/mitpress/3206.001.0001. URL https://doi.org/10.7551/mitpress/3206.001.0001.

[94] Jie Cui and Roman V Krems. Efficient non-parametric fitting of potential energy surfaces for polyatomic molecules with gaussian processes. Journal of Physics B: Atomic, Molecular and Optical Physics, 49(22):224001, 2016. URL https://iopscience.iop.org/article/10.1088/0953-4075/49/22/224001/meta?casa_token=Yj1QkZ9fbjIAAAAA:2Nx7R8c9OI_YQbnenzVgKDe_J2XLojCVhaD6ienF6BaaGYbmetL2jFx-Cn2mtAa-1IxgjQCpYw0nuRJci_qp-b_Dbug.

[95] Arthur Christianen, Tijs Karman, Rodrigo A. Vargas-Hernández, Gerrit C. Groenenboom, and Roman V. Krems. Six-dimensional potential energy surface for NaK–NaK collisions: Gaussian process representation with correct asymptotic form. The Journal of Chemical Physics, 150(6):064106, 02 2019. ISSN 0021-9606. doi: 10.1063/1.5082740. URL https://doi.org/10.1063/1.5082740.

[96] Li Yang and Abdallah Shami. On hyperparameter optimization of machine learning algorithms: Theory and practice. Neurocomputing, 415:295–316, 2020. ISSN 0925-2312. doi: https://doi.org/10.1016/j.neucom.2020.07.061. URL https://www.sciencedirect.com/science/article/pii/S0925231220311693.

[97] A.L. Fetter and J.D. Walecka. Theoretical Mechanics of Particles and Continua. Dover Books on Physics. Dover Publications, 2003. ISBN 9780486432618. URL https://books.google.com/books?id=n54oAwAAQBAJ.

[98] O. Reynolds, A.W. Brightmore, and W.H. Moorby. The sub-mechanics of the universe. Papers on Mechanical and Physical Subjects. University Press, Cambridge, UK, 1903. URL https://books.google.com/books?id=xBM2AQAAMAAJ.

[99] CLMH Navier. Memoire surles du movement des. Mem Acad. Sci. Inst. France, 1(6):414–416, 1823.

[100] G. G. Stokes. On the theories of the internal friction of fluids in motion, and of the equilibrium and motion of elastic solids. In Classics of Elastic Wave Theory. Society of Exploration Geophysicists, Tulsa, Oklahoma, 01 2007. ISBN 9781560801429. doi: 10.1190/1.9781560801931.ch3e. URL https://doi.org/10.1190/1.9781560801931.ch3e.

[101] S.R. De Groot and P. Mazur. Non-Equilibrium Thermodynamics. Dover Books on Physics. Dover Publications, New York, 2013. ISBN 9780486153506. URL https://store.doverpublications.com/0486647412.html.

[102] L.D. Landau and E.M. Lifshitz. Fluid Mechanics: Landau and Lifshitz: Course of Theoretical Physics, Volume 6. Number v. 6 in Course of Theoretical Physics. Elsevier Science, 2013. ISBN 9781483161044. URL https://books.google.com/books?id=eOBbAwAAQBAJ.

[103] John W Bond, Kenneth M Watson, and Jasper A Welch. Atomic theory of gas dynamics, volume 633 of Addison-Wesley Series in Aerospace Science. Addison-Wesley, Reading, MA, 1965. URL https://pubs.aip.org/physicstoday/article-abstract/19/1/114/424801/Atomic-Theory-of-Gas-Dynamics.

[104] Nir Navon, Robert P. Smith, and Zoran Hadzibabic. Quantum gases in optical boxes. Nature Physics, 17(12):1334–1341, Dec 2021. ISSN 1745-2481. doi: 10.1038/s41567-021-01403-z. URL https://doi.org/10.1038/s41567-021-01403-z.

[105] Xing-Yan Chen, Marcel Duda, Andreas Schindewolf, Roman Bause, Immanuel Bloch, and Xin-Yu Luo. Suppression of unitary three-body loss in a degenerate bose-fermi mixture. Phys. Rev. Lett., 128:153401, Apr 2022. doi: 10.1103/PhysRevLett.128.153401. URL https://link.aps.org/doi/10.1103/PhysRevLett.128.153401.

[106] Bo Xiong, Jiangbin Gong, Han Pu, Weizhu Bao, and Baowen Li. Symmetry breaking and self-trapping of a dipolar bose-einstein condensate in a double-well potential. Phys. Rev. A, 79:013626, Jan 2009. doi: 10.1103/PhysRevA.79.013626. URL https://link.aps.org/doi/10.1103/PhysRevA.79.013626.

[107] L. Santos, G. V. Shlyapnikov, P. Zoller, and M. Lewenstein. Bose-einstein condensation in trapped dipolar gases. Phys. Rev. Lett., 85:1791–1794, Aug 2000. doi: 10.1103/PhysRevLett.85.1791. URL https://link.aps.org/doi/10.1103/PhysRevLett.85.1791.

[108] G. Bismut, B. Laburthe-Tolra, E. Maréchal, P. Pedri, O. Gorceix, and L. Vernac. Anisotropic excitation spectrum of a dipolar quantum bose gas. Phys. Rev. Lett., 109:155302, Oct 2012. doi: 10.1103/PhysRevLett.109.155302. URL https://link.aps.org/doi/10.1103/PhysRevLett.109.155302.

[109] A. R. P. Lima and A. Pelster. Beyond mean-field low-lying excitations of dipolar bose gases. Phys. Rev. A, 86:063609, Dec 2012. doi: 10.1103/PhysRevA.86.063609. URL https://link.aps.org/doi/10.1103/PhysRevA.86.063609.

[110] T. Lahaye, J. Metz, B. Fröhlich, T. Koch, M. Meister, A. Griesmaier, T. Pfau, H. Saito, Y. Kawaguchi, and M. Ueda. $d$-wave collapse and explosion of a dipolar bose-einstein condensate. Phys. Rev. Lett., 101:080401, Aug 2008. doi: 10.1103/PhysRevLett.101.080401. URL https://link.aps.org/doi/10.1103/PhysRevLett.101.080401.

[111] M.A. Baranov. Theoretical progress in many-body physics with ultracold dipolar gases. Physics Reports, 464(3):71–111, 2008. ISSN 0370-1573. doi: https://doi.org/10.1016/j.physrep.2008.04.007. URL https://www.sciencedirect.com/science/article/pii/S0370157308001385.

[112] J. L. Bohn, R. M. Wilson, and S. Ronen. How does a dipolar bose-einstein condensate collapse? Laser Physics, 19(4):547–549, Apr 2009. ISSN 1555-6611. doi: 10.1134/S1054660X09040021. URL https://doi.org/10.1134/S1054660X09040021.

[113] T Lahaye, C Menotti, L Santos, M Lewenstein, and T Pfau. The physics of dipolar bosonic quantum gases. Reports on Progress in Physics, 72(12):126401, nov 2009. doi: 10.1088/0034-4885/72/12/126401. URL https://doi.org/10.1088/0034-4885/72/12/126401.

[114] Matthew A. Norcia and Francesca Ferlaino. Developments in atomic control using ultracold magnetic lanthanides. Nature Physics, 17(12):1349–1357, Dec 2021. ISSN 1745-2481. doi: 10.1038/s41567-021-01398-7. URL https://doi.org/10.1038/s41567-021-01398-7.

[115] C. Cao, E. Elliott, J. Joseph, H. Wu, J. Petricka, T. Schäfer, and J. E. Thomas. Universal quantum viscosity in a unitary fermi gas. Science, 331(6013):58–61, 2011. doi: 10.1126/science.1195219. URL https://www.science.org/doi/abs/10.1126/science.1195219.

[116] Boa-Teh Chu and Leslie S. G. Kovásznay. Non-linear interactions in a viscous heat-conducting compressible gas. Journal of Fluid Mechanics, 3 (5):494–514, 1958. doi: 10.1017/S0022112058000148. URL https://www.cambridge.org/core/journals/journal-of-fluid-mechanics/article/abs/nonlinear-interactions-in-a-viscous-heatconducting-compressible-gas/3FA7B6C5FCCD1AA6C44F136F785F64E3.

[117] Aimee S Morgans and Ignacio Duran. Entropy noise: A review of theory, progress and challenges. International Journal of Spray and Combustion Dynamics, 8(4):285–298, 2016. doi: 10.1177/1756827716651791. URL https://doi.org/10.1177/1756827716651791.

[118] Z-Y Ma, A M Thomas, C J Foot, and S L Cornish. The evaporative cooling of a gas of caesium atoms in the hydrodynamic regime. Journal of Physics B: Atomic, Molecular and Optical Physics, 36(16):3533, aug 2003. doi: 10.1088/0953-4075/36/16/313. URL https://dx.doi.org/10.1088/0953-4075/36/16/313.

[119] A M Thomas, S Hopkins, S L Cornish, and C J Foot. Strong evaporative cooling towards bose–einstein condensation of a magnetically trapped caesium gas. Journal of Optics B: Quantum and Semiclassical Optics, 5(2):S107, apr 2003. doi: 10.1088/1464-4266/5/2/366. URL https://dx.doi.org/10.1088/1464-4266/5/2/366.

[120] Yu. Kagan, E. L. Surkov, and G. V. Shlyapnikov. Evolution of a bose gas in anisotropic time-dependent traps. Phys. Rev. A, 55:R18–R21, Jan 1997. doi: 10.1103/PhysRevA.55.R18. URL https://link.aps.org/doi/10.1103/PhysRevA.55.R18.

[121] P. Pedri, D. Guéry-Odelin, and S. Stringari. Dynamics of a classical gas including dissipative and mean-field effects. Phys. Rev. A, 68:043608, Oct 2003. doi: 10.1103/PhysRevA.68.043608. URL https://link.aps.org/doi/10.1103/PhysRevA.68.043608.

[122] Falk Wächtler, Aristeu R. P. Lima, and Axel Pelster. Low-lying excitation modes of trapped dipolar fermi gases: From the collisionless to the hydrodynamic regime. Phys. Rev. A, 96: 043608, Oct 2017. doi: 10.1103/PhysRevA.96.043608. URL https://link.aps.org/doi/10.1103/PhysRevA.96.043608.

[123] K. Kadoya, N. Matsunaga, and A. Nagashima. Viscosity and Thermal Conductivity of Dry Air in the Gaseous Phase. Journal of Physical and Chemical Reference Data, 14(4):947–970, 10 1985. ISSN 0047-2689. doi: 10.1063/1.555744. URL https://doi.org/10.1063/1.555744.

[124] G. M. Kavoulakis, C. J. Pethick, and H. Smith. Damping of hydrodynamic modes in a trapped bose gas above the bose-einstein transition temperature. Phys. Rev. A, 57:2938–2941, Apr 1998. doi: 10.1103/PhysRevA.57.2938. URL https://link.aps.org/doi/10.1103/PhysRevA.57.2938.

[125] Thomas Schäfer. Second-order fluid dynamics for the unitary fermi gas from kinetic theory. Phys. Rev. A, 90:043633, Oct 2014. doi: 10.1103/PhysRevA.90.043633. URL https://link.aps.org/doi/10.1103/PhysRevA.90.043633.

[126] T. Schäfer. Ratio of shear viscosity to entropy density for trapped fermions in the unitarity limit. Phys. Rev. A, 76:063618, Dec 2007. doi: 10.1103/PhysRevA.76.063618. URL https://link.aps.org/doi/10.1103/PhysRevA.76.063618.

[127] W E Lewis and P Romatschke. Higher-harmonic collective modes in a trapped gas from second-order hydrodynamics. New Journal of Physics, 19(2):023042, feb 2017. doi: 10.1088/1367-2630/aa5d6a. URL https://dx.doi.org/10.1088/1367-2630/aa5d6a.

[128] Daniel A. Messenger and David M. Bortz. Weak sindy: Galerkin-based data-driven model selection. Multiscale Modeling & Simulation, 19(3):1474–1497, 2021. doi: 10.1137/20M1343166. URL https://doi.org/10.1137/20M1343166.

[129] David M. Bortz, Daniel A. Messenger, and Vanja Dukic. Direct estimation of parameters in ode models using wendy: Weak-form estimation of nonlinear dynamics. Bulletin of Mathematical Biology, 85(11):110, Oct 2023. ISSN 1522-9602. doi: 10.1007/s11538-023-01208-6. URL https://doi.org/10.1007/s11538-023-01208-6.

[130] A. Griffin, Wen-Chin Wu, and S. Stringari. Hydrodynamic modes in a trapped bose gas above the bose-einstein transition. Phys. Rev. Lett., 78:1838–1841, Mar 1997. doi: 10.1103/PhysRevLett.78.1838. URL https://link.aps.org/doi/10.1103/PhysRevLett.78.1838.

[131] E. P. Gross. Structure of a quantized vortex in boson systems. Il Nuovo Cimento (1955-1965), 20(3):454–477, May 1961. ISSN 1827-6121. doi: 10.1007/BF02731494. URL https://doi.org/10.1007/BF02731494.

[132] Lev P Pitaevskii. Vortex lines in an imperfect bose gas. Sov. Phys. JETP, 13(2):451–454, 1961. URL http://www.jetp.ras.ru/cgi-bin/e/index/r/40/2/p646?a=list.

[133] Matthew P. A. Fisher, Peter B. Weichman, G. Grinstein, and Daniel S. Fisher. Boson localization and the superfluid-insulator transition. Phys. Rev. B, 40:546–570, Jul 1989. doi: 10.1103/PhysRevB.40.546. URL https://link.aps.org/doi/10.1103/PhysRevB.40.546.

[134] K. Góral, L. Santos, and M. Lewenstein. Quantum phases of dipolar bosons in optical lattices. Phys. Rev. Lett., 88:170406, Apr 2002. doi: 10.1103/PhysRevLett.88.170406. URL https://link.aps.org/doi/10.1103/PhysRevLett.88.170406.

[135] A. Frisch, K. Aikawa, M. Mark, A. Rietzler, J. Schindler, E. Zupanič, R. Grimm, and F. Ferlaino. Narrow-line magneto-optical trap for erbium. Phys. Rev. A, 85:051401, May 2012. doi: 10.1103/PhysRevA.85.051401. URL https://link.aps.org/doi/10.1103/PhysRevA.85.051401.

[136] M. Houbiers, H. T. C. Stoof, and E. A. Cornell. Critical temperature of a trapped bose gas: Mean-field theory and fluctuations. Phys. Rev. A, 56:2041–2045, Sep 1997. doi: 10.1103/PhysRevA.56.2041. URL https://link.aps.org/doi/10.1103/PhysRevA.56.2041.

[137] Albert Frisch, Michael Mark, Kiyotaka Aikawa, Francesca Ferlaino, John L. Bohn, Constantinos Makrides, Alexander Petrov, and Svetlana Kotochigova. Quantum chaos in ultracold collisions of gas-phase erbium atoms. Nature, 507(7493):475–479, Mar 2014. ISSN 1476-4687. doi: 10.1038/nature13137. URL https://doi.org/10.1038/nature13137.

[138] T. Maier, I. Ferrier-Barbut, H. Kadau, M. Schmitt, M. Wenzel, C. Wink, T. Pfau, K. Jachymski, and P. S. Julienne. Broad universal feshbach resonances in the chaotic spectrum of dysprosium atoms. Phys. Rev. A, 92:060702, Dec 2015. doi: 10.1103/PhysRevA.92.060702. URL https://link.aps.org/doi/10.1103/PhysRevA.92.060702.

[139] S. Baier, M. J. Mark, D. Petter, K. Aikawa, L. Chomaz, Z. Cai, M. Baranov, P. Zoller, and F. Ferlaino. Extended Bose-Hubbard models with ultracold magnetic atoms. Science, 352(6282):201–205, 2016. ISSN 0036-8075. doi: 10.1126/science.aac9812. URL https://science.sciencemag.org/content/352/6282/201.

[140] L. Chomaz, S. Baier, D. Petter, M. J. Mark, F. Wächtler, L. Santos, and F. Ferlaino. Quantum-Fluctuation-Driven Crossover from a Dilute Bose-Einstein Condensate to a Macrodroplet in a Dipolar Quantum Fluid. Phys. Rev. X, 6:041039, Nov 2016. doi: 10.1103/PhysRevX.6.041039. URL https://link.aps.org/doi/10.1103/PhysRevX.6.041039.

[141] S. Baier, D. Petter, J. H. Becher, A. Patscheider, G. Natale, L. Chomaz, M. J. Mark, and F. Ferlaino. Realization of a Strongly Interacting Fermi Gas of Dipolar Atoms. Phys. Rev. Lett., 121:093602, Aug 2018. doi: 10.1103/PhysRevLett.121.093602. URL https://link.aps.org/doi/10.1103/PhysRevLett.121.093602.

[142] Krzysztof Jachymski and Paul S. Julienne. Analytical model of overlapping feshbach resonances. Phys. Rev. A, 88:052701, Nov 2013. doi: 10.1103/PhysRevA.88.052701. URL https://link.aps.org/doi/10.1103/PhysRevA.88.052701.

[143] T. Kraemer, M. Mark, P. Waldburger, J. G. Danzl, C. Chin, B. Engeser, A. D. Lange, K. Pilch, A. Jaakkola, H.-C. Nägerl, and R. Grimm. Evidence for efimov quantum states in an ultracold gas of caesium atoms. Nature, 440(7082):315–318, Mar 2006. ISSN 1476-4687. doi: 10.1038/nature04626. URL https://doi.org/10.1038/nature04626.

[144] B. Deb and L. You. Low-energy atomic collision with dipole interactions. Phys. Rev. A, 64:022717, Jul 2001. doi: 10.1103/PhysRevA.64.022717. URL https://link.aps.org/doi/10.1103/PhysRevA.64.022717.

[145] Masaaki Kitagawa, Katsunari Enomoto, Kentaro Kasa, Yoshiro Takahashi, Roman Ciuryło, Pascal Naidon, and Paul S. Julienne. Two-color photoassociation spectroscopy of ytterbium atoms and the precise determinations of $s$-wave scattering lengths. Phys. Rev. A, 77:012719, Jan 2008. doi: 10.1103/PhysRevA.77.012719. URL https://link.aps.org/doi/10.1103/PhysRevA.77.012719.

[146] Mateusz Borkowski, Piotr S. Żuchowski, Roman Ciuryło, Paul S. Julienne, Dariusz Kędziera, Łukasz Mentel, Paweł Tecmer, Frank Münchow, Cristian Bruni, and Axel Görlitz. Scattering

lengths in isotopologues of the rbyb system. Phys. Rev. A, 88:052708, Nov 2013. doi: 10.1103/PhysRevA.88.052708. URL https://link.aps.org/doi/10.1103/PhysRevA.88.052708.

[147] Guang-jiong Ni. The Levinson theorem and its generalization in relativistic quantum mechanics. Chinese Physics C, 3(4):432–449, 1979. URL http://cpc.ihep.ac.cn/article/id/ea6dcaea-599f-405e-87be-5d16571864ae.

[148] Wolfgang Ketterle and NJ Van Druten. Evaporative cooling of trapped atoms. Advances in atomic, molecular, and optical physics, 37:181–236, 1996. URL https://www.sciencedirect.com/science/article/pii/S1049250X08601019.

[149] D. A. Butts and D. S. Rokhsar. Trapped fermi gases. Phys. Rev. A, 55:4346–4350, Jun 1997. doi: 10.1103/PhysRevA.55.4346. URL https://link.aps.org/doi/10.1103/PhysRevA.55.4346.

[150] Brian Leeds Demarco. Quantum behavior of an atomic Fermi gas. PhD thesis, University of Colorado, Boulder, aug 2001. URL https://www.proquest.com/docview/304690107?pq-origsite=gscholar&fromopenview=true&sourcetype=Dissertations%20&%20Theses.

[151] C. A. Regal, M. Greiner, S. Giorgini, M. Holland, and D. S. Jin. Momentum distribution of a fermi gas of atoms in the bcs-bec crossover. Phys. Rev. Lett., 95:250404, Dec 2005. doi: 10.1103/PhysRevLett.95.250404. URL https://link.aps.org/doi/10.1103/PhysRevLett.95.250404.

[152] Rudolf Grimm, Matthias Weidemüller, and Yurii B. Ovchinnikov. Optical dipole traps for neutral atoms. volume 42 of Advances In Atomic, Molecular, and Optical Physics, pages 95–170. Academic Press, 2000. doi: https://doi.org/10.1016/S1049-250X(08)60186-X. URL https://www.sciencedirect.com/science/article/pii/S1049250X0860186X.

[153] Ryan M Wilson. Manifestations of the Roton in Dipolar Bose-Einstein Condensates. PhD thesis, University of Colorado at Boulder, 2011. URL https://www.proquest.com/docview/915692272?pq-origsite=gscholar&fromopenview=true&sourcetype=Dissertations%20&%20Theses.

[154] Chaim L Pekeris and Zipora Alterman. Solution of the boltzmann-hilbert integral equation ii. the coefficients of viscosity and heat conduction. Proceedings of the National Academy of Sciences of the United States of America, 43(11):998, 1957. URL https://www.ncbi.nlm.nih.gov/pmc/articles/PMC528572/.

[155] S.K. Loyalka, E.L. Tipton, and R.V. Tompson. Chapman–enskog solutions to arbitrary order in sonine polynomials i: Simple, rigid-sphere gas. Physica A: Statistical Mechanics and its Applications, 379(2):417–435, 2007. ISSN 0378-4371. doi: https://doi.org/10.1016/j.physa.2006.12.001. URL https://www.sciencedirect.com/science/article/pii/S0378437106013264.

[156] Mohamed Gad-el Hak. Questions in Fluid Mechanics: Stokes' Hypothesis for a Newtonian, Isotropic Fluid. Journal of Fluids Engineering, 117(1):3–5, 03 1995. ISSN 0098-2202. doi: 10.1115/1.2816816. URL https://doi.org/10.1115/1.2816816.

[157] Rick E Graves and Brian M Argrow. Bulk viscosity: past to present. Journal of Thermophysics and Heat Transfer, 13(3):337–342, 1999. URL https://arc.aiaa.org/doi/abs/10.2514/2.6443.

# Appendix A

## Matrix elements of the effective microwave shielded potential

To perform the scattering calculations on the effective single-channel microwave shielded potential energy surface in Sec. 2.2.2, we are required to compute the matrix elements of the effective microwave shielded potential $\langle \ell, m | \, V_\mu(\boldsymbol{r}) \, | \ell', m'_\ell \rangle$. We list these elements explicitly in this section. In all generality for those who might want to use this in future, I will consider the case of arbitrary microwave ellipticity, parameterized by the angle $\xi$, but with the dipoles aligned along $z$ such that:

$$V_\mu(\boldsymbol{r};\xi) = V_6(\boldsymbol{r};\xi) + V_{\rm dd}(\boldsymbol{r};\xi), \tag{A.1}$$

having defined

$$V_6(\boldsymbol{r};\xi) = \left[ \left(1 - \mathcal{F}_\xi(\phi)\right)^2 \cos^2\theta + 1 - \mathcal{F}_\xi(\phi)^2 \right] \sin^2\theta, \tag{A.2a}$$

$$V_{\rm dd}(\boldsymbol{r};\xi) = \frac{\overline{d}^2}{4\pi\epsilon_0 r^3} \left[ 3\cos^2\theta - 1 + 3\mathcal{F}_\xi(\phi) \sin^2\theta \right], \tag{A.2b}$$

and the function $\mathcal{F}_\xi(\phi) = \cos(2\phi)\sin(2\xi)$ [55].

The associated matrix elements of these potentials are then listed as follows. For the dipole-dipole potential $V_{\mu,\rm dd}$, we have:

$$\begin{aligned}
\langle \ell, m | \, V_{\mu,\rm dd}(\boldsymbol{r};\xi) \, | \ell', m'_\ell \rangle &= \frac{\overline{d}^2}{4\pi\epsilon_0 r^3} \langle \ell, m | \left[ 4\sqrt{\frac{\pi}{5}} Y_{2,0}(\theta,\phi) + 12\sqrt{\frac{2\pi}{15}} \mathrm{Re}[Y_{2,2}(\theta,\phi)] \sin(2\xi) \right] | \ell', m'_\ell \rangle \\
&= \frac{\overline{d}^2}{4\pi\epsilon_0 r^3} \left[ 4\sqrt{\frac{\pi}{5}} \int d\Omega Y^*_{\ell,m}(\Omega) Y_{2,0}(\Omega) Y_{\ell',m'_\ell}(\Omega) \right. \\
&\qquad \left. + 6\sqrt{\frac{2\pi}{15}} \sin(2\xi) \int d\Omega Y^*_{\ell,m}(\Omega) \left[ Y_{2,2}(\Omega) + Y_{2,-2}(\Omega) \right] Y_{\ell',m'_\ell}(\Omega) \right]
\end{aligned}$$

$$= \frac{\overline{d}^2}{4\pi\epsilon_0 r^3} 2(-1)^m \sqrt{(2\ell+1)(2\ell'+1)} \begin{pmatrix} \ell & 2 & \ell' \\ 0 & 0 & 0 \end{pmatrix}$$

$$\times \left\{ \begin{pmatrix} \ell & 2 & \ell' \\ -m_\ell & 0 & m'_\ell \end{pmatrix} + \sqrt{\frac{3}{2}} \sin(2\xi) \left[ \begin{pmatrix} \ell & 2 & \ell' \\ -m_\ell & 2 & m'_\ell \end{pmatrix} + \begin{pmatrix} \ell & 2 & \ell' \\ -m_\ell & -2 & m'_\ell \end{pmatrix} \right] \right\}, \tag{A.3}$$

while the matrix elements for $V_{\mu,6}(\boldsymbol{r})$ are given as

$$\begin{aligned}
\langle \ell, m_\ell | \, V_{\mu,6}(\boldsymbol{r};\xi) \, | \ell', m'_\ell \rangle &= \frac{C_6}{r^6} \langle \ell, m_\ell | \Big[ 1 - \cos^2(2\phi) \sin^2(2\xi) \\
&\qquad + (1 - \cos(2\phi)\sin(2\xi))^2 \cos^2\theta \Big] \sin^2\theta \, | \ell', m'_\ell \rangle \\
&= 4\sqrt{\pi} \frac{C_6}{r^6} \langle \ell, m_\ell | \Bigg[ \frac{1}{15}(\cos(4\xi)+5) Y_{0,0}(\theta,\phi) \\
&\qquad - \frac{1}{7}\sqrt{\frac{2}{15}} \sin(2\xi) Y_{2,-2}(\theta,\phi) \\
&\qquad - \frac{2}{21}\sqrt{\frac{1}{5}} (\cos(4\xi)+2) Y_{2,0}(\theta,\phi) \\
&\qquad - \frac{1}{7}\sqrt{\frac{2}{15}} \sin(2\xi) Y_{2,2}(\theta,\phi) \\
&\qquad - \frac{1}{3}\sqrt{\frac{2}{35}} \sin^2(2\xi) Y_{4,-4}(\theta,\phi) \\
&\qquad - \frac{2}{21}\sqrt{\frac{2}{5}} \sin(2\xi) Y_{4,-2}(\theta,\phi) \\
&\qquad + \frac{1}{105}(\cos(4\xi)-5) Y_{4,0}(\theta,\phi) \\
&\qquad - \frac{2}{21}\sqrt{\frac{2}{5}} \sin(2\xi) Y_{4,2}(\theta,\phi) \\
&\qquad - \frac{1}{3}\sqrt{\frac{2}{35}} \sin^2(2\xi) Y_{4,4}(\theta,\phi) \Bigg] \, | \ell', m'_\ell \rangle \\
&= \frac{C_6}{r^6} 2(-1)^{m_\ell} \sqrt{(2\ell+1)(2\ell'+1)} \\
&\quad \times \Bigg[ \frac{1}{15}(\cos(4\xi)+5) \begin{pmatrix} \ell & 0 & \ell' \\ 0 & 0 & 0 \end{pmatrix} \begin{pmatrix} \ell & 0 & \ell' \\ -m_\ell & 0 & m'_\ell \end{pmatrix} \\
&\qquad - \frac{1}{7}\sqrt{\frac{2}{3}} \sin(2\xi) \begin{pmatrix} \ell & 2 & \ell' \\ 0 & 0 & 0 \end{pmatrix} \begin{pmatrix} \ell & 2 & \ell' \\ -m_\ell & -2 & m'_\ell \end{pmatrix} \\
&\qquad - \frac{2}{21}(\cos(4\xi)+2) \begin{pmatrix} \ell & 2 & \ell' \\ 0 & 0 & 0 \end{pmatrix} \begin{pmatrix} \ell & 2 & \ell' \\ -m_\ell & 0 & m'_\ell \end{pmatrix}
\end{aligned}$$

$$
\begin{aligned}
&- \frac{1}{7}\sqrt{\frac{2}{3}}\sin(2\xi)\begin{pmatrix}\ell & 2 & \ell'\\ 0 & 0 & 0\end{pmatrix}\begin{pmatrix}\ell & 2 & \ell'\\ -m & 2 & m'\end{pmatrix}\\
&- \sqrt{\frac{2}{35}}\sin^2(2\xi)\begin{pmatrix}\ell & 4 & \ell'\\ 0 & 0 & 0\end{pmatrix}\begin{pmatrix}\ell & 4 & \ell'\\ -m_\ell & -4 & m'_\ell\end{pmatrix}\\
&- \frac{2}{7}\sqrt{\frac{2}{5}}\sin(2\xi)\begin{pmatrix}\ell & 4 & \ell'\\ 0 & 0 & 0\end{pmatrix}\begin{pmatrix}\ell & 4 & \ell'\\ -m_\ell & -2 & m'_\ell\end{pmatrix}\\
&+ \frac{1}{35}(\cos(4\xi)-5)\begin{pmatrix}\ell & 4 & \ell'\\ 0 & 0 & 0\end{pmatrix}\begin{pmatrix}\ell & 4 & \ell'\\ -m_\ell & 0 & m'_\ell\end{pmatrix}\\
&- \frac{2}{7}\sqrt{\frac{2}{5}}\sin(2\xi)\begin{pmatrix}\ell & 4 & \ell'\\ 0 & 0 & 0\end{pmatrix}\begin{pmatrix}\ell & 4 & \ell'\\ -m_\ell & 2 & m'_\ell\end{pmatrix}\\
&- \sqrt{\frac{2}{35}}\sin^2(2\xi)\begin{pmatrix}\ell & 4 & \ell'\\ 0 & 0 & 0\end{pmatrix}\begin{pmatrix}\ell & 4 & \ell'\\ -m_\ell & 4 & m'_\ell\end{pmatrix}\Bigg]. \qquad \text{(A.4)}
\end{aligned}
$$

Even more conveniently for the reader, I will also list the simplified matrix elements for circularly polarized microwaves ($\xi = 0$) explicitly below:

$$
\begin{aligned}
\langle \ell, m_\ell | \, V_{\mu,\mathrm{dd}}(\boldsymbol{r};0) \, | \ell', m' \rangle &= \frac{d_{\mathrm{eff}}^2}{4\pi\epsilon_0 r^3} \langle \ell, m_\ell | \left[ 4\sqrt{\frac{\pi}{5}} Y_{2,0}(\theta,\phi) \right] | \ell', m'_\ell \rangle \\
&= \frac{d_{\mathrm{eff}}^2}{4\pi\epsilon_0 r^3} \left[ 4\sqrt{\frac{\pi}{5}} \int d\Omega Y^*_{\ell,m_\ell}(\Omega) Y_{2,0}(\Omega) Y_{\ell',m'_\ell}(\Omega) \right] \\
&= \frac{d_{\mathrm{eff}}^2}{4\pi\epsilon_0 r^3} 2(-1)^{m_\ell} \sqrt{(2\ell+1)(2\ell'+1)} \begin{pmatrix}\ell & 2 & \ell'\\ 0 & 0 & 0\end{pmatrix}\begin{pmatrix}\ell & 2 & \ell'\\ -m_\ell & 0 & m'_\ell\end{pmatrix},
\end{aligned}
\qquad \text{(A.5a)}
$$

$$
\begin{aligned}
\langle \ell, m_\ell | \, V_{\mu,6}(\boldsymbol{r};0) \, | \ell', m'_\ell \rangle &= \frac{C_6}{r^6} \langle \ell, m_\ell | \left(1+\cos^2\theta\right) \sin^2\theta \, | \ell', m'_\ell \rangle \\
&= 4\sqrt{\pi}\frac{C_6}{r^6} \langle \ell, m_\ell | \left[ \frac{2}{5} Y_{0,0}(\theta,\phi) - \frac{2}{7}\sqrt{\frac{1}{5}} Y_{2,0}(\theta,\phi) - \frac{4}{105} Y_{4,0}(\theta,\phi) \right] | \ell', m'_\ell \rangle \\
&= \frac{C_6}{r^6} 2(-1)^m \sqrt{(2\ell+1)(2\ell'+1)} \\
&\quad \times \left[ \frac{2}{5} \begin{pmatrix}\ell & 0 & \ell'\\ 0 & 0 & 0\end{pmatrix}\begin{pmatrix}\ell & 0 & \ell'\\ -m_\ell & 0 & m'_\ell\end{pmatrix} - \frac{2}{7} \begin{pmatrix}\ell & 2 & \ell'\\ 0 & 0 & 0\end{pmatrix}\begin{pmatrix}\ell & 2 & \ell'\\ -m_\ell & 0 & m'_\ell\end{pmatrix} \right.
\end{aligned}
$$

$$-\frac{4}{35}\begin{pmatrix}\ell & 4 & \ell'\\ 0 & 0 & 0\end{pmatrix}\begin{pmatrix}\ell & 4 & \ell'\\ -m_\ell & 0 & m'_\ell\end{pmatrix}\Bigg]. \tag{A.5b}$$

There you go, matrix elements on a silver platter.

# Appendix B

## Optical dipole traps for atoms and molecules

In the parlance of classical physics, an oscillating electric field results in the separation of positive and negative charges within a neutral atom, inducing an electric dipole moment. This dipole can in turn interact with its very maker, the oscillating field, either resonantly or not. Below resonance (red detuned), the dipole-field interaction energy is negative, pulling the atom into the region of highest electric field intensity. The converse process occurs above resonance (blue detuned). In real quantum mechanical atoms, a Gaussian laser beam could act as the oscillating field, which dresses the atom's internal electronic states to induce a dipole transition. With the intensity maximal at the Gaussian peak, a red detuned laser is best used to trap the atoms close to the energetic minima of the beam center. And that folks, is how you get optical confinement [152].

More rigorously, the external laser field can be modeled by the electric field $\boldsymbol{\mathcal{E}}(\boldsymbol{r})e^{i\omega t}$, oscillating at a frequency $\omega$. A proportional dipole moment

$$\boldsymbol{d}_{\mathrm{ind}}(\boldsymbol{r}) = \tilde{\alpha}\boldsymbol{\mathcal{E}}(\boldsymbol{r}), \tag{B.1}$$

is then induced in the atom, with an atomic species, laser frequency and polarization dependent proportional constant $\tilde{\alpha}$, known as the *complex atomic polarizability*. The interaction of $\boldsymbol{d}(\boldsymbol{r})$ with $\boldsymbol{\mathcal{E}}(\boldsymbol{r})$ then results in the potential energy felt by the atom as

$$V_{\mathrm{trap}}(\boldsymbol{r}) = -\frac{1}{2}\langle \boldsymbol{d}_{\mathrm{ind}}(\boldsymbol{r},t)\cdot\boldsymbol{\mathcal{E}}(\boldsymbol{r},t)\rangle_t = -\,\mathrm{Re}\{\tilde{\alpha}\}|\boldsymbol{\mathcal{E}}(\boldsymbol{r})|^2, \tag{B.2}$$

where $\langle\ldots\rangle_t$ is a time average over the rapid oscillating terms. For an elliptic Gaussian beam

propagating along $z$, its intensity profile is given as

$$|\boldsymbol{\mathcal{E}}(\boldsymbol{r})|^2 = \frac{P}{\pi c \epsilon_0 w_x(z) w_y(z)} \exp\left[-2\left(\frac{x^2}{w_x^2(z)} + \frac{y^2}{w_y^2(z)}\right)\right], \tag{B.3}$$

with laser power $P$, beam width along axis $i$:

$$w_i(z) = W_i \sqrt{1 + \frac{z^2}{R_i^2}}, \tag{B.4}$$

Rayleigh length $R_i = \pi W_i^2/\lambda$, minimum beam width $W_i$ and laser wavelength $\lambda$.

For optical trapping in 3-dimensions, 2 of such Gaussian beams are generally utilized in a crossed configuration, so that the electric fields are orthogonal to each other and add linearly in intensity. As a result, the crossed optical dipole trap resultant from lasers propagating along $x$ and $y$ is described by the potential:

$$\begin{aligned} V_{\mathrm{ODT}}(\boldsymbol{r}) = &-\frac{2\alpha_1 P_1}{\pi w_{1,y}(x) w_{1,z}(x)} \exp\left(-\frac{2y^2}{w_{1,y}^2(x)} - \frac{2z^2}{w_{1,z}^2(x)}\right) \\ &- \frac{2\alpha_2 P_2}{\pi w_{2,x}(y) w_{2,z}(y)} \exp\left(-\frac{2x^2}{w_{2,x}^2(y)} - \frac{2z^2}{w_{2,z}^2(y)}\right), \end{aligned} \tag{B.5a}$$

where $\alpha_i = \mathrm{Re}\{\tilde{\alpha}_i\}/(2c\epsilon_0)$ is the polarizability constant. Close to the minima of this potential, $V_{\mathrm{ODT}}$ can be expanded up to second order in spatial coordinates as

$$V_{\mathrm{harm}}(\boldsymbol{r}) = \sum_i A_i r_i^2, \tag{B.6}$$

dropping all constants as they simply amount to an energy offset, with harmonic coefficients

$$A_x = \frac{\alpha_1 P_1 \lambda_1^2 \left(W_{1,y}^4 + W_{1,z}^4\right)}{\pi^3 W_{1,y}^5 W_{1,z}^5} + \frac{4\alpha_2 P_2}{\pi W_{2,x}^3 W_{2,z}}, \tag{B.7a}$$

$$A_y = \frac{4\alpha_1 P_1}{\pi W_{1,y}^3 W_{1,z}} + \frac{\alpha_2 P_2 \lambda_2^2 \left(W_{2,x}^4 + W_{2,z}^4\right)}{\pi^3 W_{2,x}^5 W_{2,z}^5}, \tag{B.7b}$$

$$A_y = \frac{4\alpha_1 P_1}{\pi W_{1,y}^3 W_{1,z}} + \frac{4\alpha_2 P_2}{\pi W_{2,x}^3 W_{2,z}}. \tag{B.7c}$$

Comparing Eq. (B.6) to Eq. (3.2) finally identifies the harmonic trap frequencies as

$$\omega_i^2 = \frac{2}{m} A_i. \tag{B.8}$$

# Appendix C

## The method of averages

I utilize the method of averages to derive Enskog equations in this appendix chapter. For some observable quantity of interest $\chi(\boldsymbol{r},\boldsymbol{p},t)$, the method of averages multiplies it with the Boltzmann equation (3.1) and takes an integral over phase space to give

$$\frac{1}{N}\int d^3p d^3r\,\chi(\boldsymbol{r},\boldsymbol{p},t)\left(\frac{\partial}{\partial t}+\sum_i\frac{p_i}{m}\frac{\partial}{\partial r_i}-\sum_i\frac{\partial V(\boldsymbol{r})}{\partial r_i}\frac{\partial}{\partial p_i}\right)f(\boldsymbol{r},\boldsymbol{p},t)$$
$$=\frac{1}{N}\int d^3p d^3r\,\chi(\boldsymbol{r},\boldsymbol{p},t)\mathcal{I}_{\rm coll}[f]. \tag{C.1}$$

Each term on the left hand side of Eq. (C.1) is evaluated as

$$\int d^3p\int d^3r\left(\chi\frac{\partial f}{\partial t}\right)=\int d^3p\int d^3r\,\left(\frac{d}{dt}(\chi f)-f\frac{\partial\chi}{\partial t}\right)$$
$$=N\frac{d\langle\chi\rangle}{dt}-N\left\langle\frac{\partial\chi}{\partial t}\right\rangle, \tag{C.2a}$$
$$\int d^3p\int d^3r\sum_j\frac{p_j}{m}\frac{\partial f}{\partial r_j}\chi=\int d^3p\int d^3r\sum_j\left(\frac{\partial}{\partial r_j}\left(\frac{p_j}{m}\chi f\right)-\frac{p_j}{m}\frac{\partial\chi}{\partial r_j}f\right)$$
$$=\int d^3p\left(\oint_{\partial S}\chi f\sum_j\frac{p_j}{m}\hat{n}_j-\int d^3r\sum_j\frac{p_j}{m}\frac{\partial\chi}{\partial r_j}f\right)$$
$$=-\int d^3p\int d^3r\sum_j\frac{p_j}{m}\frac{\partial\chi}{\partial r_j}f$$
$$=-N\left\langle\frac{\boldsymbol{p}}{m}\cdot\boldsymbol{\nabla}_r\chi\right\rangle, \tag{C.2b}$$
$$\int d^3p\int d^3r\chi\sum_j\frac{\partial V(\boldsymbol{r})}{\partial r_j}\frac{\partial f}{\partial p_j}=\int d^3p\int d^3r\sum_j\left(\frac{\partial}{\partial p_j}\left(\chi f\frac{\partial V(\boldsymbol{r})}{\partial r_j}\right)-\frac{\partial V(\boldsymbol{r})}{\partial r_j}\frac{\partial\chi}{\partial p_j}f\right)$$
$$=\int d^3r\left(\oint_{\partial S_p}\chi f\sum_j\frac{\partial V(\boldsymbol{r})}{\partial r_j}\hat{n}_j-\int d^3pf\sum_j\frac{\partial V(\boldsymbol{r})}{\partial r_j}\frac{\partial\chi}{\partial p_j}\right)$$

$$= -\int d^3r \int d^3p \sum_j \frac{\partial V(\boldsymbol{r})}{\partial r_j} \frac{\partial \chi}{\partial p_j} f$$

$$= -N\langle \boldsymbol{\nabla} V(\boldsymbol{r}) \cdot \boldsymbol{\nabla}_p \chi \rangle, \tag{C.2c}$$

where $\hat{n}_j$ is the $j$-th unit vector component normal to the surface $\partial S$.

Putting these terms together, the phase-space averaged substantial derivative evaluates to

$$\frac{1}{N} \int d^3p \int d^3r \, \chi(\boldsymbol{r}, \boldsymbol{p}, t) \left( \frac{\partial}{\partial t} + \sum_i \frac{p_i}{m} \frac{\partial}{\partial r_i} - \sum_i \frac{\partial V(\boldsymbol{r})}{\partial r_i} \frac{\partial}{\partial p_i} \right) f(\boldsymbol{r}, \boldsymbol{p}, t)$$

$$= \frac{d\langle \chi \rangle}{dt} - \left\langle \frac{\partial \chi}{\partial t} \right\rangle - \left\langle \frac{\boldsymbol{p}}{m} \cdot \boldsymbol{\nabla}_r \chi \right\rangle - \langle \boldsymbol{F} \cdot \boldsymbol{\nabla}_p \chi \rangle. \tag{C.3}$$

Then having $\chi$ by $\chi = r_i^2, p_i^2, r_i p_i$, performing the averaging procedure described above results in the system of equations in (3.8).

# Appendix D

## Equilibrium dipolar mean-field per particle

The dipolar mean-field energy per particle $\varepsilon_{\rm mf}$, used in Sec. 3.3.3 is derived here. First, $\varepsilon_{\rm mf}$ is written in terms of the integral

$$\varepsilon_{\rm mf} = \frac{1}{2N}\int d^3\boldsymbol{r} n(\boldsymbol{r})\int d^3\boldsymbol{r}' n(\boldsymbol{r}')\Phi_{\rm dd}(\boldsymbol{r}-\boldsymbol{r}'). \tag{D.1}$$

I assume a cylindrically symmetric trap, which simplifies the derivation and asserts a number density distribution $n(\boldsymbol{r})$ given by

$$n(\boldsymbol{r}) = \frac{N}{(2\pi)^{3/2}\sigma_\rho^2\sigma_z}\exp\left(-\frac{\rho^2}{2\sigma_\rho^2}-\frac{z^2}{2\sigma_z^2}\right), \tag{D.2}$$

where $\rho^2 = x^2+y^2$ and $\sigma_j$ is the standard standard deviation of particles along axis $j$. To evaluate this, I will utilize the convolution theorem:

$$\begin{aligned}\int d^3\boldsymbol{r}' n(\boldsymbol{r}')\Phi_{\rm dd}(\boldsymbol{r}-\boldsymbol{r}') &= n(\boldsymbol{r}) * \Phi_{\rm dd}(\boldsymbol{r})\\ &= \mathcal{F}^{-1}\left[\mathcal{F}\left[n(\boldsymbol{r})\right]\cdot\mathcal{F}\left[\Phi_{\rm dd}(\boldsymbol{r})\right]\right]\\ &= \mathcal{F}^{-1}\left[\tilde{n}(\boldsymbol{k})\cdot\tilde{\Phi}_{\rm dd}(\boldsymbol{k})\right]\\ &= \frac{1}{\sqrt{(2\pi)^3}}\int d^3k\,\tilde{n}(\boldsymbol{k})\tilde{\Phi}_{\rm dd}(\boldsymbol{k})e^{i\boldsymbol{k}\cdot\boldsymbol{r}}.\end{aligned} \tag{D.3}$$

where $\mathcal{F}[\ldots] = \frac{1}{\sqrt{(2\pi)^3}}\int d^3\boldsymbol{r}(\ldots)e^{-i\boldsymbol{k}\cdot\boldsymbol{r}}$ is a Fourier transform and tildes denote Fourier transformed functions. Putting this back into the full integral gives

$$\varepsilon_{\rm mf} = \frac{1}{2N\sqrt{(2\pi)^3}}\int d^3\boldsymbol{r}\, n(\boldsymbol{r})\int d^3k\,\tilde{n}(\boldsymbol{k})\tilde{\Phi}_{\rm dd}(\boldsymbol{k})e^{i\boldsymbol{k}\cdot\boldsymbol{r}}$$

$$= \frac{1}{2N} \int d^3k\, \tilde{n}(\boldsymbol{k}) \tilde{\Phi}_{\mathrm{dd}}(\boldsymbol{k}) \left( \frac{1}{\sqrt{(2\pi)^3}} \int d^3\boldsymbol{r}\, n(\boldsymbol{r}) e^{i\boldsymbol{k}\cdot\boldsymbol{r}} \right)$$

$$= \frac{1}{2N} \int d^3k\, \tilde{n}^2(\boldsymbol{k}) \tilde{\Phi}_{\mathrm{dd}}(\boldsymbol{k}). \tag{D.4}$$

The Fourier transforms of the integrand functions are given by

$$\tilde{n}(\boldsymbol{k}) = \frac{N}{(2\pi)^{3/2}} \exp\left[ -\frac{1}{2} \left( \langle \rho^2 \rangle k_\rho^2 + \langle z^2 \rangle k_z^2 \right) \right], \tag{D.5a}$$

$$\tilde{\Phi}_{\mathrm{dd}}(\boldsymbol{k}) = \frac{d^2}{4\epsilon_0} \Big[ 2 \sin^2\alpha \sin^2\theta_k \cos(2\phi_k) + 2 \sin(2\alpha) \sin(2\theta_k) \cos\phi_k + \frac{1}{6} (3\cos(2\alpha) + 1)(3\cos(2\theta_k) + 1) \Big], \tag{D.5b}$$

with the result for $\tilde{\Phi}_{\mathrm{dd}}(\boldsymbol{k})$ taken from R. Wilson's thesis in Ref. [153]. Plugging these in and evaluating the integral gives $\varepsilon_{\mathrm{mf}}$ as written in Eq. (3.47).

# Appendix E

## Deriving the collisional efficiency toward thermalization

Obtaining the form of $\varepsilon_{ij}$ in Eq. (4.20) follows a very similar procedure to that in Sec. 4.1, since after all, $\varepsilon_{ij}$ is just the reciprocal of $\mathcal{N}_{ij}$. So once more with $\langle\chi_i\rangle = k_B(\mathcal{T}_i - T_{\rm eq})$, the Enskog equations that govern the relaxation of $\langle\chi_j\rangle$ is derived to be:

$$\frac{d\langle\chi_i\rangle}{dt} = \mathcal{C}[\chi_i], \tag{E.1a}$$

$$\mathcal{C}[\chi_i] = \frac{\langle n\rangle}{2}\int \frac{d^3\boldsymbol{p}_r}{m} p_r c_r(\boldsymbol{p}_r,t)\int d^2\Omega' \mathcal{D}_{\rm el}\Delta\chi_i. \tag{E.1b}$$

Then Taylor expanding the relative momentum distribution with respect to the temperature perturbation $\delta_i/k_BT_0$, gives

$$\begin{aligned} c_r(\boldsymbol{p}_r,0) &= \prod_i \left(\frac{1}{4\pi m k_B T_i}\right)^{1/2} \exp\left(-\frac{p_{r,i}^2}{4mk_BT_i}\right) \\ &\approx c_r^{(0)}(\boldsymbol{p}_r)\left[1+\left(\frac{p_{r,i}^2}{4mk_BT_0}-\frac{1}{2}\right)\frac{\delta_i}{k_BT_0}\right], \end{aligned} \tag{E.2a}$$

$$c_r^{(0)}(p_r) = \frac{1}{(4\pi m k_B T_0)^{3/2}}\exp\left(-\frac{p_r^2}{4mk_BT_0}\right). \tag{E.2b}$$

The expressions above render the collision integral

$$\begin{aligned} \mathcal{C}[\chi_j] &\approx \frac{\langle n\rangle}{2}\int\frac{d^3\boldsymbol{p}_r}{m} p_r c_r^{(0)}(\boldsymbol{p}_r)\left[1+\left(\frac{p_{r,i}^2}{4mk_BT_0}-\frac{1}{2}\right)\frac{\delta_i}{k_BT_0}\right]\int d^2\Omega'\mathcal{D}_{\rm el}\left(\frac{p_{r,j}'^2-p_{r,j}^2}{4m}\right) \\ &= \frac{\delta_i}{16(mk_BT_0)^2}\frac{\langle n\rangle}{2}\int\frac{d^3\boldsymbol{p}_r}{m}c_r^{(0)}(\boldsymbol{p}_r)p_r\int d^2\Omega'\mathcal{D}_{\rm el}'p_{r,i}^2\left(p_{r,j}'^2-p_{r,j}^2\right), \end{aligned} \tag{E.3}$$

which upon utilizing the time-reversal symmetry of elastic collisions

$$\mathcal{C}[\chi_j] \approx \frac{\delta_i}{16(mk_BT_0)^2}\frac{\langle n\rangle}{2}\int p_r^2 dp_r c_r^{(0)}(p_r)\frac{p_r}{m}\int d^2\Omega d^2\Omega'\mathcal{D}_{\rm el}'p_{r,i}^2\left(p_{r,j}'^2-p_{r,j}^2\right)$$

$$= \frac{\delta_i}{16(mk_BT_0)^2}\frac{\langle n\rangle}{2}\int p_r^2 dp_r c_r^{(0)}(p_r)\frac{p_r}{m}\int d^2\Omega' d^2\Omega \mathcal{D}'_{\rm el} p'^2_{r,i}\left(p^2_{r,j}-p'^2_{r,j}\right), \tag{E.4}$$

the expression above can also be written in a form that is explicit in the symmetry under exchange of indices $i$ and $j$:

$$\mathcal{C}[\chi_j] = -\frac{\delta_i}{32(mk_BT_0)^2}\frac{\langle n\rangle}{2}\int \frac{d^3\boldsymbol{p}_r}{m} c_r^{(0)}(p_r)p_r\int d^2\Omega' \mathcal{D}'_{\rm el}\left(p'^2_{r,i}-p^2_{r,i}\right)\left(p'^2_{r,j}-p^2_{r,j}\right). \tag{E.5}$$

I have used the suggestive notation $\mathcal{D}'_{\rm el} = \mathcal{D}_{\rm el}(p_r,\Omega')$. Plugging $\mathcal{C}[\chi_j]$ as written into Eq. (E.1a) and taking $\mathcal{T}_j(t) - T_{\rm eq} = \epsilon_j/k_B$, we obtain

$$\begin{aligned}
\gamma_{ij} &= -\frac{\mathcal{C}[\mathcal{T}_j]}{(\mathcal{T}_j(t)-T_{\rm eq})} \\
&= -\frac{k_B}{\epsilon_j}\mathcal{C}[\mathcal{T}_j] \\
&= \frac{\delta_i}{\epsilon_j}\frac{\langle n\rangle}{512}\int \frac{p_r^2 dp_r}{(\pi m k_B T_0)^{3/2}}\exp\left(-\frac{p_r^2}{4mk_BT_0}\right)\frac{p_r}{m}\int d^2\Omega d^2\Omega' \mathcal{D}'_{\rm el}\left(\frac{p'^2_{r,i}-p^2_{r,i}}{mk_BT_0}\right)\left(\frac{p'^2_{r,j}-p^2_{r,j}}{mk_BT_0}\right).
\end{aligned} \tag{E.6}$$

Finally, taking the limit of $\delta_i/(k_BT_0)\to 0$, we obtain $\varepsilon_{ij}$ in Sec. 4.2.2, having defined $\alpha_{ij} = \delta_i/\epsilon_j$ and using the equipartition theorem ($T_{\rm eq} = T_0 + \delta_i/3k_B$) to get

$$\frac{\delta_i}{\epsilon_j} = \begin{cases} 3/2, & i = j, \\ -3, & i \neq j. \end{cases} \tag{E.7}$$

# Appendix F

## The equilibrium Boltzmann equation

This appendix evaluates the Boltzmann equation at thermal, but not necessarily hydrodynamic equilibrium. The treatment here extends the derivation of the equilibrium Boltzmann Equation found in [103], to include arbitrary external potentials.

At thermal equilibrium, the left-hand side of the Boltzmann equation is given as

$$\frac{\mathcal{D}}{\mathcal{D}t} f_0 = \left( \frac{\partial}{\partial t} + v_i \partial_i - \frac{\partial_i V(\boldsymbol{r})}{m} \frac{\partial}{\partial u_i} \right) f_0 \tag{F.1}$$

$$= f_0 \left( \frac{\partial}{\partial t} + v_i \partial_i - \frac{\partial_i V(\boldsymbol{r})}{m} \frac{\partial}{\partial u_i} \right) \ln f_0, \tag{F.2}$$

where $f_0$ is of the form in Eq. (3.5) but with $\boldsymbol{v}$ replaced with $\boldsymbol{u}$, and $n_0$ is determined by the form of $V(\boldsymbol{r})$, so that

$$\ln f_0 = \frac{3}{2} \ln \left( \frac{m}{2\pi} \right) + \ln\left( n_0 \beta^{3/2} \right) - \frac{1}{2} \beta m \boldsymbol{u}^2. \tag{F.3}$$

The material derivative is defined as

$$\frac{D}{Dt} = \frac{\partial}{\partial t} + U_i \partial_i, \tag{F.4}$$

so that the $\mathcal{D}/\mathcal{D}t$ operator can be rewritten as

$$\frac{\mathcal{D}}{\mathcal{D}t} = \frac{D}{Dt} + u_i \partial_i - \frac{\partial_i V(\boldsymbol{r})}{m} \frac{\partial}{\partial u_i}. \tag{F.5}$$

We now treat the derivatives term by term.

First considering $u_i \partial_i \ln f_0$, we have

$$u_i \partial_i \ln f_0 = u_i \partial_i \left[ \ln(n_0) + \frac{3}{2} \ln(\beta) - \beta \frac{m \boldsymbol{u}^2}{2} \right]$$

$$= u_i \partial_i \ln(n_0) + \left( \beta \frac{m\boldsymbol{u}^2}{2} - \frac{3}{2} \right) u_i \partial_i \ln T + \beta m u_i u_j \partial_i U_j. \tag{F.6}$$

As for $D \ln f_0 / Dt$, we first consider the equations of conservation at thermal equilibrium which read

$$\frac{D}{Dt} \ln n_0 = -\partial_j U_j, \tag{F.7a}$$

$$\frac{D}{Dt} \ln T = -\frac{2}{3} \partial_j U_j, \tag{F.7b}$$

$$\frac{D}{Dt} U_i = -\frac{k_B T}{m} \partial_i \ln(n_0 T) - \frac{1}{m} \partial_i V(\boldsymbol{r}). \tag{F.7c}$$

The material derivative of $\ln f_0$ then becomes

$$\begin{aligned} \frac{D}{Dt} \ln f_0 &= \frac{D}{Dt} \left[ \ln(n_0) + \frac{3}{2} \ln(\beta) - \beta \frac{m\boldsymbol{u}^2}{2} \right] \\ &= -\frac{\beta}{3} m\boldsymbol{u}^2 \partial_j U_j - \beta u_i \partial_i V(\boldsymbol{r}) - u_i \partial_i \ln(n_0) - u_i \partial_i \ln T. \end{aligned} \tag{F.8}$$

Finally, the term explicit in the potential is

$$-\frac{\partial_i V(\boldsymbol{r})}{m} \frac{\partial \ln f_0}{\partial u_i} = \frac{\beta \partial_i V(\boldsymbol{r})}{2} \frac{\partial \boldsymbol{u}^2}{\partial u_i} = \beta u_i \partial_i V(\boldsymbol{r}). \tag{F.9}$$

Putting all these terms together, we get

$$\begin{aligned} \frac{\mathcal{D}}{\mathcal{D}t} \ln f_0 &= \frac{D}{Dt} \ln f_0 + u_i \partial_i \ln f_0 - \frac{\partial_i V(\boldsymbol{r})}{m} \frac{\partial}{\partial u_i} \ln f_0 \\ &= \left[ -\frac{\beta}{3} m\boldsymbol{u}^2 \partial_j U_j - u_i \partial_i \ln T - \beta u_i \partial_i V(\boldsymbol{r}) - u_i \partial_i \ln(n_0) \right] \\ &\quad + \left[ \beta m u_i u_j \partial_i U_j + u_i \partial_i \ln(n_0) + \left( \beta \frac{m\boldsymbol{u}^2}{2} - \frac{3}{2} \right) u_i \partial_i \ln T \right] \\ &\quad + \left[ \beta u_i \partial_i V(\boldsymbol{r}) \right], \end{aligned} \tag{F.10}$$

which gives the final result

$$\frac{\mathcal{D}}{\mathcal{D}t} \ln f_0 = \left( \beta \frac{m\boldsymbol{u}^2}{2} - \frac{5}{2} \right) u_i \partial_i \ln T + \beta m \left( u_i u_j - \frac{1}{3} \delta_{ij} \boldsymbol{u}^2 \right) \partial_i U_j. \tag{F.11}$$

This result is exactly that derived by Chapman and Enskog in the absence of an external potential, showing that $V(\boldsymbol{r})$ does not affect the derivation of the transport tensors.

# Appendix G

## Transport tensors from microscopic collisions

Deriving the transport tensors in the Chapman-Enskog fashion can be pretty gnarly [69], especially when anisotropic cross sections are involved. I'll do my best to make all the steps clear in this appendix chapter, for anyone who wants to utilize this method.

As detailed in App. F, the left-hand side of Eq. (5.7) evaluates to

$$\left(\frac{\partial}{\partial t} + v_k\partial_k - \frac{\partial_k V(\boldsymbol{r})}{m}\frac{\partial}{\partial u_k}\right) f_0 = f_0\big[V_k\partial_k(\ln T) + m\beta W_{k\ell}D_{k\ell}\big]. \tag{G.1}$$

where

$$V_i(\boldsymbol{u}) \equiv \left(\frac{m\beta\boldsymbol{u}^2}{2} - \frac{5}{2}\right)u_i, \tag{G.2a}$$

$$W_{ij}(\boldsymbol{u}) \equiv u_iu_j - \frac{1}{3}\delta_{ij}\boldsymbol{u}^2, \tag{G.2b}$$

$$D_{ij}(\boldsymbol{U}) \equiv \frac{1}{2}\left(\partial_jU_i + \partial_iU_j\right) - \frac{1}{3}\delta_{ij}\partial_kU_k. \tag{G.2c}$$

The collision integral (ignoring quantum statistical effects) on the right-hand side of Eq. (5.7) is then

$$C[f] \approx \int d^3\boldsymbol{u}_1|\boldsymbol{u}-\boldsymbol{u}_1|f_0(\boldsymbol{u})f_0(\boldsymbol{u}_1)\int d\Omega'\frac{d\sigma}{d\Omega'}\Delta\Phi, \tag{G.3}$$

where $\Delta\Phi = \Phi' + \Phi'_1 - \Phi - \Phi_1$ as in Sec. 3.2. Since Eq. (G.3) is linear in $\Phi$, and Eq. (G.1) is linear in the quantities $\partial_i \ln T$ and $\partial_jU_i$, one can infer an *ansatz* for the scalar function $\Phi$, of the form

$$\Phi(\boldsymbol{u},\beta) = \mathcal{B}_k\partial_k(\ln T) + m\beta\mathcal{A}_{k\ell}D_{k\ell}, \tag{G.4}$$

where $\boldsymbol{\mathcal{B}}$ (vector) and $\boldsymbol{\mathcal{A}}$ (rank-2 tensor) are functions of $\boldsymbol{u}$ and $\beta$. The *ansatz* above allows separation of Eq. (5.7) into an equation in velocity gradients, and those in temperature gradients:

$$f_0\, W_{k\ell} D_{k\ell} \approx C[f_0 \mathcal{A}_{k\ell}] D_{k\ell}, \tag{G.5a}$$

$$f_0\, V_k \partial_k (\ln T) \approx C[f_0 \mathcal{B}_k] \partial_k (\ln T). \tag{G.5b}$$

Upon further comparison of terms, it is only suitable to write $\boldsymbol{\mathcal{B}}$ and $\boldsymbol{\mathcal{A}}$ as

$$\mathcal{A}_{ij}(\boldsymbol{u}, n_0, \beta) = W_{k\ell}(\boldsymbol{u}) a_{k\ell ij}(u, n_0, \beta), \tag{G.6a}$$

$$\mathcal{B}_i(\boldsymbol{u}, n_0, \beta) = V_j(\boldsymbol{u}) b_{ji}(u, n_0, \beta), \tag{G.6b}$$

where $u = |\boldsymbol{u}|$, while $a_{k\ell mn}(u, n_0, \beta)$ and $b_{k\ell}(u, n_0, \beta)$ are introduced as variational coefficients that can, in general, be expanded into a basis of Sonine polynomials (a.k.a. associated Laguerre polynomials). The assumption of a low temperature gas however, allows us to approximate $\boldsymbol{a}$ and $\boldsymbol{b}$ with only the first basis term, which is independent of $u$. This truncation leaves us with

$$\Phi(\boldsymbol{u}, \beta) = V_\ell(\boldsymbol{u}) b_{\ell k}(n_0, \beta) \partial_k (\ln T) + m\beta W_{ij}(\boldsymbol{u}) a_{ijk\ell}(n_0, \beta) D_{k\ell}, \tag{G.7}$$

which has shown to give good accuracy (relative errors of $\sim 1\%$) in computing transport coefficients for gases of isotropic scatterers [62, 154, 155] Determining $\boldsymbol{a}$ and $\boldsymbol{b}$ will eventually allow us to evaluate $\boldsymbol{\kappa}$ and $\boldsymbol{\mu}$, but requires consideration of the micro-scale collisional physics. So, I'll do just that.

## G.1 Anisotropic thermal conductivity

Thermal conduction in a collisional gas arises through a transfer of kinetic energy by kinetic transport of the gaseous atoms, out of a region of fluid, resulting in a heat flux [101]

$$J_i(\boldsymbol{r}, t) = \int d^3\boldsymbol{u} f(\boldsymbol{r}, \boldsymbol{u}, t) \frac{1}{2} m \boldsymbol{u}^2 u_i. \tag{G.8}$$

In the first-order approximation with Eq. (G.4), the $\boldsymbol{\mathcal{A}}$ associated term does not contribute to the heat flux integral, leaving

$$J_i = \frac{m}{2} \int d^3\boldsymbol{u} f_0(\boldsymbol{u}) \left[1 + \Phi(\boldsymbol{u})\right] \boldsymbol{u}^2 u_i$$

$$= \left( \frac{k_B m \beta}{2} \int d^3\boldsymbol{u}\, f_0(\boldsymbol{u}) \boldsymbol{u}^2 u_i V_k b_{kj} \right) \partial_j T, \tag{G.9}$$

where the local temperature $T(\boldsymbol{r}, t)$ is written in terms of its kinetic definition,

$$\frac{3}{2} k_B T = \frac{1}{n(\boldsymbol{r}, t)} \int d^3\boldsymbol{u}\, f(\boldsymbol{r}, \boldsymbol{u}, t) \frac{1}{2} m \boldsymbol{u}^2. \tag{G.10}$$

Across a temperature gradient $\partial_j T$, Fourier's law of heat conduction dictates that the flow of heat across it follows the relation

$$J_i = -\kappa_{ij} \partial_j T. \tag{G.11}$$

A comparison of Eq. (G.9) and Eq. (G.11), then relates the thermal conductivity to the integral

$$\begin{aligned} \kappa_{ij} &= -\left( \frac{k_B m \beta}{2} \int d^3\boldsymbol{u}\, f_0(\boldsymbol{u}) \boldsymbol{u}^2 u_i V_k \right) b_{kj} \\ &= -\frac{5 n_0 k_B}{2 m \beta} b_{ij}, \end{aligned} \tag{G.12}$$

with the coefficients $b_{kj}$ introduced in Eq. (G.7). Referring back to Eq. (G.5b), multiplying Eq. (G.5b) by $V_i(\boldsymbol{u})$ and integrating over $\boldsymbol{u}$ gives

$$\left( \int d^3\boldsymbol{u}\, f_0(\boldsymbol{u}) V_i(\boldsymbol{u}) V_j(\boldsymbol{u}) \right) \partial_j (\ln T) \approx \left( \int d^3\boldsymbol{u}\, V_i(\boldsymbol{u}) C[f_0 V_k] \right) b_{kj} \partial_j (\ln T), \tag{G.13}$$

imposing that the coefficients of $\partial_j (\ln T)$ satisfy

$$K_{ik} b_{kj} = \delta_{ij}, \tag{G.14a}$$

$$\text{where} \quad K_{ik} \equiv \frac{2 m \beta}{5 n_0} \int d^3\boldsymbol{u}\, V_i C[f_0 V_k]. \tag{G.14b}$$

The integrals above are made complicated by the highly anisotropic differential cross section for dipoles, but that's not going to stop me from computing them! In fact, its evaluation is pretty identical to that already described in Sec. 3.2.1. So with much the same Mathematica® finagling as in Sec. 3.2.1, I arrived at the thermal conductivities in Eq. (5.8) of the main text.

## G.2 Anisotropic viscosity

Now comes the other transport tensor, viscosity. With twice as many indices, it's a real treat. On each differential parcel of fluid, the stress tensor $\boldsymbol{\varsigma}$ describes the forces in direction $\hat{\boldsymbol{r}}_j$, acting

on its surface defined by normal vectors $\hat{\boldsymbol{r}}_i$. These forces are illustrated schematically in Figure G.1, where all vectors appear to have the same length, although this is not always true in the fluid. Quite generally, the stress tensor can be written as

$$\varsigma_{ij} = -P\delta_{ij} + \tau_{ij}, \tag{G.15}$$

where $P$ is the thermodynamic pressure which, in a sufficiently dilute collisional gas, is related to the density and temperature by the ideal gas law. The remaining part, $\boldsymbol{\tau}$, is the viscous stress tensor, i.e., the part arising from viscosity. In a Newtonian fluid, the viscous shear is assumed to be a linear function of the velocity gradients:

$$\tau_{ij} = \mu_{ijk\ell}\, \partial_\ell U_k, \tag{G.16}$$

where $\boldsymbol{\mu}$ is the rank-4 viscosity tensor and the flow velocity gradients $\partial_\ell U_k$, characterize the rate of strain on differential fluid volumes. It turns out, however, that ultracold elastic collisions leave only a symmetrized portion of $\partial_\ell U_k$ relevant, as will be shown soon enough.

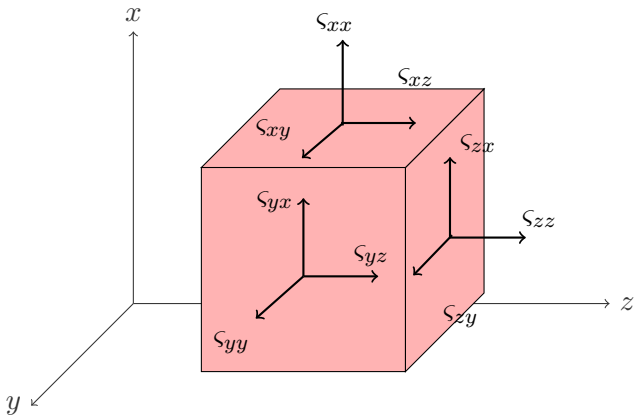


Figure G.1: Cartoon of the stresses (black arrows) on a differential fluid volume element (light red cube) due to thermodynamic pressure and velocity field gradients.

Microscopically, the fluid stress tensor arises from the decrease in flux of molecular momentum directed along $j$, across the plane oriented along axis $i$:

$$\varsigma_{ij} = -\int d^3\boldsymbol{u} f(\boldsymbol{u}) u_i p_j$$

$$= -m \int d^3\boldsymbol{u} f_0(\boldsymbol{u}) \left[1 + \Phi(\boldsymbol{u})\right] u_i u_j$$
$$= -\frac{n_0}{\beta}\delta_{ij} - 2\left(m^2\beta \int d^3\boldsymbol{u} f_0(\boldsymbol{u}) u_i u_j W_{mn} a_{mnk\ell}\right) D_{k\ell}. \tag{G.17}$$

This expression identifies the thermodynamic pressure as $P = n_0/\beta$, and the quantity in parentheses as related to the shear viscosity. Notice, the viscosity tensor in Eq. (G.16) gives the stresses in terms of the unsymmetrized rank-2 tensor $\partial_l U_k$, while the microscopic evaluation of stresses (G.17) relates these stresses only to the symmetrized tensor $\boldsymbol{D}$. The difference is telling: generally, this tensor can be reduced in the usual way into the traceless $\boldsymbol{D}$ tensor, along with an antisymmetric tensor $\boldsymbol{R}$, and a scalar:

$$\partial_\ell U_k = D_{k\ell} + R_{k\ell} + \frac{1}{3}\delta_{k\ell}\boldsymbol{\nabla}\cdot\boldsymbol{U}, \tag{G.18}$$

where

$$R_{k\ell} = \frac{1}{2}\left(\partial_\ell U_k - \partial_k U_\ell\right). \tag{G.19}$$

The absence of the antisymmetric tensor and the scalar from the expression connotes that there are no rotational viscosities, nor bulk viscosities in a dilute gas of particles with no internal degrees of freedom [69, 156, 157]. Without loss of generality, the viscous stress tensor can now be written as

$$\tau_{ij} = 2\mu_{ijk\ell} D_{k\ell}. \tag{G.20}$$

Note that this conclusion is independent of the form of the collision cross section of the molecules.

The relation between the two forms of the symmetrized tensors is conveniently handled via a contraction,

$$W_{ij}(\boldsymbol{u}) = \mathcal{I}_{ijk\ell} u_k u_\ell = u_k u_\ell \mathcal{I}_{k\ell ij}, \tag{G.21a}$$

$$D_{ij}(\boldsymbol{U}) = \mathcal{I}_{ijk\ell}\partial_\ell U_k = \partial_\ell U_k \mathcal{I}_{k\ell ij}, \tag{G.21b}$$

with the traceless symmetric tensor

$$\mathcal{I}_{ijmn} = \frac{\delta_{im}\delta_{jn} + \delta_{in}\delta_{jm}}{2} - \frac{1}{3}\delta_{ij}\delta_{mn}. \tag{G.22}$$

Written in these terms, the expression for the shear stress tensor in Eq. (G.17) is

$$\tau_{ij} = -2m^2\beta \int d^3\boldsymbol{u} f_0 u_i u_j u_m u_n \mathcal{I}_{mnop} a_{opk\ell} D_{k\ell}. \tag{G.23}$$

The integrand now consists of products of components of the peculiar velocity $\boldsymbol{u}$, multiplied by the known equilibrium velocity distribution. All such integrals are readily evaluated (many leading to Kronecker delta functions), whereby the viscosity tensor ultimately becomes

$$\mu_{ijk\ell} = -\frac{2n_0}{\beta}\mathcal{I}_{ijmn} a_{mnk\ell}. \tag{G.24}$$

To obtain explicit forms for the variational coefficients $a_{ijk\ell}$ and hence the viscosities by Eq. (G.24), we rewrite the right-hand side of Eq. (G.5a) as

$$\begin{aligned} 2C[f_0 W_{mn}] a_{mnk\ell} D_{k\ell} &= 2C[f_0 W_{mn}] \left(\mathcal{I}_{mnrs} a_{rsk\ell}\right) D_{k\ell} \\ &= -\frac{\beta}{n_0} C[f_0 W_{mn}] \mu_{mnk\ell} D_{k\ell}. \end{aligned} \tag{G.25}$$

Multiplying both sides of Eq. (G.5a) by $W_{ij}$ and integrating over $\boldsymbol{u}$ then gives

$$T_{ijk\ell} = M_{ijmn}\mu_{mnk\ell}. \tag{G.26}$$

where

$$T_{ijk\ell} = \int d^3\boldsymbol{u} f_0(\boldsymbol{u}) W_{ij} W_{k\ell} = \frac{2n_0}{(m\beta)^2}\mathcal{I}_{ijk\ell}, \tag{G.27a}$$

$$M_{ijmn} = -\frac{\beta}{n_0}\int d^3\boldsymbol{u} W_{ij}\mathcal{C}[f_0 W_{mn}]. \tag{G.27b}$$

The collision integrals of Eq. (G.27b) are evaluated with the collision-varied quantity

$$\Delta W_{ij} = \Delta(u_i u_j) = \frac{1}{2}\left(u'_{r,i}u'_{r,j} - u_{r,i}u_{r,j}\right), \tag{G.28}$$

and differential cross sections of Ref. [35], aided once more by Mathematica® [16]. Even after doing so, obtaining $\boldsymbol{\mu}$ requires $\boldsymbol{M}$ to be inverted (in the matrix sense), which is most easily performed by converting $\boldsymbol{M}$ into its matrix representation denoted by an overhead circle, $\mathring{\boldsymbol{M}}$. This representation is constructed by mapping index pairs to single indices $(i,j) \to (i')$, using the map

$$i' = 3(j-1) + i, \tag{G.29}$$

rendering $M_{ijk\ell} \to \mathring{M}_{i'k'}$. In its $9 \times 9$ matrix representation, the inherent symmetries of $\boldsymbol{M}$ reduces its matrix rank from 9 to 5. This prevents us from inverting the matrix in its current representation, so we are now required to perform a change of basis transformation which decomposes the $9 \times 9$ matrix into a block-diagonal matrix with a $5 \times 5$ irreducible block. The desired change of basis matrix $\mathring{\boldsymbol{C}}$, is obtained by diagonalizing the isotropic tensor $\boldsymbol{\mathcal{I}}$ in its matrix representation,

$$\mathring{\boldsymbol{\mathcal{I}}} = \mathring{\boldsymbol{C}} \left( \boldsymbol{I}_{5\times5} \oplus \boldsymbol{0}_{4\times4} \right) \mathring{\boldsymbol{C}}^{-1}, \tag{G.30}$$

where $\boldsymbol{I}$ and $\boldsymbol{0}$ are the identity and zero matrices respectively, with dimensions specified by their subscripts, and $\oplus$ denotes a direct sum. Applying the transformation $\mathring{\boldsymbol{C}}$ to Eq. (G.26) gives

$$\begin{aligned} \mathring{\boldsymbol{C}}^{-1} \mathring{\boldsymbol{T}} \mathring{\boldsymbol{C}} &= \mathring{\boldsymbol{C}}^{-1} \left( \mathring{\boldsymbol{M}} \mathring{\boldsymbol{\mu}} \right) \mathring{\boldsymbol{C}} \\ &= \left( \mathring{\boldsymbol{C}}^{-1} \mathring{\boldsymbol{M}} \mathring{\boldsymbol{C}}^{-1} \right) \left( \mathring{\boldsymbol{C}} \mathring{\boldsymbol{\mu}} \mathring{\boldsymbol{C}} \right), \end{aligned} \tag{G.31}$$

which leaves both sides of the equation above to only have a $5 \times 5$ non-trivial matrix block. The structure of these matrices is shown more explicitly by writing

$$\left[ \mathring{\boldsymbol{C}}^{-1} \mathring{\boldsymbol{T}} \mathring{\boldsymbol{C}} \right]_{5\times5} \oplus \boldsymbol{0}_{4\times4} = \left[ \left( \mathring{\boldsymbol{C}}^{-1} \mathring{\boldsymbol{M}} \mathring{\boldsymbol{C}} \right) \left( \mathring{\boldsymbol{C}}^{-1} \mathring{\boldsymbol{\mu}} \mathring{\boldsymbol{C}} \right) \right]_{5\times5} \oplus \boldsymbol{0}_{4\times4}. \tag{G.32}$$

The direct sum with $\boldsymbol{0}_{4\times4}$ is trivial, leaving only the $5 \times 5$ irreducible subspace to handle. This now allows $\mathring{\boldsymbol{M}}$ to be effectively inverted by

$$\left[ \mathring{\boldsymbol{C}}^{-1} \mathring{\boldsymbol{\mu}} \mathring{\boldsymbol{C}} \right]_{5\times5} = \left[ \left( \mathring{\boldsymbol{C}}^{-1} \mathring{\boldsymbol{M}} \mathring{\boldsymbol{C}} \right) \right]_{5\times5}^{-1} \left[ \left( \mathring{\boldsymbol{C}}^{-1} \mathring{\boldsymbol{T}} \mathring{\boldsymbol{C}} \right) \right]_{5\times5}, \tag{G.33}$$

and taking the direct sum of the expression above with $\boldsymbol{0}_{4\times4}$, to give

$$\mathring{\boldsymbol{\mu}} = \mathring{\boldsymbol{C}} \left( \mathring{\boldsymbol{C}}^{-1} \mathring{\boldsymbol{M}}^{+} \mathring{\boldsymbol{C}} \right) \left( \mathring{\boldsymbol{C}}^{-1} \mathring{\boldsymbol{T}} \mathring{\boldsymbol{C}} \right) \mathring{\boldsymbol{C}}^{-1} = \mathring{\boldsymbol{M}}^{+} \mathring{\boldsymbol{T}}, \tag{G.34}$$

where $\mathring{\boldsymbol{M}}^{+}$ is a pseudo-inverse of $\mathring{\boldsymbol{M}}$ defined by the procedure above, satisfying $\mathring{\boldsymbol{M}}^{+} \mathring{\boldsymbol{M}} \mathring{\boldsymbol{\mu}} = \mathring{\boldsymbol{\mu}}$. Finally, I apply the inverse mapping of Eq. (G.29) to attain the rank-4 tensor form of $\boldsymbol{\mu}$, presented in Eq. (5.10) of the main text.

## Appendix H

## Spatial averaging for an effective welter model

To obtain the spatially averaged equations of motion in Sec. 5.4, I start by defining a notation for spatially averaged quantities:

$$\langle \dots \rangle_r = \frac{1}{N} \int n(\boldsymbol{r}, t) \, (\dots) \, d^3\boldsymbol{r}. \tag{H.1}$$

This renders the density averaged equation for $\sigma_i(t)$ as

$$\begin{aligned} \frac{\langle r_i^2 T \rangle_r}{\sigma_i^2(t)} - \langle r_i \partial_i T \rangle_r &= \frac{m}{k_B} \left( \frac{\ddot{\sigma}_i(t)}{\sigma_i(t)} + \omega_i^2 \right) \langle r_i^2 \rangle_r - \sum_{j,k,\ell} \frac{\dot{\sigma}_k}{\sigma_\ell} \delta_{k,\ell} \int \frac{d^3\boldsymbol{r}}{N k_B} r_i \partial_j \mu_{ijk\ell}(T) \\ &= \frac{m}{k_B} \left( \frac{\ddot{\sigma}_i(t)}{\sigma_i(t)} + \omega_i^2 \right) \sigma_i^2(t) - \sum_{j,k,\ell} \frac{\dot{\sigma}_k}{\sigma_\ell} \int \frac{d^3\boldsymbol{r}}{N k_B} r_i \partial_j \mu_{ijk\ell}(T) \delta_{k,\ell}. \end{aligned}$$

As for the temperature balance equation:

$$\begin{aligned} &\frac{\partial T(\boldsymbol{r}, t)}{\partial t} + \sum_i U_i \partial_i T(\boldsymbol{r}, t) + \frac{2}{3} \sum_i \partial_i U_i T(\boldsymbol{r}, t) \\ &\qquad = \frac{2}{3 n(\boldsymbol{r}, t) k_B} \sum_{i,j,k,\ell} (\partial_j U_i)(\partial_\ell U_k) \mu_{ijk\ell}(T) + \frac{2}{3 n(\boldsymbol{r}, t) k_B} \sum_{i,j} \partial_i \left[ \kappa_{ij} \partial_j T(\boldsymbol{r}, t) \right], \end{aligned} \tag{H.2}$$

the product rule gives

$$\begin{aligned} \frac{d\langle T \rangle_r}{dt} &= \int \frac{d^3\boldsymbol{r}}{N} \left[ n(\boldsymbol{r}, t) \frac{\partial T(\boldsymbol{r}, t)}{\partial t} + T(\boldsymbol{r}, t) \frac{\partial n(\boldsymbol{r}, t)}{\partial t} \right] \\ &= \left\langle \frac{\partial T}{\partial t} \right\rangle_r + \sum_i \frac{\dot{\sigma}_i(t)}{\sigma_i(t)} \left( \frac{\langle r_i^2 T \rangle_r}{\sigma_i^2(t)} - \langle T \rangle_r \right), \end{aligned} \tag{H.3}$$

where I've utilized the continuity equation. Then multiplying the temperature balance equation by $n(\boldsymbol{r}, t)/N$ and integrating over $d^3\boldsymbol{r}$ gives

$$\frac{d\langle T \rangle_r}{dt} + \frac{5}{3} \sum_i \frac{\dot{\sigma}_i(t)}{\sigma_i(t)} \langle T \rangle_r - \sum_i \frac{\dot{\sigma}_i(t)}{\sigma_i(t)} \left( \frac{\langle r_i^2 T \rangle_r}{\sigma_i^2(t)} - \langle r_i \partial_i T \rangle_r \right)$$

$$= \frac{2}{3Nk_B}\sum_{i,j,k,\ell}\frac{\dot{\sigma}_i(t)}{\sigma_i(t)}\delta_{i,j}\left(\int d^3\boldsymbol{r}\mu_{ijk\ell}\right)\delta_{k,\ell}\frac{\dot{\sigma}_\ell(t)}{\sigma_\ell(t)} + \frac{2}{3Nk_B}\sum_{i,j}\int d^3\boldsymbol{r}\left[\partial_i(\kappa_{ij}\partial_j T)\right]. \quad \text{(H.4)}$$

Combining equations (H.2) and (H.4), we get

$$\begin{aligned}
&\frac{d\langle T\rangle_r}{dt} + \frac{5}{3}\sum_i \frac{\dot{\sigma}_i(t)}{\sigma_i(t)}\langle T\rangle_r - \frac{m}{k_B}\sum_i \dot{\sigma}_i(t)\left[\ddot{\sigma}_i(t) + \omega_i^2\sigma_i(t)\right] \\
&\quad\approx \frac{2}{3Nk_B}\sum_{i,j,k,\ell}\frac{\dot{\sigma}_i(t)}{\sigma_i(t)}\delta_{i,j}\left(\int d^3\boldsymbol{r}\mu_{ijk\ell}\right)\delta_{k,\ell}\frac{\dot{\sigma}_\ell(t)}{\sigma_\ell(t)} - \frac{1}{Nk_B}\sum_{i,j,k,\ell}\frac{\dot{\sigma}_i(t)}{\sigma_i(t)}\left(\int d^3\boldsymbol{r}r_i\partial_j\mu_{ijk\ell}\right)\delta_{k,\ell}\frac{\dot{\sigma}_k}{\sigma_\ell} \\
&\quad\quad + \frac{2}{3Nk_B}\sum_{i,j}\int d^3\boldsymbol{r}\left[\partial_i(\kappa_{ij}\partial_j T)\right]. \quad \text{(H.5)}
\end{aligned}$$

At this point, conservation of energy has that

$$\begin{aligned}
E_{\text{total}} &= \frac{m}{2}\sum_i\left(\omega_i^2\langle r_i^2\rangle_r + \int\frac{d^3\boldsymbol{r}d^3\boldsymbol{v}}{N}f(\boldsymbol{r},\boldsymbol{v},t)v_i^2\right) \\
&= \frac{m}{2}\sum_i\left(\omega_i^2\sigma_i^2 + \int\frac{d^3\boldsymbol{r}d^3\boldsymbol{v}}{N}f(\boldsymbol{r},\boldsymbol{v},t)v_i^2\right), \quad \text{(H.6)}
\end{aligned}$$

where $E_{\text{total}}$ is the total energy of the hydrodynamic system. Therefore, the relation above along with Eqs. (5.3) and (5.32) motivates the form for $\langle T\rangle_r$ as

$$\langle T\rangle_r = \frac{2E_{\text{total}}}{3k_B} - \frac{m}{3k_B}\sum_i\left[\omega_i^2\sigma_i^2(t) + \dot{\sigma}_i^2(t)\right], \quad \text{(H.7)}$$

and its time-derivative

$$\frac{d\langle T\rangle_r}{dt} = -\frac{2m}{3k_B}\sum_i\left[\omega_i^2\dot{\sigma}_i(t)\sigma_i(t) + \ddot{\sigma}_i(t)\dot{\sigma}_i(t)\right]. \quad \text{(H.8)}$$

Plugging these relations into Eq. (H.5) and assuming each axis can be solved independently, we obtain

$$\begin{aligned}
&\dot{\sigma}_i(t)\left[\ddot{\sigma}_i(t) + \omega_i^2\sigma_i(t)\right] + \frac{\dot{\sigma}_i(t)}{\sigma_i(t)}\left[\frac{1}{3}\sum_j\left(\omega_j^2\sigma_j^2(t) + \dot{\sigma}_j^2(t)\right) - \frac{2E_{\text{total}}}{3m}\right] \\
&\quad\approx \frac{3}{5Nm}\sum_{j,k,\ell}\frac{\dot{\sigma}_i(t)}{\sigma_i(t)}\left(\int d^3\boldsymbol{r}r_i\partial_j\mu_{ijk\ell}\right)\delta_{k,\ell}\frac{\dot{\sigma}_k}{\sigma_\ell} \\
&\quad\quad - \frac{2}{5Nm}\sum_{j,k,\ell}\frac{\dot{\sigma}_i(t)}{\sigma_i(t)}\delta_{i,j}\left(\int d^3\boldsymbol{r}\mu_{ijk\ell}\right)\delta_{k,\ell}\frac{\dot{\sigma}_\ell(t)}{\sigma_\ell(t)} \\
&\quad\quad - \frac{2}{5Nm}\sum_j\int d^3\boldsymbol{r}\left[\partial_i(\kappa_{ij}\partial_j T)\right]. \quad \text{(H.9)}
\end{aligned}$$

Finally, the conserved total energy $E_{\text{total}}$, is made up of the potential energy and thermal equilibrium temperature $T_0$:

$$E_{\text{total}} = \frac{3}{2}k_B T_0 + \frac{m}{2}\sum_i \omega_i^2 \sigma_{0,i}^2 = 3k_B T_0, \tag{H.10}$$

where we utilized that $\sigma_{0,i} = \sqrt{k_B T_0 / m\omega_i^2}$.

# Appendix I

## Quasi-empirical determination of the hydrodynamic volume

The quasi-empirical rigmarole I used to infer a functional form for the effective hydrodynamic volume parameter $\eta$, is a little involved. That's why I tucked it away here in the appendix, where sleepful nights go to die. But if you've stuck around till this point, I'll give you the details you asked for. Otherwise, Ref. [19] has them too.

Returning to the regularly scheduled program of Chap. 5, Eq. (5.34) is expected to be a reasonable representation of dynamics, provided the shape of the gas remains nearly Gaussian. To employ these equations, a value of the effective hydrodynamic volume must first be established. A first guess at this volume is given in Eq. (5.38), which left available a free parameter $\eta$, that may depend on $\lambda$ and Kn. As noted in Sec. 5.4, Kn is implicitly dependent on $N$ and $\Theta$, which are taken as the relevant independent variables for this study.

To extract $\eta$, I perform a bunch of DSMC (see Sec. 3.3) runs while varying $\lambda$, $N$ and $\Theta$, providing me time traces of $T_p(t)$ (5.36) for each combination of parameter values. I then fit $T_p(t)$ as computed from Eq. (5.34) to those from the DSMC simulations while floating $\eta$, such that it minimizes the relative root-mean-squared error

$$\varepsilon(\eta) = \sqrt{\sum_t \left( \frac{T_p^{\mathrm{DMSC}}(t) - T_p^{\mathrm{theory}}(t;\eta)}{T_p^{\mathrm{DMSC}}(t)} \right)^2}. \tag{I.1}$$

In these numerical experiments, we tune the trap anisotropy in a manner that does not affect Kn, by setting $\omega_\perp = \overline{\omega}/\lambda^{1/6}$ and $\omega_z = \overline{\omega}\lambda^{1/3}$. This construction ensures that $\overline{\omega}$, and therefore Kn, both remain independent of $\lambda$. The dipoles are taken to point along $\hat{\boldsymbol{x}}$ ($\Theta = 90^\circ$) for the data shown.

Dependence on dipole orientation will be included below.

Results of several such fits are shown in Fig. I.1, which compares the $T_p$ time traces for a series of cross-dimensional rethermalization experiments with $N = 5 \times 10^5$ (Kn $\approx 0.04$) over a range of $\lambda = 0.13$ to 8.0, as obtained from DSMC simulations (solid black curves) and my fitted theory (dashed red curves). Noticeably, there is a clear beating of various modes with different frequencies which our theory is able to describe, showing favorable agreement in both the amplitude and phase of oscillations. A representative comparison plot of $\mathcal{T}_r(t)$ as obtained from DSMC and Eq. (5.34) is also provided in Fig. I.2, with $N = 5 \times 10^5$ (Kn $\approx 0.04$) and $\lambda = 0.32$. Good agreement is seen in all $\mathcal{T}_{r_i}(t)$ time traces as well. We note that temperature time traces tend to show better agreement with the DSMC ones for excitation along the long axis of a prolate trap, even for larger Knudsen numbers (Kn $\approx 0.1$). So, I'll stick to this excitation geometry for a more focused study.

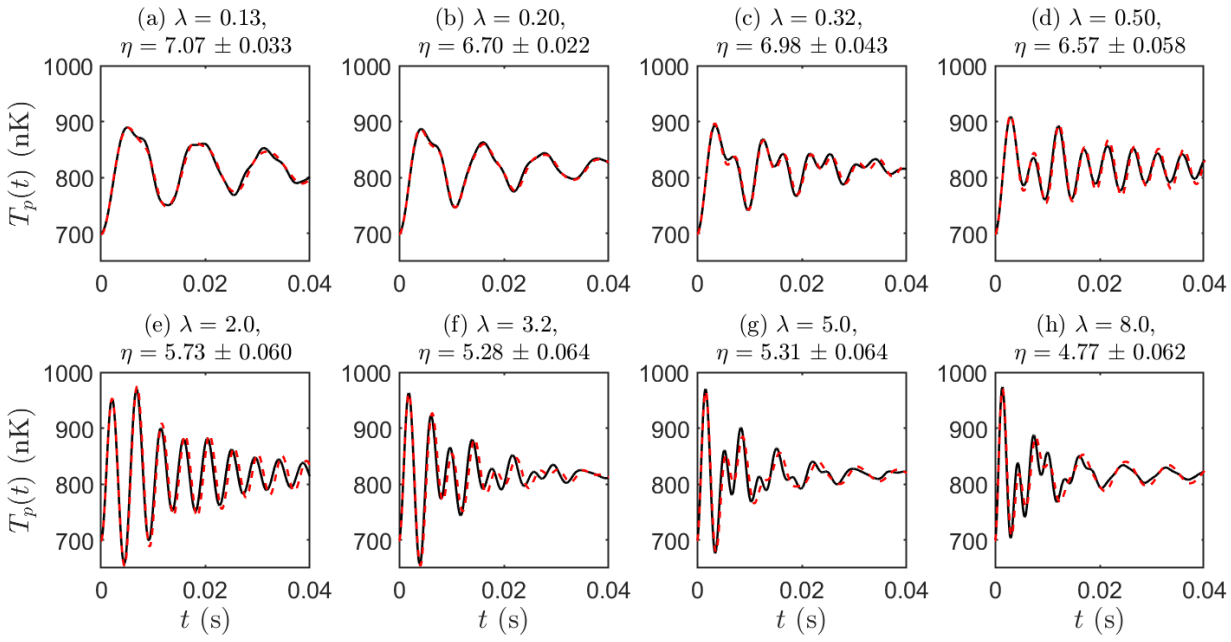


Figure I.1: Comparison of the momentum space temperature $T_p$ (5.36) vs time $t$, obtained from DSMC simulations (black solid curves) and our theory (red dashed curves) with $N = 5 \times 10^5$ (Kn $\approx 0.04$), $\Theta = 90°$. The subplots (a) to (h) correspond to various values of trapping anisotropy with $\lambda = 0.13$ to 8.0 as labeled in the subplot headers. The fitted values of $\eta$ are also provided in the subplot headers with their fitting standard uncertainties.

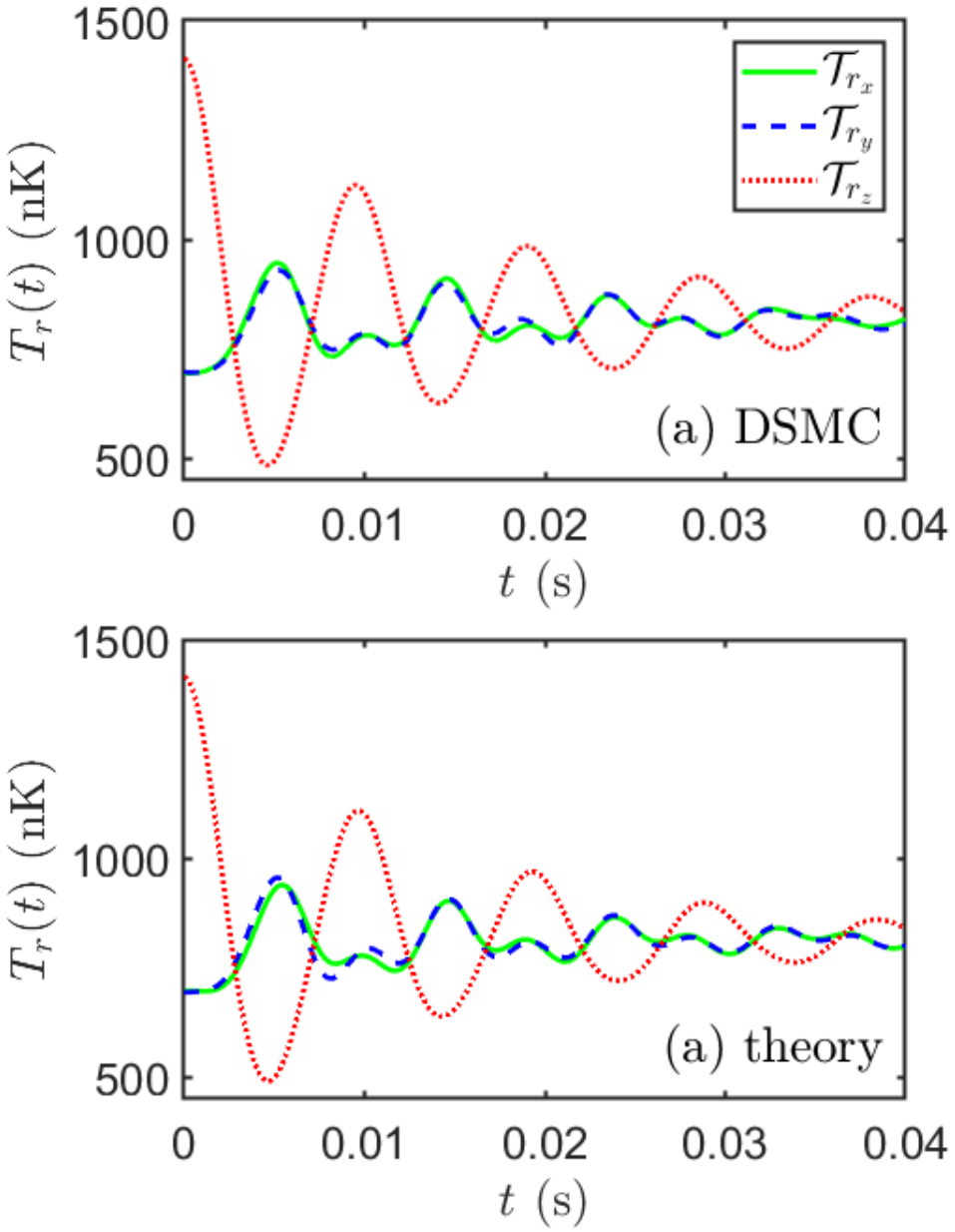


Figure I.2: Comparison of the position space pseudotemperatures $\mathcal{T}_r$ vs time $t$, obtained from DSMC simulations (upper subplot a) and our theory (lower subplot b) with $\Theta = 90°$, $N = 5 \times 10^5$ (Kn $\approx 0.04$) and $\lambda = 0.32$.

For a given orientation of the dipoles, it may be expected that $\eta$ depends on both the trap aspect ratio $\lambda$ and the number of molecules $N$. Increasing $N$, *ceteris paribus*, evidently increases the density and hence likely the hydrodynamic volume. As for aspect ratio, a tentative $\lambda$ dependence of $\mathcal{V}_{\text{hy}}$ is already taken into account by (5.38), whereby the scaling parameter $\eta$ may depend only

weakly on $\lambda$. This hypothesis is supported by the numerics shown in subplot (a) of Fig. 5.11, where $\eta$ is linearly dependent on $N$, but mostly independent of $\lambda$ for the range of these parameters explored.

Finally, for a given $\lambda$ and $N$, it remains to resolve the dependence of $\eta$ on the dipole orientation $\hat{\boldsymbol{\mathcal{E}}}$. In this context, recall that the dilute and hydrodynamic regimes are distinguished by the Knudsen number, which is inversely proportional to the collision cross section, Eq. (5.28). Sec. 5.4 detailed how this cross section results in anisotropic viscosities, that work to bring local thermodynamic fluctuations back to equilibrium. Having accounted for this aspect of differential scattering, I posit that $\eta$ should only depend on the cross section that's averaged over post-collision angles $\sigma = \int d\Omega' \frac{d\sigma}{d\Omega'}$, which still preserves an incoming-collision angle dependence [35]. As to how so, I present the following argument. Prolate traps have a weak trapping axis $z$, along which the gas has a larger thermal width. As a result, the mean-free path along that axis is relatively smaller compared to the sample size, and consequently more hydrodynamic. Collisions that occur with relative momentum directed along the long axis, are then most able to keep molecules behaving collectively as hydrodynamic. The bulk total cross section is, therefore, most simply taken to be

$$\sigma = a_d^2 \frac{\pi}{3}\left[3 + 18\cos^2(\hat{\boldsymbol{\mathcal{E}}}\cdot\hat{\boldsymbol{e}}_{\rm hy}) - 13\cos^4(\hat{\boldsymbol{\mathcal{E}}}\cdot\hat{\boldsymbol{e}}_{\rm hy})\right], \tag{I.2}$$

where $\hat{\boldsymbol{e}}_{\rm hy} = \hat{\boldsymbol{z}}$ denotes the most hydrodynamic axis (weakest trap frequency) so that $\hat{\boldsymbol{\mathcal{E}}}\cdot\hat{\boldsymbol{e}}_{\rm hy} = \Theta$.

Sure enough, I find that $\eta$ follows a $\Theta$ dependence very similar to that of Eq. (5.40), when comparing $\eta$ as obtained from DSMC experiments, to a fitting function of the form $(\sigma/\overline{\sigma})\alpha + \beta$ in subplot (b) of Fig. 5.11, where $\overline{\sigma} = (4\pi)^{-1}\int \sigma(\hat{\boldsymbol{e}}_{\rm hy}) d\hat{\boldsymbol{e}}_{\rm hy} = 32\pi a_d^2/15$ is the angular averaged total cross section. The observations above motivate the functional form

$$\eta \approx a + b\left(\frac{N}{10^5}\right)\left[1 + c\left(\frac{\sigma(\Theta)}{\overline{\sigma}}\right)\right], \tag{I.3}$$

for some constants $a, b$ and $c$, which I determine from fits to be $a \approx 2.21 \pm 0.017$, $b \approx 0.67 \pm 0.020$ and $c \approx 0.26 \pm 0.015$. The empirically determined hydrodynamic volume is therefore that presented in Eq. (5.39) of the main text.